NATIONAL TECHNICAL UNIVERSITY OF ATHENS
SCHOOL OF MECHANICAL ENGINEERING
DEPARMENT OF THERMAL ENGINEERING

Diploma thesis

with the topic

«Experimental and numerical study of methane thermal partial oxidation in a fuel reformer based on a wall flow filter»

submitted by

Benekos Sotiris
ID:02109722

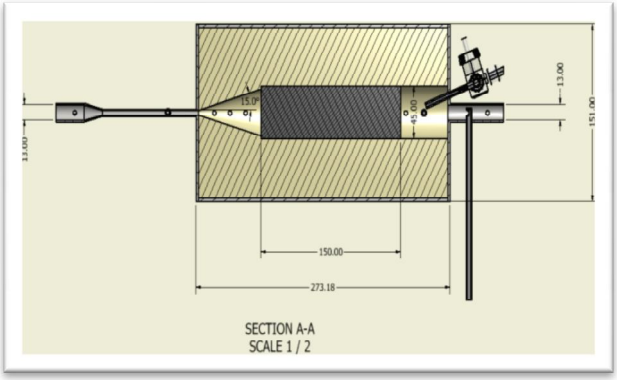

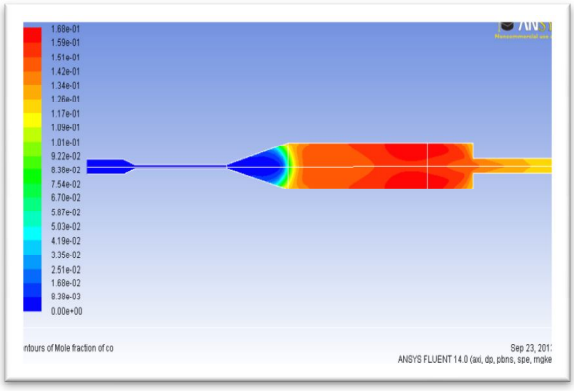

Supervisor: Prof. Dr.-Ing M. Founti

Athens 2013

Table of Contents

Abstract

This diploma thesis was realized in the framework of the Erasmus student exchange program in cooperation between National Technical University of Athens (Laboratory of Heterogeneous Mixtures and Combustion Systems) (Prof.M.Founti) and Technical University Bergakademie Freiberg (chair for Gas and Heat Technology) (Prof.D.Trimis).

An experimental and a numerical study was conducted for a thermal partial oxidation process of methane in a fuel reformer based on a wall flow filter or as so called soot trap. In the experimental part which was conducted in TU Freiberg was evaluated the enhancement in the characteristics of reforming process by utilizing a ceramic porous structure such as the soot trap, and further soot emission abatement in one component, the conditions of soot regeneration, the efficiency and the particulate emissions by measurements of soot particles distributions in the Scanning Mobility Particle Sizer (SMPS) and the exhaust gas analysis in its chemical species.

Concerning the numerical work, was elaborated a simplified model of the T-POX reactor in the ANSYS-Fluent commercial CFD package including chemical kinetics of the partial oxidation process. In this part a pressure drop model for soot trap of Konstandopoulos-Johnson as well as a reduced GRI-MECH were introduced and different cases in terms of thermal load and air equivalence ratios were simulated and were compared with the experimental results.

In both experimental and numerical work the thermal load which was investigated more, was 1,5 kW since the constructed reformer had a small size. The experimental results showed that efficiency reaches to 47% for air equivalence ratio 0,5 and to 56% during soot regeneration for air equivalence ratio 0,6. The soot point appeared for air equivalence ratio 0,42. The efficiency is notable and it could be increased more by operation in higher thermal loads and in combined with an optimization design. This maybe leads to lower soot points and could make the reformer based on a soot trap competitive.

Numerical work shows that it is possible the soot trap to be simulated in terms of pressure drop prediction by a porous packed bed domain in ANSYS take under consideration the real characteristics of soot trap. The results of chemical kinetic simulations were compared with the experimental and it was observed a good agreement except from the methane volume fractions where the simulation over predicted it.

Acknowledgements

I would like to thank my supervisors Prof. Dr.-Ing M. Founti and Prof. Dr.-Ing D. Trimis in Greece and in Germany respectively, for their confidence to be assigned me the work of this diploma thesis and i am grateful for every kind support that were provided me . I would especially like to thank my mentor Mrs. Alexandra Loukou and Mrs. Isabel Frenzel for their support in the designing, in the constructing and in the conducting of the experimental part of this diploma thesis. I would also like to thank Mrs. Alexandra Loukou for the guidance, advice and comments on the final text of the thesis. Furthermore, i would also like to thank my mentor in Greece Mr. Dr. G. Skevis for his support with guidance, knowledge, and advice on the final text. Concerning the numerical part of this work, i would like to thank the network administrators of the institute Mr. Freitag Jürgen and Mr. Degenkolb Christian for their substantial contribution in technical issues and support. Finally i would like to thank the staff of workshop for their fast response in the construction of experiment's components contributing in this way to be conducted more experimental investigations.

Chapter 1st: Introduction

1.1 Hydrogen technology

In this diploma thesis certain aspects of hydrogen technology were studied. In recent years there is an increasing interest in developing hydrogen technology because for several reasons is the fuel of the future. Hydrogen contains more energy per unit mass than any other fuel and produces minimum emissions when combusted and essentially no emissions when electrochemically converted to electricity in a fuel cell. Unfortunately, hydrogen is not readily accessible in its pure form and hence has to be produced from atomic bounded hydrogen in available sources e.g. water, hydrocarbon e.t.c. Reformation of hydrocarbons (mainly fossil fuels) is the most common process for producing H_2. Reforming requires the use of a fuel reformer, a topic which will be discussed below.
Reforming hydrocarbons advantages over other processes since for hydrogen production using fossil fuels upon which the current economy, with already infrastructure, have been developed. Therefore the necessity of a smooth transition to a hydrogen based economy have to be achieved, in order to meet the actual energy demand. Furthermore the already existent fossil fuels can be used to give us energy more efficiently, with fewer emissions.
Some special categories of high temperature hydrogen fuel cells HTFCs (high temperature fuel cells) such as the SOFCs (solid oxide fuel cells) and MCFCs (molten carbonate fuel cells) are in developed novel technologies for H_2-based energy production. These fuel cells are fuel flexible and can operate either on hydrocarbon or reformed hydrocarbon fuels. However, SOFC operation directly on hydrocarbon fuels is currently at a laboratory scale for small scale stacks, while for large scale stacks the fuel reformer may be integrated in the stack construction. By reforming can get H_2 and CO. The mixture consisting mainly of H_2 and CO is called "synthesis gas" or "syngas". Practical small scale systems rely entirely on fuel reforming processes in order to convert the fuel into syngas.
The syngas can be produced from liquid fuels (e.g heating oil, gasoline,diesel) and gaseous fuels (e.g natural gas, LPG) through reformate processes and used directly in HTFCs to generate electricity in combined heat and power applications CHP (combined head and power systems).CHP systems are quite promising for industrial and domestic applications. High pressure operation in hybrid systems is also a possibility and efficiencies up to 70% in combined SOFC-gas turbine power systems can be expected. Therefore SOFCs are particularly attractive compared to convectional energy systems because their high efficiency and low emissions. SOFCs have potential of very high efficiencies at elevated operating temperatures (600 ^{o}C-1000 ^{o}C) and another advantage compared to other fuel cells is that they have potential to operate in robust energy systems in a wide range of temperatures and in a wide range of syngas composition.

1.2 Reforming-syngas production

According to the above the focus must be on the procedures of syngas production which is necessary for fuel SOFCs. As we have already mentioned, this can be achieved through reforming fossil fuels or even biomass. A fuel reformer is necessary to integrate in the system, where the hydrocarbon will be converted into syngas.
Although numerous technologies exist for producing hydrogen, there three main prevailing:

- Steam reforming (SR)
- Autothermal refoming (ATR)
- Partial oxidation (POX) which means burning a rich mixture

Comparison of reforming processes

Partial oxidation and autothermal reforming processes have better dynamic responses and are more compact than a comparative steam reformer. The exothermic POX process appears advantageous in terms of system complexity and integration, since there is no need for an external heat source or a water balance. However, at the same time it is characterized by a relatively low hydrogen yield compared with SR or ATR processes.
In order to increase hydrogen production, POX reformers operate at very low air to fuel ratios (λ). However, due to the low temperatures prevailing at low λ the overall reaction rate reduced while the system leads to the production of very high quantities of soot thus increasing the risk of carbon deposition over the fuel cell anode and consequent deactivation. The overall reaction rate can be enhanced by the use of catalyst as in C-POX reformer, allowing to operate soot-free at very low air to fuel ratio, close to the stoichiometric optional conditions. However catalyst are sensitive against poisoning, get easily damaged by temperatures above 1000^{o}C and show tendency to degenerate by age.

1.3 T-POX reformer and "Superadiabatic" combustion in Inert Porous Medium (IPM)

A very promising alternative would be to enhance the reaction rate by internal heat recirculation that can be achieved by performing the POX in an inert porous material. This is a **T-POX reformer**. Furthermore, the stability of the flame is increased and the low adiabatic temperatures are tackled.

The better operating characteristics accomplished by the combustion inside of a porous medium, due to the phenomenon of "excess enthalpy combustion" which is explained below: Combustion in stationary porous media occurs inside the voids of the porous matrix. Energy is transferred to the solid by convection from the hot gases. Conduction and radiation through the solid porous medium, which has much higher thermal conductivity than the gas mixture and additionally radiates significantly, distributes some of this energy to the region upstream of the flame. This in turn transfers energy via convection to the incoming reactants. The porous matrix acts in essence as an internal preheater. This preheating allows for higher combustion temperatures and increased stability compared to a free premixed laminar flame. Furthermore, locally the flame zone may reach temperatures higher than the adiabatic flame temperature of the unburned mixture, which gives the name "superadiabatic" to this combustion technology. Finally, performing hydrocarbon oxidation processes in inert porous media result in flame speeds that are 10-30 times higher than the laminar flame speed due to the aforementioned intensive heat recuperation, which results in a higher reaction rates and higher flame stability.
The recent years, based on this phenomenon had developed porous burners which can provide high radiant flux for many industrial high temperatures systems and they called PRBs (Porous Radiant Burners)[10].

Chapter 2nd: Principles of combustion in IPM

2.1 Propagation and stabilization of flame in an IPM

This is a phenomenon of transport, where the heat and mass diffusion take place to a significant extent. The dimensionless numbers of Peclet and Lewis are used and generally defined as follows:

Peclet$=\frac{flow}{diffusion}$ → for heat Pe$=\frac{LU}{a}=Re\cdot Pr$ {Eq.2.1}

→ for mass Pe$=\frac{LU}{D}=Re\cdot Sc$ {Eq.2.2}

Re: dimensionless Reynolds number
Sc: dimensionless Schmidt number
L: characteristic length [m]
U: flow velocity [m/s]
D: mass diffusivity [m^2/s]
α: thermal diffusivity [m^2/s]

$\alpha=\frac{K}{\rho\, C_p}$
K: Thermal conductivity [W/mK]
ρ: density [Kg/m^3]
Cp: coefficient of thermal capacity[J/KgK]

Lewis$=\frac{thermal\ diffusivity}{mass\ diffusivity}=\frac{a}{D}=\frac{Sc}{Pr}$ {Eq.2.3}

Flame propagation experiments in porous media were carried out for mixtures with different Lewis numbers in order to determine the critical Peclet number, above which flame is possible. Flame propagation in porous inert media, depends on the structure and physical properties of the combustible gas. The resulting flame propagation modes can be classified into different regimes, which some important parameters are given in the following figure2-1.

Regime	Speed of combustion wave m/s	Mechanism of flame propagation
Low velocity (LVR)	$0 - 10^{-4}$	Heat conduction and interphase heat exchange
High velocity (HVR)	$0.1 - 10$	High convection
Rapid combustion (RCR)	$10 - 100$	Convection, low pressure gradient
Sound velocity (SVR)	$100 - 300$	Convection with significant pressure gradient
Low velocity detonation (LVD)	$500 - 1000$	Self ignition with shock wave
Normal detonation (ND)	$1500 - 2000$	Detonation with momentum and heat loss

Fig. 2.1: Flame propagation regimes in porous media [5]

2.1.1 Influence of heat transport in porous medium

Concerning the flame stabilization in porous inert media, significant differences occur in comparison with free flames. The stabilization depends mainly on the heat transport properties of the solid matrix. The heat transport inside of porous medium, is often described by an effective heat conductivity which comprises radiation and heat conduction of both solid and gas phase and additionally gas convection and dispersive mechanisms. The effective heat transport inside of a porous medium is 2-3 orders of magnitude higher than in free flames and can be considered the dominant parameter for flame propagation for most cases. Compared with free flames, the higher heat transfer, leads to faster flame propagation which hampers flame stabilization in porous media. For solving the task of flame stabilization in porous media, different approaches have been developed, which are summarized in figure 2.2.

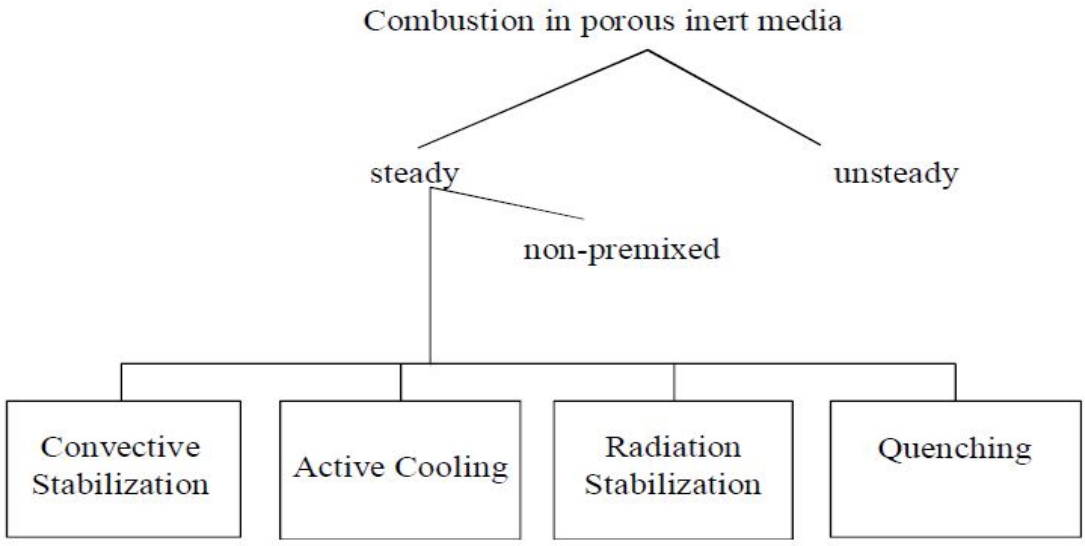

Fig. 2.2: Overview of stabilization methods in porous media [5]

In the most relevant for burner applications, LVR and HVR regimes flame propagation or extinction, can be described by a modified Peclet number, which is defined as follow:

$$\text{Pe}= \frac{S_L \cdot d_{p,eff} \cdot \rho_f \cdot C_{P,f}}{\lambda_f} = \frac{S_L \cdot d_p}{a_f} \qquad \{\text{Eq.2.4}\}$$

S_L: laminar flame speed [m/s]

$d_{p,eff}$: effective diameter pore [m]

ρ_f: density of fluid [Kg/m^3]

$C_{P,f}$: coefficient capacity of the fluid [J/KgK]

λ_f: thermal conductivity of the fluid [W/mK]

a_f: thermal diffusivity [m^2/s]

Subscripts
L: Laminar
p: pore
eff: effective
f: fluid

Pe is formed with the laminar flame speed S_L instead of a flow velocity and describes the ratio between the heat release due to combustion in a pore and the heat removal on the walls of a pore. This ratio must exceed a critical value for flame propagation in a cold medium, which it given as 65$\pm$45.
Flame propagation in this regime is dominated by convection but also the high conductivity and radiative properties of the solid matrix influence the flame speed. Further parameters of Pe are the effective pore diameter $d_{p,eff}$ and thermal diffusivity a_f. $d_{p,eff}$ represent an equivalent length scale for heat transport. The decision whether or not, flame propagation in porous inert medium will occur can be made by the choice of the pore size of the solid matrix. Thus, a critical pore size exists above which flame propagation and below which flame quenching occurs. Nevertheless, flame propagation may also occur in subcritical cavities if the temperature of the matrix is high enough, so that the reactions are not quenched by flow wall temperature. This kind of operation is often called filtration combustion.

2.1.2 Stabilization in steady combustion

In supercritical porous media in principle the same mechanisms of flame propagation act as in free flames but the higher effective heat conductivity must be taken into consideration. The effective heat conductivity as well as the thermal diffusivity are 2-3 orders of magnitude higher than in a gas. Following the simplified theory of flame propagation, the flame speed S is proportional to square root of the thermal diffusivity a_f:

$$S= \sqrt{\frac{\alpha_f}{\tau}} \qquad \{\text{Eq.2.5}\}$$

τ: the characteristic time scale of reaction

From this results that the flame speed in supercritical porous media is 10-30 times higher than the laminar flame speed. One possibility to stabilize the combustion, in supercritical porous media, is to induce a change of flow speed by stepwise or continuous change of the cross-sectional area, as in figure 2.3.For methane/air mixtures, in porous media, the required flow speed to avoid flashback, lies in the range of 2-5 m/s which is about ten times higher than in free flames [5].

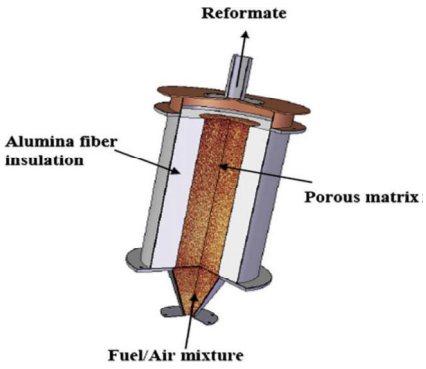

Fig. 2.3: A TPOX reformer [3] where the stabilization of flame is accomplished by changing of the cross-sectional area (conical geometry)

Another possibility for flame stabilization, is to apply cooling of the reaction zone e.g. by embedded water-cooled tubes in the main reaction zone. The cooling can also be realized by intense radiation from the reaction zone. In figure 2.4 these two principles are schematically shown. The porous surface extracts heat from the flame and radiates to the environment. Effective heat transport by radiation only occurs at high temperatures above the ignition limits. This means that for radiation-cooled burners the porous matrix must be subcritical, because otherwise the flame could slowly move into the porous matrix, which finally would lead to flashback.

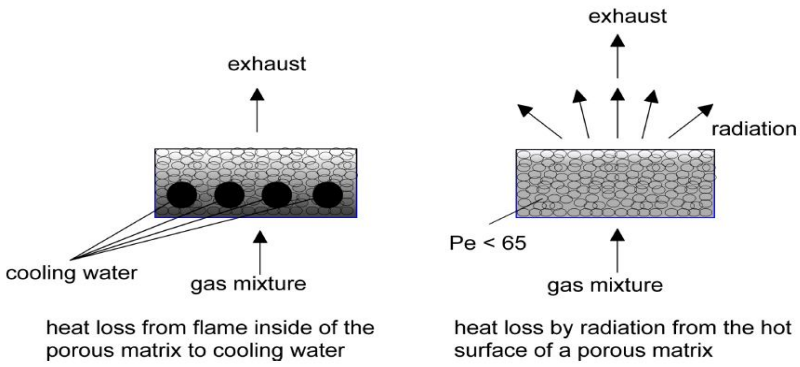

Fig. 2.4: Flame stabilization in porous media by cooling [5]

In another principle for flame stabilization was introduced which made use of thermal flame quenching. The combination of two regions with different pore sizes. The first region has subcritical Peclet number and the second region has supercritical Peclet number. Pe=65 assumed as critical.

In the first region through which the uncreated

cold gas mixture flows, combustion is not possible due to the subcritical Peclet number, so combustion only occurs in the supercritical second region at the interface between the two regions. This arrangement allows flame stabilization at the same position over a wide range of flow velocities. In order to prevent flashback the amount of heat which is transported against the flow direction, must not be higher than the amount which is carried convectively by the fresh gas mixture into the combustion region, because otherwise a combustion wave can develop starting from the hot interface between two regions, which possibly travels against the flow direction. This can be satisfied by means of a low conductivity first region which allows only a small amount of transport against the flow direction. In contrast, the second region should feature a high effective heat conductivity because this allows operation at high flow rate without the danger of blow-off. Typically, thermal heat loads of 3000 kW/m^2 and up to 4500 kW/m^2 for peak loads are feasible.

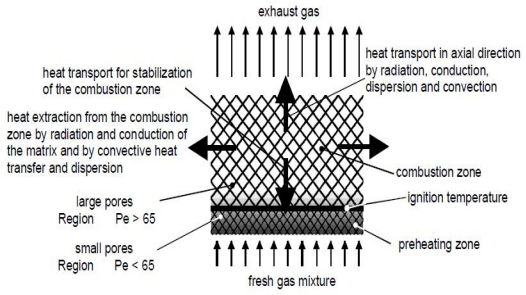

Fig.2.5: Heat transport and flame stabilization in a two-layer porous burner [5]

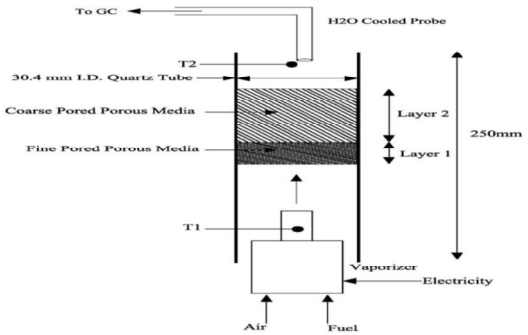

Fig.2.6:Heat transport and lame stabilization in a two layer porous burner[9]

2.1.3 Influence of diffusive mass transport

There are many ways for flame stabilization, as already mentioned, based on Peclet number. Nevertheless, in these cases, the influence of the diffusive mass transport, has not investigated intensively and this is the reason that for certain gas mixtures flame instabilities could be observed although the design of porous flame trap has based on value of Peclet number. The ratio between diffusive mass transport and heat transport can be described by Lewis-number Le_c of a component c of the gas mixture.

$$Le_c = \frac{\lambda_f}{D_c \cdot \rho_f \cdot C_{P,f}} = \frac{a_f}{D_c} \qquad \text{Eq.\{2.6\}}$$

ρ_f: density[Kg/m^3]

$C_{P,f}$: coefficient of thermal capacity[J/KgK]

λ_f: thermal conductivity of fluid[W/mK]

a_f: thermal diffusivity [m^2/s]

D_c: mass diffusivity [m^2/s]

Subscripts
c: component
f: fluid

The flame structure changes for Lewis-numbers smaller than unity. For many widely used gases, e.g. methane/air mixtures, Le is close to unity and therefore its influence is often neglected. However, mixtures with Lewis-numbers far below one require the consideration of mass diffusion. For example, hydrogen/air and hydrogen/chlorine mixtures feature Lewis-numbers of about 0.4. For such low values one can expect a strong influence of the diffusion on the flame stabilization in porous media.

2.2 Important parameters of hydrogen production in T-POX methane process.

There are some important parameters which influence the production of syngas and ultimately the production of hydrogen. These parameters are the initial mixture preheating, the residence time which relates with thermal load, the air/fuel ratio and also the properties of porous medium.

Many numerical and experimental studies for TPOX process of methane, have been conducted at Technical University of Freiberg in Germany (TU-Bergakademie Freiberg, Institute of thermal Engineering, Gas and Heat Technology)[1],[2],[3]. The prototype reformer, which is used for preliminary numerical simulation in this thesis paragraph 3.5, has the same design as the reformer which studied at [1],[2],[3]. Details of the design will be given in the respective paragraph. Thus, we considered that it was necessary to present a review of the reformer's study in order to take better understanding of the phenomena in a TPOX process, to summarize the issues that concern reforming and to look at new aspects for studying in this diploma thesis.

2.2.1 Equilibrium and chemical phenomena in methane partial oxidation.

By means of equilibrium calculations the optimum conditions of the partial oxidation process can been determined. Kinetic calculations deliver the information about how fast the reactions proceed under different conditions, e.g. the excess air ratio and the operating temperature. By the coupling of the thermodynamic and kinetic examinations, optimum set of parameters can

be found. The kinetic study for TPOX process with methane which conducted at TU-Bergakademie Freiberg investigated the influence of temperature and air/fuel ratio at the final production of hydrogen.

In the figure 2.7 shows the adiabatic temperature for methane/air mixture as a function of preheating temperature for different air ratio values. To avoid the destruction of the reactor, the reaction temperature above 1900 K should be avoided. At the same time, the reaction temperature should be as high as possible to ensure fast kinetics and complete conversion in a practical reactor size. In the figure 2.8 shows the progress of the hydrogen concentration in the reformate gas as a function of residence time for λ=0.4 and different reaction temperatures.

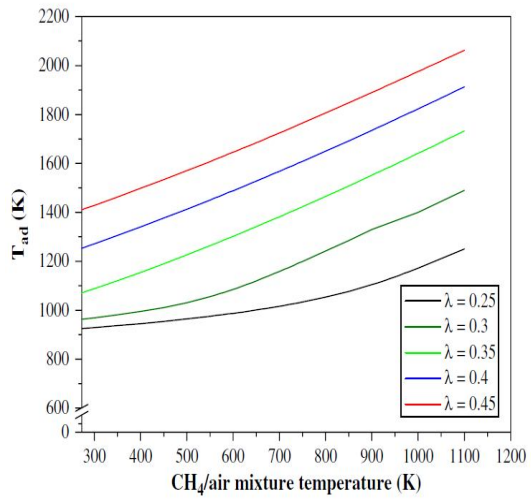

Fig.2.7: The adiabatic temperature for methane/air mixture as a function of preheating temperature for different air ratio values [3].

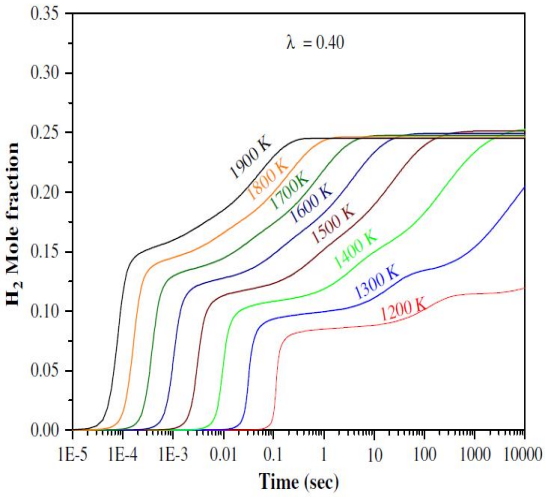

Fig.2.8: The progress of the hydrogen concentration in the reformate gas as a function of residence time for λ=0.4 and different reaction temperatures [3].

The figure 2.8 shows *that the reaction temperature has no influence to the final concentration of produced hydrogen and ultimately has low influence to the synthesis of syngas*. This is clear for temperatures above 1400°K and for temperatures above 1300°K and 1400°K which the residence time takes big values.

However, *the reaction temperature has significant influence to the residence time that the equilibrium reached*. For the case of 1900K, the equilibrium time is about 0.1s, while at 1400K it is about 1000s. From figure 2.7 and 2.8 it can be seen that for a preheating temperature of 1000K the adiabatic flame temperature is 1700K for the case of λ=0.4. At these conditions, the hydrogen mole fraction will be 20% after about 1 s.

For lower air ratio values, higher preheating temperature is needed to achieve higher reaction temperature. With such preheating, the risk of self-ignition increases. It can be concluded that an air ratio down to 0.4 is a practical limit for the thermal partial oxidation of methane.

2.2.2 Reformer studies in TPOX methane for Thermal load/Preheating/Soot point

As mentioned in reference [3], at the experimental part of investigation of TPOX methane process in porous reactor, conducted experiments at the reformer which shown at figure 2.9 below. Temperature measurements were taken at the center axis of the TPOX reactor, reformate samples were also taken and concentration of major species H_2, CO, CO_2, CH_4, O_2, C_2H_2, H_2O determined. Two different porous materials were used in the TPOX reactor as a reaction zone, Al_2O_3 static mixer and SiC foam (10 ppi). The experiments were performed with different preheating temperatures, air ratios and different thermal loads. The soot point was investigated for each case using Bacharach test. The residence time in the reactor (400 mm long) is in the range of 2.45 s at 3kW-0.29 s for the case of 30 kW.

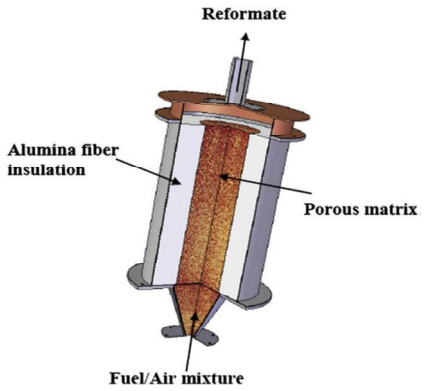

Fig. 2.9: A 3D representation of the TPOX reformer

- Influence of **Thermal load**

The results of this experimental study [3] show that the H_2 concentration was higher for higher thermal loads although the residence time was smaller. This is happened because the heat losses are more at high thermal loads in comparison with cases of low thermal loads. Consequently, lower temperature profile was measured in the case of low thermal. Furthermore, it show that the temperature level is decreasing in the downstream due to the heat loss. Thus, the soot point at the higher power was at lower air ratio than in the case of low power.

- Influence of **preheating**

In accordance with the aforementioned kinetic study [3] and from the experimental results show that the air preheating has low effect on the final concentration of the produced H_2.However, preheating affects the temperature profile of reformer and the soot point.

- **Soot point**

As already mentioned, soot point depends from preheating [3]. Soot point is the point where the conditions favour the production of soot. For POX methane within Al_2O_3 static mixer and 500^{o}C soot point was detected for air ratio λ=0.45 while for the case of 700^{o}C, soot point was detected for λ=0.48. SiC foam based reformer can operates at lower air ratio in comparison

with Al_2O_3 static mixer one because the SiC foam properties favour higher heat recuperation (paragraph 1.3) and therefore soot point appears in lower ratios.

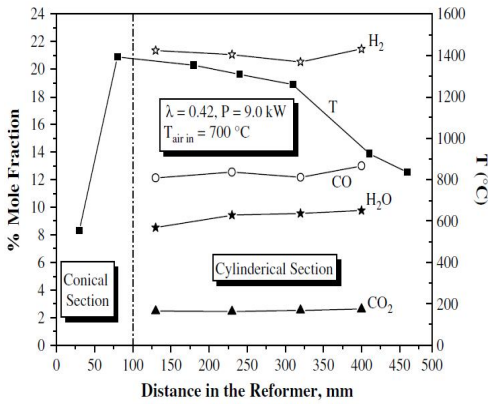

Fig. 2.10: The concentration of the different species and the temperature level in the TPOX reformer at a thermal power of kW, λ=0.42 (the soot point) and preheating temperature of 700°C with SiC foam as a reaction zone.

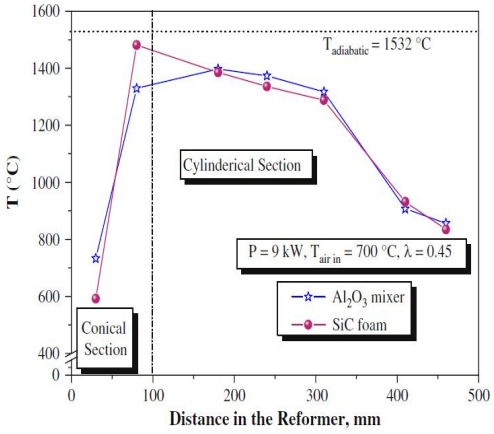

Fig. 2.11: Temperature profile in the SiC foam based reactor and in the Al_2O_3 mixer one for λ=0.45, thermal power of 9 kW and air preheating temperature of 700°C.

The characteristics of a SiC foam based reformer was chosen for the preliminary numerical simulation at the present work as the properties of SiC foam enable higher temperature profile compared to Al_2O_3 mixer (Fig.2.11) and ultimately the appearance of soot point is at lower air ratio. Practically, a SiC foam based reformer for air preheating temperature of 700°C and for thermal load 9kW, appears soot point at air ratio λ=0.42 (Fig.2.10). Additionally the position of maximum temperature indicating the location of the flame stabilization was shifted in the upstream direction in comparison to the Al_2O_3 structure case. This finding is a result of the higher internal heat recuperation in the SiC case caused by the higher effective conductivity. The SiC material has a higher conductivity (20-50 W/mK at1000°C) than the alumina one (5-6 W/mK at 1000°C) and also shows a higher emissivity (almost black body) than the alumina structure. Thus, a higher H_2 concentration level is reached in the reformer earlier.

2.3 Soot regeneration

According to the above- mentioned, the lower air ratio leads to higher production of hydrogen at a T-POX process, but at the same time increasing the production of soot if the air ratio is under the soot point. In a such case, the risk of carbon deposition over the fuel cell anode is increased and as a consequence leads to its deactivation.

A solution at this problem according to the paragraph 2.2.2 is to preheat the air and fuel mixture. Preheating leads to a higher temperature level profile and as a consequence the air ratio of soot point (λc) shifted to lower values compared to the air ratio of operation.

Indicatively, the kinetic study showed that the combination of preheating at 700°C and combustion is able to increase the temperature of the reaction zone at 1400°C . In this case for SiC foam based reformer, the air ratio is quite low λ=0.42 and the prevailing operating condition without produce of soot.

However, more preheating must be done, in the case that more lower air ratio is required, in order to be greater the operating air ratio (λ) than air ratio (λc) where soot point appears. But the decreasing of air ratio has a restriction which depends by the limit of preheating increase. For high temperature preheating the risk of spontaneous combustion increases.

Therefore, in the case that low air ratio chosen in order to produce more concentration of hydrogen, the simultaneous production of soot is inevitable and its presence should be addressed.

Nevertheless, soot removal can become seriously problematic in these plants due to the absence of oxygen in the syngas. Traditional processes for soot trap regeneration such as the technologies adopted for diesel engines, cannot be used in passive regeneration system since they are based on combustion.

Particulate abatement solutions, based mainly on the adoption of specific Diesel Particulate Filters or DPF (fig. 2.12) that can trap the soot within specific ceramic porous structures, have been introduced recently by the automotive sector in order to tackle such emissions in the environment.

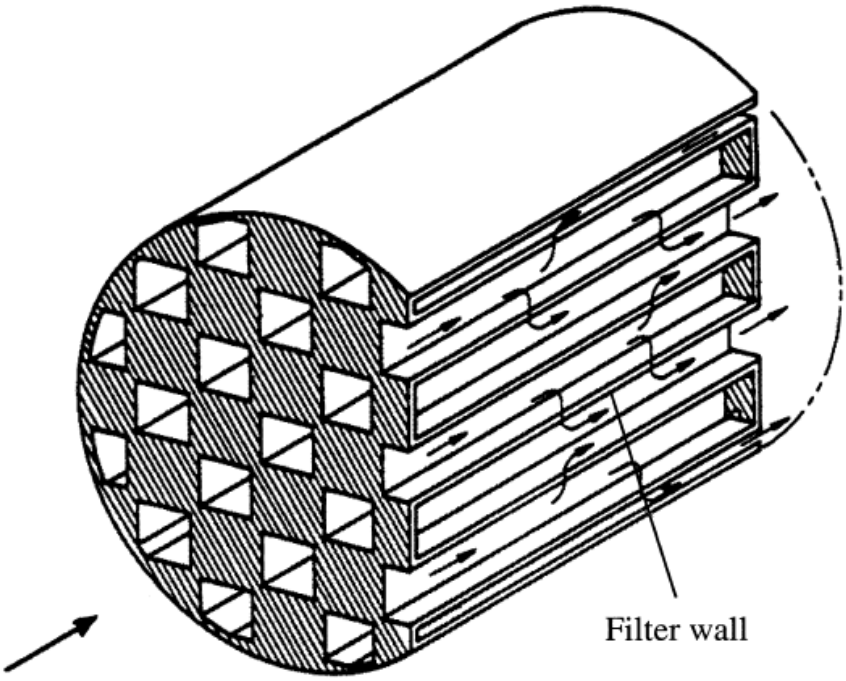

Fig. 2.12: Wall flow particulate filter

The retention of the particulate within these filters generates a drawback concerning the progressive increase in the backpressure on the system. As a specific value of pressure is achieved, that has to be fixed by each system on the basis of its technical characteristics, the particles have to be removed. The possibility of removing particulate, by burning it with oxygen, in a process called **regeneration**. However, considering that the fuel processor here developed has the aim of feeding a SOFC, it is not easy to apply standard regeneration with

oxygen. Oxygen at higher temperatures than 500°C can in fact oxidize the catalysts at the fuel cells anode, generally Ni-based, and alternative solutions should
be considered in order to combine the TPOX reforming of fossil fuels with SOFCs. A promising solution is mainly based on soot gasification via syngas, operating the reformer together with a soot-trap.
The syngas produced by POX reforming is mainly constituted by H_2,CO,H_2O,CO_2 and a non-negligible percentage of C_2H_2 (considered a major soot precursor). The possibility of gasifying the soot in this specific environment can be reached by operating continuously at high temperatures above 700°C inside the trap, according to the most important gasification following reactions:

$$C + CO_2 \rightarrow 2CO \quad (\Delta H = 131\ kj/mol) \qquad (React.2.1)$$
$$C + H_2O \rightarrow CO + H_2 \quad (\Delta H = 172\ kj/mol) \qquad (React.2.2)$$

In particular, reaction (2.1), which is also called the reverse Boudouard reaction (K. Nagase et al. 1999), presents interesting carbon gasification properties at the common operating temperatures of the actual systems based on SOFC technology, even in the absence (M. Haghighi et al. 2007, T. Osaki et al. 2006).

Practically, gasification would be possible if a wall flow filter or so called soot trap was mounted immediately next to the outlet of the reformer in order to achieve decoupling of time scales between flow and gasification, giving more time at the soot to gasified within soot trap. It is a simple solution for the retention of soot and for the protection of fuel cell anode, while guarantees its good operation for a long time and low particulate emissions in accordance with current legislation.

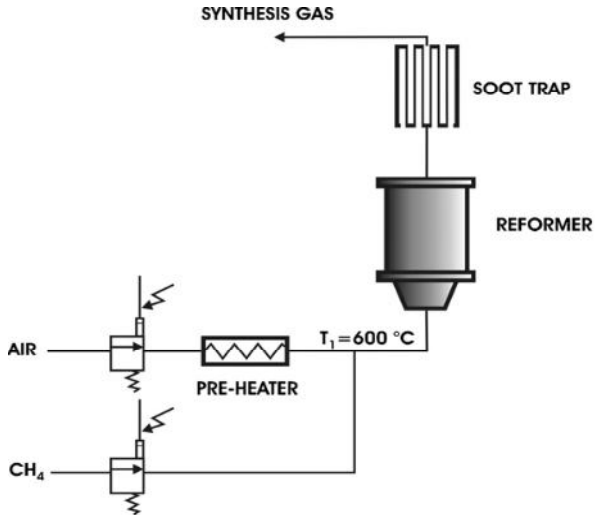

Fig. 2.13: Schematic diagram of a reforming system with an incorporated soottrap [4].

The possibility of soot gasification within a soot trap working in combination with a TPOX reformer has already investigated. The experimental stack in the figure 2.13 above derives from the reference [4] where the problem of soot retention by syngas was studied. This study was conducted at Department of Materials Science and Chemical Engineering, Politecnico di

Torino in 2008. It proved that it was achievable a continues gasification of soot directly with syngas at high temperatures (remarkable gasification showed for trap temperatures higher than 900 ^{o}C).

More specifically, the solution is based on the possibility of establishing a dynamic equilibrium, where the soot produced by the reactor is first trapped and then gasified within a wall-flow filter, thus guaranteeing a constant backpressure. This route represents a major goal in the development of a multi-fuel processor for synthesis gas production to feed HTFC (High Temperature Fuel Cells) for small-scale applications.

Two more detailed experimental studies [1], [2] followed concerning the regeneration of soot and relevant issues. These studies was conducted at TU-Bergakademie Freiberg, Institute of thermal Engineering, Gas and Heat Technology, in 2010 and in 2011. In the next part, these important studies will be analyzed in order to show a full coverage of soot regeneration issues, because *soot regeneration will be one of the subject of an experimental study of this diploma thesis in an new concept that aims to increase the efficiency of the reforming process without the problems that are caused by soot.*

In reference [1] and [2] was studied the influence of the parameters below : preheating of air stream for different thermal loads, the influence of air ratio to accumulation/gasification of soot within a soot trap which is mounted next to the outlet of the reformer as in figure 2.13. The soot- trap (fig.2.12) was constituted by a SiC wall-flow filter, which presents a higher filtration efficiency than 99%.The component was made in a ceramic porous material in order to allow the exhaust gas to pass through the porosities and retain the soot particles. The progressive accumulation of particles within the wall-flow channels creates a solid structure, that is called cake, which generates an increase in the pressure drop. An excessive backpressure of the filter, that in the specific case and in real operating conditions of the whole system is assumed around 10 mbar, is a drawback to the correct operation of the system. It is therefore necessary to define a proper regeneration strategy in order to gasify the particulate and re-establish the normal operating conditions in the system. The route of deactivation the application and cleaning the filter is not practical, instead it is more practical to regenerate the soot in continues operation as we have already mentioned. Soot regeneration is possible in a specific range of air ratio and was determined for some cases in reference [1] and [2]. The soot dynamics in the wall flow channels were analyzed by examining the difference in pressure between the filter inlet and outlet, and this was considered an indirect index of the deposition/gasification in the channels. The temperatures of the experiment was over 800 ° C in order to favor the reactions 2.1, 2.2.

2.3.1 Influence of equivalence air ratio in regeneration

The effect of the regeneration evaluated over a wide range operating range [2]. It was shown that it was achievable to control the back pressure of the filter (amount of soot in the filter wall) if the system is operated at specific values of lamda. In particular high lamda showed fast filter regenerations.

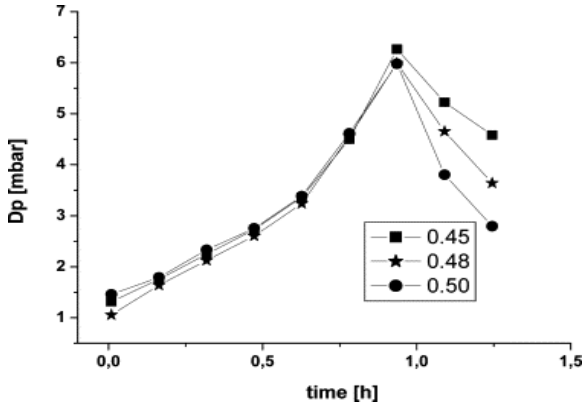

Fig. 2.14: Evaluation of the effect of air ratio alone on trap regeneration (Thermal load 8kw, loading lamda 0.40,preheating temperature 550^{o}C)

2.3.2 Influence of preheating air in regeneration

The preheating influence was evaluated at the same experimental study [2]. It was shown that the preheating has a slight effect on the filter loading and regeneration but seems to be correlated to a slower loading of the wall-flow channels. This positive effect could, however, also be related to more efficient reforming process and a smaller amount of produced particulate (see figs.2.15 and 2.16)

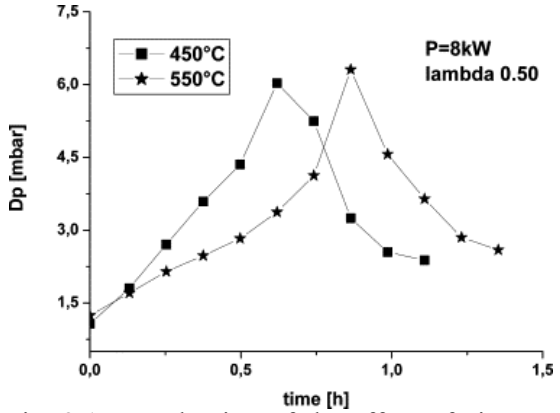

Fig. 2.15: Evaluation of the effect of air pre-heating on the regeneration of the soot-trap at lamda 0.50 (thermal load 8 kW, loading lamda 0.40 kW)

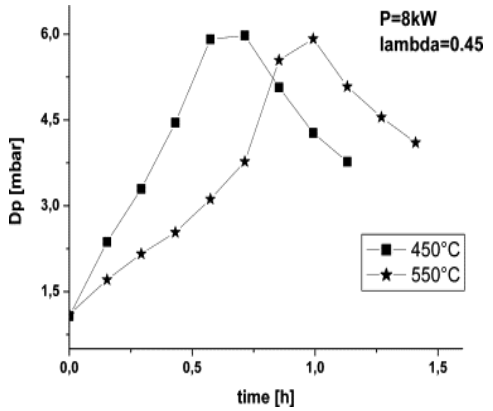

Fig. 2.16: Evaluation of the effect of air pre-heating on the regeneration of the soot-trap at lamda 0.45 (thermal load 8 kW, loading lamda 0.40 kW)

2.4 Soot formation processes

Soot formation is an important and constantly studied aspect of combustion. Since in substoichiometric combustion as in a TPOX reactor can lead to a production of soot, the basic theories of soot formation processes are referred in this section.

The carbon atom is unique among all other elements because it forms thermodynamically and kinetically extremely stable bonds to hydrogen- or other carbon atoms. This is the reason for the formation of solid carbon particles even in a high-temperature environment as it is found in understoichiometric combustion. Soot, however, is a side product in the process of energy production, and is unwanted because it exerts a large warming influence on global climate, and soot particles in the atmosphere are found to be a serious hazard to human health (see, for example cancer, mortality, and allergies). Because our civilization still relies on the combustion of fossil fuels for power generation, the formation of soot has a tremendous impact on mankind [21]

Under ideal conditions, stoichiometric combustion of hydrocarbons leads to carbon dioxide and water, but conditions in practical combustion devices may locally deviate from ideality. Depending on the proportions of air and fuel involved in a specific combustion reaction it can be classified as stoichiometric, lean, or rich. Parameter used to describe these proportions are the air/fuel ratio lambda (λ).

$$\lambda = \frac{m_{fuel} / m_{oxidizer}}{\left(m_{fuel} / m_{oxidizer} \right)_{stoichemtr\,ic}} \qquad \{Eq\ 2.7\}$$

For stoichiometric reactions, $\lambda = 1$, there is enough oxygen present to convert all fuel completely into carbon dioxide and water. No excess oxygen is left after reaction termination. Lean combustion, $\lambda > 1$ is characterized by an excess of oxygen needed for fuel conversion, whereas the term rich combustion, $\lambda < 1$ describes a lack of oxygen in combustion reactions.

Substoichiometric combustion as in the TPOX reactor can lead to the production of soot. The formation of soot in hydrocarbon combustion processes cannot be explained solely by a thermodynamic reasoning.

It is a result of a complex set of chemical reactions occurring in the gas phase that leads to formation of polycyclic aromatic hydrocarbons (PAH). [22]

The formation of the PAHs and the processes taking place during the soot formation are shown in figure 2.17 and are explained in the next sections of this chapter in summary.

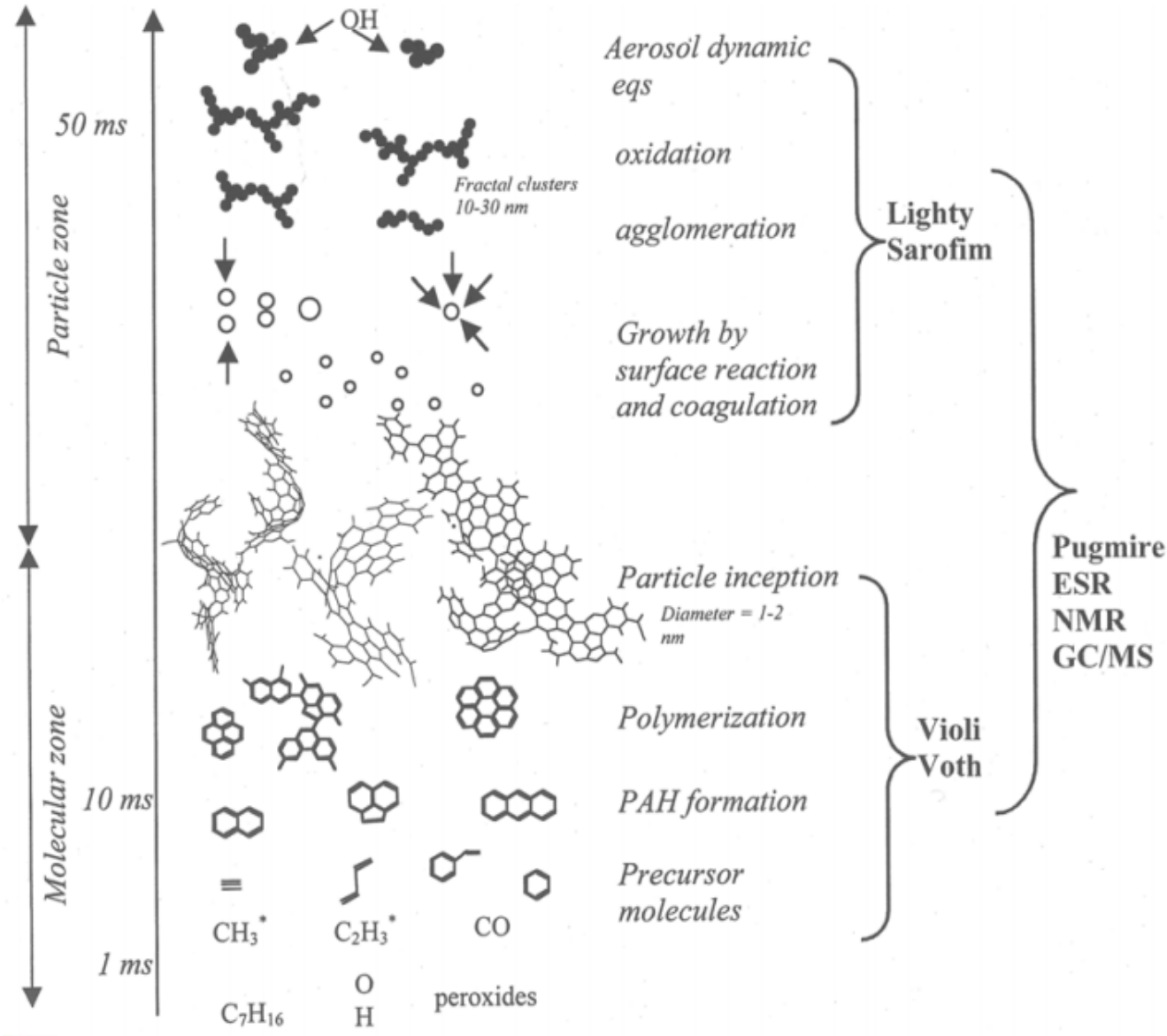

Fig. 2.17: A rough picture for soot formation in homogeneous mixtures (premixed flames).

Reactions in the Gas Phase

There have been made several principal proposals regarding the general nature of soot particle inception; these involve polyacetylenes , ionic species, or polycyclic aromatic hydrocarbons as the key gaseous precursors to soot. During the recent decades two primary theories for the gas phase chemistry associated with soot formation have been promoted: An ionic theory and a

theory based on the reactions of free radicals. The majority opinion at present, supported by numerous experimental and modelling studies, is that soot particles form via PAHs.

The PAH hypothesis also embraces the recent proposals on particle inception through formation of aromatic-aliphatic-linked hydrocarbons which graphitize later. [24]

The ionic theory for soot formation is primarily advocated by Calcote and co-workers [25] and is schematically illustrated in figure 2.18. The theory suggests that formation of soot origins from a sequential growth of ions starting with the chemi ion $C_3H_3^+$. The growth of positive hydrocarbon ions occurs via addition of small neutral species, typically acetylene or diacetylene, and each addition is followed by a dehydrogenation step. Once the positive ion reaches a certain critical size, it may recombine with a negative ion and produce the first neutral primary soot particle. Calcote [25] presents a number of arguments in his released work and argues against the radical nature of chemical reactions being responsible for the formation of soot and claims that neutral species can not possibly explain the fast growth rates, whereas those of ions can. [22]

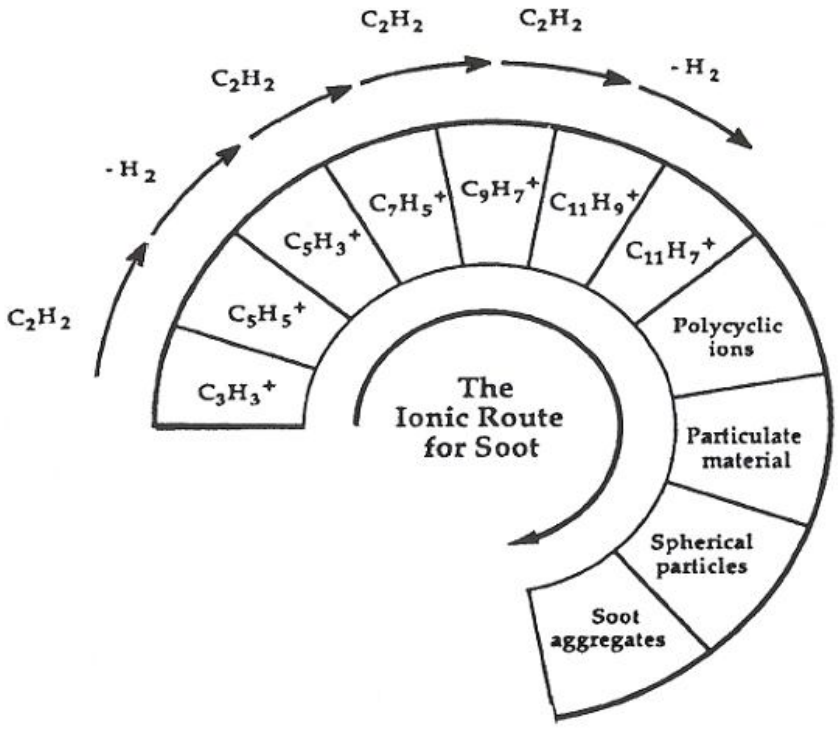

Fig. 2.18: Schematic illustration of soot formation according to the ionic theory. [22]

The foundation of the evolution to a more realistic understanding of free radical gas phase chemistry associated to soot formation was laid in the so-called “Hydrogen Polymerisation Theory”. The pioneers of these theory suggested that three groups of species take part in the reaction pathways, which can lead to carbon formation in aliphatic and aromatic hydrocarbon fuels:

1. Acetylene and polyacetylenes (mass range 26 – 146 amu),
2. Polycyclic aromatic hydrocarbons (mass range 78 - ~300 amu) and
3. Reactive polycyclic aromatic hydrocarbons, probably with side chains (mass range from about 150 to >550 amu).

During combustion of aliphatic hydrocarbons, formation of the first aromatic component, benzene or phenyl, is commonly regarded to be a primary bottleneck in soot formation. This has initiated numerous works during the last decades, which have investigated the formation of the first aromatic ring by means of experiments and modelling in turn, to deduce the chemistry and kinetics related to ring formation. The number of ring formation reactions is limited. Considering only bimolecular reactions, the two reactants should collectively contain precisely six carbon atoms and roughly six hydrogen atoms. An ultimate goal would be to determine which of the conceivable benzene formation pathways are important, but the answer is complex and will probably depend on the type of fuel, type of reactor and on the reaction conditions.

The growth process from small molecules such as benzene to larger and larger PAH appears to involve both the addition of C_2, C_3 or other small units, among which acetylene has received much attention, to PAH radicals, and reactions among the growing aromatic species, such as PAH–PAH radical recombination and addition reactions. The relative contribution of the different types of growth reactions seems to depend strongly on the fuel. In the case of aromatic fuels such as benzene, acetylene and other active reactants for aromatics formation are formed in relatively large concentrations in the breakdown of the fuel, whereas in the case of aliphatic fuels such as acetylene, ethylene or methane, the first aromatic ring must be formed from fuel decomposition products by a sequence of elementary reactions in which the active ring formation reactants are in lower concentrations than in the aromatics flames. [26]

The primary focus is on the formation of the first aromatic ring from small aliphatics, because this step is perceived by many to be the rate-limiting step in the reaction sequence to larger aromatics. Arguments revolve between several possibilities. The most important pathways of formation of aromatics are explained in detail in [24] and are not discussed here.

As complex as formation of the first aromatic ring may seem, the growth beyond the first ring and formation and growth of subsequent polycyclic aromatic hydrocarbons will seem even more complex, and these processes are not nearly as well documented as those of the formation of the first aromatic ring. However, during the last decade a significantly improved knowledge and understanding of PAH growth in combustion processes has been achieved and have proposed mechanisms based on the chemistry of free radicals for PAH species.

Many of the proposed growth mechanisms employ a sequence of successive additions of smaller chemical species such as acetylene to larger PAH molecules; these types of growth mechanisms are addressed as *successive growth mechanisms*.
The best known of the successive growth mechanisms is probably the alternating Hydrogen Abstraction C_2H_2 Addition (HACA) mechanism proposed by Frenklach [24]. The term ‘‘HACA’’ is used as an acronym for ‘‘H-abstraction-C_2H_2-addition.”. An alternative to the

successive growth mechanisms is the *combinative growth mechanism*, which allows a rapid growth of PAH by direct combination of aromatic species.

2.5 Summary Objectives of this work

This work consists of two parts. A simulation part and an experimental part.The main purpose of the experimental investigation is to evaluate a prototype T-POX reactor concerning to its operating characteristics, its efficiency and to evaluate the possibility of regeneration in very low air-fuel ratios . This prototype T-POX reformer will based on a soottrap for reasons which are explained below.

The soot regeneration , as we referred in the paragraph 2.3, is potential under specific conditions. In particular, the air ratio, the temperature and the concentration of water in the syngas are the important parameters which determine the regeneration.

From previous research of T-POX reactors, as in [1],[4], the soot retention and regeneration was realized in a DPF filter which was placed immediately after the reactor. The temperature of syngas was reducing up to 400 or 500oC because of the thermal losses which are difficult to limit even with good insulation. In particular, for a temperature of 900^{o}C in the DPF, the soot point was appearing for air-ratio of λ=0.45. But if we have the possibility to eliminate the thermal losses and to retain the temperature in high levels, the soot point would be appeared in lower air-ratio. Lower-air ratio in a T-POX process, means better efficiency in terms of more production of hydrogen. However, the limitations of insulation technology doesn't allow to achieve high levels of temperatures in the DPF.
An alternative solution, in order to have high level of temperature, lower soot point, lower air ratio and thus more efficiency, is to incorporate the DPF inside of the reactor and this new prototype of T-POX reactor will be investigated.

The purpose of the numerical part is the simulation of chemical kinetics, applied a reduced GRI mechanism in the real geometry of the reformer which combined with a porous domain for the soottrap simulation. The estimation of chemical species, the pressure drop at the domain of the reformer and the comparison of their values with the experimental results is the main aim of this numerical work. Furthermore, the estimation of chemical species inside of the conical section could utilized in a future work as an input in a channel geometry of a soottrap for a second simulation which aims to study the reactive flow and the soot dynamics.

Chapter 3[d] : Development of Numerical Model for T-POX reformer

3.1 The 2D geometry of reformer

Both of geometries which described below were designed as axisymmetric, since they have cylindrical parts and are intended for 2D simulation.

1st prototype for preliminary simulations

The first geometry was designed based on the design of reformer in [7]. This geometry was used only for preliminary simulations which was aiming for familiarizing with the ANSYS environment and porous media model simulation. It will be used for a parametric flow analysis in the case that the domain has a porous packed bed medium. The geometry is shown below figure 3.1. It consists of a conical section and a cylindrical one. A typical design of reformer for reasons which explained at 2.1.2.

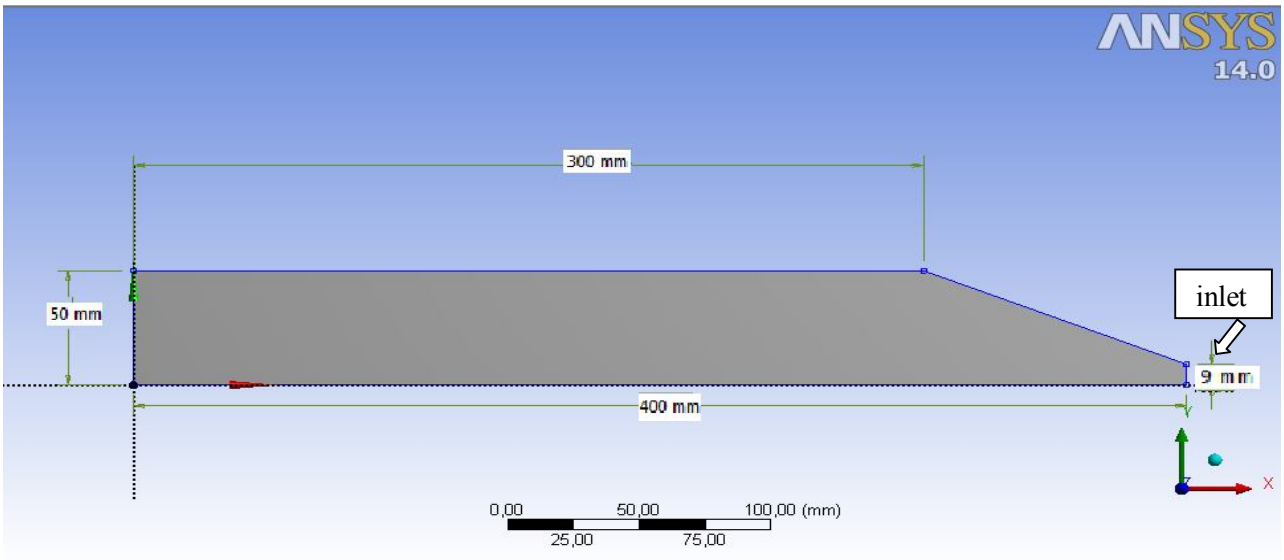

Fig. 3.1: The axisymmetric geometry of first prototype

2nd prototype final simulations

The second geometry was designed at TU Freiberg in Germany in order to be conducted simulation and experimental study for the evaluation of a soottrap based reformer. The experimental study is described in chapter 4 and there are more drawings and cross sections of this geometry which was designed at Inventor Autodesk. The second geometry will be used for simulation of chemical kinetics which is the aim of the numerical study of this work and will be presented in the chapter 5. The domain of soottrap since it has as a difficult flow field, will be trying to simulate as porous packed bed. The geometry is shown in figure 3.2 is designed in Designed Modeler of ANSYS.

As it is shown the geometry consists of a conical and cylindrical part for the same reasons of flame stabilization which was explained in 2.1.2. It is chosen a small diameter tube for inlet aiming to increase the momentum and to prevent the possibilities of flash back since the

thermal load would be low and therefore the velocities. From the perspective of simulation the geometry consists of three zones, the inlet zone, the porous-"soottrap" zone and the exhaust zone. Only the porous zone is considered that is filled by the existence of soottrap. The two other zones are empty. The empty conical section is interested to be the reaction zone and for simulation both for experiment. The geometry of soottrap based reformer is further described at 4.1.1.

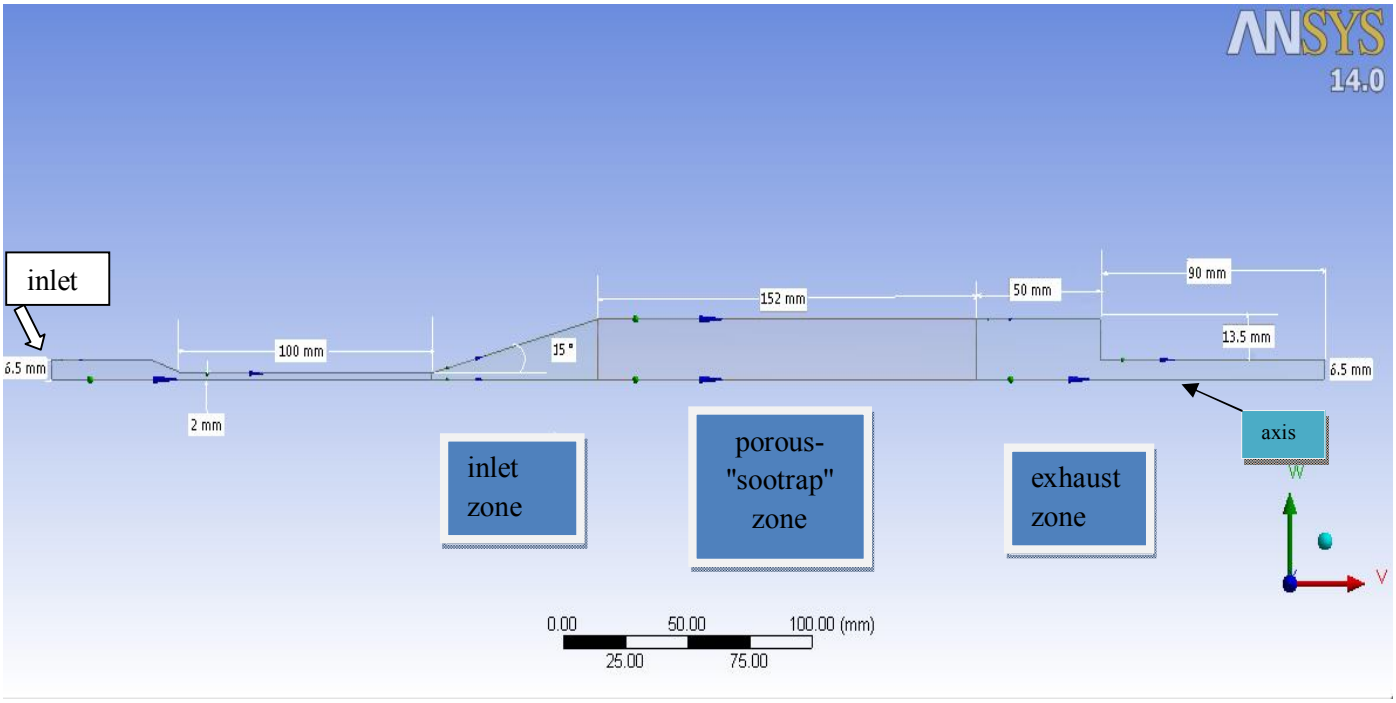

Fig. 3.2: The axisymmetric geometry of second prototype

3.2 Review of turbulence models for the reforming process.

3.2.1 Reynolds-Averaging and the Boussinesq-Approximation.

Reynolds-Averaging is implemented in the continuous and momentum equation in order to model the turbulent flow, where the magnitude of transportation φ (such as: velocity, pressure) is expressed by its average value plus the disorder of its fluctuation, an example for the velocity is: $u = \bar{u} + u'$.

In the incompressible flow (mach<0.3), using the method of Reynolds-Averaging in the continuous equation there are not any additional terms as we notice below, in contrast with the momentum equation where additional terms are appeared, named Reynolds stresses $-\rho\overline{u_i' u_j'}$.

Continuity equation using method of Reynolds-Averaging:

$$\frac{\partial \rho}{\partial t} + \frac{\partial}{\partial x_i}(\rho u_i) = 0 \qquad \text{Eq.\{3.1\}}$$

Momentum equation using method of Reynolds-Averaging:

$$\frac{\partial}{\partial t}(\rho u_i) + \frac{\partial}{\partial x_j}\left(\rho u_i u_j\right) = -\frac{\partial p}{\partial x_i} + \frac{\partial}{\partial x_j}\left[\mu\left(\frac{\partial u_i}{\partial x_j} + \frac{\partial u_j}{\partial x_i} - \frac{2}{3}\delta_{ij}\frac{\partial u_l}{\partial x_l}\right)\right] + \frac{\partial}{\partial x_j}\left(-\rho\overline{u'_i u'_j}\right) \qquad \text{Eq.\{3.2\}}$$

As regards the compressible flow, these additional terms appear both in the continuity and momentum equation . In order to avoid the aforementioned terms in the continuity equation an improved method of Reynolds-Averaging which called Favre or Mass-Averaging method is applied for compressible fluid. In this case, the additional terms appears only in the momentum equation.

Consequently the problem of simulation of turbulent flow is to define the correlation of these additional terms (Reynolds stresses) that result from the Reynolds or Favre-averaging, as function of the initial magnitudes of the equations in order to reduce the unknown factors and solve the system.

Finally the above desired correlation was made considering the Boussinesq approximation. The Boussinesq approximation based on the observation that the Reynolds stresses have the same behavior as the molecular stresses (i.absorption of kinetic energy by the average flow, or thermal losses. ii. increased transfer of mass, energy and momentum) and in combination that the molecular stresses are proportional to kinematic viscosity (property of fluid), leads to the hypothesis that Reynolds stresses $-\rho\overline{u_i' u_j'}$ can be expressed mathematically in similar way and can be proportional to a new magnitude which called turbulent viscosity or eddy viscosity v_t (property of flow) instead of kinematic viscosity.

Boussinesq approximation

$$-\rho\overline{u'_i u'_j} = \mu_t\left(\frac{\partial u_i}{\partial x_j} + \frac{\partial u_j}{\partial x_i}\right) - \frac{2}{3}\left(\rho k + \mu_t\frac{\partial u_k}{\partial x_k}\right)\delta_{ij} \qquad \text{Eq.\{3.3\}}$$

At this point the models of turbulent flow are involved aiming at the modeling of the turbulent kinetic viscosity $v_t = \frac{\mu_t}{\rho}$. A relevant example is the mix-length models that are depended by the characteristic length of turbulent flow L:

$$v_t = C_1 * L * q \qquad \text{Eq.}\{3.4\}$$

where: C_1 constant, L characteristic length of turbulent flow, q characteristic velocity of turbulent flow. Von Karman correlated q with L.

3.2.2 Classification of turbulence models and the differential equations of k and ε.

First classification of turbulence models according to the number of equations.

A basic classification of models is attained using the number of equations that have to be solved in order to estimate the turbulent kinetic viscosity v_t in the flow field. For this reason, based on the equations the models are classified as are shown below:

- Class 0 → algebraic with basic models of Baldwin-Lomax (knowledge of boundary layer's thickness is not needed) and Cebeci-Smith (knowledge of boundary layer's thickness is needed).
- Class 1st → Spalart Allmaras
- Class 2nd → for example k-ε, k-ω, q-ω

The second class's models require the solution 2 partial differential equations.

The turbulent flow's model that chosen for the simulation of the flow inside the reformer is the model k-ε. It is second class's model as it solves two partial differential equations for the estimation of turbulent viscosity v_t. The first equation deals with k, the turbulent kinetic energy [tke], while the second one deals with ε, the destruction of turbulent energy dissipation [ted]. These two terms are related with the turbulent kinematic viscosity:

$$v_t = C_\mu * \frac{K^2}{\varepsilon} \qquad \text{Eq.}\{3.5\}$$

where $C_\mu = 0.09$

Partial differential equations of k and ε.

$$\frac{\partial}{\partial t}(\rho k) + \frac{\partial}{\partial x_i}(\rho k u_i) = \frac{\partial}{\partial x_j}\left[\left(\mu + \frac{\mu_t}{\sigma_k}\right)\frac{\partial k}{\partial x_j}\right] + G_k + G_b - \rho\varepsilon - Y_M + S_k \qquad \text{Eq.}\{3.6\}$$

$$\frac{\partial}{\partial t}(\rho \varepsilon) + \frac{\partial}{\partial x_i}(\rho \varepsilon u_i) = \frac{\partial}{\partial x_j}\left[\left(\mu + \frac{\mu_t}{\sigma_\varepsilon}\right)\frac{\partial \varepsilon}{\partial x_j}\right] + C_{1\varepsilon}\frac{\varepsilon}{k}(G_k + C_{3\varepsilon}G_b) - C_{2\varepsilon}\rho\frac{\varepsilon^2}{k} + S_\varepsilon \qquad \text{Eq.}\{3.7\}$$

In these equations, G_k represents the generation of turbulence kinetic energy due to the mean velocity gradients, G_b is the generation of turbulence kinetic energy due to buoyancy, Y_M represents the contribution of the fluctuating dilatation in compressible turbulence to the

overall dissipation rate. $C_{1\varepsilon}$, $C_{2\varepsilon}$, $C_{3\varepsilon}$ are constants of the model and the values are presented below. $\sigma_\kappa, \sigma_\varepsilon$ are the turbulence Prandl numbers for the k and ε respectively whereas S_k and S_ε are terms of a source.

$C_{1\varepsilon}$=1.44, $C_{2\varepsilon}$=1.92, C_μ=0.09, σ_k=1.0, σ_ε=1.3

Second classification of turbulence models whether Low-Re_t or High-Re_t flows.

The second method of classification related with the way of finding the solution in the domain. If the integration is carried out until the end of the wall or not. **Low-Re_t** are named the flows that are solved until the end of the wall, because near the wall the parameter k is low and consequently the turbulence velocity or differently the turbulence Reynolds number is low. On the other hand, **High-Re_t** are named the flows that are solved until a region where the turbulence velocity is high or the the turbulence Reynolds number is high. The turbulence velocity is $u_\tau = \sqrt{\frac{\tau_w}{\rho}}$ with τ_w is the wall's stress and ρ the fluid's density.

In the case of Low-Re_t flows the integration of solution is carried out until the wall but in this case must be given notice at the value of magnitude $y^+ = \frac{y * u_t}{v}$ (where v is the kinematic viscosity) to be $y^+ < 1$ at the first node of mesh in y axis direction and the rest nodes of mesh to be $30 < y^+ < 50$. In addition, it must be referred that in order to approach the real phenomena, some corrective terms added to the partial differential equations of k and ε when the integration carried out near to the wall. These terms called Low-Reynolds-Terms (LRT).

High-Re_t flows defined as the flows where the integration of solution doesn't carried out until the wall. In this case the solution near to the wall results from wall functions which are empirical functions which results from experiments of boundary layers.

The advantage of High-Re_t flows or otherwise using wall functions for the boundary layers near to the wall is that it is not necessary to have increased density of nodes near to the wall in order to get the real phenomenon.

3.2.3 Improved k-ε RNG turbulence model instead of k-ε.

The Fluent program of ANSYS where the simulation of reformer was conducted, had the option of k-ε turbulence model which is High-Re_t type or otherwise has wall functions. Specifically an improved turbulence flow model of k-ε used, which called k-ε RNG.

The RNG k-ε model was derived using a statistical technique called renormalization group theory. It is similar in form to the standard k-ε model, but includes the following refinements:

- The RNG model has an additional term in its equation that improves the accuracy for rapidly strained flows.
- The effect of swirl on turbulence is included in the RNG model, enhancing accuracy for swirling flows.

- The RNG theory provides an analytical formula for turbulent Prandtl numbers, while the standard k-ε model uses user-specified, constant values.

While the standard k-ε model is a high-Reynolds number model, the RNG theory provides an analytically-derived differential formula for effective viscosity that accounts for low-Reynolds number effects. Effective use of this feature does, however, depend on an appropriate treatment of the near-wall region.

These features make the RNG k-ε model more accurate and reliable for a wider class of flows than the standard k-ε model.

3.2.4 Conditions in an incompressible fluid flow (mach<0.3)

In an incompressible fluid flow the boundary conditions which must determined are the pressure the velocity and the turbulence intensity. The pressure could be determined at the outlet or in the inlet of the field but it is usual to be determined in the outlet. Furthermore its value could be any value since the magnitude of pressure is occurred as derivative in the momentum equation. It is usual its initial value to be zero. It is also needed to be determined the value of velocity in the inlet and the turbulence intensity which is received values from 0,5% for low to 5% for high turbulence flows.

3.3 Meshing and grid independence

Mesh generation is one of the most critical aspects of engineering simulations. Too many cells may result in long solver runs, and too few may lead to inaccurate results. In order to make a representative mesh , the independence of the field's solution from the mesh must be verify. This process which the mesh tested is crucial and called "grid independence". The grid independence was tested for the two prototypes of reformers separately .

In order to verify the grid independence the model was run with different number of nodes were conducted consecutively. In every run the nodes were increased until the field's solution for the velocity was not changed further.

1st preliminary prototype

Three runs were conducted for the first preliminary prototype. The nodes of each run were shown at the following table 3.1:

Table 3.1

Cases	Number of nodes
a	21632
b	27604
c	38912

From each case of solution is presented the velocity profiles in different cross sections of the field as are shown to the figure 3.3 below:

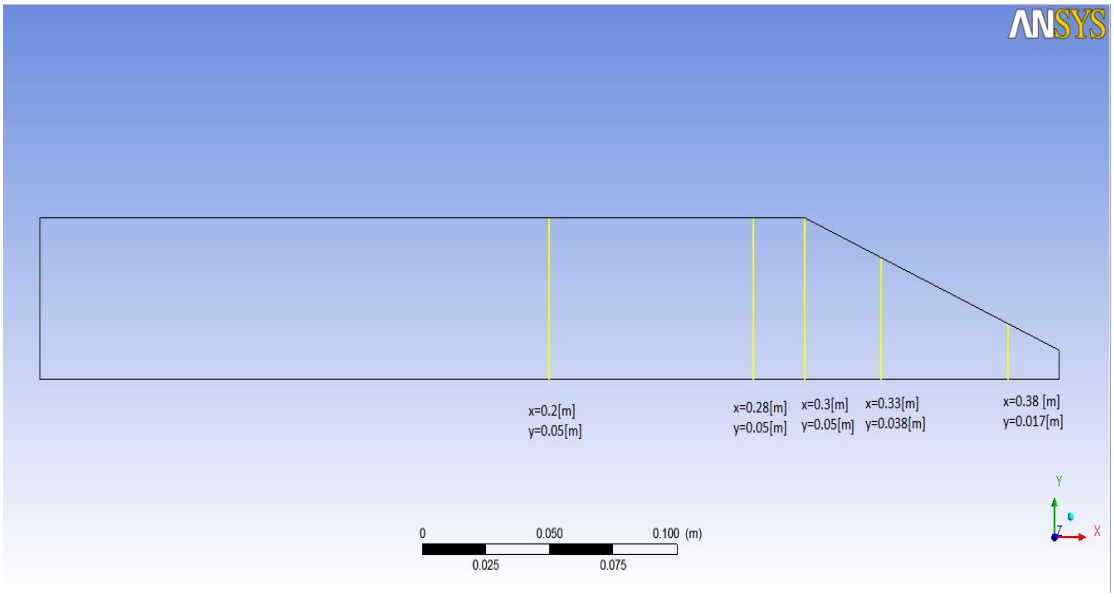

Fig. 3.3: Different cross sections which the velocity profiles are presented for different number of nodes.

The diagrams of velocity profiles in each cross section for all cases of number of nodes, are presented below:

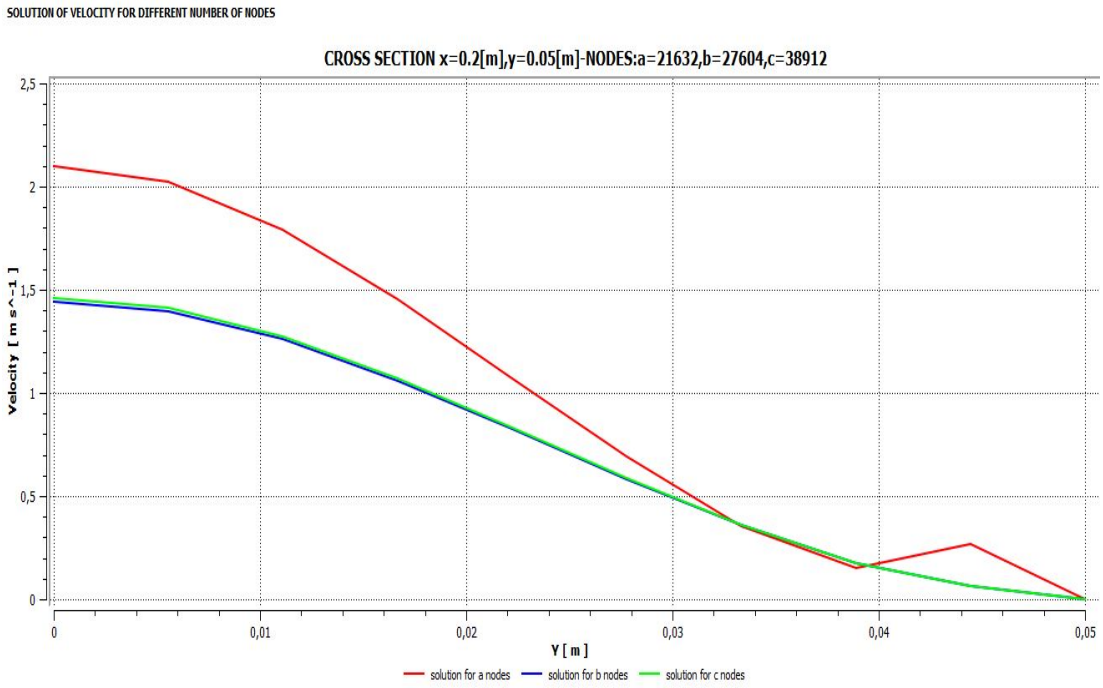

Fig. 3.4: Profiles of velocity at cross section x=0.2 [m], y=0.05[m] for different number of nodes a=21632 (red line), b=27604 (blue line), c=38912 (green line).

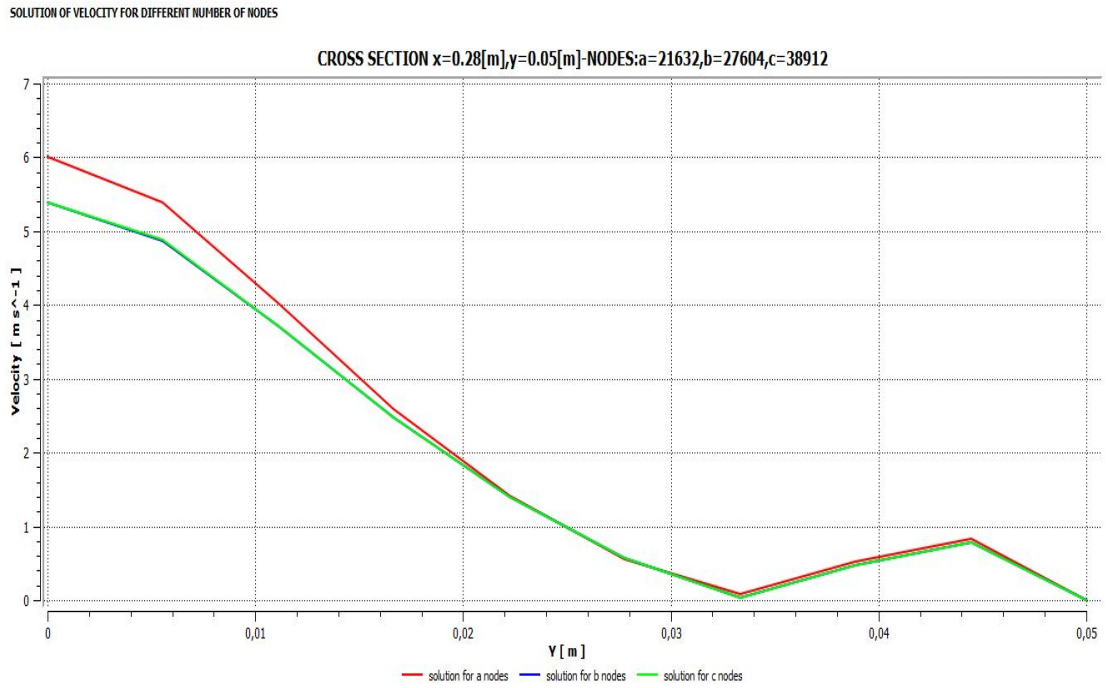

Fig. 3.5: Profiles of velocity at cross section x=0.28 [m], y=0.05[m] for different number of nodes a=21632 (red line), b=27604 (blue line), c=38912 (green line).

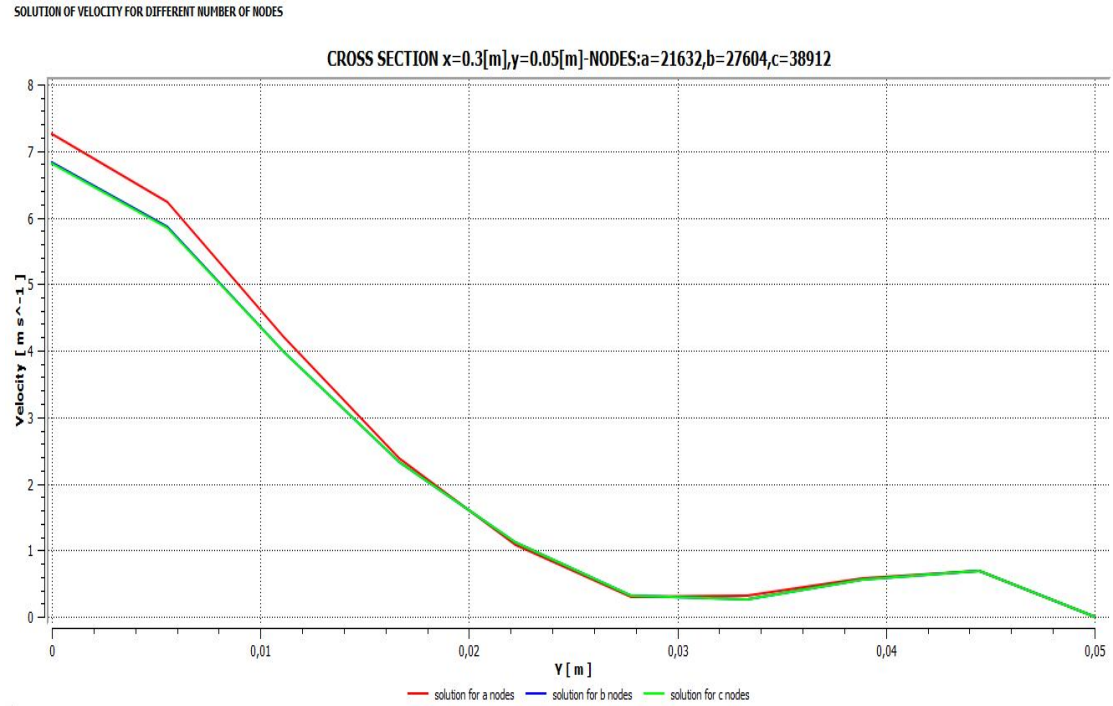

Fig. 3.6: Profiles of velocity at cross section x=0.3 [m], y=0.05[m] for different number of nodes a=21632 (red line), b=27604 (blue line), c=38912 (green line).

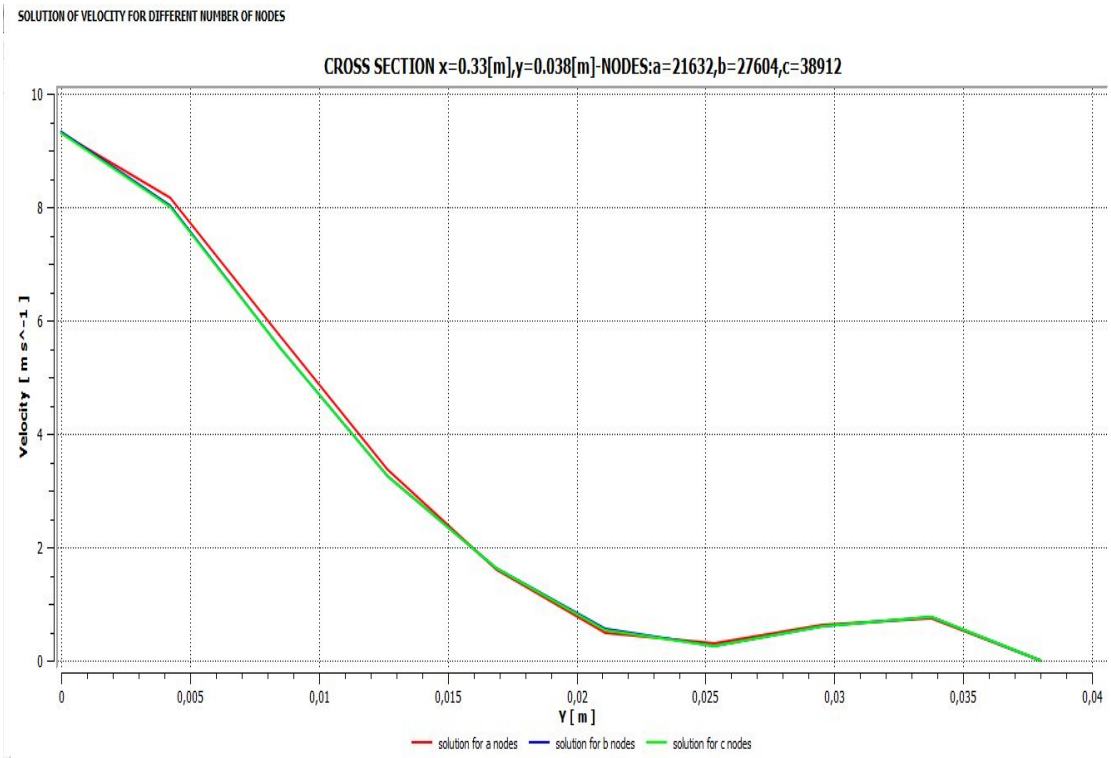

Fig. 3.7: Profiles of velocity at cross section x=0.38 [m], y=0.038[m] for different number of nodes a=21632 (red line), b=27604 (blue line), c=38912 (green line).

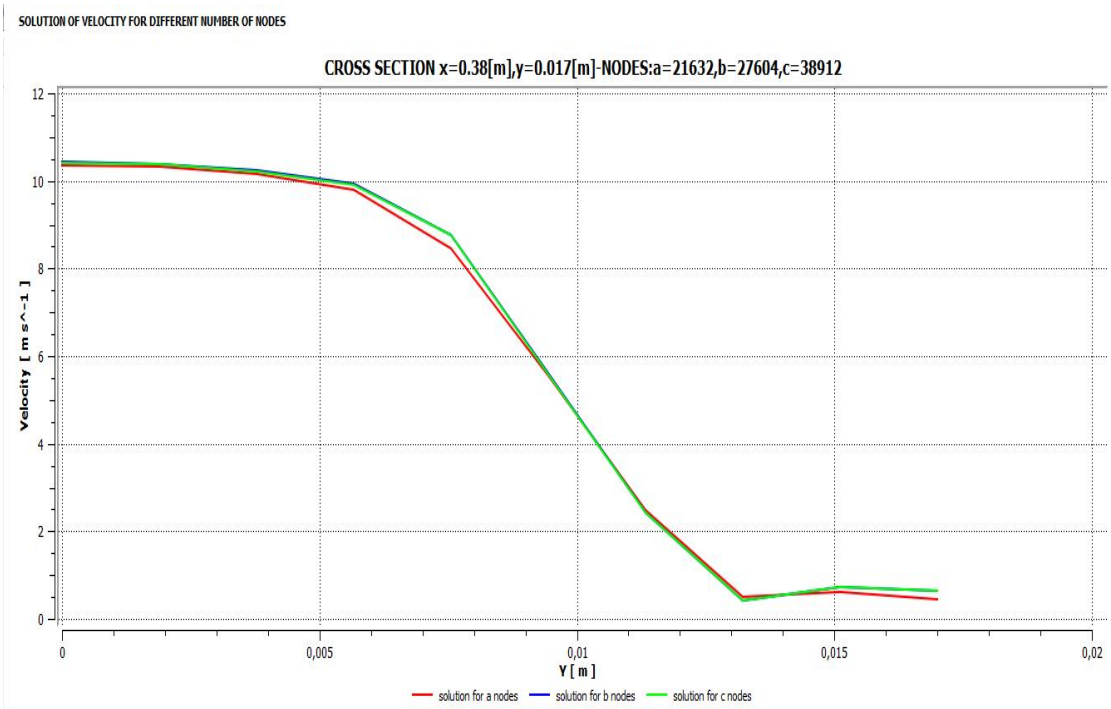

Fig. 3.8: Profiles of velocity at cross section x=0.38 [m], y=0.017[m] for different number of nodes a=21632 (red line), b=27604 (blue line), c=38912 (green line).

From the above diagrams are shown that the b and c cases of nodes give identical solutions of velocity, which means that for number of nodes above of 27604 the solution is independence of the grid. Thus for the next simulations of this work, the number of nodes for the *1st prototype of reformer will be 27604 nodes*.

2nd prototype

Five runs was conducted for the second prototype. The nodes of each run were shown at the following table 3.2:

Table 3.2

Cases	element size [mm]	number of nodes
a	0.5	24705
b	0.48	27001
c	0.45	29968
d	0.42	35175
e	0.4	38143

From each case of solution is presented the velocity profiles in different cross sections of the field as are shown to the figure 3.9 below:

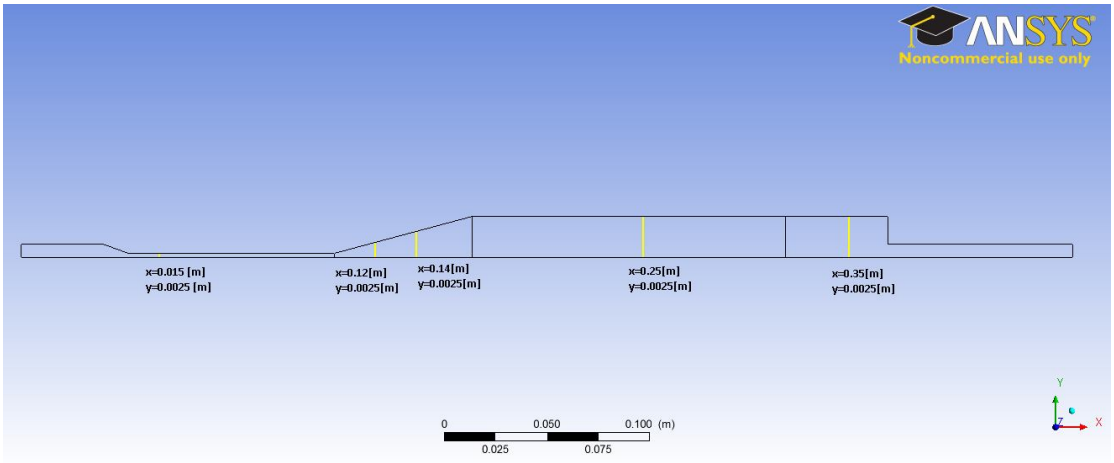

Fig. 3.9: Different cross sections which the velocity profiles are presented for different number of nodes.

The diagrams of velocity profiles in each cross section for all cases of number of nodes, are presented below:

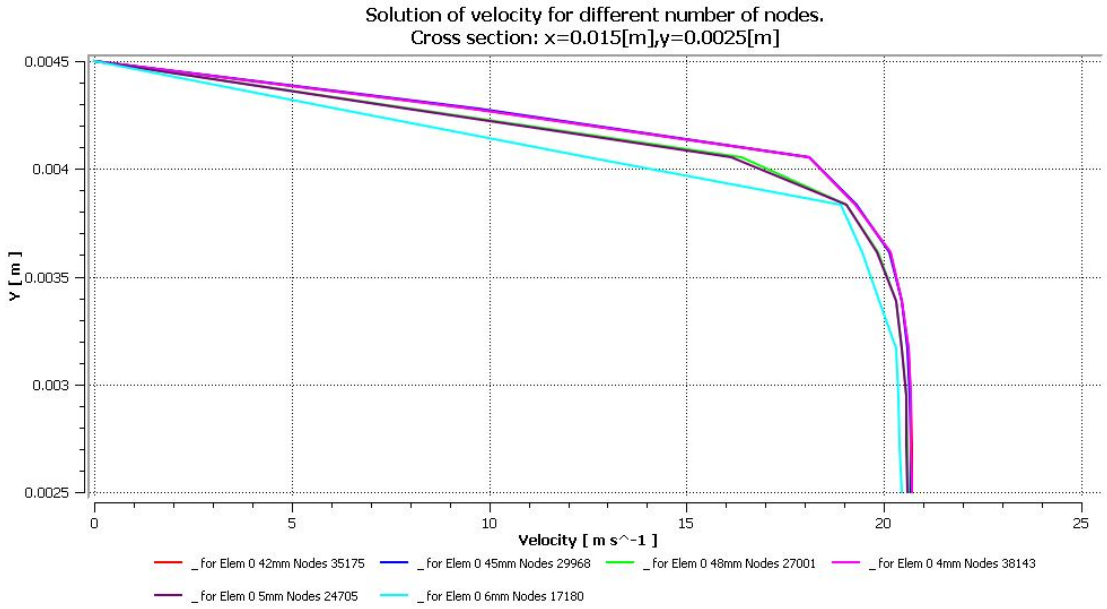

Fig. 3.10: Profiles of velocity at cross section x=0.2 [m], y=0.05[m] for different number of nodes.

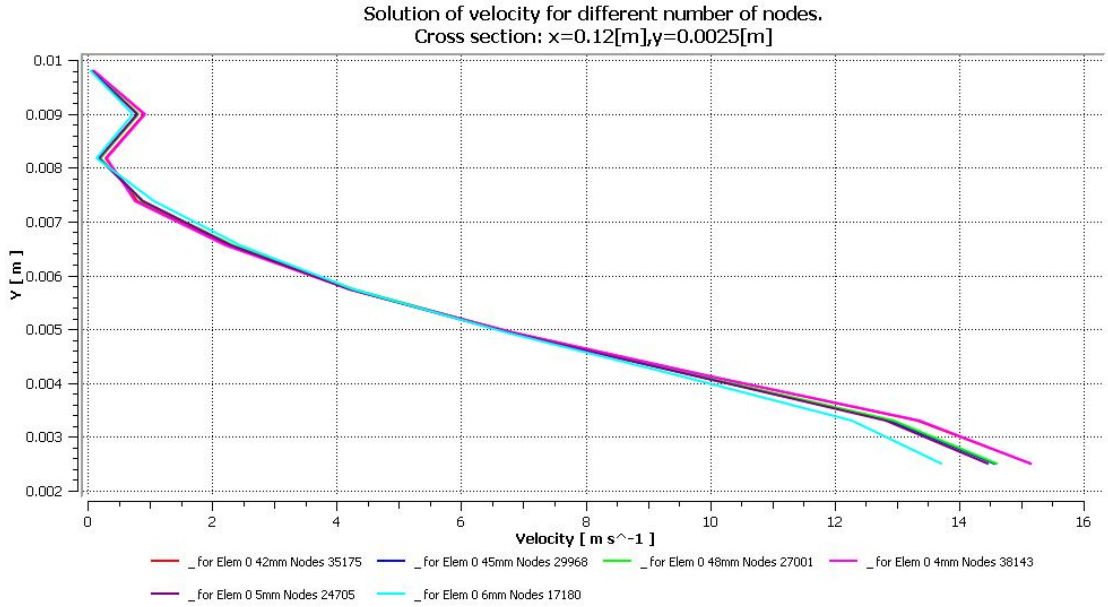

Fig. 3.11: Profiles of velocity at cross section x=0.2 [m], y=0.05[m] for different number of nodes.

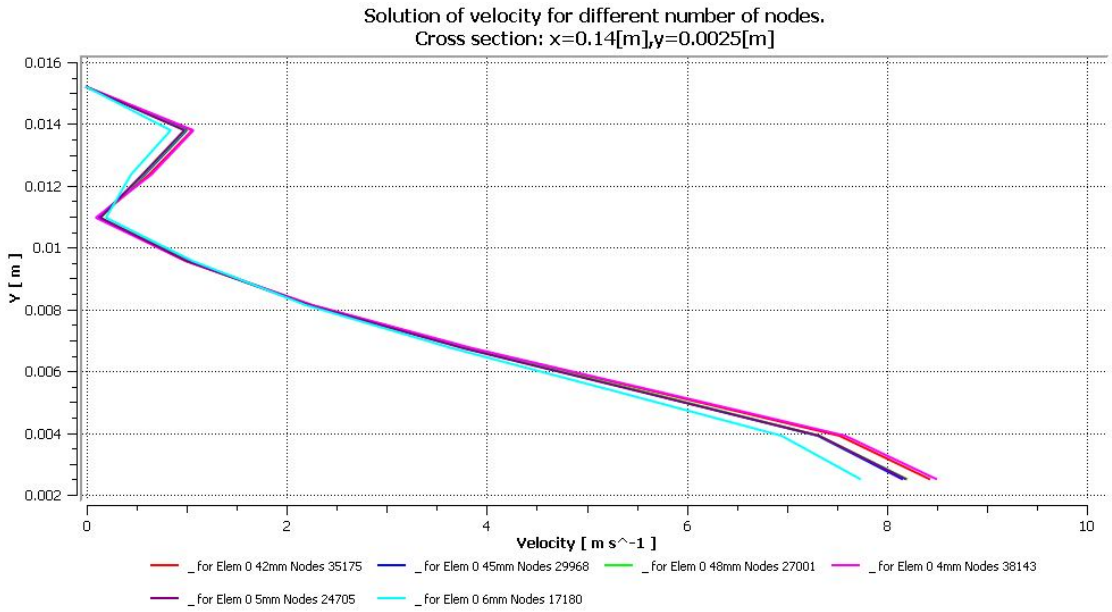

Fig. 3.12: Profiles of velocity at cross section x=0.2 [m], y=0.05[m] for different number of nodes.

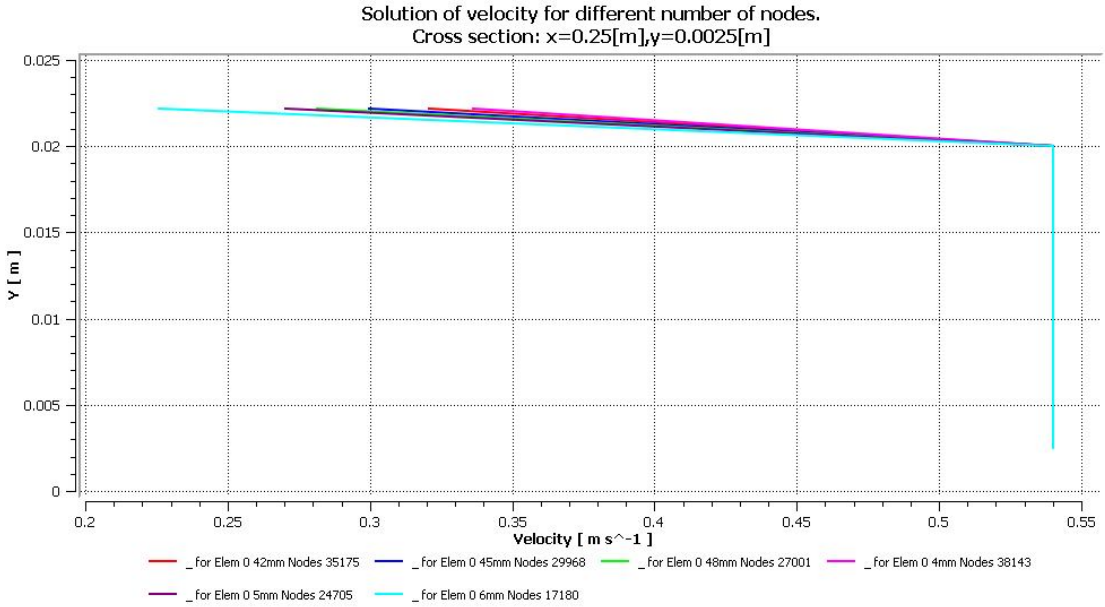

Fig. 3.13: Profiles of velocity at cross section x=0.2 [m], y=0.05[m] for different number of nodes.

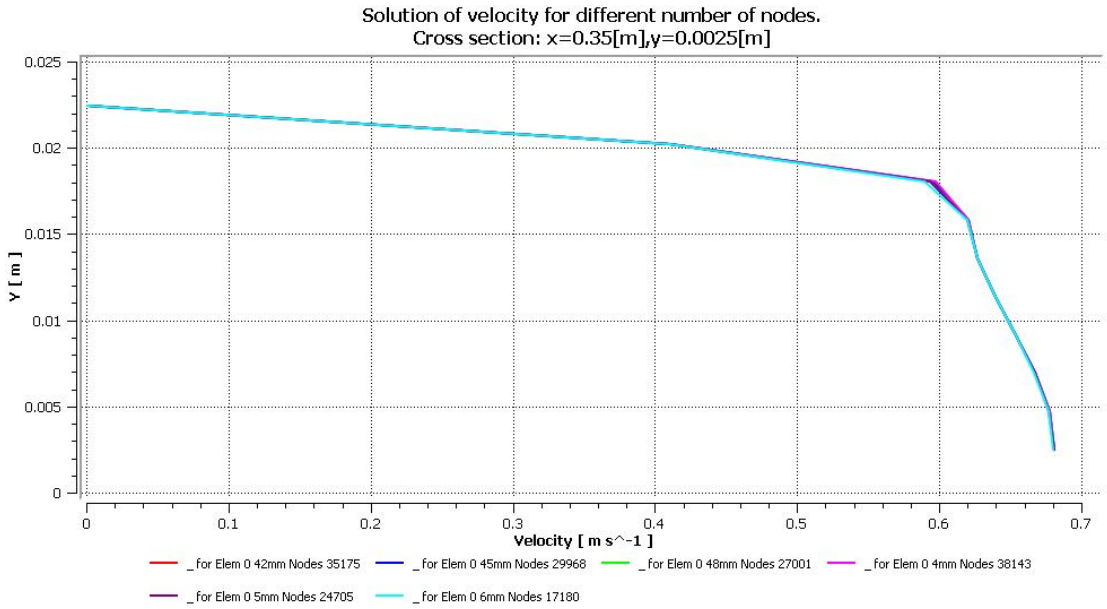

Fig. 3.14: Profiles of velocity at cross section x=0.2 [m], y=0.05[m] for different number of nodes.

From the above diagrams are shown that the d and e cases of nodes give identical solutions of velocity, which means that for number of nodes 35175 the solution is independence of the grid. Thus for the next simulations of this work, the number of nodes for the *2nd prototype of reformer will be 35175 nodes end size element 0.42 mm.*

3.4 Basic equations for simulation of porous medium

The porous media models for single phase flows and multiphase flows use the Superficial Velocity Porous Formulation. ANSYS FLUENT calculates the superficial phase or mixture velocities based on the volumetric flow rate in a porous region. Porous media are modeled by the addition of a momentum source term to the standard fluid flow equations. The source term is composed of two parts: a viscous loss term (Darcy, the first term on the right-hand side of Equation 3.8 , and an inertial loss term (the second term on the right-hand side of Equation 3.8)

$$S_i = -\left(\sum_{j=1}^{3} D_{ij}\mu v_j + \sum_{j=1}^{3} C_{ij}\frac{1}{2}\rho|v|v_j\right) \qquad \text{Eq.}\{3.8\}$$

where is the source term for the i th (x,y , or z) momentum equation, $|v|$ is the magnitude of the velocity and D and C are prescribed matrices. This momentum sink contributes to the pressure gradient in the porous cell, creating a pressure drop that is proportional to the fluid velocity (or velocity squared) in the cell.

To recover the case of simple homogeneous porous media the source term simplified:

$$S_i = -\left(\frac{\mu}{\alpha}v_i + C_2\frac{1}{2}\rho|v|v_i\right) \quad \text{Eq.\{3.9\}}$$

where α is the permeability and C_2 is the inertial resistance factor, simply specify D and C as diagonal matrices with 1/α and C_2, respectively, on the diagonals (and zero for the other elements).

3.4.1 Darcy's law in porous media

In laminar flows through porous media, the pressure drop is typically proportional to velocity and the constant C_2 can be considered to be zero. Ignoring convective acceleration and diffusion, the porous media model then reduces to Darcy's Law wich represents the pressure drop due to viscous losses:

$$\nabla p = -\frac{\mu}{\alpha}\vec{v} \quad \text{Eq.\{3.10\}}$$

Equations for simulation of porous medium as packed bed

3.4.2 Inertial losses in porous media

At high flow velocities, the constant C_2 in Equation 3.8 provides a correction for inertial losses in the porous medium. This constant can be viewed as a loss coefficient per unit length along the flow direction, thereby allowing the pressure drop to be specified as a function of dynamic head. If we have flow in a tube where the permeability is α=1 then we would have pressure drop only due to inertial losses. So the Equation 3.9 simplify to the follow form:

$$\nabla p = -\sum_{j=1}^{3} C_{2_{ij}}\left(\frac{1}{2}\rho v_j|v|\right) \quad \text{Eq.\{3.11\}}$$

3.4.3Ergun and Blake-Kozeny equation. a, C2 calculation.

Semi-empirical equations as the Ergun equation which is shown below, are used in order to predict the pressure drop in a porous medium.

$$\frac{|\Delta p|}{L} = \frac{150\mu}{D_p^2}\frac{(1-\varepsilon)^2}{\varepsilon^3}v_\infty + \frac{1.75\rho}{D_p}\frac{(1-\varepsilon)}{\varepsilon^3}v_\infty^2 \quad \text{Eq.\{3.12\}}$$

The Ergun equation without the second term in the r.h.s called Blake-Kozeny. This equation which is shown below, used for the laminar flow simulation in packed bed media.

$$\frac{|\Delta p|}{L} = \frac{150\mu}{D_p^2}\frac{(1-\varepsilon)^2}{\varepsilon^3}v_\infty \qquad \text{Eq.\{3.13\}}$$

In these equations, μ is the viscosity, D_P is the mean particle diameter, L is the bed depth, and ε is the void fraction, defined as the volume of voids divided by the volume of the packed bed region.

Comparing Equation 3.10 and Equation 3.11 with Equation 3.12 , *the permeability* Eq.3.14 and *inertial loss coefficient* Eq.3.15 in each component direction may be identified as

$$\alpha = \frac{D_p^2}{150}\frac{\varepsilon^3}{(1-\varepsilon)^2} \qquad \text{Eq.\{3.14\}}$$

$$C_2 = \frac{3.5}{D_p}\frac{(1-\varepsilon)}{\varepsilon^3} \qquad \text{Eq.\{3.15\}}$$

3.5 Numerical investigation of flow field of the 1st preliminary prototype geometry for air stream.

The first prototype which used for preliminary simulations based on the geometry and characteristics of the reformer which mentioned to [7]. The porous medium is SiSiC. The properties of this porous material are shown to the table below:

IPM property	SiSiC porous foam
Porosity, ϕ	0.90
Extinction coef., β (m^{-1})	100
Scattering albedo, ω	0.70
Emissivity, ε	0.85
Porous structure dimension, d_p (m)	6×10^{-4}
Specific surface area, a_v (m^2/m^3)	500
C in Eq. (5)	0.137
n in Eq. (5)	1.2

Table 3.3: Properties of SiSiC porous foam

The reverse value of permeability α [m^2] i.e. the viscous resistance Rv [$1/m^2$], the inertial loss or inertial resistance C_2 and the porosity Φ or ε of porous medium are requested for the simulation of a porous medium in Fluent of ANSYS. The values of this parameters are demanded for the directions x and y. In our case we consider the same values in both directions because the SiSiC material assumed as an isotropic material. They calculated by the equations 3.14 and 3.15 and they are:

viscous resistance Rv =5715592,14 [1/m²]
inertial resistance Ri = 0,00124971 [m]
porosity φ or ε =0,9

In additional, for this simulation the inlet velocity was *U=11,7 [m/s],* the temperature of air stream *Θ=20[°C],* the turbulence model was the k-ε RNG and the criteria of convergence was 10^{-4} for the mass flow.

Results of flow field for air stream in the first prototype geometry of reformer

In the figure 3.15 is shown the velocity flow field and how the contour of flow is formed in the porous domain. In figure 3.16 it can be observed a recirculation which was formed in the conical domain.

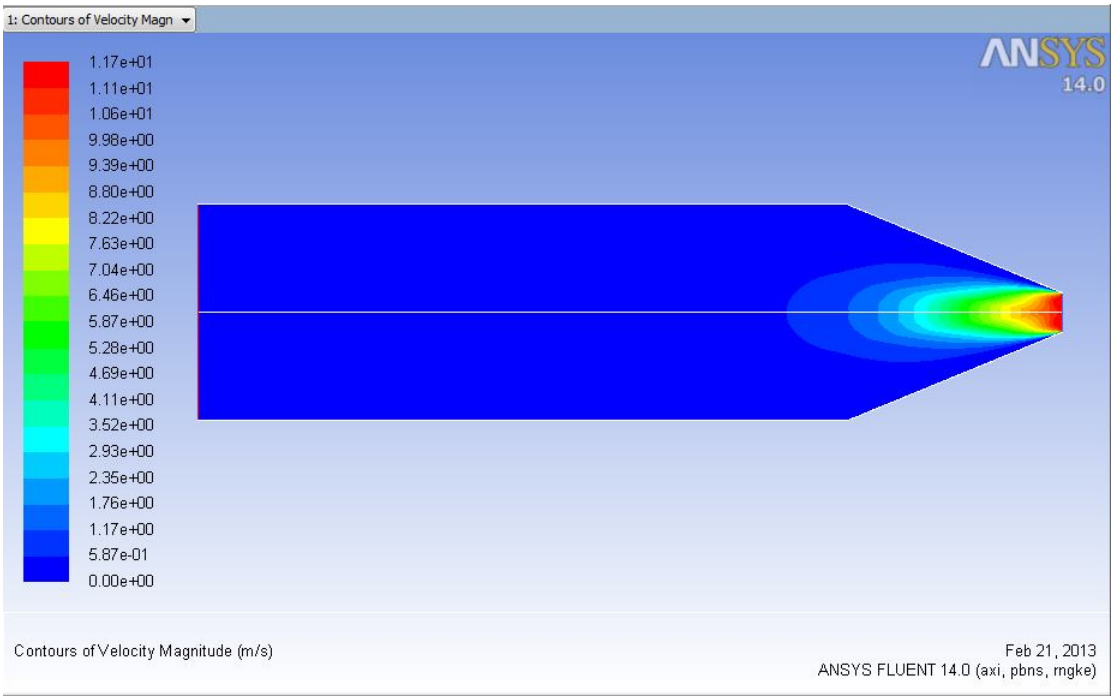

Fig. 3.15: Velocity distribution of flow field for air stream with the characteristics SiSiC as porous medium material.

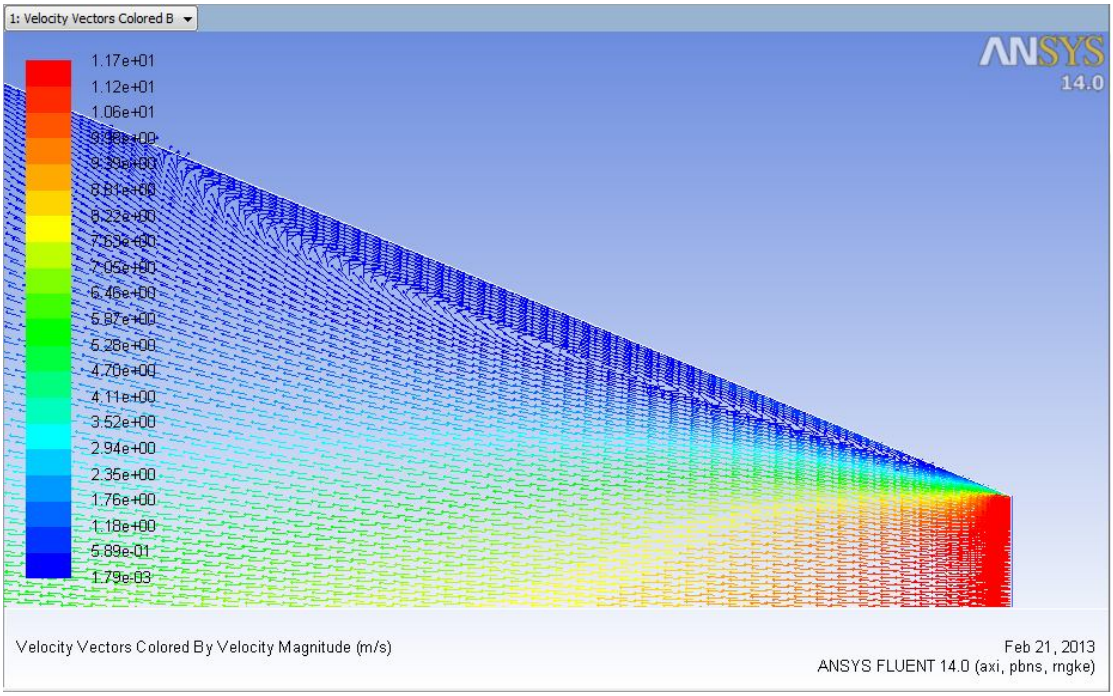

Fig. 3.16: Observed recirculation at the inlet of the reformer.

3.5.1 Parameterization of fluid flow inside of reformer for different porosity of porous medium

The basic parameters as shown in the equations 3.14 and 3.15 which influence the flow in a porous medium are the diameter particulate Dp, porosity or volume fraction (φ or ε) which defined as the ratio of pore volume to its total volume. Practically φ=1 means empty space.

Taking the one of the above parameters constant and varying the second, the viscous 1/α and inertial C_2 resistance was calculated by the equation 3.14 and 3.15 .Numerical simulations of flow in the porous medium domain were conducted for each case of parameters. The values of the calculated parameters are shown in the following tables:

Table 3.4

Dp=ct.=6,00E-04 [m]	case 1	case 2	case 3	case 4	case 5
ε	0,7	0,75	0,8	0,85	0,95
Rv= (1/α) [1/m2]	1,09E+08	61728395,1	3,26E+07	1,53E+07	1,21E+06
Ri=C2 [m]	0,000196	0,00028929	0,000438857	0,000702	0,00294

Dp=ct.=6,00E-04 [m]	continuity of Table 3.4			
	case 6	case 7	case 8	case 9
ε	0,93	0,87	0,88	0,89
Rv= (1/α) [1/m2]	2,54E+06	1,07E+07	8,80E+06	7,15E+06
Ri=C2 [m]	0,00197	0,00086836	0,000973531	0,001099

Table 3.5

ε=ct.=0,9	case 1	case 2	case 3	case 4	case 5
Dp [m]	5,00E-04	5,50E-04	6,50E-04	7,00E-04	8,00E-04
Rv= (1/α) [1/m2]	8,23E+06	6,80E+06	4,87E+06	4,20E+06	3,22E+06
Ri=C2 [m]	0,001041	0,00114557	0,001353857	0,001458	0,001666

ε=ct.=0,9	continuity of Table 3.5	
	case 6	case 7
Dp [m]	9,00E-04	1,00E-03
Rv= (1/α) [1/m2]	2,54E+06	2,06E+06
Ri=C2 [m]	0,001875	0,00208286

The results of velocity distribution in the flow field for **Dp=6,00E-04 m** and for **different values of porocity ε** are shown in the following figures:

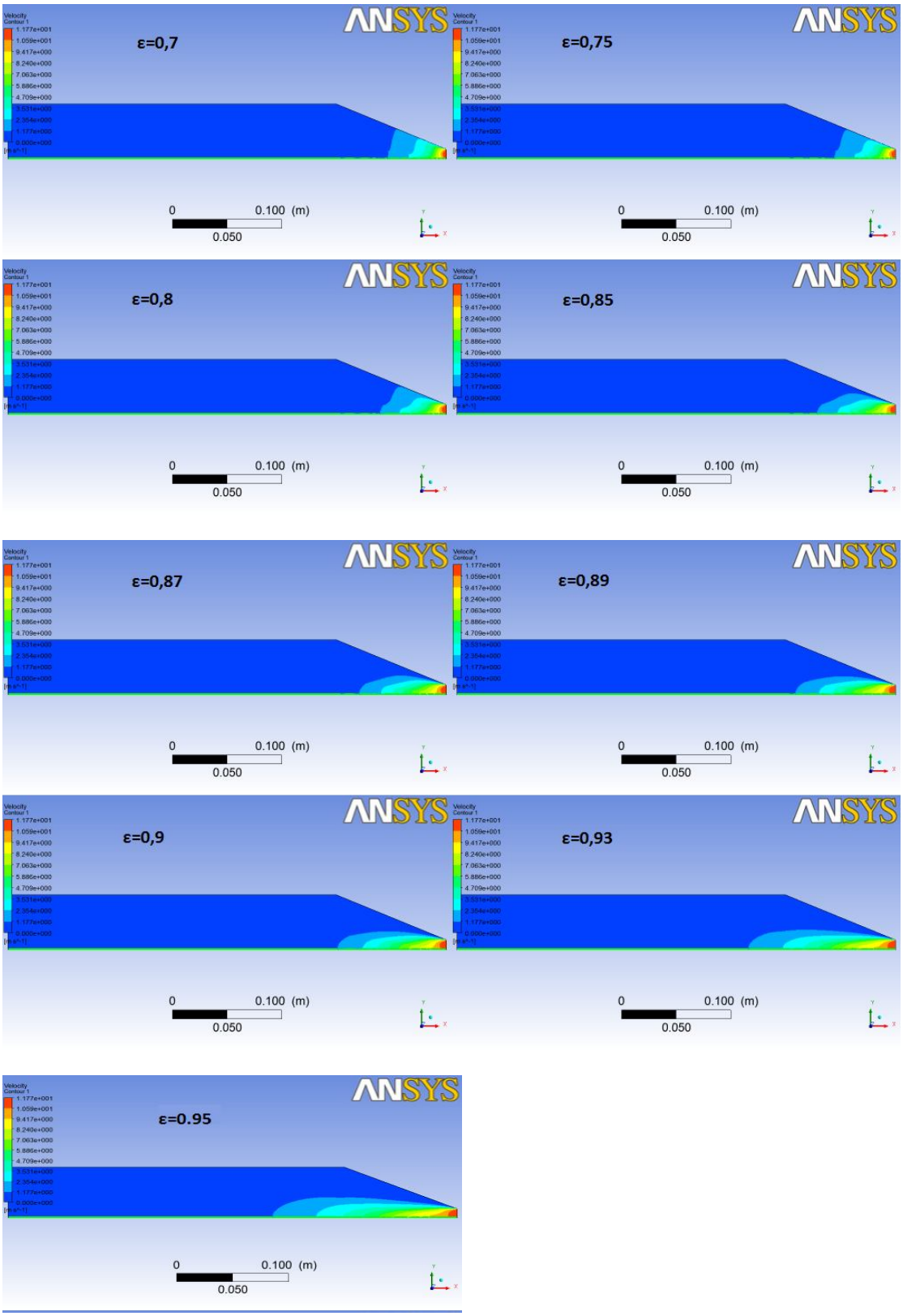

Fig. 3.17: Air stream propagation in the porous medium domain for different values of porosities, inlet velocity 11,7 [m/s] and temperature 293.15 [K].

While the results of velocity distribution in the flow **field for ε=0,9** and **for different values of particulate diameter Dp** are shown in the following figures**:**

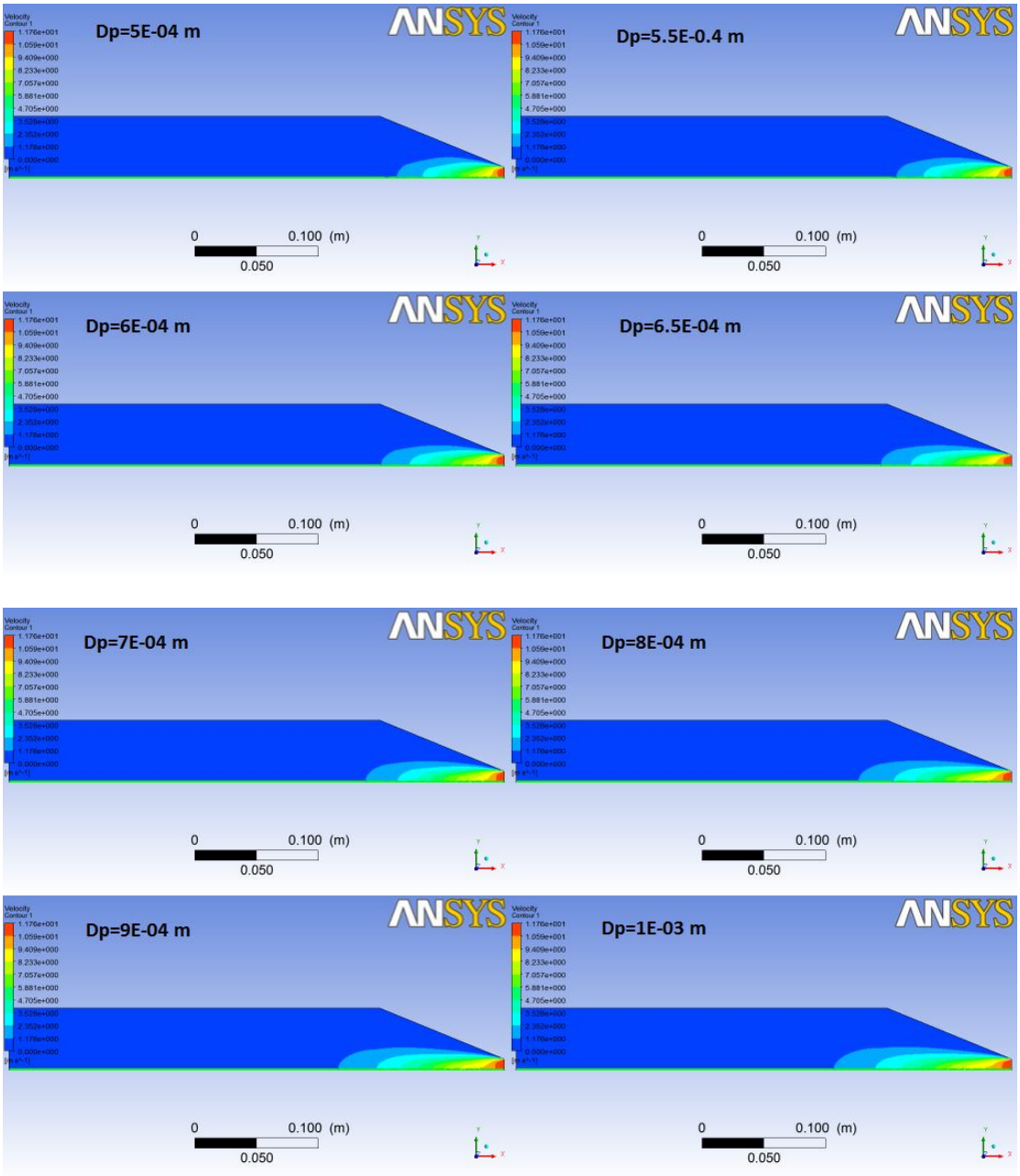

Fig. 3.18: Air stream propagation in the porous medium domain for different values of porous medium particle diameter, inlet velocity 11,7 [m/s] and temperature 293.15 [K].

In figures 3.17 and 3.18 it can be observed the influence of particle diameter of porous medium and its porocity in the velocity flow field. It can be observed as was expected that high values of porocities reduce the air stream propagation since high porocity means reduce empty volume. In the other hand as the particle diameter of porous medium get high values as was expected the propagation of air stream increasing since high particle diameter increasing the empty space of porous medium.

3.6 Simulation of soot trap as porous packed bed using Konstandopoulos-Johnson model

3.6.1 Konstandopoulos-Johnson model

This pressure drop model can be used to calculate the pressure drop across the diesel particulate filters DPF like the soottrap. It first derived for a clean filter, and then could be extended to a loaded filter as described in [15]. This model will used later in order to simulate the pressure drop in ANSYS fluent model. In figure 3.19 presented a cross sectional view of a DPF inlet channel. As is shown the channel has a width α and a wall thickness w. The accumulated deposit is the form of a cake layer and is of thickness w_s.

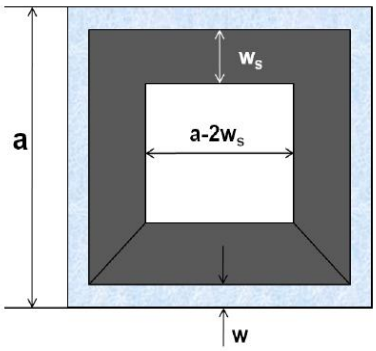

Fig. 3.19: Cross section of a loaded filter channel

The basic pressure drop equation for clean filter of this model, is shown below:

$$\Delta P_{clean} = \frac{\mu_{ex}}{k_o}\frac{U\,a}{4L}w + \frac{2\,\mu\,F}{3a^2}UL \qquad \text{Eq.\{3.16\}}$$

Where:

μ_{ex}: is the exhaust dynamic viscosity $\left[\frac{g}{cm\,s}\right]$
U: is the inlet velocity in $\left[\frac{cm}{s}\right]$
α: is the width $[cm]$
w: is the wall thickness $[cm]$
F: is a factor equal to 28,454
L: is the length of the filter $[cm]$
k_o: is the clean filter wall permeability $[cm^2]$

Also, the velocity U can be written as function of exhaust volumetric flow rate $\dot{Q}_{ex}$ $\left[\frac{cm}{s}\right]$:

$$U = \frac{8\,\dot{Q}_{ex}}{\pi\,{D_f}^2\sigma\,\alpha^2} \qquad \text{Eq.\{3.17\}}$$

where:

D_f : is the filter diameter $[cm]$

σ: is the filter cell density with the unit of $\left[\frac{1}{cm^2}\right]$ and it given by,

$$\sigma = \frac{1}{(a+w)^2} \qquad \text{Eq.\{3.18\}}$$

In addition the total volume $[cm^3]$ of the filter can be calculated as:

$$V_{trap} = \frac{\pi\, {D_f}^2 L}{4} \qquad \text{Eq.\{3.19\}}$$

Therefore, equation 3.16 can be rewritten as:

$$\Delta P_{clean} = \frac{\mu_{ex}\, \dot{Q}_{ex}}{2\, V_{trap}}\, (a+w)^2 \left(\frac{w}{k_o\, a} + \frac{8\, F\, L^2}{3\, a^4}\right) \qquad \text{Eq.\{3.20\}}$$

or

$$\Delta P_{clean} = \frac{\mu_{ex}\, \dot{Q}_{ex}}{2\, V_{trap}}\, (a+w)^2 \left(\frac{w}{k_o\, a} + \frac{4\, F\, L^2}{3\, a^4} + \frac{4\, F\, L^2}{3\, a^4}\right) \qquad \text{Eq.\{3.21\}}$$

At the second equation 3.21 is shown that the $\frac{8\, F\, L^2}{3\, a^4}$ term has splited into 2 terms. From physical respect the one term represents the frictional losses along the inlet channel, while the other one represents the frictional losses along the outlet channel.

3.6.2 Simulation of soottrap in ANSYS as a porous packed bed

The ANSYS equation for packed bed medium is:

$$\Delta P = \left(\frac{\mu_{in}}{K_{an}}\, U_{in} + C_2 \frac{1}{2}\, \rho_{in}\, {U_{in}}^2\right) L \qquad \text{Eq.\{3.22\}}$$

where,

μ_{in}*: dynamic viscosity at the inlet of porous medium* $\left[\frac{kg}{m\, s}\right]$

K_{an}*: permeability* $[m^2]$

U_{in}*: velocity at the inlet of porous medium* $\left[\frac{m}{s}\right]$

C_2*: inertial resistance* $\left[\frac{1}{m}\right]$

ρ_{in}*: density at the inlet of porous medium*

L*: length of porous medium* $[m]$

We express U_{in} *as function of volumetric flow* $\dot{Q}_{ex}$ *at the exit of medium :*

$$U_{in} = \frac{\dot{Q}_{in}}{A} \qquad \text{Eq.\{3.23\}}$$

$$\dot{Q}_{ex} = \frac{\rho_{in}}{\rho_{ex}} \dot{Q}_{in} \qquad \text{Eq.\{3.24\}}$$

Therefore from equations 3.23 ,3.24:

$$U_{in} = \frac{\rho_{ex}}{\rho_{in}} \frac{\dot{Q}_{ex}}{A} \qquad \text{Eq.\{3.25\}}$$

Applying the equation 3.25 to 3.22 we get the following ANSYS equation:

$$\Delta P = \frac{\mu_{in}}{K_{an}} \frac{\rho_{ex}}{\rho_{in}} \frac{\dot{Q}_{ex}}{A} L + C_2 \frac{1}{2} \rho_{in} \left(\frac{\rho_{ex}}{\rho_{in}} \frac{\dot{Q}_{ex}}{A} \right)^2 L \qquad \text{Eq.\{3.26\}}$$

The equation 3.20 of Konstandopoulos-Johnson model can be written in the following form:

$$\Delta P_{clean} = \frac{\mu_{ex} \dot{Q}_{ex}}{2 V_{trap}} (a+w)^2 \frac{w}{k_o a} + \frac{\mu_{ex} \dot{Q}_{ex}}{2 V_{trap}} (a+w)^2 \frac{8 F L^2}{3 a^4} \qquad \text{Eq.\{3.27\}}$$

Now comparing, the first term of equation 3.26 with the first term of equation 3.24 as well the second terms respectively, we get the equation of K_{an} and C_2 which can simulate the pressure drop of soottrap as a packed bed in ANSYS.

$$K_{an} = \frac{\mu_{in} \rho_{ex} 2 L V_{trap} K_o a}{\mu_{ex} \rho_{in} A (a+w)^2 w} \qquad \text{Eq.\{3.28\}}$$

$$C_2 = \frac{\mu_{ex} \rho_{in} 16 L F A^2 (a+w)^2}{6 V_{trap} a^4 \rho_{ex}{}^2 \dot{Q}_{ex}} \qquad \text{Eq.\{3.29\}}$$

The volumetric flow rate at the exit, can be calculated by:

$$\dot{Q}_{ex} = \frac{\rho_{mix,f.c.}}{\rho_{mix,ex}} \dot{Q}_{mix,f.c} \qquad \text{Eq.\{3.30\}}$$

Where $\rho_{mix,f.c.}$, $\dot{Q}_{mix,f.c}$ the density of air-methane mixture at the flow controllers (temperature reference 273,15 [K]) and volumetric flow rate of mixture at the flow controllers. ρ_{in} is the density at the inlet of soottrap or packed bed, thus the temperature at the inlet needs in order to calculate this quantity. The equations of calculation for density and volumetric flow rates of mixtures will be explained at the paragraph 3.7.2.1.

The coefficients K_{an} *and* C_2 could also be written as function of inlet velocity as are shown below.

$$\rho_{in} = \frac{\dot{m}_{air}}{A\, U_{in}} \qquad \text{Eq.\{3.31\}}$$

Applying the equation [3.31] to [3.22] we get the following Ansys equation:

$$\Delta P = \frac{\mu_{in}}{K_{an}} \cdot U_{in} \cdot L + C_2 \cdot 0.5 \frac{\dot{m}_{air}}{A} \cdot U_{in} \cdot L \qquad \text{Eq.\{3.32\}}$$

Comparing the first term of equation [3.27] with the first term of equation [3.32] as well as the second terms respectively, we get the equation of $\boldsymbol{K_{an}}$ and $\boldsymbol{C_2}$ as function of Uin.

$$K_{an} = \frac{\mu_{in}\ U_{in}\ L\ \ 2\ V_{trap}\ K_o\ a}{\mu_{ex}\ Q_{ex}\ (a+w)^2\ w} \qquad \text{Eq.\{3.33\}}$$

$$C_2 = \frac{2\ A\ \mu_{ex}\ Q_{ex}\ (a+w)^2\ 8\ F\ L^2}{2\ V_{trap}\ 3\ a^4\ \dot{m}_{air}\ U_{in}\ L} \qquad \text{Eq.\{3.34\}}$$

3.6.2.1 Comparison of pressure drop prediction of Konstandopoulos-Johnson model with pressure drop of soot trap as packed bed in ANSYS.

In order to evaluate the idea and the equations of the previous paragraph, some simulations were conducted for a rectangular axisymmetric domain which has the size of the soottrap. Firstly the pressure drop was calculated by Konstandopoulos-Johnson model, equation 3.27, for each case of volumetric flow rate. The ANSYS coefficients K_{an} and C_2 for the packed bed were also calculated by the equations 3.33 and 3.34 respectively. The mathematical correctness of the coefficients' values verified through the ANSYS equation 3.22 where the pressure drop prediction must be equal to the pressure drop prediction of Konstandopoulos-Johnson equation 3.27.

At the following table 3.6 are shown the cases which are simulated, the conditions at the inlet and at the outlet of the domain, the pressure drop prediction by Konstandopoulos-Johnson equation, the calculated coefficients K_{an} and C_2 and their verification through ANSYS equation. Thereafter the results of ANSYS simulations are presented in figures for each case and a diagram which includes the results for pressure drop from simulations and from Konstandopoulos-Johnson equation is also presented, in order the results to be evaluated.

Table 3.6

cases	Q_{air} [lt/min]	$T_{f.c}$ [K]	$\rho_{air\ f.c}$ [kg/m^3]	m_{air} [kg/s]	T_{in} [K]	ρ_{in}[kg/m^3]	Q_{in} [m^3/s]	U_{in} [m/s]	μ_{in} [kg/m*s]
1	17	273,15	1,29213601	0,000366	773,15	0,456505	0,000802	0,638514	3,547E-05
2	27	273,15	1,29213601	0,000581	773,15	0,456505	0,0012737	1,014111	3,547E-05
3	35	273,15	1,29213601	0,000754	773,15	0,456505	0,0016511	1,314588	3,547E-05

Continued of Table 3.6

T_{ex} [K]	ρ_{ex} [kg/m^3]	Q_{ex} [m^3/s]	μ_{ex} [kg/m*s]	DP [Pa] (Equation 3.27)
773,15	0,456505144	0,000801974	3,5475E-05	227,3825177
773,15	0,456505144	0,001273723	3,5475E-05	361,1369399
773,15	0,456505144	0,001651123	3,5475E-05	468,1404777

Continued of Table 3.6

Kan [m^2]	1/Kan [1/m^2] (Equation 3.33)	C2 [1/m] (Equation 3.34)	DP [Pa] (Equation 3.22 for verification)
2,25645E-08	44317309,93	6692,623046	227,3825177
2,25645E-08	44317309,93	4213,87377	361,1369399
2,25645E-08	44317309,93	3250,702623	468,1404777

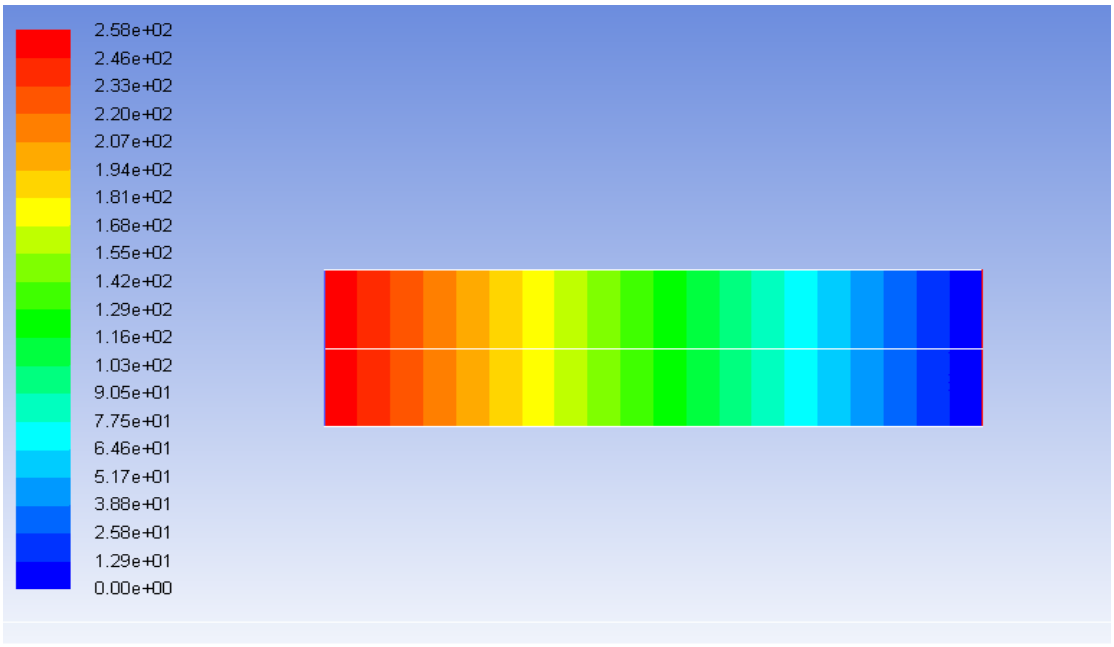

Fig. 3.20: Pressure drop in [Pa] for an isothermal (773.15 K) flow of air and for volumetric flow 17 [lt/min].

Table 3.7	Pressure drop [Pa]
Simulation ANSYS	258
Konstandopoulos-Johnson model	227,38

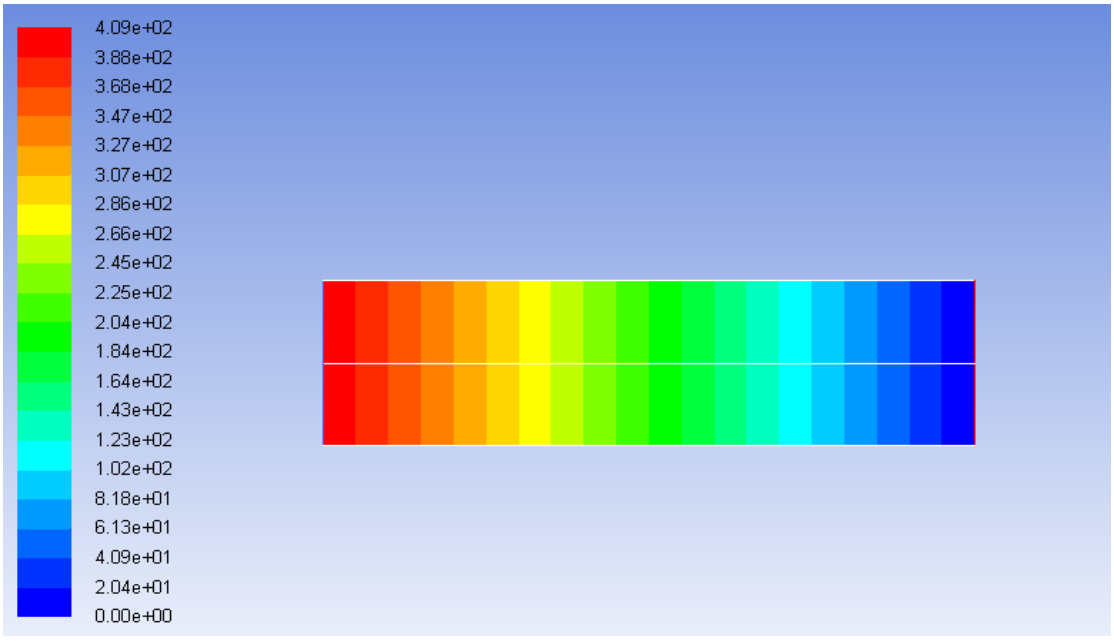

Fig. 3.21: Pressure drop in [Pa] for an isothermal (773.15 K) flow of air and for volumetric flow 27 [lt/min].

Table 3.8	Pressure drop [Pa]
Simulation ANSYS	461,14
Konstandopoulos-Johnson model	409

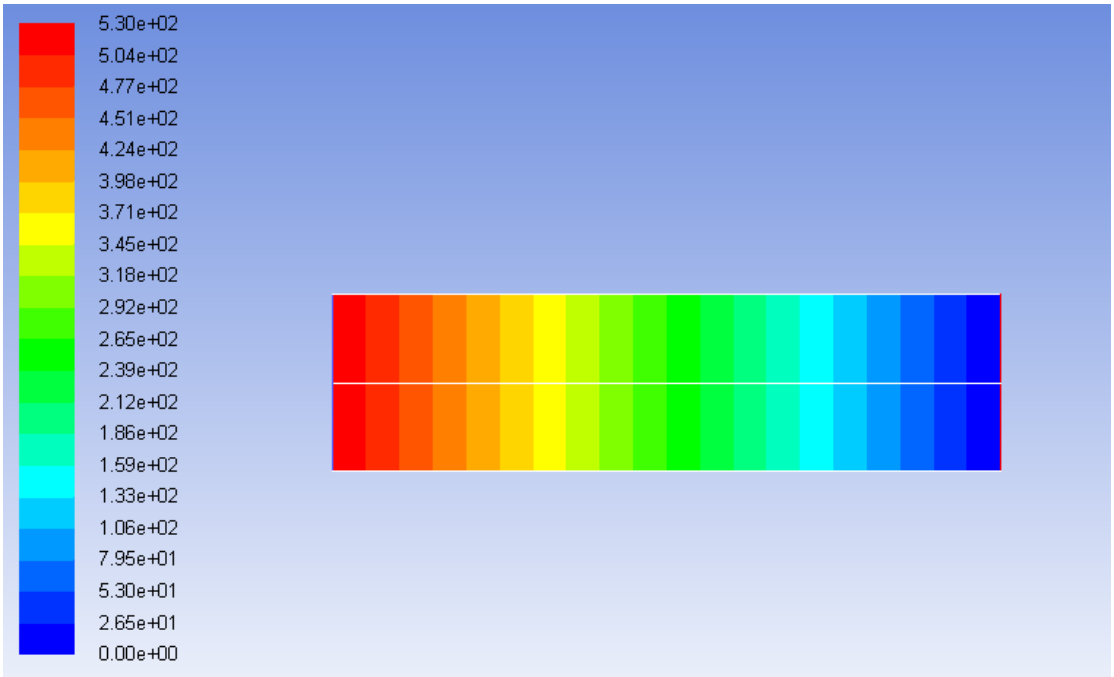

Fig. 3.22: Pressure drop in [Pa] for an isothermal (773.15 K) flow of air and for volumetric flow 35 [lt/min].

Table 3.9	Pressure drop [Pa]
Simulation ANSYS	468,14
Konstandopoulos-Johnson model	530

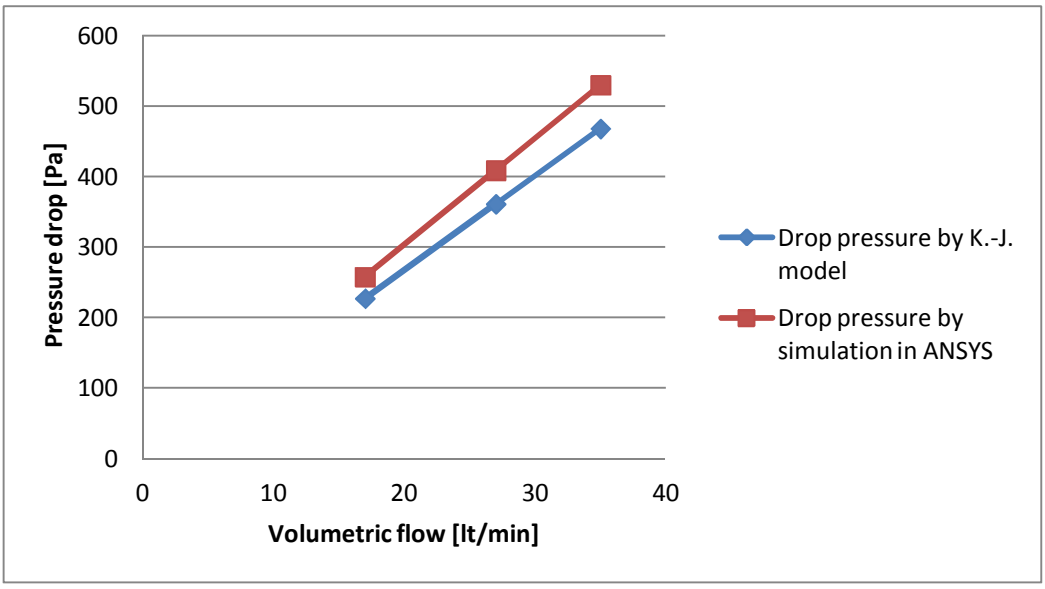

Fig. 3.23: Comparison between the results of pressure drop from Konstandopoulos-Johnson model and soot trap as porous packed bed in ANSYS, for different air volumetric flows and inlet temperature 773,15 [K].

As it can been seen from the above figures, the approach of the soottrap as packed bed in ANSYS seems to have satisfactory agreement with the prediction of pressure drop Konstandopoulos-Johnson model. However , it can be observed that the deviation between Konstandopoulos-Johnson model and ANSYS simulation is increasing for higher volumetric flows. These results allowed us , in the chemical kinetics simulation of *chapter 5* to simulate the reformer's domain which represents the soot trap, as porous packed bed and to be accomplished downstream of the reaction zone in the conical section, a real pressure field where its characteristics are determined by the real characteristics of soot trap as was described in 3.6.2. This approach is quite convenient since the real geometry of soot trap could not be simulated in an axisymmetric problem in ANSYS. However the a non-true geometry doesn't allowed us to evaluate the real flow field which formed inside of the soot trap and leads us to underestimate the residence time of the flow which is an important parameter in the chemical processes.

Chapter 4th: Experimental investigation of a prototype fuel reformer

4.1Based on wall flow filter TPOX reactor

The main purpose of the experimental investigation is to evaluate a prototype T-POX reactor based on a wall flow filter or so called soottrap, concerning to its operating characteristics, its efficiency and to evaluate the possibility of regeneration in very low air-fuel ratios as was mentioned in the paragraph 2.5.

4.1.1The drawing and construction of TPOX reactor

The same versions of the T-POX reactor were constructed twice for the experimental investigation. The operating characteristics and conditions were mainly investigated at the first version and additionally at the second version a soot measurement system was incorporated. The drawing of the second version of T-POX reactor which is shown below, has tubes for the thermocouples such as the first version and an incorporated sampling system for soot measurements.

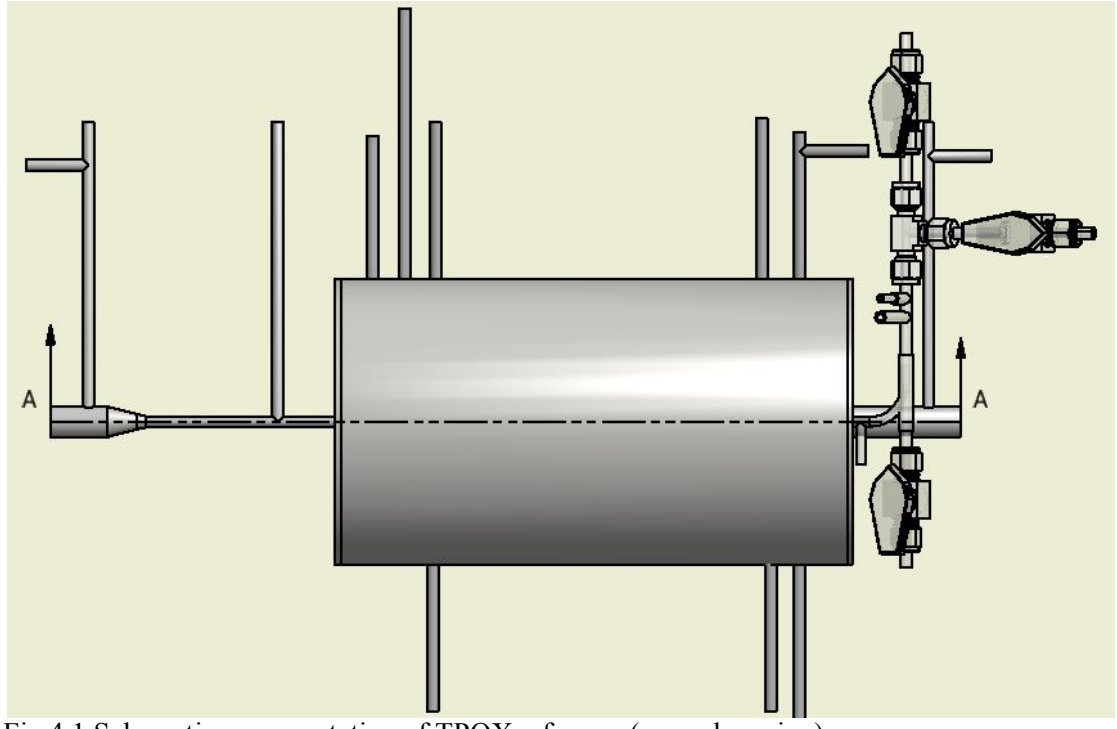

Fig.4.1 Schematic representation of TPOX reformer (second version).

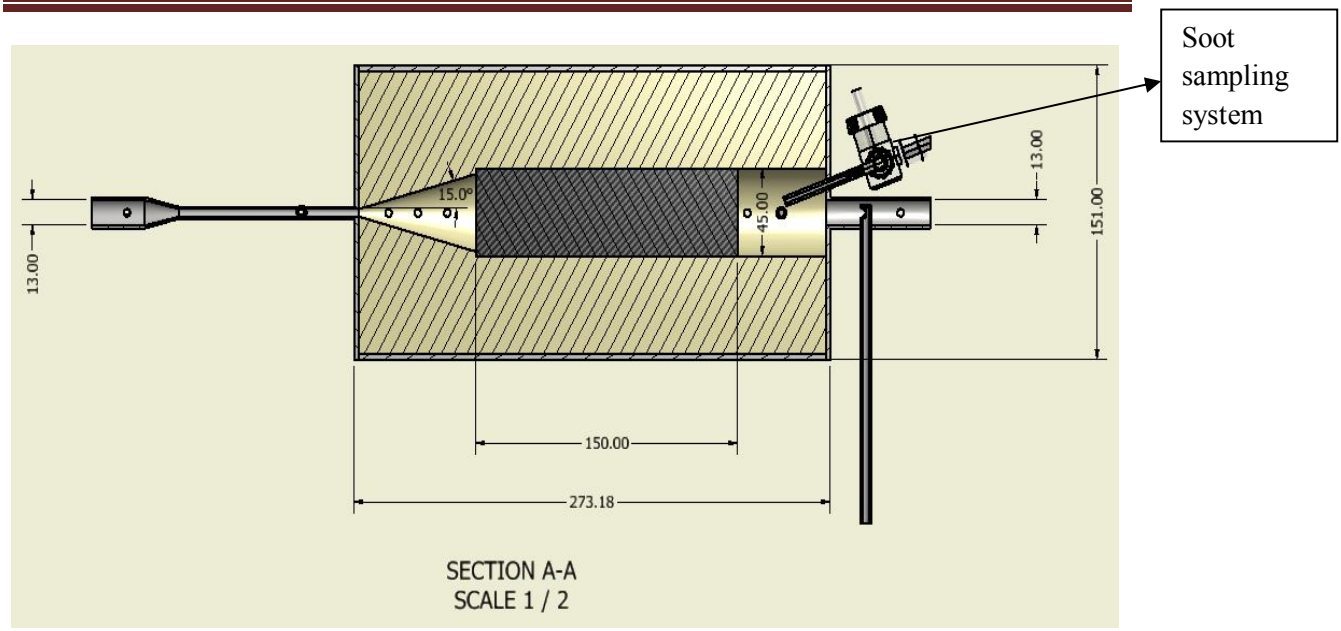

Fig.4.2 Schematic cross section representation of the based on soottrap TPOX reformer (second version).

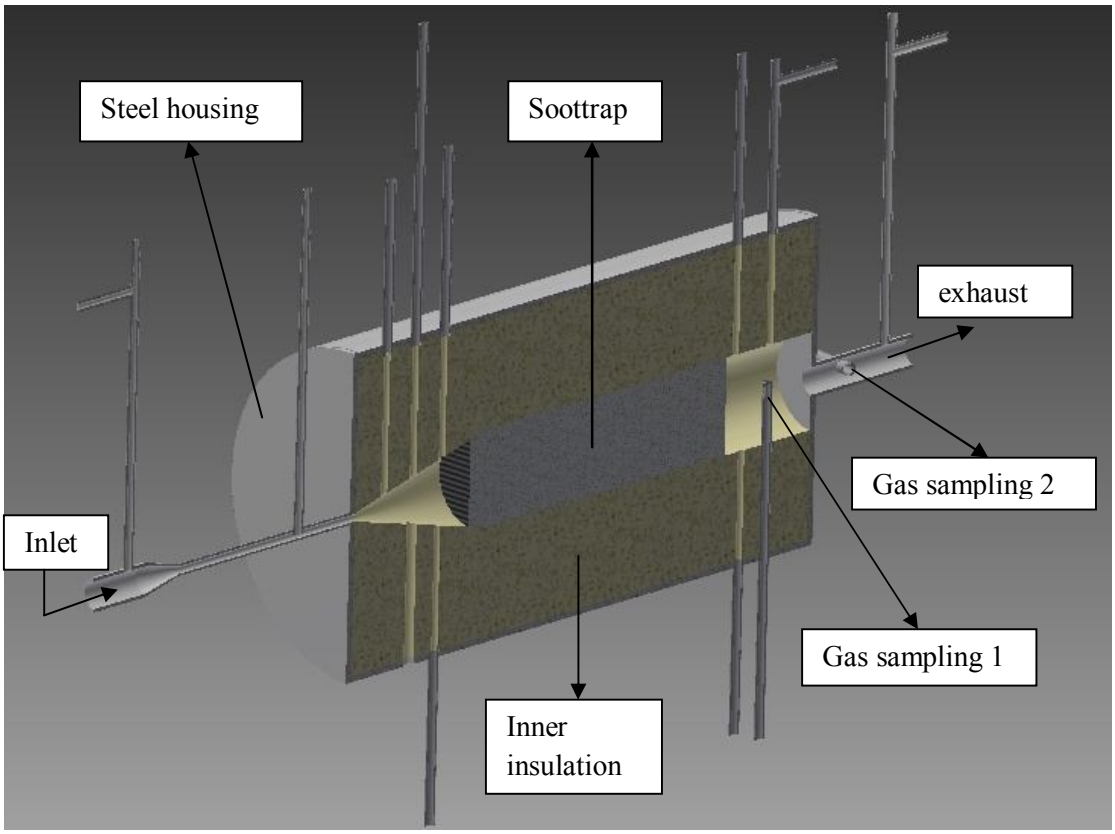

Fig.4.3 Schematic 3D cross section representation of the soottrap based TPOX reformer.

The reformer has been designed with the aim of having a stationary TPOX process, for a wide range of operating conditions, which is accomplished within a single component geometry. This geometry consists of two sections, a conical one, which enables a self-adjustment in the position of the stationary combustion zone depending on operating conditions and a cylindrical

one where slow endothermic reforming reactions take place inside of the soot trap. It is chosen a small diameter tube for reactants' inlet aiming to increase the momentum and to prevent the possibilities of flash back since the thermal load would be low and therefore the velocities.In the above schematic representation the soottrap is not represented by an inside geometry as it is in the reality.

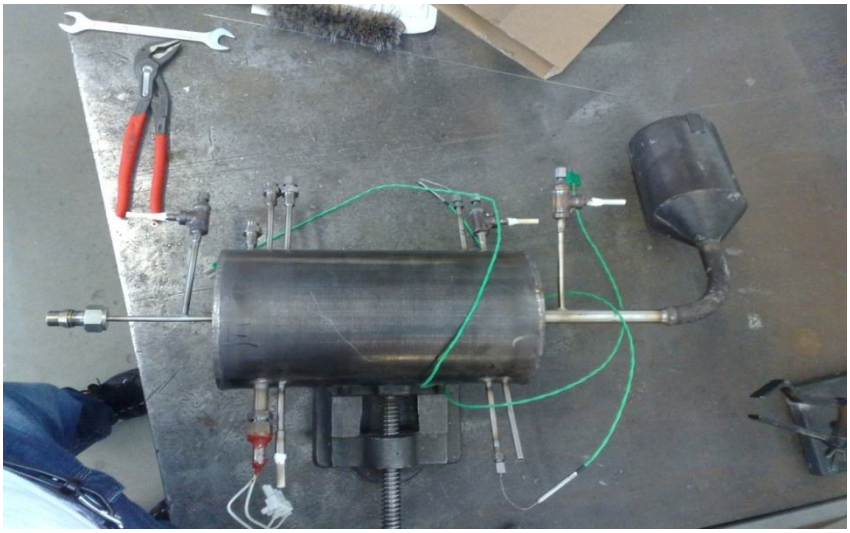

Fig.4.4 TPOX reformer (first version) welded with the postcombustor during the construction.

Fig.4.5 The soot trap by SiSic ceramic material.

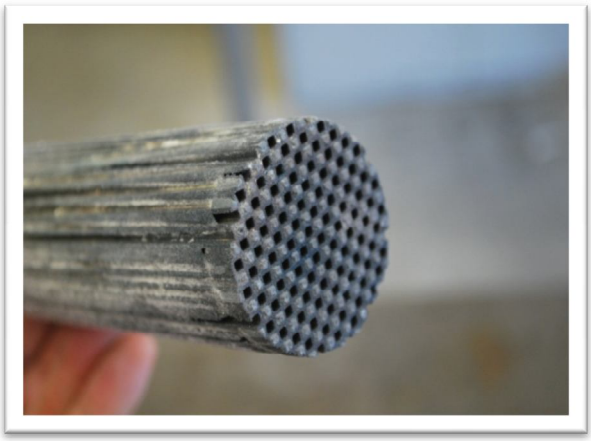

Fig.4.6 The soot trap after treatment. It was incorporated to the T-POX reactor.

In figure 4.6 is shown the soot trap which was incorporated in the T-POX reactor, and it was originated after specific treatment by the matrix of a bigger in size soot trap which is shown in figure 4.5. The properties of this type of soot trap have are presented in the following tables 4.1 and 4.2.

Property	SiC
Material density (kg/m^3)	3080
Porosity (%)	42
Cell size (mm)	1.49 × 1.49
Wall thickness (mm)	0.4
Wall density (kg/m^3)	1800
Mean pore size (μm)	9
Permeability (m^2)	3.7×10^{-13}

Table 4.1. Properties of single-channel filter The permeability here refers as Ko.

Type	SiC 14/200
Diameter	143.8 mm
Length	152.4 mm
Cell concentration	200 cells/in^2
Cell pitch	1.89 mm
Wall thickness	0.4 mm

Table 4.2. Diesel particulate filter specifications.

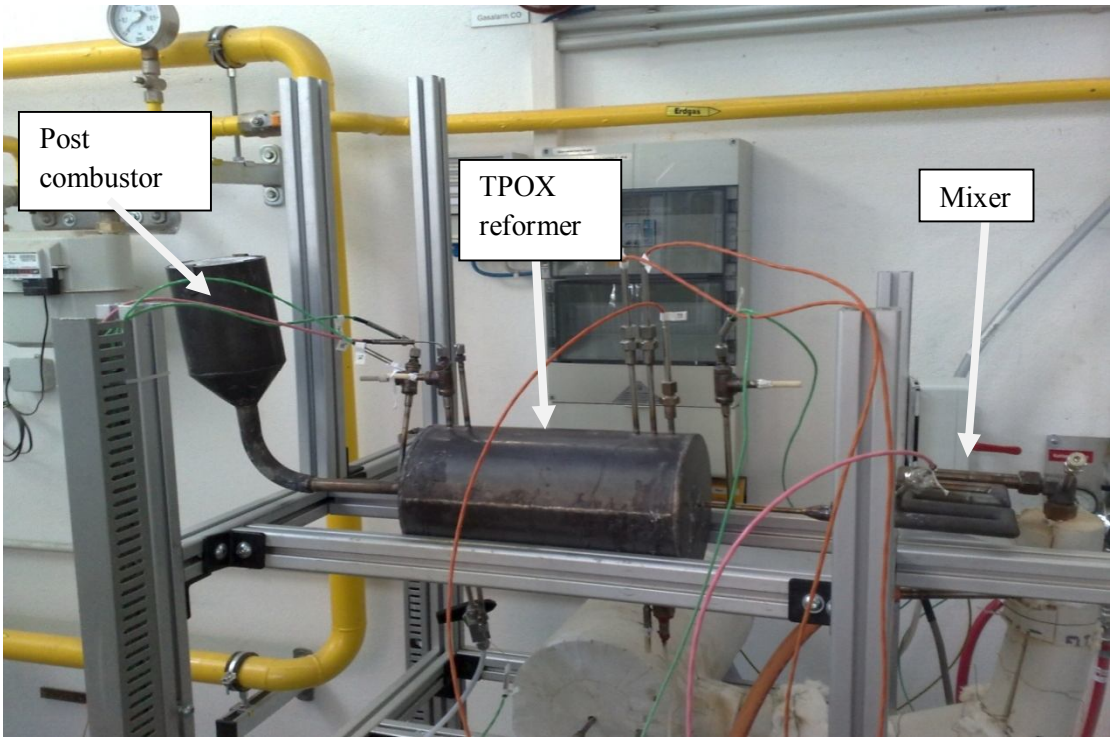

Fig.4.7 The TPOX reformer (first version) without insulation.

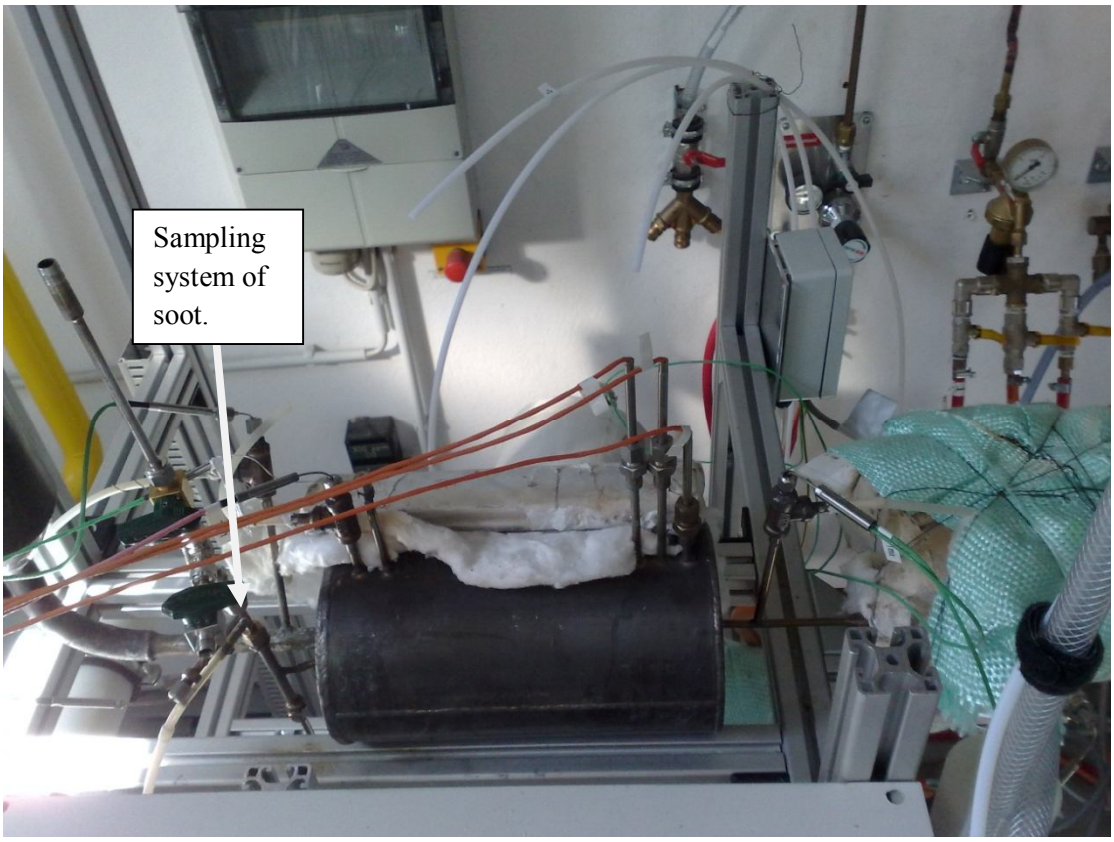

Fig.4.8 During the preparation of insulation the TPOX reformer (second version) with the sampling system of soot and thermocouples.

Fig.4.9 The T-POX reformer (first version) insulated with the main insulation layers.

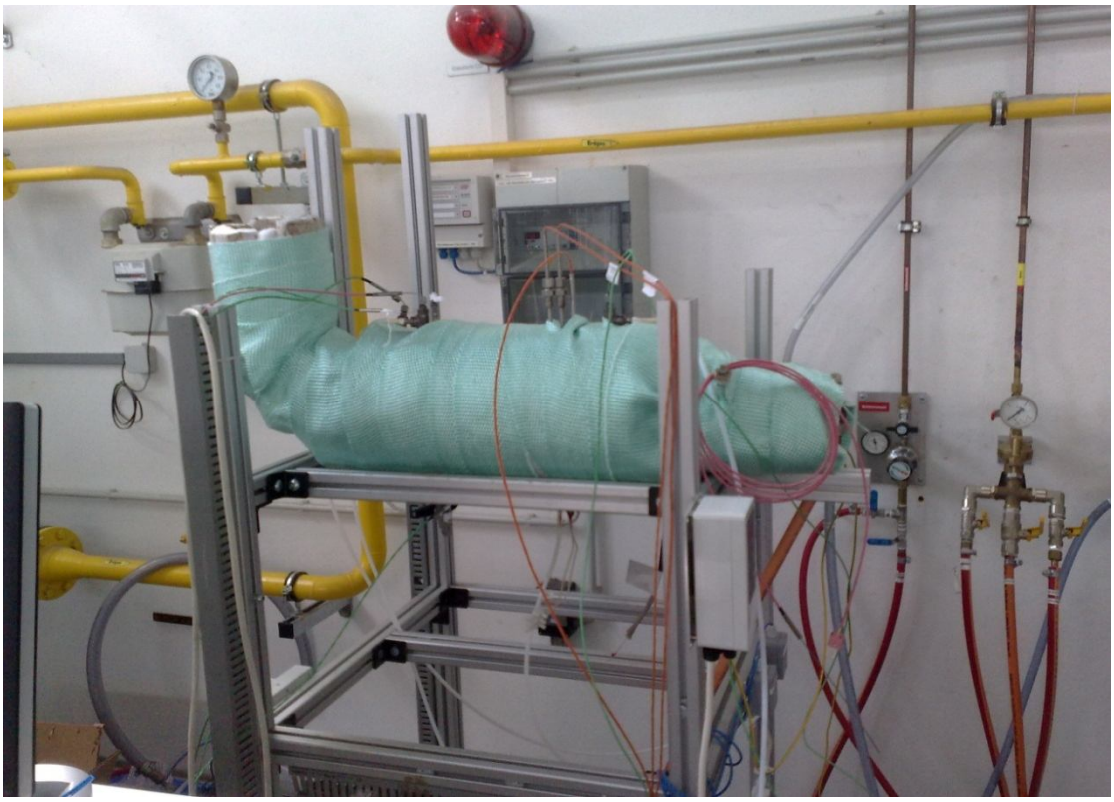

Fig.4.10 The T-POX reformer (first version) with the final insulation.

Fig.4.11 The final assembly (second version) with the thermodiluter head of dilution system which is analyzed thoroughly in the paragraph 4.1.5.

4.2 Description of the experimental setup

The utilized test setup is described in this chapter. The corresponding measuring periphery were already available. Many modifications and additions had to be performed to the test-rig so as to enable the conduction of accurate and reliable soot size distributions and concentrations of chemical species measurements.

The setup illustrated in Fig.4.12 was used for the conduction of the experimental investigations. The setup consisted of the TPOX reformer as well as control and measurement instrumentation.

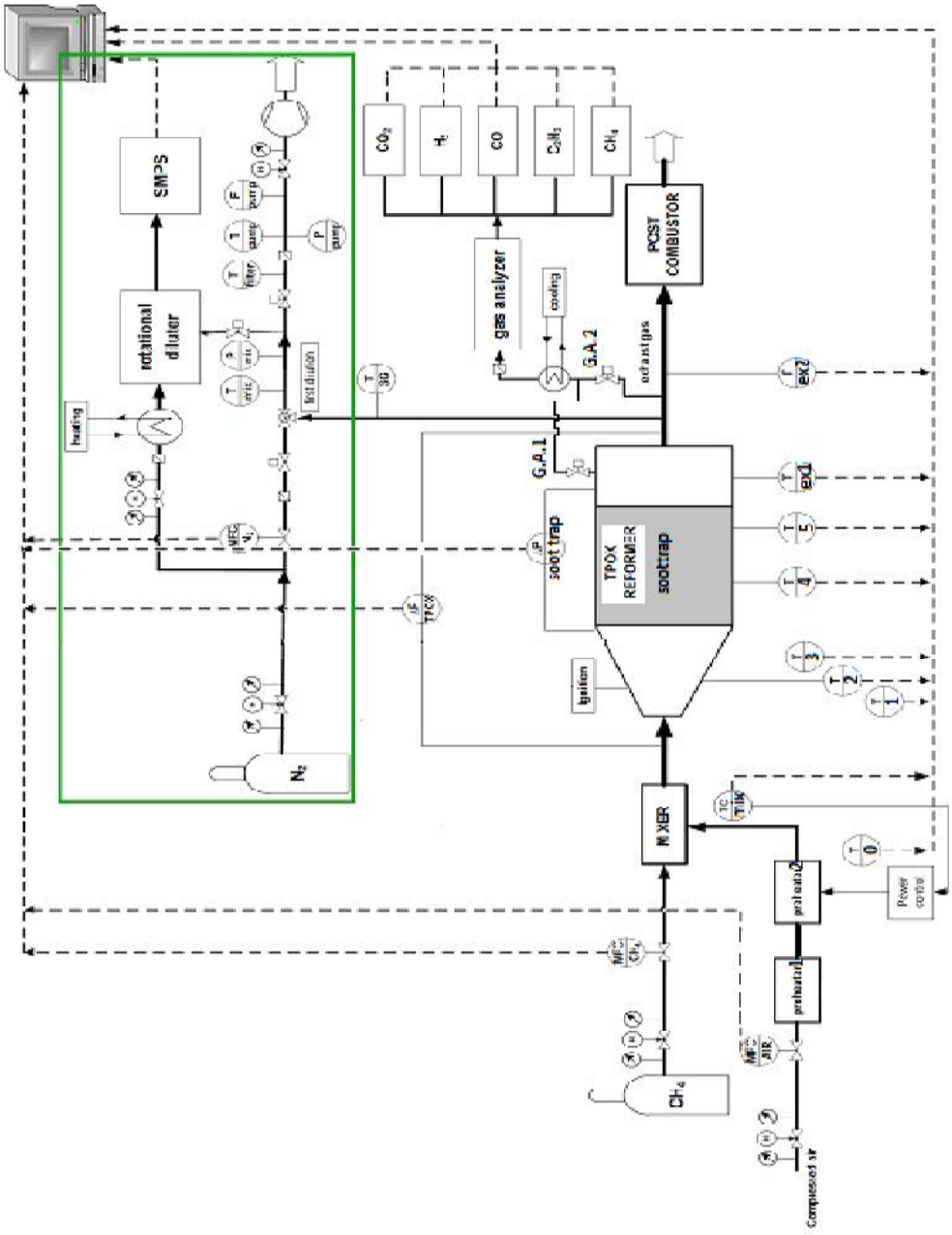

Fig.4.12 Flow sheet of the experimental setup

The two gas streams were supplied to the system via thermal mass flow controllers. Pure methane 2.5 (>99.5%) from high pressure bottles was used as fuel. Electrical preheating was used to simulate temperature conditions of the air stream similar to the ones expected from recovering heat within an integrated SOFC based micro CHP-system. Two preheaters were utilized for this purpose. The first one was increasing the temperature of air to the desired value and the second one was complementing the energy of thermal losses and controlling the final value of temperature in the inlet via a feedback of a thermocouple (Tmix) .

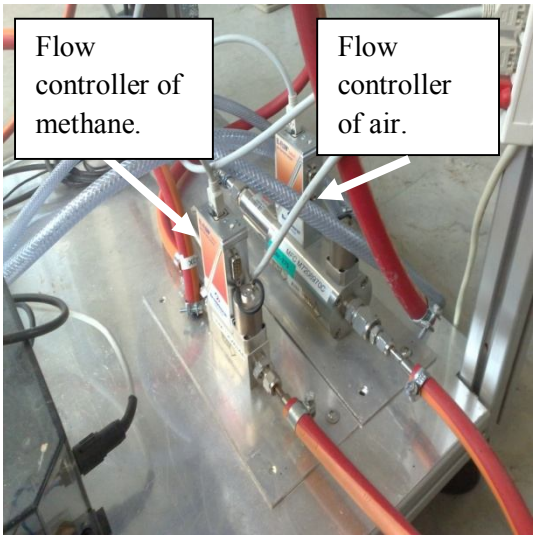

Fig.4.13 The mass flow controllers.

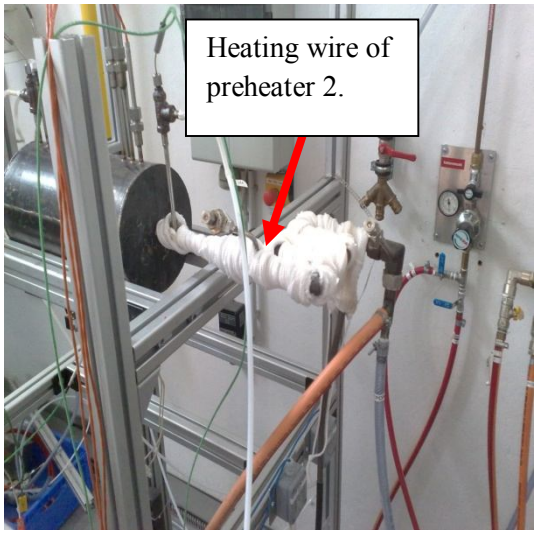

Fig.4.14 The heating wire wrapped around of mixing tube

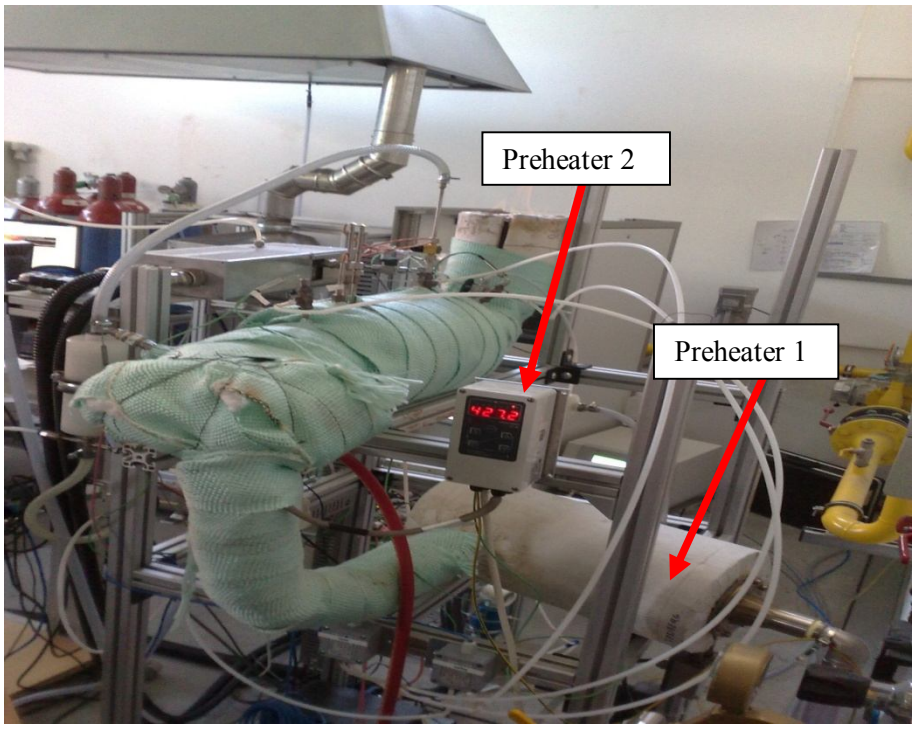

Fig.4.15 The positions of two preheaters

The educts, namely the methane and the preheated air stream had to be properly mixed before entering the reforming zone. Thus, a mixing section was used upstream the reformer, designed so as to eliminate the problems of spontaneous mixture ignition and flame flashback.

Fig.4.16 Mixing tube

Fig.4.17 The position of mixing tube

4.2.1Temperature and pressure measurements

An N-type thermocouple (with Inconel protection sheath of 3.00 mm in diameter) with the name T_{mix} was used for monitoring and controlling at the same time the temperature of the methane-air mixture upstream the reforming section. The temperature distribution within the reaction zone (empty conical section) was measured with S-type thermocouples (thermo wire protected by 3.00 mm ceramic seath). The names of these thermocouples are T_1,T_2,T_3.Two N-type thermocouples was placed inside of the soottrap at 30mm and 70mm respectively from the back side of the soottrap, T_4 and T_5 . Also a K-type thermocouple T_{ex1} was placed immediately after the exit of the soottrap and a N-Type T_{ex2} was placed at the exit of the reformer. The accuracy of the thermocouples is ± 2°C for the K-type, ± 3°C for the S-type and ± 4°C for the N-type. All the thermocouples were connected to the data acquisition system through a data acquisition board and the obtained values were recorded with a sampling frequency of 1 Hz. Sensitive differential pressure transducers were utilized to continuously monitor the two most important pressure drops in the system: between inlet and outlet of the reformer and between inlet and outlet of the soottrap. They have a measurement range of (0-2500) Pa with an error of linearity of ± 0.8% of the final value and a reproducibility of 0.1% of the final value. The control of the volumetric flows and the observation of the conditions in the test-rig were realized through a Lab-View 8.5 software.

Fig.4.18 The Lab-View software for the controlling and observation of the experiment conditions

4.2.2Gas measurements

There were two probes in different positions for the sampling of the gas. The first was immediately after the exit of the soottrap and the second one about ten millimeters after exit of the reformer. The sampling probes didn't employ simultaneously when the one was opened the second was closed and reversed .

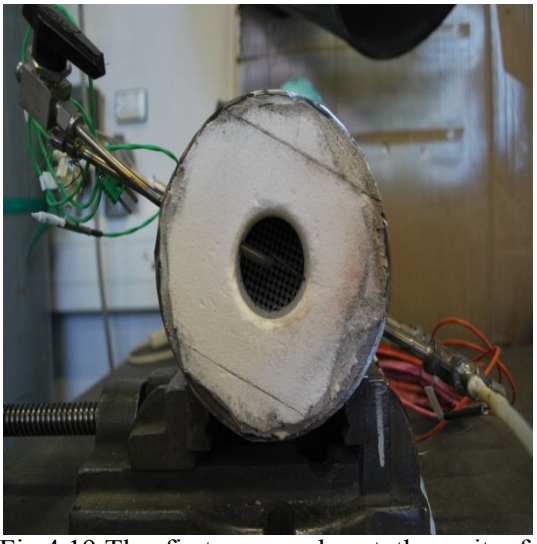

Fig.4.19:The first gas probe at the exit of soottrap

Fig.4.20:The inlet configuration of the probe

The probed sample was sent to calibrated gas analyzers and was on-line analyzed for the major species H_2, CO, CO_2 and the minor species CH_4, C_2H_2 which is considered as the main

precursor for soot formation in such processes. Condensed phases were removed upstream the gas analyzers via a TEFLON filter and a condensate trap. The ABB analyzer was composed of the following modules: Caldos17 (thermal conductivity analyzer module) for H_2, Uras14 (infrared analyzer module) for CO, CO_2, CH_4, C_2H_2 and Magnos106 (paramagnetic oxygen analyzer module) for O_2 measurement. All the water content of the sample gas had to be condensated before entering the gas analyzer modules and therefore, the amount of H_2O had to be recalculated from the measurements of the major species and the mass balance of the process. The signals from the gas analyzer modules were connected to the data acquisition system and the obtained values were recorded with a sampling frequency of 1 Hz.

The remaining major part of the explosive and toxic product gas was incinerated in a post-combustor to primarily decrease the carbon monoxide content.

Fig.4.21 The gas analyzers in laboratory

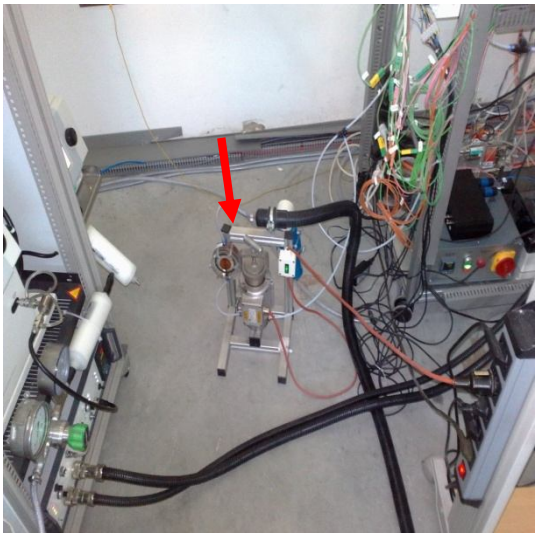

Fig.4.22 The filter before the gas analyzer

4.2.3Soot measurements

For the reliable soot size distributions proper sampling and conditioning of the soot-laden gas had to be assured and the respective dilution method and equipment is described thoroughly in the 4.4 paragraph. The commercial Scanning Mobility Particle Sizer (SPMS) device (TSI Mobel 3080) was used for the detection of soot particles and the measurements of particle size distributions (PSD).Prior to SMPS scanning, the extracted gas samples were highly diluted with nitrogen. The SMPS and the dilution system analyzed thoroughly in the paragraphs 4.3 and 4.4.

4.3Principles of the SMPS technique

The size of aerosol particles can be determined based on their motion within an electrostatic field and commercial instruments which use this principle to measure particle size distributions are known with the term Scanning Mobility Particle Sizer (SMPS). The method is actually the most widely applied for this purpose and it has been proven quite effective for studying Soot Particle Size Distributions (SPSDs) at different moments of their evolution, close to - and after inception, and has provided a huge amount of information concerning coagulation dynamics not only in soot aerosols but also in other types of aerosols.
For the experimental study of the reformer of this thesis, the SMPS method the appropriate equipment was used for obtaining SPSDs. The principles of its operation and the parts which consists of the equipment are analyzed in the following paragraphs. In additional, an other possibility for in-situ measurement of solid particles is with optical methods. As there is no optical access to the inside of the TPOX reformer, optical measurement techniques can not be used at the moment.

Differential Mobility Analysis and Scanning Mobility Particle Sizers

The method involves probing of gas sample from the examined flame and measurement of the mobility of the particles in an imposed electric field. In practice the measurements are usually carried out with SMPS instruments which consist of the Differential Mobility Analyzer (DMA) figure 4.24 and the Condensation Particle Counter (CPC) figure 4.26. The term Electrostatic Classifier is also used to describe the DMA section.

4.3.1Measuring particle size

The DMA consists of two concentric cylinders. The center rod is maintained at a controlled voltage (usually negative) while the outer cylinder is electrically grounded and in this way the electric field is created in the annular space between them. The particles carried in the sample (qα) enter the field after having passed from a small chamber containing a radioactive source (e.g. krypton-85, polonium-210). The role of source is to ionize the air molecules in this chamber so that the particles can be ´´neutralized´´ during their residence time there. The term "neutralization" means that they will leave the chamber having an equilibrium charge state. This state is characterized by a known distribution of charges on the particles which depends on their size (Boltzmann equilibrium distribution) [Hinds, p.337]. Wiedensohler [1998] has developed an approximation of the bipolar charge distribution for particles in the submicron range which is applied in practice for SMPS instruments.
The polydisperse aerosol with the charged particles and sheath air (qsh) are introduced at the top of DMA and flow down the annular space between the cylinders. The aerosol surrounds the inner core of sheath air, and both flows pass down the annulus with no mixing of the two laminar streams. Particles are precipitated along the length of the center rod depending on their electrical mobility $\boldsymbol{Z_p}$ in (m2/Vs), the geometry of the cylinders and the flow rates. Particles within a narrow range of electrical mobility exit through a small slit located at the bottom of the center rod, in the form of a monodisperse aerosol (qm). The remaining particles are removed from Crassifier via the excess air flow (qe).

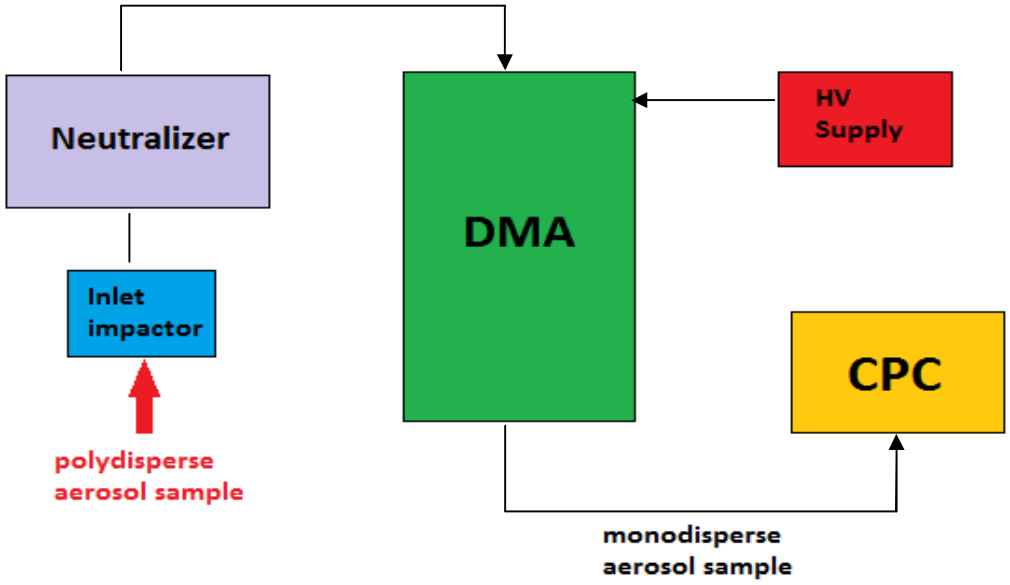

Fig.4.23 SMPS basic flow sheet

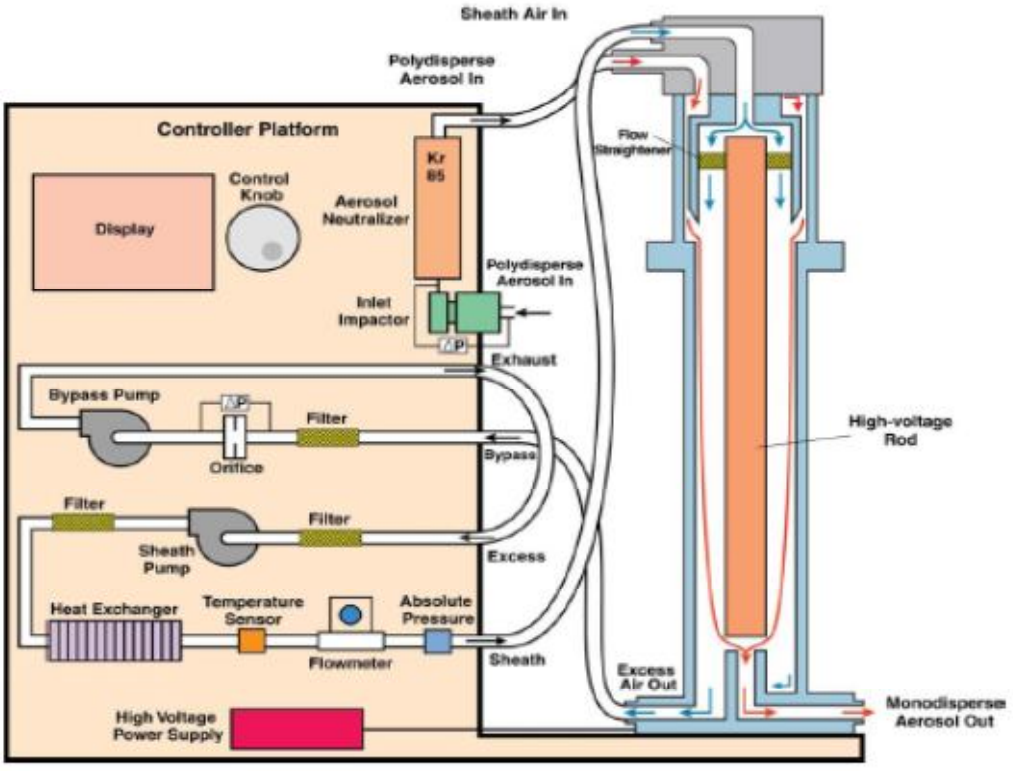

Fig.4.24: Flow diagram for Electrostatic Classifier and Differential Mobility Analyzer. [36]

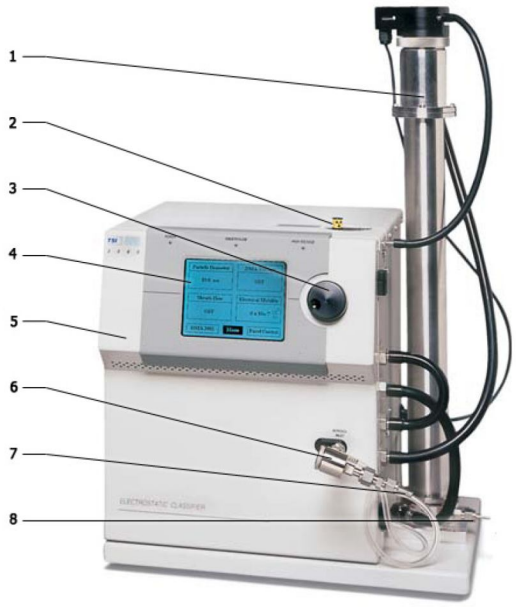

Fig.4.25: Parts of the SMPS with: 1 Differential Mobility Analyzer; 2 Neutralizer (radioactive source: Kr85); 3 Control; 4 Display; 5 Electrostatic Classifier; 6 Impactor; 7 Input of polydispersive aerosol (syngas with soot); 8 Output monodispersive aerosol (soot particles with defined size). [36]

The measured electrical mobility [Knutson 1975] within the DMA is a function of the particle-free carrier gas flow rate, of the applied voltage V, and of the geometrical characteristics of the classifier, inner radius r_1, outer radius r_2 and L is the length of the classifying region:

$$Z_p = \frac{q_{sh}}{2\pi VL}\ln\left(r_2/r_1\right) \qquad \text{Eq.}\{4.1\}$$

In general, an expression for the electric mobility of a charged particle involving the particle diameter is obtained by equating the electric field force with the Stokes drag force.

$$Z_p = \frac{neC_c}{3\pi\mu\widetilde{D}_P} \qquad \text{Eq.}\{4.2\}$$

Equation 4.2 is valid only for spherical particles and μ is the viscosity of the carrier gas within the DMA, e is the electron charge, and n is the number of charges on the particle. The Cunningham slip correction factor Cc at Eq.4.3, accounts for the transition from the Stokes continuum regime where viscous dissipation of the fluid dominates the particle fluid movement, to the free molecule regime where the direct collision between the particles and the gas molecules is the dominant mechanism for momentum transfer. It should be mentioned that expressions like the NN are empirical.

$$C_c = 1 + Kn\,A + Bexp\,\frac{E}{Kn} \qquad \text{Eq.}\{4.3\}$$

The C_c factor is a function of the Knudsen number:

$$Kn = \frac{2\lambda}{D_p} \qquad \text{Eq.}\{4.4\}$$

where λ is the mean free path of the gas carrier and $\boldsymbol{D_p}$ is the particle diameter. The term mobility diameter $\boldsymbol{\tilde{D}_P}$ is often used in the literature to refer to diameter estimations resulting from this method. As already mentioned, equation 4.2 is valid only for spherical particles, so in the case of large and very large particles which are aggregates the estimated diameter is rather than an effective diameter characterizing the particle structure. In the case of extremely small particles (<10nm) the accuracy of the diameter estimation is also a topic for discussion. It has been suggested that correction functions should be applied in order to account for all the effects occuring when particle sizes approach molecular dimensions. For example Abid and Wang (bockhorn book.) have proposed the following correlation between real particle diameter and mobility diameter, for particles with sizes in the range $1 \leq D_p \leq 100\ nm$:

$$R_p/\tilde{R}_p = 1.0676 - \frac{0.2232}{\tilde{R}_p}\tanh\left(1.4334 + 0.02496\tilde{R}_p\right) \qquad \text{Eq.}\{4.5\}$$

4.3.2Measuring particle concentrations

The particle size (or mobility) distribution is obtained by counting the particles in the monodisperse aerosol that exits the DMA varying the voltage within the electric field. The particles are counted downstream by the Condensation Particle Counter (CPC). In the CPC a controlled growth of their size is promoted via heterogeneous condensation of a vaporized medium, usually butanol or water. Once the particles have grow to an optically detectable size (typically, 2 to 3 μm), they pass through a light beam, scatter light onto a photo-detector. The pulse of light scattered by each particle is counted separately and the concentration is computed from the frequency of pulses. The efficiency of commercial CPC units is an important technical aspect that affects the measurements again when it comes to the extremely small particles. The particle size limit for 100% counting efficiency varies between the different devices and the lowest possible with the current CPC technologies lies at 3nm.

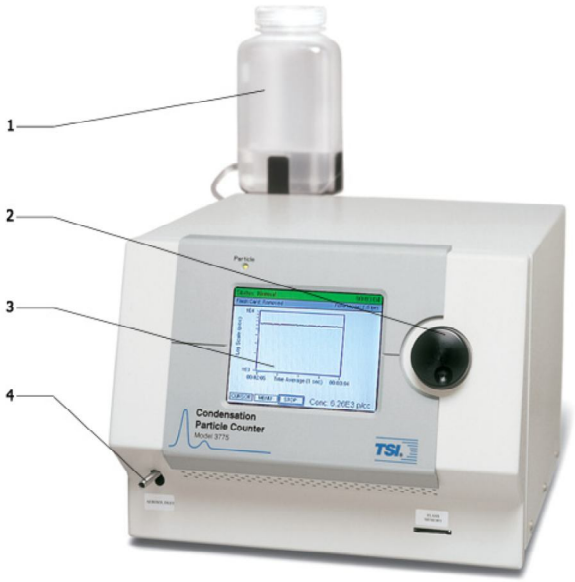

Fig. 4.26: Condensation Particle Counter with 1 Storing tank for butanol; 2 Control panel; 3 Display; 4 Input monodispersive aerosol.

4.3.3Particle sampling

Particle sampling is a very important stage in SMPS measurements and when not appropriately conducted, it can actually lead to significant errors in the characterization of soot particle size distributions SPSDs. Potential problems include particle losses in the sample probe through particle-particle coagulation or diffusive losses to the walls along the sampling line [39]. The flame gas usually contains about 10^{10} per cm^3 or more particles make it more clear if it is a general case. Immediate dilution close to the sampling point is essential; the loss of 10% particles by particle-particle coagulation in the probe is estimated to occur in approximately 20 ms, assuming that the coagulation kernel is that of a pair of particles 5 nm in diameter [38]. The dilution also quenches chemical reactions and prevents the particles from further size growth in the sampling line.

There are several studies available concerning proper probing from flames where the different groups have studied the influence of the dilution ratio and of the residence time of the sample within the probe [38],[39],[40]. It is currently accepted that measurements which reflect the soot size distributions in the flame with adequate accuracy require dilution of ~$\mathbf{10^4}$. Zhao [38] studied the effect of sample dilution on measured SPSDs for gas probed from an ethylene flame.The dilution level was increased constantly until dilution independent size distributions could be obtained from the SMPS. The results clearly show that only after reaching a certain number concentration N of particles in the diluted sample(~5x10^5/cm3) coagulation effects in the sampling probes could be eliminated.

For less sooting flames like the one investigated in [39] coagulation becomes less important and the differences caused by the variation of dilution ration decrease as shown in for dilution

ratio of 3000 vs. 330. However, the importance of the high inlet flow rate to the SMPS in reducing diffusion losses becomes evident in this case where particles are significantly small.

Fig.4.27 The SMPS system which were conducted the soot measurements in this study, in the laboratory of Technical University Bergakademie of Freiberg in Germany.

4.4 The dilution system of experiment

As apparent to the above paragraphs, in order to sample from the TPOX reformer a suitable sampling, a dilution system has to be designed so that to measure reliable and accurate soot size distributions. Taking into consideration of the process characteristics and the geometrical restrictions of the examined application, a three-stage dilution method was setup with the aim to achieve a total dilution of $>10^4$. The maximum gas inlet temperature of the described diluter head is 200°C, but the temperature of the sampled syngas reaches more than 800°C. Therefore a pre-dilution stage is necessary. The chemical reactions and gas phase kinetics in the sample have to be quenched fast and very close to the sampling position so as to minimize the particle losses due to coagulation, thermophoresis, condensation, etc. The flowsheet of the realized overall soot measurement equipment with sampling and dilution system is presented in figure 4.28.

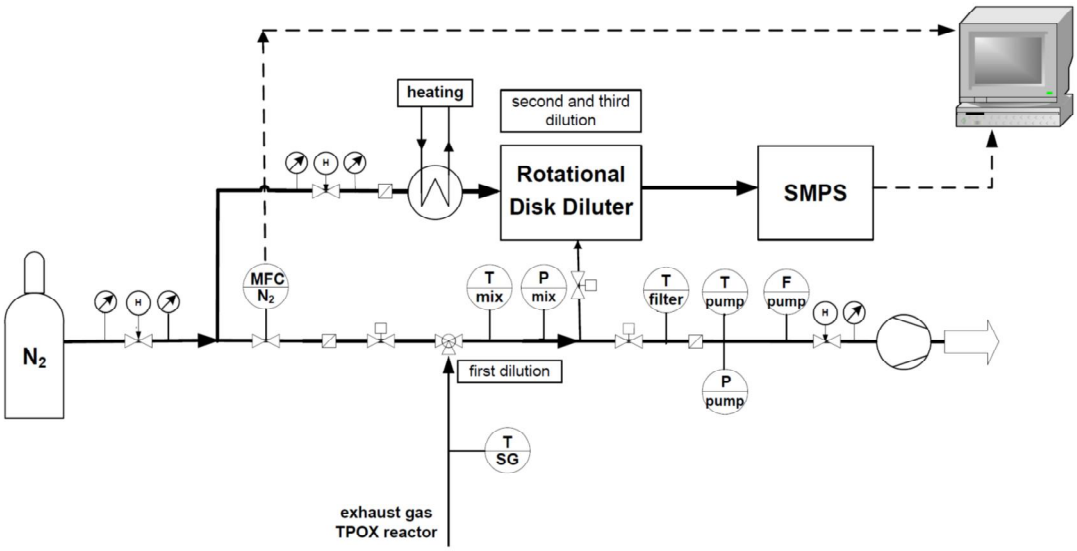

Fig.4.28: Flowsheet of the soot measurement equipment with sampling and dilution system.

4.4.1First Stage of Dilution

The first dilution stage is the most important in terms of quenching the chemical reactions in the syngas. It has to be performed almost instantaneously so as to prevent a slow cooling of the sample gas. In this manner it can be guaranteed that sample gas is not be affected by gaseous phase and aerosol chemistry processes. The TPOX reactor with the first stage dilution system is shown in figure 4.29 schematically.

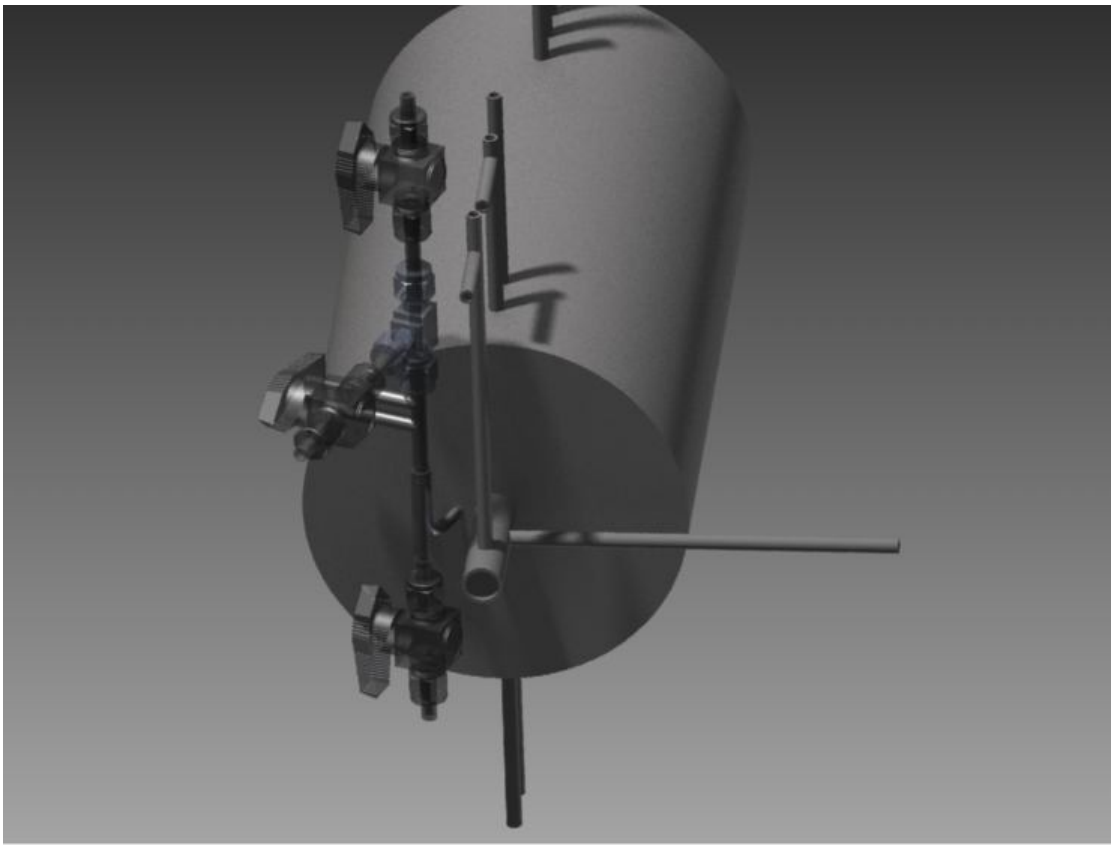

Fig.4.29: 3D model of TPOX reactor with first stage dilution system (CAD Inventor).

A sample of the syngas which produced in the TPOX was taken at the exit of the soottrap. The probe tube was ID 5 mm and OD 2 mm , shown in figure 4.31, was placed angled and its tip reached almost the centre axis of the reactor. The temperature of the syngas at this point was measured with thermocouple Tex_1 and was in the range from 800°C to 900°C. During the residence time of the sample in the reactor no cooling is expected because the temperature in the sampling tube which is inside of the reformer, is equals nearly the reactor temperature.

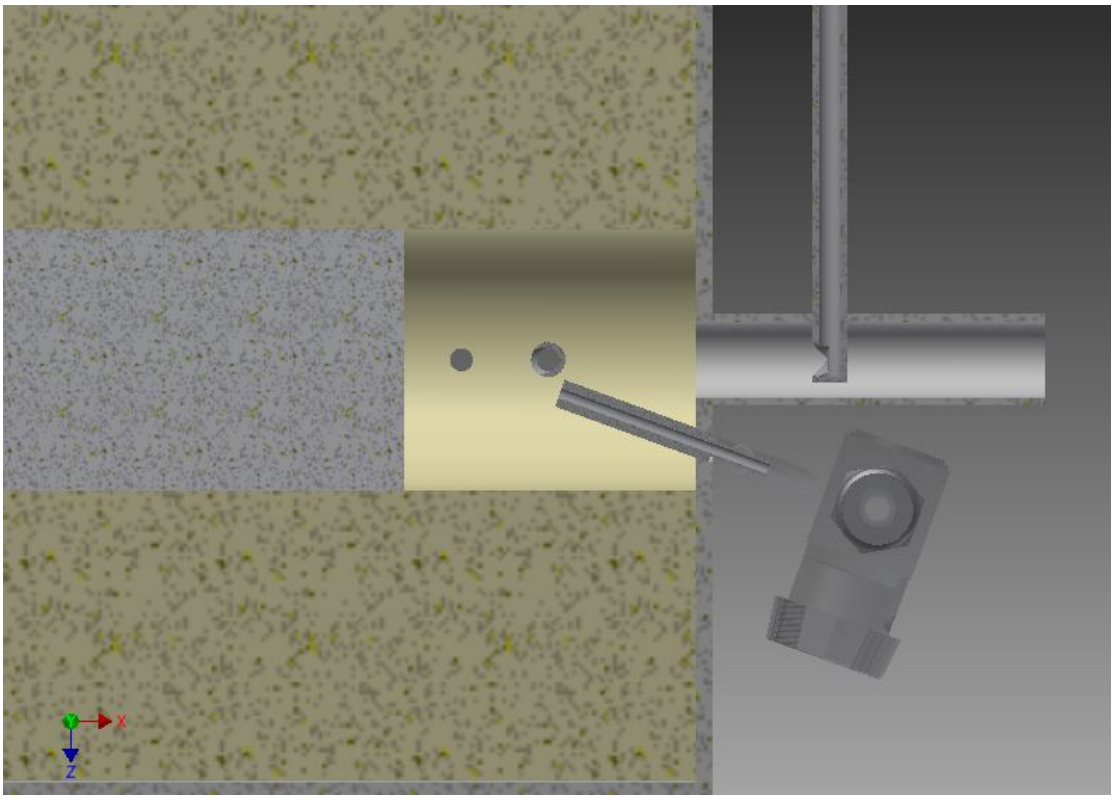

Fig.4.30: Illustration of the angled placed sampling syngas pipe which leads it to the first dilution stage.

When the sample gas exits the reformer it cools down due to the following heat transport mechanisms:

- forced convection because of the hot syngas inside the pipe,
- heat conduction through the wall of the sampling pipe, and
- natural convection because of the ambient air at the outside of the pipe.

There was no valve to stop the out coming syngas flow, because the length of the sampling tube outside the reactor had to be as short as possible to decrease the temperature drop. In order to decrease the thermal losses, the pipe covered with an insulation material having a conductivity of 0.03 W/(m*K).

The pipe was bended 90° and ended in the larger mixing tube, which was placed vertically with an ID of 5 mm and OD of 8 mm. In this manner, an annular gap of 0.5 mm is created (see Figure 4.31).

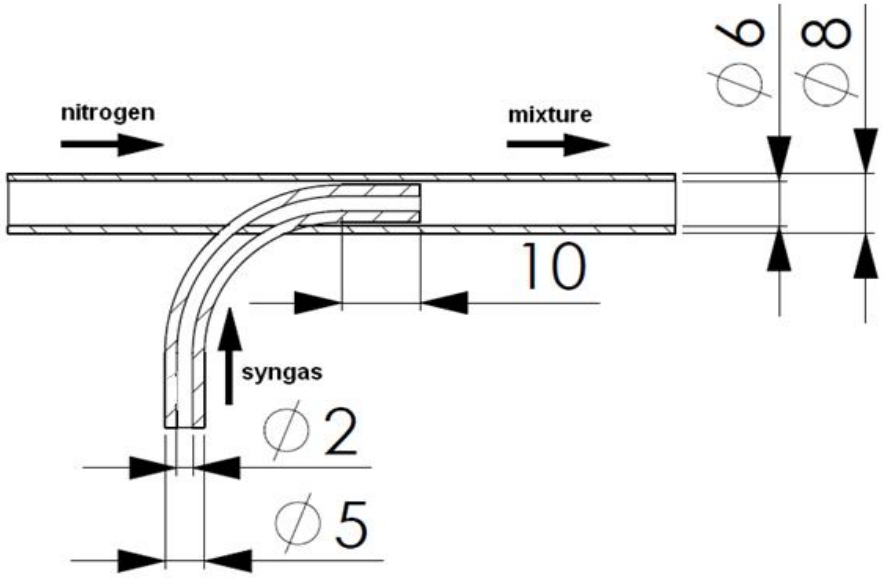

Fig.4.31: Illustration of the arrangement of syngas and nitrogen pipe.

Nitrogen, with a purity of 2.8, was used as diluent for the syngas, because it is an inert gas and should not change the properties of the soot particles. A lot of research groups used air as diluent, but it is expected that the soot particles oxidize with the air oxygen and thus change [37]. Furthermore an explosive and thus dangerous mixture would be formed due to the high amounts of hydrogen and carbon monoxide in the syngas. In the SMPS there is a high electrical power source, which could spark the gas mixture.

In order to prevent a back flow of the syngas when no nitrogen is in the line, a valve was placed before the mixing point. The nitrogen flowed through the gap of the outer mixing tube and the inner sampling tube mixed with the hot syngas at the exit of the small sample tube. The mixing temperature and pressure were continuously monitored with a 1.5 mm K-type thermocouple and a pressure sensor respectively. The mixture flow was created by a membrane pump which was protected by a HEPA filter (maximum operating temperature of 88°C).The mixing temperature measured about 160°C. A mixing temperature about 150°C is desired, because this is the preheating temperature of the diluter head and thus an equilibrium in the temperature of the tubing between mixing point and diluter head inlet results.

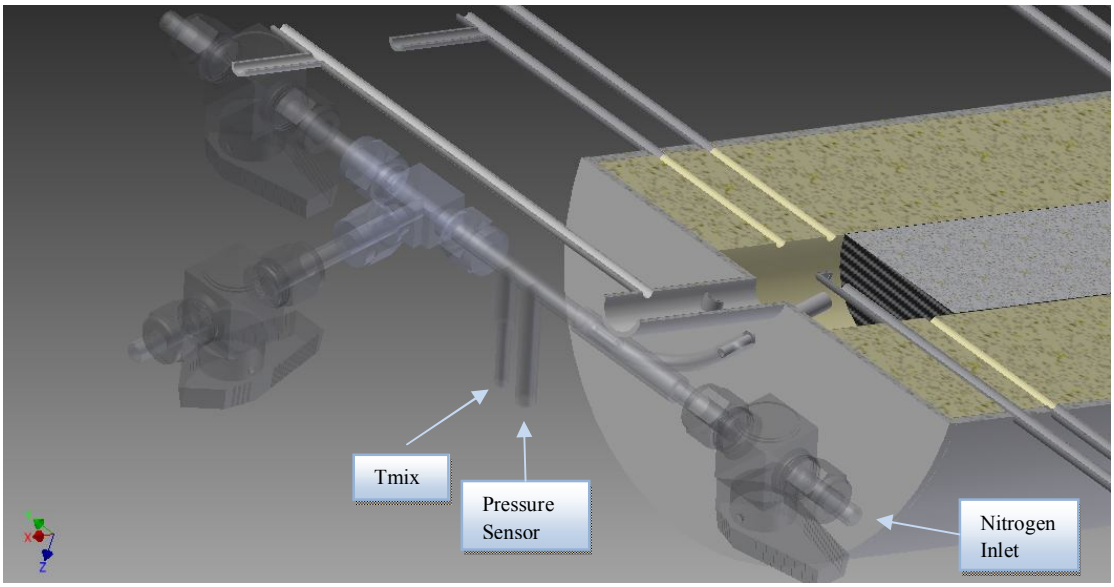

Fig. 4.32:Illustration of valves, of the position of thermocouple for mixing temperature and of the position for pressure sensor of first dilution stage system.

Fig. 4.33:The cutted back side of the second version reformer during reconstruction. It is shown the first dilution system, the postcombustor, the Tmix thermocouple and the position of pressure sensor.

Fig. 4.34: It is shown the tube for syngas sampling in order to be measured for soot.

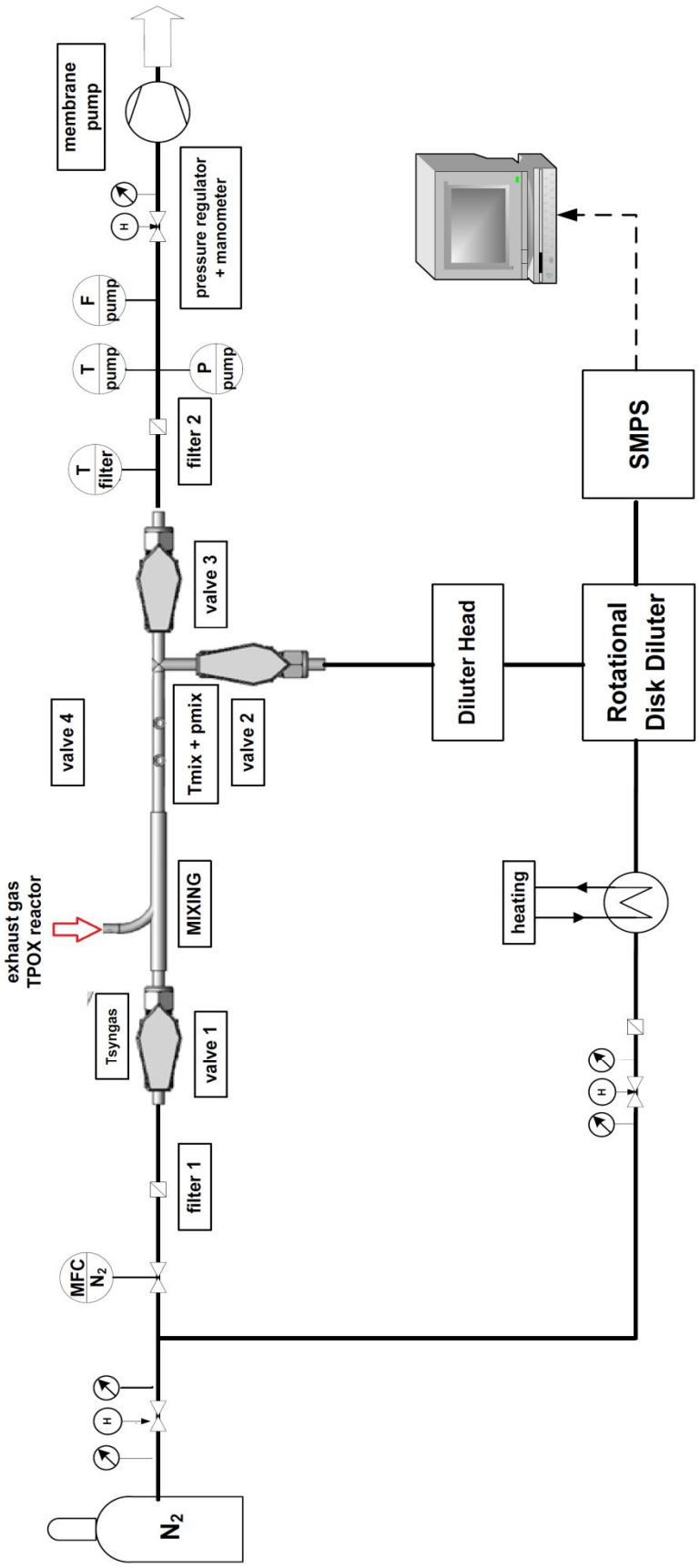

Fig. 4.35: Flowsheet of dilution system with detailed first stage dilution.

The pumped flow depends on the created under pressure of the pump and this can be adjusted with a pressure reducer valve with manometer which is positioned in front of the pump. The temperature and the pressure of the pump flow were measured by a 1.5 mm N-type thermocouple and a pressure sensor, respectively.

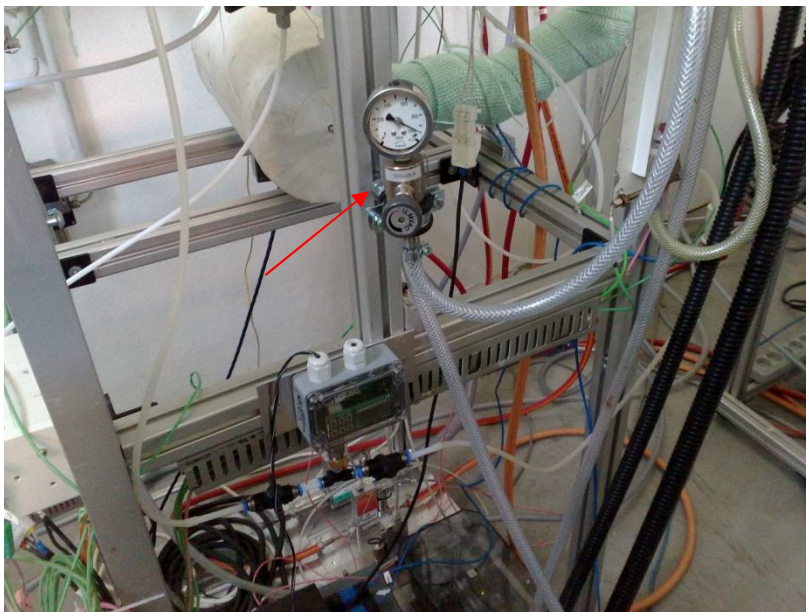

Fig. 4.36: The pressure reducer valve

The nitrogen flow was set by the MFC (Mass Flow Controller) and the pump flow was set higher than this with adjusting the pressure reducer valve. In this way it was possible to regulate the amount of sampled syngas. The pump flow should be always higher than the diluent flow in actual conditions, because otherwise an overpressure is created and the system can be destroyed.

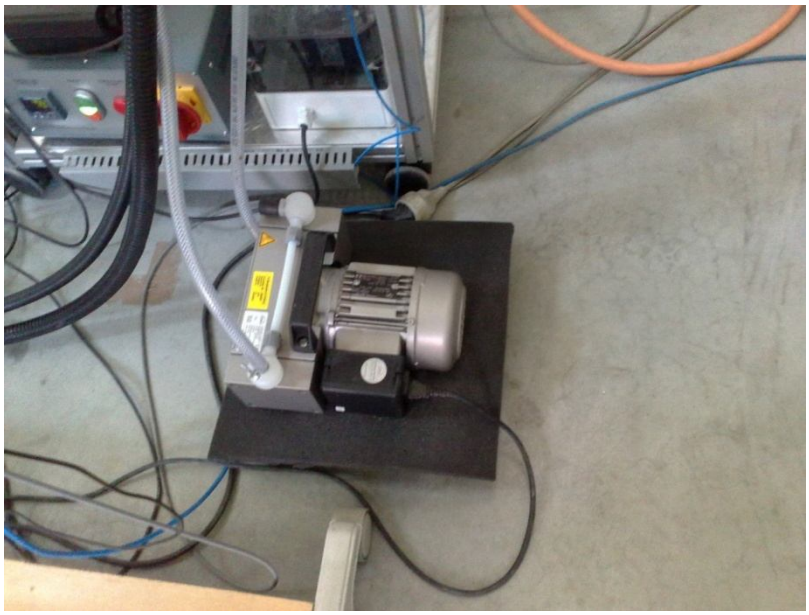

Fig. 4.37:The pump

The measurement of the flow sampled by the pump is a very important factor by defining the dilution ratio. It was measured in front of the pump with a rotameter which has an accuracy of 1.6% of the final value. The measurement range of it is about 0 l/min to 33 l/min.

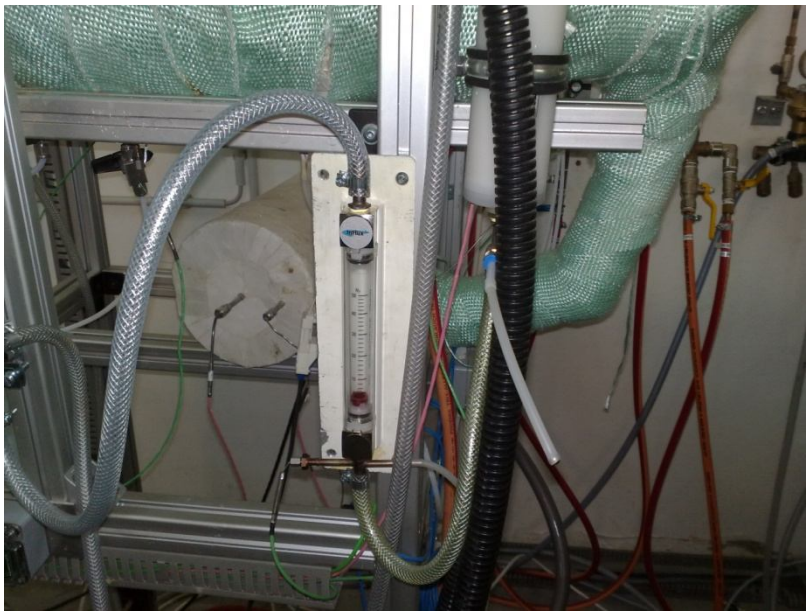

Fig. 4.38: The rotameter

It has to be mentioned that there are flowmeters with higher accuracies, as for example flowmeters operating with a measurement principle on the basis of the mediums heat capacity. However, they are proven to be sensitive by the presence of humidity in the measuring gas and thus their accuracy is decreased. Even though in this setup water condensation is not expected in any stage of the process the utilization of such instruments was avoided.

The syngas produced in the process of TPOX is a wet gas containing not only the gases H_2, CO, CO_2, CH_4, C_2H_2 and N_2, but H_2O as well. The temperature of the syngas is high, so that it never falls under 100°C and the water steam condensates into liquid water. But when it is highly diluted with nitrogen a much lower temperature is reached and the formation of water droplets in the gas mixture is possible. However, the partial pressure of water in the diluted sample is very low for all conditions and consequently the respective saturation temperatures.

The main part of the syngas/nitrogen mixture flowed straight through a plastic tube (ID 10) to the filter and later to rotameter and pump. But a small amount of the mixture was taken by the diluter pump directly after the measurement positions for mixing temperature and mixing pressure. This pump drew between 1.2 Nl/min and 2 Nl/min of gas, which is later analyzed in the SMPS.

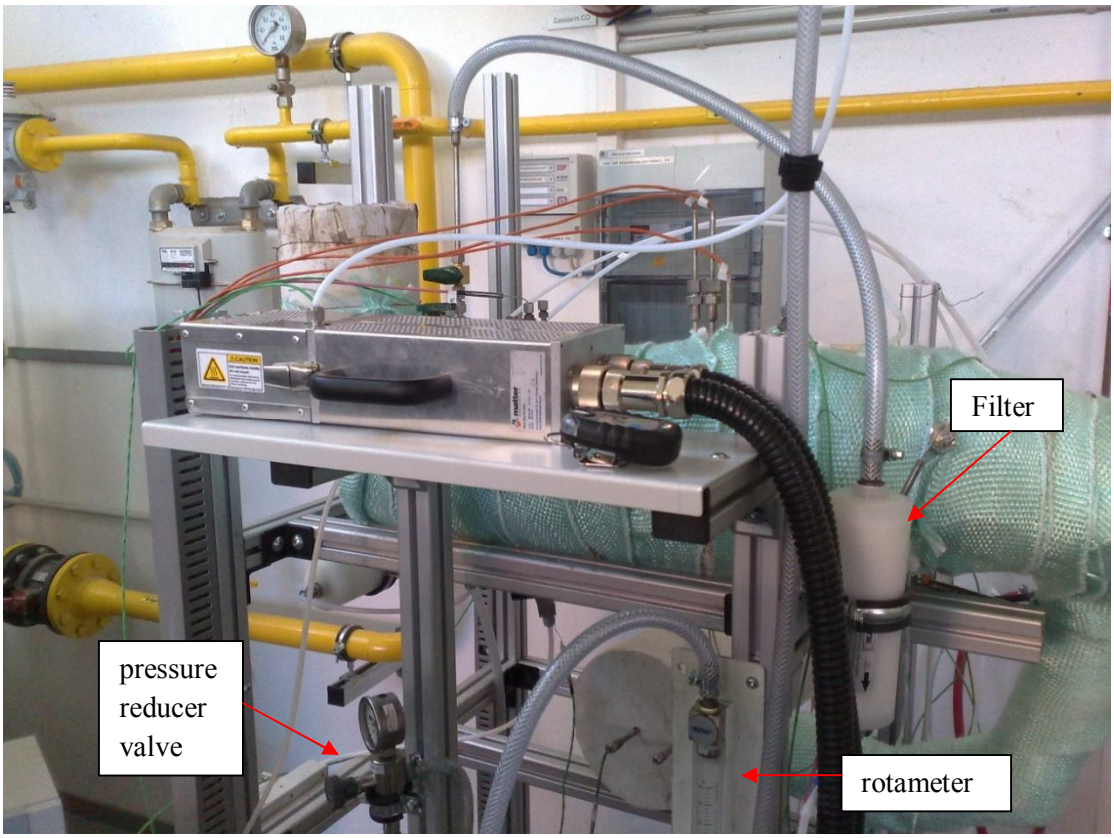

Fig. 4.39:In this picture illustrated some the important components of the system.

The two paths of the gas mixture (to membrane pump and to diluter head) were equipped with valves for safety reasons and to be sure that no syngas flows through the tubes when the nitrogen flow is off. The entire system setup of the first stage dilution is shown in figure 4.38 in reality and in the flowsheet in figure 4.33 schematically.

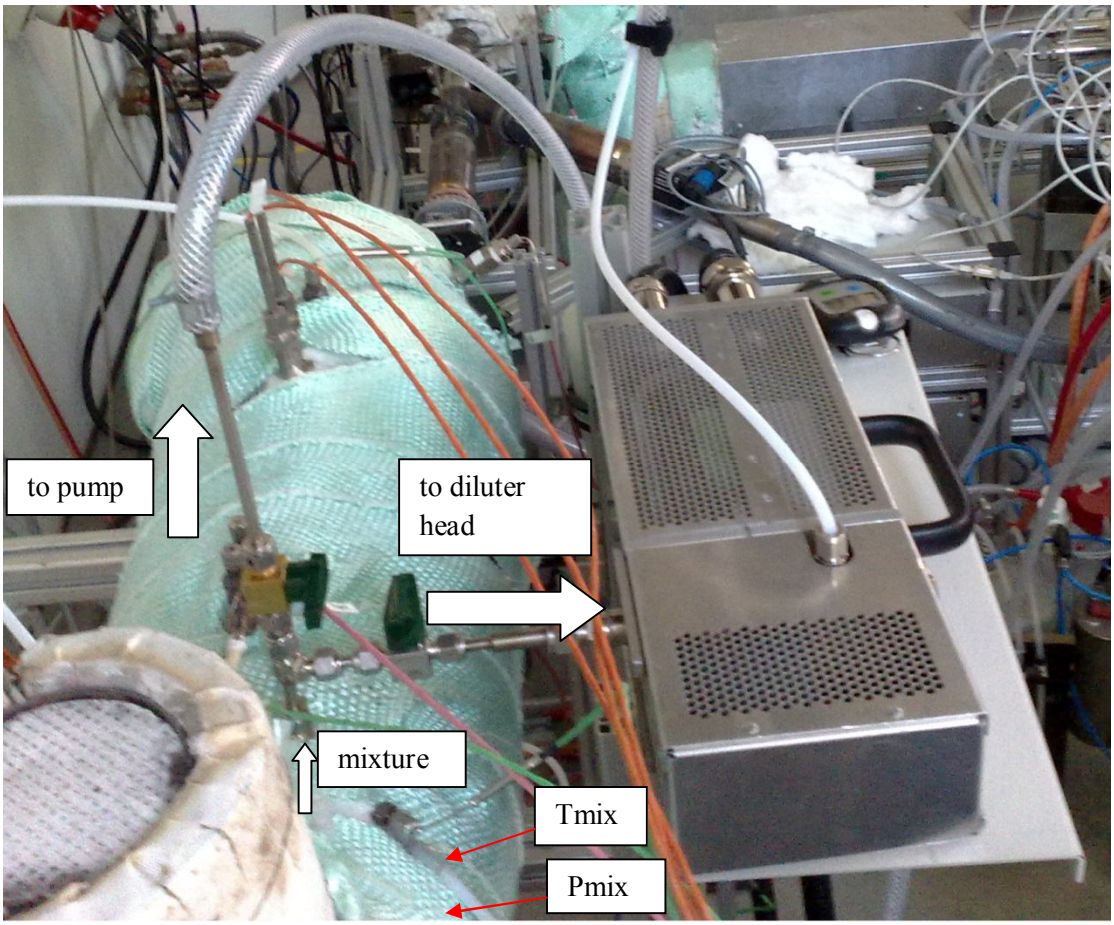

Fig. 4.40:Realised sampling system.

The nitrogen flow was set by the MFC and was usually 21 Nl/min. With the density at 0°C and 1 bar the mass flow $\dot{m}_{N_2}$ can be determined.

The dilution ratio of the mixture defined as the ratio of nitrogen flow at norm conditions $\dot{V}_{N_2}$ to syngas flow at norm conditions $\dot{V}_{SG}$.

$$DR = \frac{\dot{V}_{N_2}}{\dot{V}_{SG}} \qquad \text{Eq.\{4.6\}}$$

The dilution ratio of the experimental procedure was calculated and it was DR=5.5, thus the volumetric flow of syngas $\dot{V}_{SG}$ can be calculated as well as its mass flow.

In addition to the fast dilution and hence cooling of the syngas it is important as well that the path of the soot-laden gas through the conditioning system is as short as possible. The distance between sampling point and measurement device should be small to decrease e.g. diffusion losses and coagulation processes as described in chapter 4.5. Additionally the velocities of the gas in the pipes should be high so that the residence time in the system is low.

In the diluter head the syngas/nitrogen mixture of the first dilution stage was diluted furthermore with a dilution ratio between 15 and 3000 as described in the next chapter.

4.4.2Second Stage of Dilution – Rotating Disk Thermodiluter

Usually instruments which determine nanoparticle number concentrations have specific measuring ranges, wherein measurements are possible or best accuracy of the determined values can be reached. With the rotating disk diluter it is possible to adapt particle number concentrations to the measuring range of the applied particle sensor.

Particles in the nanometer range tend to coagulate which means smaller primary particles meet together and build larger secondary particles. This leads to lower particle numbers and a displacement of the particle size distributions.

In the diluter the particle concentrations are reduced as close to their emission source as possible before being transported to the measuring sensor and the coagulation effects are reduced significantly. [36]

The Model 379020A Rotating Disk Thermodiluter can dilute raw gas by a dilution factor between 15 and 3000. The working principle of the dilution system is illustrated schematically in **Σφάλμα! Το αρχείο προέλευσης της αναφοράς δεν βρέθηκε.**.

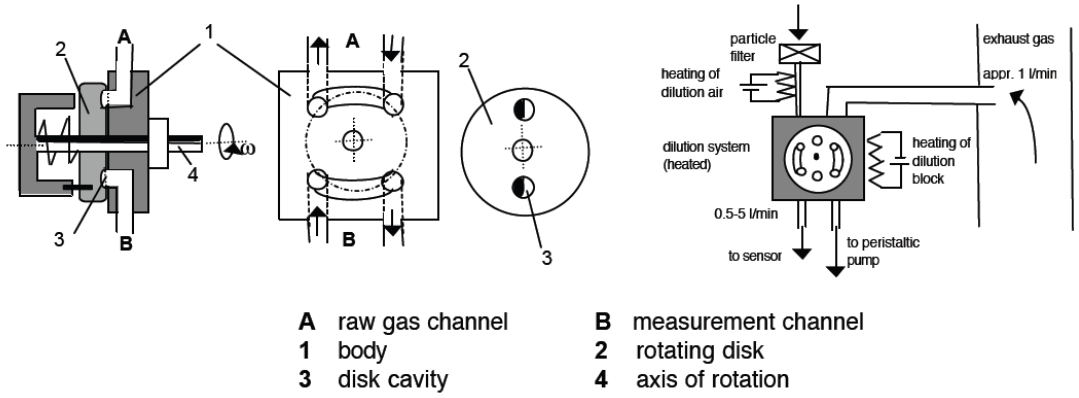

Fig. 4.41:Schematic illustration of the dilution system. [36]

A stainless-steel block (5.0 x 5.0 x 2.5 cm3) contains two channels, one for the undiluted aerosol sample (aerosol channel) and the other for the particle free gas (dilution gas channel). Originally the diluter is made for air as dilution gas, but here nitrogen is used. Both channels have holes at the same outer plane of the steel block. From outside, a disk is pressed onto this outer plane by a spring. The disk and the spring are positioned and rotationally supported by an axle which is passed through the steel block and a step motor is used to rotate the disk with an adjustable frequency.

The disk has a given number of circularly arranged cavities and a single cavity has a volume of 0.04 cm^3 and the shape of a truncated cone. The cavities are facing towards the steel block and are passing over the holes of the two channels when the disk rotates. Those cavities are therefore filled with the aerosol over the one hole; then moved to the other hole, where the aerosol portions are flushed into the dilution gas channel. The dilution process is realized in a single step and on a fast time scale.

The dilution ratio itself is a linear function of number and volume of the cavities as well as of the dilution gas flow and the disk rotation frequency.

The Rotating Disk Thermodiluter is using the principle of hot dilution which means that the sample probe head block and dilution gas are heated up to temperatures of 80°C, 120°C or 150°C. This method keeps evaporated liquids above their dew points, during and after the dilution, and avoids the generation of volatile nanoparticles by nucleation.

Tightness between the aerosol channel and the dilution gas channel and between channels and environment is crucial for this dilution principle. It is necessary that the contact surfaces of the disk and the steel block are sufficiently flat and as smooth as possible. The diluting parts, i.e., heated thermodiluter block and rotating disk are placed in the thermodiluter head which is an external part of the device. It can be fixed as close as possible to the source of the aerosol which should be diluted for subsequent measuring. It is connected to the control unit by one electrical and one pneumatic three meter long connection.

The control unit contains the following components: power supply, temperature and speed controls, signal LEDs and control electronics. The control unit supplies the dilution nitrogen as well, which is filtered and provided to the thermodiluter head, and a membrane pump which uses vacuum to draw the raw aerosol through the thermodiluter block. The rotational speed of the thermodiluter disk depends on the dilution nitrogen flow which is determined in the control unit as well.

The complete system containing thermodiluter head (a), control unit (b) and pneumatic and electrical connections (c) is shown in figure 4.42.

(a) (b) (c)

Fig.4.42: (a) Thermodiluter Head, (b) Control Unit and (c) Pneumatic and Electric Connection. [36]

Depending on fuel and combustion parameters, such as air humidity, temperatures, and residual times, combustion generated aerosols do mostly not only contain CO_2 and solid particles, but also water vapour and other volatile components which may condense out if the temperatures drop to ambient conditions, resulting in liquid particles which may damage or pollute the measuring sensor.
These components are at first evaporated and then diluted in the thermodiluter head. At low concentrations, they remain dissolved in the surrounding gas and do; therefore, not affect solid particle measurements anymore.

The dilution factor of the Rotating Disk Thermodiluter can be calculated with

Dilution factor DF = calibration factor / pot[%]

For the here used eight cavities disk the calibration factor is 14687. The calibration sheets refer to a heating temperature of 80°C selected. If other temperatures are chosen, the formula for the dilution factor has to be compensated by the f[°C] factors mentioned above.

Dilution factor DF = f[°C] · calibration factor / pot[%]

The dilution ratio has a linear relationship to the rotation frequency of the disk and the dilution gas flow F_d. The rotation frequency is:

f_{rot} ~ *adjusted dilution ratio* · F_d.

F_d is given by the gas flow drawn by the connected sensors. To compensate its influence, F_d is measured and electronically multiplied with the set value for the dilution ratio. The dynamic range of the rotation frequency is limited to a nominal frequency of approx. 2.5 Hz when the potentiometer is set to 100 % and the dilution gas flow F_d is 1.5 Nl/min. The Model 379020A Rotating Disk Thermodiluter can be combined with the ASET15 secondary dilution system and a digital control unit. The pneumatic block diagram in figure 4.44 and the picture in figure 4.41 show the ASET15-1 combined with the raw gas rotating disk diluter forming a Thermo- Diluter system.

Fig.4.43: Model 379020A Rotating Disk Thermodiluter and Model 379030 Thermal Conditioner. [36]

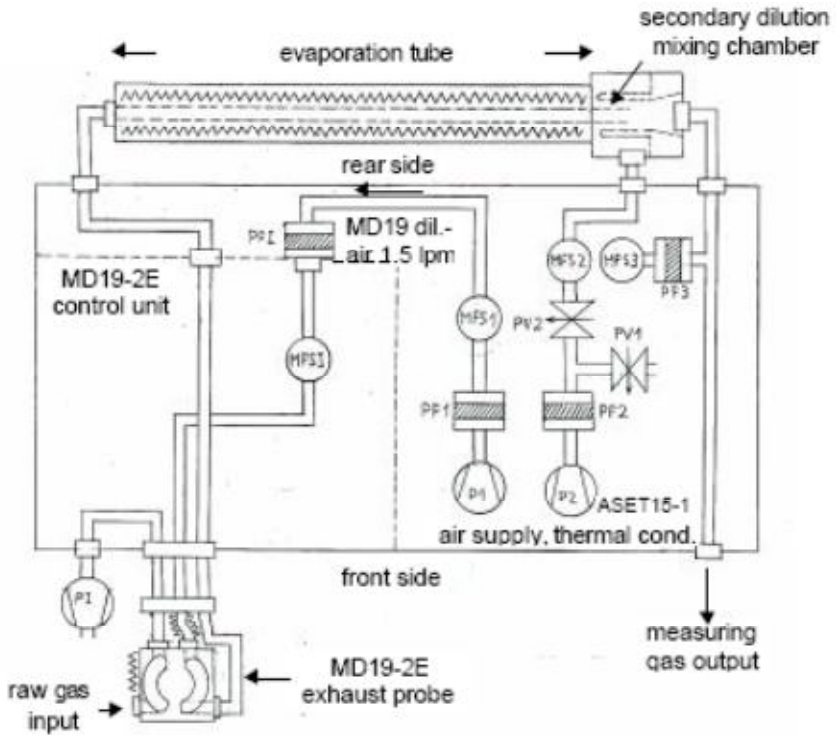

Fig.4.44: Pneumatic block diagram of ASET15-1 and rotating disk diluter in combination. [36]

The measuring gas (1.5 Nl/min) after primary dilution in the rotating disk diluter enters the evaporation tube of the conditioner on the rear side. Volatile particles are evaporated if their evaporation temperature is below the adjusted and electronically controlled heating temperature. Cooling down and secondary dilution takes place in the mixing chamber following the evaporation tube. No recondensing takes place when the concentration of the gaseous components is below the dew point. The construction of the secondary diluting section is optimized for minimal thermophoretical losses by mixing the aerosol with the secondary dilution nitrogen in a laminar flow section where the dilution nitrogen builds a sheath between the cold walls and the aerosol from the conditioner. Secondary dilution nitrogen is generated by a pump and two proportionality valves are used to adjust and control the flow within the range of (0–15) Nl/min corresponding to a secondary dilution factor from 1:1 to 1:11. The calibrated flow can be set on the scaled 10-turn potentiometer on the front panel. If the measuring gas flow drawn by the sensor (in our case the SMPS) connected to the evaporation tube inlet is 1.5 l/min the potentiometer reading corresponds directly to the dilution factor.

The dilution factors of Rotational Disk Thermodiluter and Conditioning Unit have to be multiplied to get the total dilution factor of the whole thermodiluter system. But it has to be mentioned, that the third dilution in the ASET 15-1 is in comparison with the other dilution stages less important.

Very near the sampling point the dilution factor has to be very high to stop unwanted chemical reactions in the soot-laden gas very fast. When the gas enters the long pneumatic pipe which

connects the diluter head with the rest of the Thermodiluter system the gas sample has to be already high diluted to minimize losses in the transport line.

After the last dilution stage in the Conditioner Unit, the path for the measuring gas is only short until the inlet of the SMPS and thus the third dilution factor is always kept at 2, the lowest possible factor for correct operation of the diluter. [36]

4.5 Losses in soot measurements

It is desirable that the sample of a soot-laden gas is representative like in its original environment and not affected by the sampling process. Such characteristics as particle mass and number concentration and size distribution should remain unchanged between the point at which the aerosol is sampled and the instrument performing the measurement: This is representative sampling. It is, however, difficult to prevent changes from occurring during aerosol sampling and transport.

Particles, because of their inertia, do not always enter the sampling inlet representatively. They can be lost from the sample flow by contact with the walls of the sampling system. Inertial, gravitational, and diffusion forces are among the mechanisms that can act to move the particles toward a wall. Many of the mechanisms that inhibit representative sampling depend on the particle size so that a given sampling system may exhibit representative sampling over some range of particle size but not for particles larger or smaller than that range.

Generally speaking, larger particles are strongly influenced by gravitational and inertial forces and more difficult to sample representatively; smaller particles with higher diffusion coefficients are more easily lost to the walls of the sampling system by diffusion. If the sampled particles are charged, they can interact with electric fields near and inside the inlet. Use of conductive inlets, sampling lines, and storage containers can often minimize the effects of electrical charge on particles. Employing a sampling system that samples representatively for the particle size range of interest is of paramount importance. The potential factors that can cause changes in soot particle characteristics during the sampling process or can otherwise contribute to a non representative sample are

1. Aspiration efficiency and deposition in the sampling inlet during sample extraction.
2. Deposition during transport through a sampling line or during storage.
3. Extremes (high or low) or inhomogeneity in the ambient particle concentration.
4. Agglomeration of particles during transport through the sampling line.
5. Evaporation and/or condensation of soot material during transport through the sampling line.
6. Re-entrainment of deposited particles back into the sample flow.
7. High local deposition causing flow restriction or plugging.
8. Inhomogeneous particle concentrations in inlets and transport tubes. [27]

Burtscher [28] investigated the soot formation in diesel combustion processes and summarizes the processes which lead to losses in the sampling system, including inertial impaction, diffusion, thermophoresis, and electrostatic deposition. These losses have to be minimized by an adequate design of the sampling system. Furthermore the sample contains not only particles formed in the combustion process but also secondary particles formed during cooling in the exhaust and sampling lines.

In this chapter some of the loss mechanisms which are important for the used soot measurement system are described.

4.5.1Sampling Losses

A soot-laden gas sample is extracted from its point of origin into an inlet for transport to the measuring instrument. Drawing a representative sample into an inlet is not trivial. The velocity and direction of the gas from which the sample is being drawn, the orientation of the aerosol sampling probe, the size and geometry of the inlet, the velocity of the sample flow, and the particle size are important factors in how representative an extracted sample is. For extracting a sample, a particle must be sufficiently influenced by the sample gas flow to be drawn into the inlet. The particle must also be transported through the inlet without being deposited there. Particle inertia and gravitational settling are impediments to representative sample extraction, and representative sampling is more difficult with increasing aerodynamic particle size. Withdrawal of a sample from its environment into the sampling system requires making a particle enter the sampling inlet and conveying it to the transport portion of the system. The efficiency with which this is accomplished is called the *inlet efficiency*. There are two components to the inlet efficiency: the aspiration and the transmission efficiency. The aspiration efficiency of a given particle size is defined as the concentration of the particles of that size in the gas entering the inlet divided by their concentration in the environment from which the sample is taken. The transmission efficiency of a given particle size is defined as the fraction of aspirated particles of that size that are transmitted through the inlet to the rest of the sampling system. There are different types of sampling and are described in detail in [27].

4.5.2Diffusion Losses

When particles collide with a surface they adhere due to van der Waals force, electrostatic force and surface tension. Diffusion is the primary transport mechanism for particles smaller than 100 nm. The smaller the particle the more rapid is the diffusion. Thus, if an aerosol particle diffuses to the wall of its measurement flow path, there are diffusion losses, and the measured size distribution under represent small particles. Since the SMPS spectrometer measures particles in the size range of 3 nm – 1000 nm, diffusion losses are unavoidable. They are however, quantifiable. Diffusion losses are frequently characterized in terms of penetration. It is equal to the ratio of the concentration of particles exiting to that entering a tube, $P = \frac{N_{out}}{N_{in}}$ and the fraction of particles lost to the walls is *1-P*. [29]. More mathematical expression could be found in [30]

4.5.3Thermophoretic Losses

Thermophoresis is the phenomenon in which particles are driven toward colder regions in a gas environment with a temperature gradient. The local particle drift velocity can be expressed in terms of a thermophoretic diffusivity, local gas temperature, and temperature gradient grad.[31]

4.5.4Coagulation

As Hepp et al. mentioned in their work [32] coagulation is the most important loss mechanism and it shifts the particle size distributions towards larger particles. Coagulation is an aerosol growth process that results from the collision of aerosol particles with each other.

When the particle concentration is high, coagulation is always fast but the change from coalescence-controlled to collision-controlled growth is primarily a result of a change in coalescence. [22] In the coalescent growth regime particles are usually assumed to be spherical. They collide and coalesce completely, forming new spherical particles.

If the collisions are the result of Brownian motion, the process is called *thermal coagulation;* if they are the result of motion caused by external forces, the process is termed *kinematic coagulation.* Thermal coagulation is in some ways analogous to growth by condensation except that other particles diffuse to a particle's surface rather than molecules that cause the growth. It differs from condensation in the fact that a supersaturation is not required, and it is a one-way process of growth with no equivalent process corresponding to evaporation. The result of many collisions between particles is an increase in particle size and a decrease in aerosol number concentration. In the absence of any loss or removal mechanisms there is no change in mass concentration as a result of coagulation.

The easiest coagulation mechanism is simple monodisperse coagulation. The assumption is made that the particles are monodisperse, they stick if they contact one another, and they grow slowly. The latter two are valid assumptions for most aerosol particles and situations. Aerosol particles exhibit Brownian motion and diffuse like gas molecules, but their diffusion occurs at a much slower pace; consequently, the diffusion coefficients for aerosol particles can be a

million times smaller than those for gas molecules.
The derivation developed by *Smoluchowski* in 1917 is based on the diffusion of other particles to the surface of each particle. It has been established that the *Smoluchowski* master equations have asymptotic solutions resulting in self-preserving distributions of particle sizes. Coagulation is a rapid process at high number concentration and a slow one at low concentrations.

4.5.5Polydisperse Coagulation

The previous description of coagulation is accurate enough for a wide variety of situations, but it requires the assumption of a monodisperse aerosol. In the real case usually the aerosol is polydisperse, and the situation is more complicated. Because the coagulation process is governed by the rate of diffusion of particles to the surface of each particle, the process is enhanced when small particles with their high diffusion coefficients diffuse to a large particle with its large surface.For polydisperse aerosols requires the use of numerical methods because the coagulation for every combination of particle sizes has a different value of K and has to be calculated separately.

For the case of coagulation of an aerosol with a lognormal size distribution having a count median diameter (CMD) and a geometric standard deviation σ_g, an equation derived by Lee and Chen (1984) can be used to calculate the average coagulation coefficient K.

Maricq [33] used a DMA to investigate the size and charge of soot particles in rich premixed ethylene flames. He considered what happens to the size and charge distributions at long times, after new particle nucleation stops.

Some researchers (e.g. [33] and [34]) showed that an aerosol of spherical particles undergoing coalescent collisions according to the *Smoluchowski* equation for coagulation evolved to an asymptotic or selfpreserving size distribution, in comparison to the lognormal distribution.

Another process leading to measurement artifacts is reentrainment of material previously deposited in the exhaust gas system. This material may be reentrained as larger agglomerates and can lead to irreproducible results, because this process occurs intermittently and erratically. Due to adhesive *Van der Waals* forces the probability of reentrainment of particles in the accumulation mode is very small. Usually reeintrained particles are significantly larger. While the effect of non-isokinetic sampling is small for particles in the size range of main interest (below some 100 nm), it may be significant for reentrained agglomerates.
To eliminate artifacts by reentrainment an impactor or cyclone can be applied to remove large particles before the measurement. During phases of high exhaust temperature following periods of operation at lower temperature, reentrainment may also occur by volatilization of material deposited during the low-temperature phase.
The main problem when measuring the number concentration is that it is subject to changes due to coagulation. Further on, diffusion losses are more important for a measurement of the particle number than of particle mass, because it weights the smaller particles more strongly. Short residence times and sufficient dilution are required to obtain reliable results. In addition, a careful treatment of volatile material is required to avoid that undesired nucleation particles dominate the number concentration.
The third potential problem is the lower size limit of the CPC, which lies usually in the range of 3 nm to 15 nm, depending on the used model and system settings. If a substantial number of

particles with sizes around the detection limit are present, measurements become unreliable. Solid particles of this size may exist even if nucleation is prevented. Differences in the reading of two CPC's with slightly different cutoff diameters could in principle be used as an indicator for the presence of such particles. Unfortunately, the lower detection limits of CPC's are known to depend on age and maintenance status of these devices. An extension of this technique can be used to measure size distributions of particles in the nucleation mode as well. [28]

4.5.6 Corrections for Losses

In the SMPS software AIM there is the possibility to use three different types of corrections for losses: the multiple charge correction, the diffusion correction and the option of analysing the nanoparticle aggregate mobility.

Multiple Charge Correction Option

The Multiple Charge Correction enables a mathematical correction for particles with multiple charges. Multiple charges on a particle increase its mobility. Since the AIM assumes a particle has only one charge, the effect of multiple charges on a particle allows the particle to be incorrectly binned into a smaller-sized particle channel. Multiple Charge Correction, if activated, turns on an internal algorithm that attempts to correct the sample data for the effects of the multiple charged particles. The algorithm performs corrections based on a 64-channel resolution. The program assumes the impactor removes any particles larger than its cut-point size. Therefore, the particles in the size channel smaller than the impactor cut-point size must be made up of single-charged particles, because particles with multiple charges are larger in size than the D_{50} cut point. The concentration in each size bin is calculated. Once the concentration for a bin is determined, the program subtracts the number of multiple-charged particles that it would have been expected to fall in smaller-sized bins. The SMPS program then moves to progressively smaller size channels and continues to subtract the effect of multiple-charged particles. The effects of multiple-charged particles are most pronounced for particles above approximately 100 nm. The efficiency of multiple charge correction is dependent on several factors and assumptions. Ideally, the D_{50} for the impactor should be precisely at the upper valid measurement range. The impactor removes particles based on their aerodynamic size. The program sizes particles based on their electrical mobility, which closely matches particles' geometric diameter.

Diffusion Correction Option

The Diffusion Correction enables a mathematical correction for diffusion losses of particles in their flow path within the SMPS system. It is especially important to use diffusion loss correction when sizing aerosols smaller than 100 nm, since in this size regime diffusion becomes increasingly important.

Nanoparticle Aggregate Mobility Analysis Option

Nanoparticle Aggregate Mobility Analysis enables a mathematical analysis of mobility data for nanoparticle aggregates. By default, the software analyses the mobility raw data for a spherical particle model. However, not all particles are necessarily spherical. For example, urban ultrafine particles and particle emissions from combustion sources such as diesel engines are typically aggregates. The nanoparticle mobility analysis yields a more accurate estimate of the number, surface area and volume distributions of nanoparticle aggregates. The primary particle diameter, i.e., diameter of the primary particles that constitutes the aggregate has to be entered. The assumption is that aggregates are composed of primary particles all of which have the same (known) diameter. Furthermore the orientation of aggregate (parallel or random with respect to the electric field) has to be given for the correction. The nanoparticle aggregate mobility analysis option is not used in the here realized experiments, because aggregates in the syngas are not expected. Anyway, later the soot particles have to be analyzed with a Transmission Electron Microscope to be sure about this fact. [35]

4.6 Experimental procedure and tested cases

The procedure was applied for conducting the experimental investigations is presented to the following paragraphs.

During start-up, the air stream was electrically preheated so as to reach temperature levels which, after the introduction and mixing with methane, would yield the desired mixture temperatures of the reactants (400^{o}C for all the tests). After the initial warm-up phase the reformer was ignited at a relatively high air equivalence ratio (λ=0.7) inside of the conical section. The flame propagated and stabilized within the conical section, operating conditions in terms of thermal loads and equivalence ratios were set to the tests points for each run, keeping stable the preheating temperature of the unburned mixture. During transition from one test point to another, the reformer would run until completely stationary operation could be assured before any measurement was taken for evaluation.

The operating behaviour of the reformer was scanned varying the equivalence ratio from λ=0.4 up to λ=0.5 and the fuel flow in the range of equivalent thermal power from 1 kW to 4 kW.

For all tested points temperature profiles within the reformer and exhaust gas compositions were recorded, while for selected conditions soot particle size distributions were measured as well. For the soot measurements the power was at 1.5 kW and the variation of equivalence ratio started from λ=0.5, decreased consecutively to λ=0.46 and λ=0.42 for which evident soot formation was expected and after increased consecutively to λ=0.5 and λ=0.6. Gas samples were scanned by the SMPS in intervals of 90s. Following 10 samples were taken with a scanning time of 100 s and were averaged for getting the final distributions.

In order to measure the species concentration of H_2, CO, CO_2, CH_4 and C_2H_2 in the syngas the sampled gas was cooled very fast down to 180°C and transported to the gas analysis modules by a preheated at 180°C transfer line. All the water content of the sample gas had to be condensated before the entrance to the gas analyzer modules and therefore only the dry

composition could be finally measured. The amount of water in the syngas was calculated from the other species and the mass balance of oxygen. Its calculation is shown in the 4.7.2 section.

Concerning the soot size distributions the temperature of the rotational disk diluter was set to 150°C. The nitrogen as dilution gas was set to 21 Nl/min supplied by a mass flow controller. The utilized membrane pump was adjusted in order to draw the nitrogen as well as a sample of the syngas from the TPOX reactor and therefore the mixture flow was created. As soon as the temperature of the sampled syngas and of the nitrogen/syngas mixture reached stable values, sample scans with the SMPS could be initiated.

The tested cases. Thermal load/Air equivalence ratio/Flows/Temperatures

Table 4.3. *Tested cases of first version experiment of reformer*

cases	N [kW]	λ	mch4 [kg/s]	mair [kg/s]	mmix [kg/s]	Qair [lt/min]	Q ch4[lt/min]	Tmix [°C]
1	2	0,5	3,996E-05	0,000343	0,00038296	15,927	3,359	403
2	2	0,45	3,996E-05	0,000309	0,00034866	14,334	3,359	401
3	2	0,4	3,996E-05	0,000274	0,00031436	12,742	3,359	400
4	1,5	0,45	2,997E-05	0,000232	0,00026149	10,751	2,519	392
5	1,5	0,5	2,997E-05	0,000257	0,00028722	11,945	2,519	392
6	1,5	0,52	2,997E-05	0,000268	0,00029751	12,423	2,519	393
7	1,5	0,4	2,997E-05	0,000206	0,00023577	9,556	2,519	410,42
8	1,5	0,42	2,997E-05	0,000216	0,00024606	10,034	2,519	398,5

Table 4.4. *Tasted cases of second version experiment of reformer*

cases	N [kW]	λ	mch4 [kg/s]	mair [kg/s]	mmix [kg/s]	Qair [lt/min]	Q ch4[lt/min]	Tmix [°C]
1	1	0,6	1,998E-05	0,000206	0,00022578	9,556	1,679	425,6
2	1,5	0,5	2,997E-05	0,000257	0,00028722	11,945	2,519	418
3	1,5	0,52	2,997E-05	0,000268	0,00029751	12,423	2,519	385,7
4	1,5	0,5	2,997E-05	0,000257	0,00028722	11,945	2,519	407,8
5	1,5	0,46	2,997E-05	0,000237	0,00026664	10,990	2,519	416,7
6	1,5	0,42	2,997E-05	0,000216	0,00024606	10,034	2,519	141,3
7	1,5	0,42	2,997E-05	0,000216	0,00024606	10,034	2,519	407,3
8	1,5	0,42	2,997E-05	0,000216	0,00024606	10,034	2,519	393,3
9	1,5	0,42	2,997E-05	0,000216	0,00024606	10,034	2,519	390
10	1,5	0,42	2,997E-05	0,000216	0,00024606	10,034	2,519	423,4
11	1,5	0,4	2,997E-05	0,000206	0,00023577	9,556	2,519	393,3
12	1,5	0,5	2,997E-05	0,000257	0,00028722	11,945	2,519	413
13	1,5	0,5	2,997E-05	0,000257	0,00028722	11,945	2,519	425,1
14	1,5	0,6	2,997E-05	0,000309	0,00033867	14,334	2,519	390
15	1,5	0,6	2,997E-05	0,000309	0,00033867	14,334	2,519	422

Mass flow rates $\dot{m}\left[\frac{kg}{s}\right]$, volumetric flow rates of methane and air in flow controllers $\dot{Q}_{mix,f.c}\left[\frac{lt}{min}\right]$ and the average density of mixture $\rho_{mix,f.c.}\left[\frac{kg}{m^3}\right]$, calculated based on thermal power N[kW] , equivalence air ratio λ and also considering that the volumetric flow rate in

flow controllers results for temperature $T_{f.c} = 273{,}15\ K$. The calculation of the above quantities for each case was carried out in accordance of the following equations:

$$\dot{m}_{CH4} = \frac{N}{Hu} \qquad \text{Eq.\{4.7\}}$$

where, $Hu = 50050\ \left[\frac{kJ}{kg}\right]$ the lower heating value of methane and N is the thermal power [kW].

The air equivalence ratio defined as:

$$\lambda = \frac{\left(\frac{\dot{m}_{air}}{\dot{m}_{CH4}}\right)}{\left(\frac{\dot{m}_{air}}{\dot{m}_{CH4}}\right)_{st}} \rightarrow \quad \dot{m}_{air} = \lambda \cdot \left(\frac{\dot{m}_{air}}{\dot{m}_{CH4}}\right)_{st} \cdot \dot{m}_{CH4} \qquad \text{Eq.\{4.8 \}}$$

Where the stoichiometric air-methane ratio is:

$$\left(\frac{\dot{m}_{air}}{\dot{m}_{CH4}}\right)_{st} = 17.167 \qquad \text{Eq.\{4.9\}}$$

The reference conditions at the flow controllers are:

$$P = 101325\ Pa$$

$$T_{f.c} = 273{,}15\ K$$

The densities can be calculated from ideal gas equation and the units are [Pa] for pressure P, [g/mole] for molar weight Mw, [J/kg K] for gas constant and [K] for the temperature.

$$\rho_{air,f.c.} = \frac{P\ MW_{air}}{R\ T_{f.c}} \cdot 10^{-3}\ \left[\frac{kg}{m^3}\right] \qquad \text{Eq.\{4.10\}}$$

$$\dot{Q}_{air,f.c} = \frac{\dot{m}_{air}}{\rho_{air,f.c.}}\ \left[\frac{m^3}{s}\right] \qquad \text{Eq.\{4.11\}}$$

$$\rho_{CH4,f.c.} = \frac{P\ MW_{CH4}}{R\ T_{f.c}} \cdot 10^{-3}\ \left[\frac{kg}{m^3}\right] \qquad \text{Eq.\{4.12\}}$$

$$\dot{Q}_{CH4,f.c} = \frac{\dot{m}_{CH4}}{\rho_{air,f.c.}}\ \left[\frac{m^3}{s}\right] \qquad \text{Eq.\{4.13\}}$$

4.7 Experimental results

4.7.1 Investigation of the operating range

The operational regime of the soottrap based reformer was investigated mainly in its first version. The tested cases was not enough for a complete map of operational regime. Nevertheless the figure 4.45 shows the tested cases and their operational regimes and also the areas of the map where the each operational regime would be expected.Data have been plotted in dependence of the equivalence ratios and thermal power in the ranges of 0.4-0.6 and 1-4 kW respectively. The limit where the border of extinction would was appearing was not specified. The lowest conditions which applied in terms of thermal load (1kW) were shown stable operation. Stable operation is the operational regime where the flame stabilization is in the conical section. For 4kW which means high velocities and for 0.4 air equivalence ratio the stable operation but within of soottrap observed, where the flame front moved down-stream at the middle of soottrap. Furthermore, for the presented tests of operational conditions flash-back of the flame was not observed.

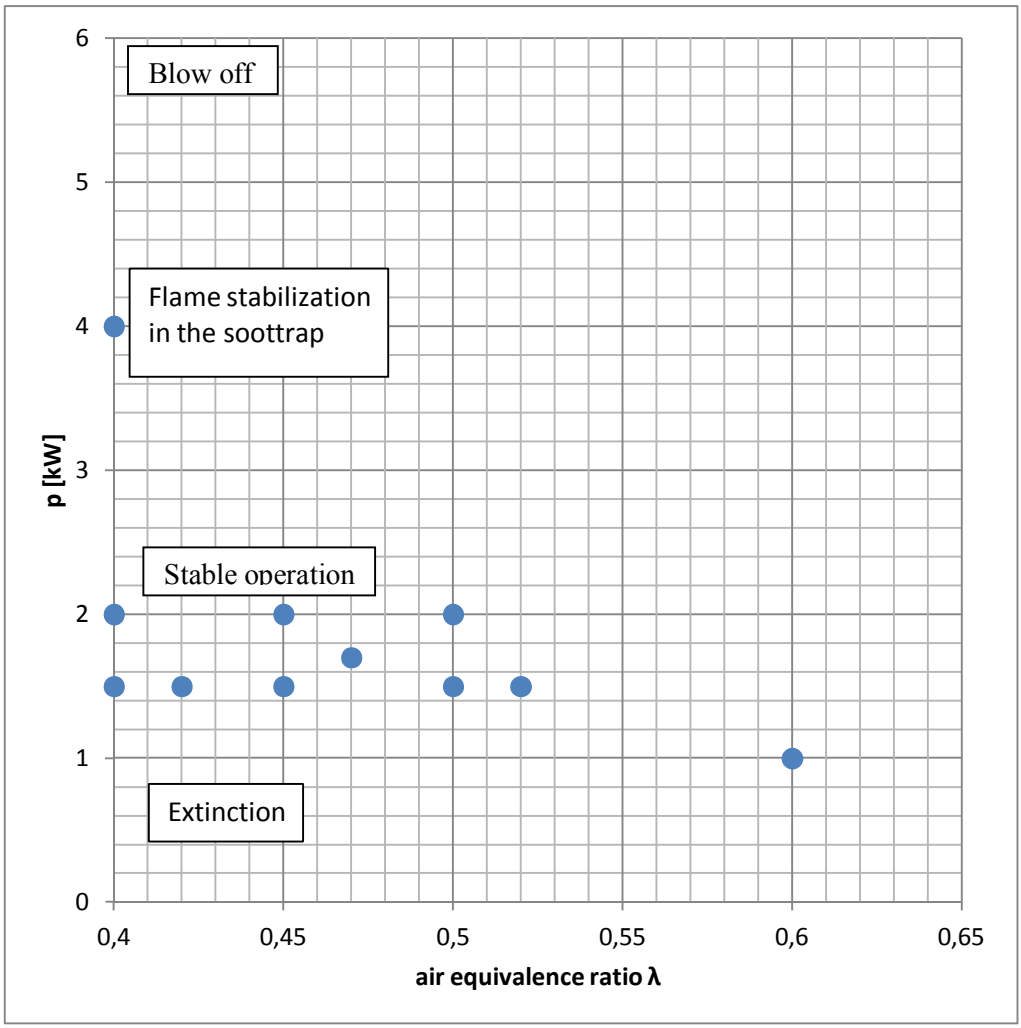

Fig.4.45. Operating regimes of the soottrap based reformer for reactants preheated at 400°C.

4.7.2 Temperature profiles and major species

The temperature profiles were recorded for all tested cases. The positions of thermocouples with the more interest were three at the conical section where the reaction zone was expected, two thermocouples within of soottrap and one immediately at its exit. The figure 4.46 below shows the positions. Furthermore, the figure below shows the two sampling tube of gas (G.A.1 and G.A.2). Both of them are existing only at the second version of reformer while in the first version only G.A.1 existed. The G.A.2 was additional at the second version in order to compare measurements of species with the G.A.1 measurements.

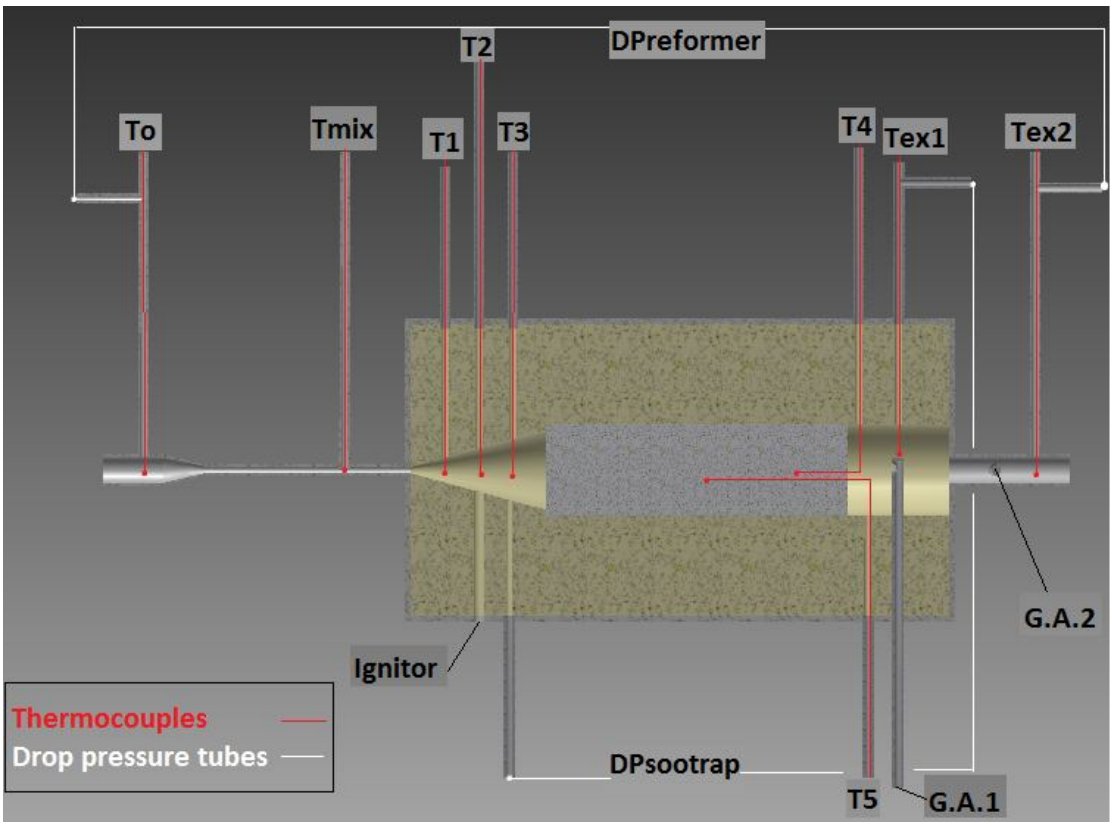

Fig.4.46. Positions of sensors for measurement of temperature, pressure drops and gas sampling.

Temperatures profiles for both experiment versions of reformer

Firs experiment version of soottrap based reformer

From the experimental investigation at the first version of soottrap, recorded the temperatures for thermal loads 1.5kW, 1.7kW, 2kW and 4kW for different air equivalence ratios. The temperature profiles are presented below.

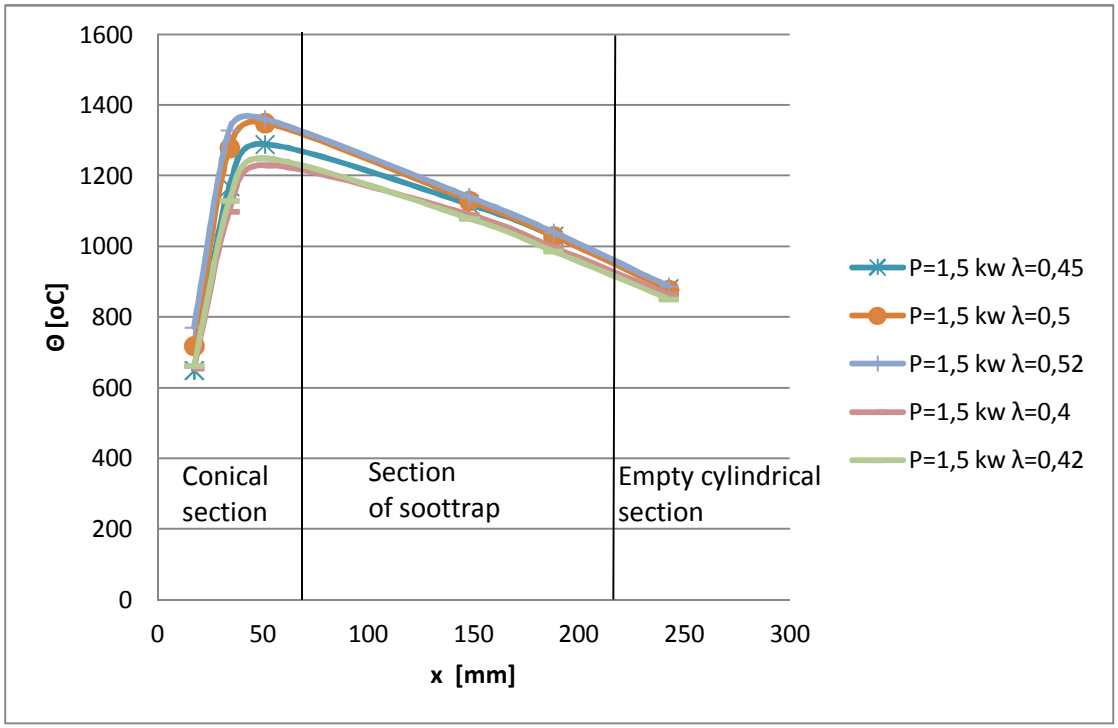

Fig.4.47. Temperature profiles were measured for different equivalence ratios within the reaction region of the soottrap based reformer, for reactants preheated at 400°C and thermal load of 1.5 kW.

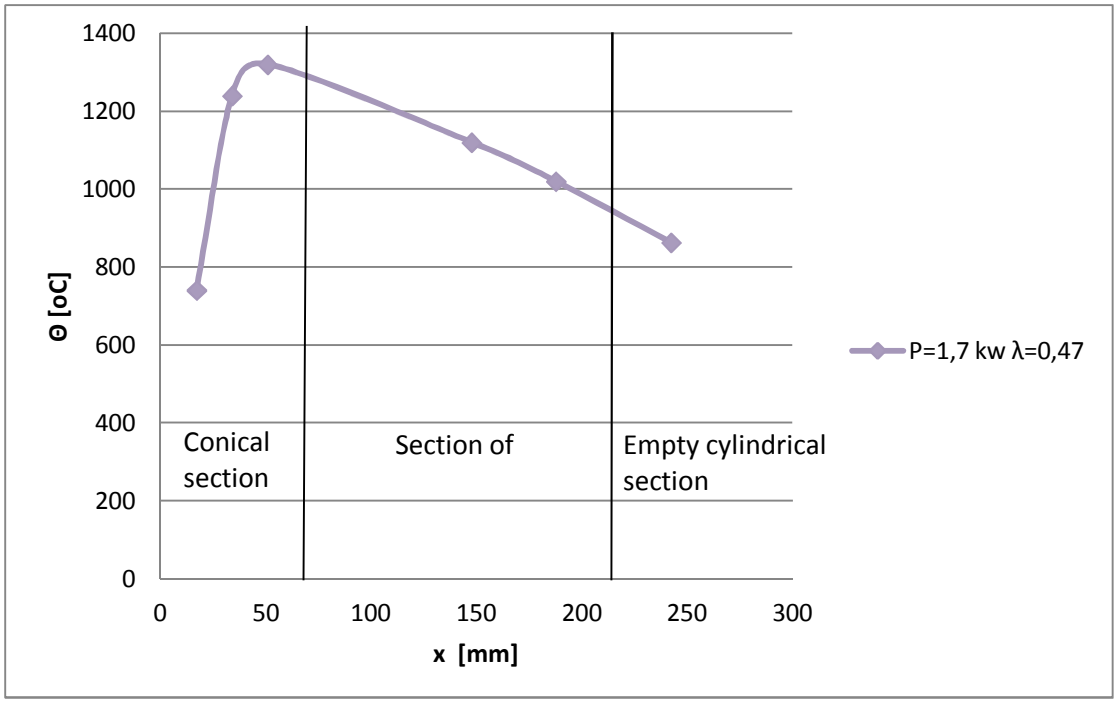

Fig.4.48. Temperature profiles were measured within the reaction region of the soottrap based reformer, for reactants preheated at 400°C, thermal load of 1.5 kW and air equivalence ratio of 0.47.

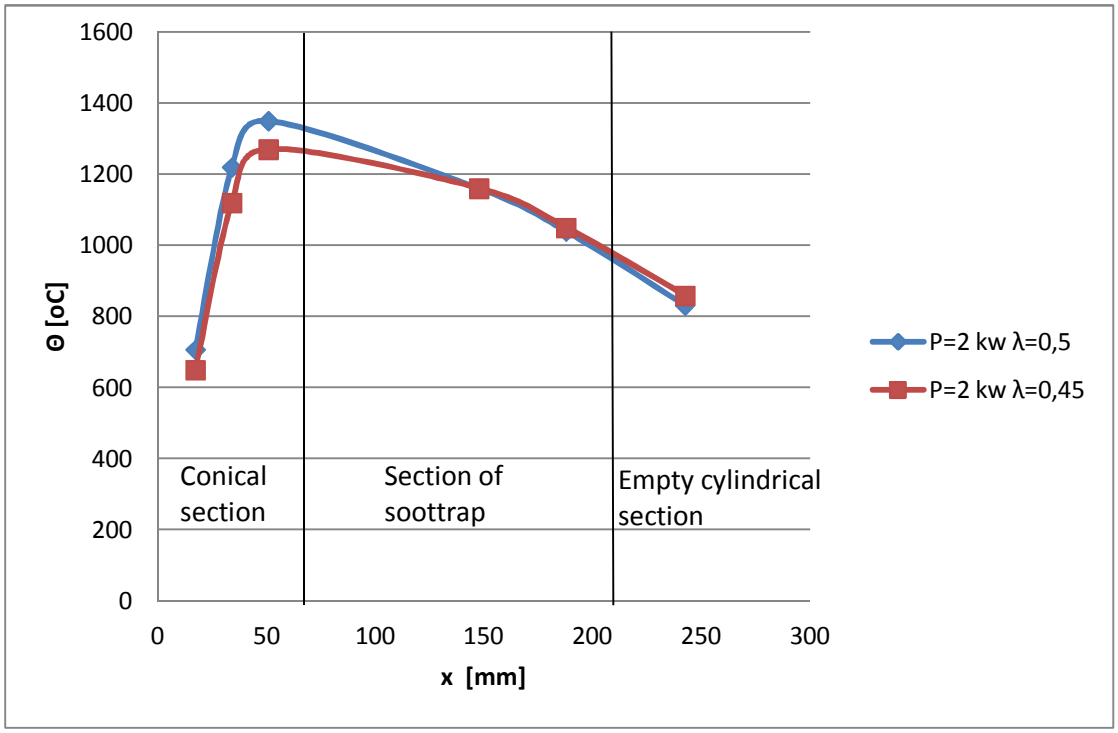

Fig.4.49. Temperature profiles were measured for different equivalence ratios within the reaction region of the soottrap based reformer, for reactants preheated at 400°C and thermal load of 2kW.

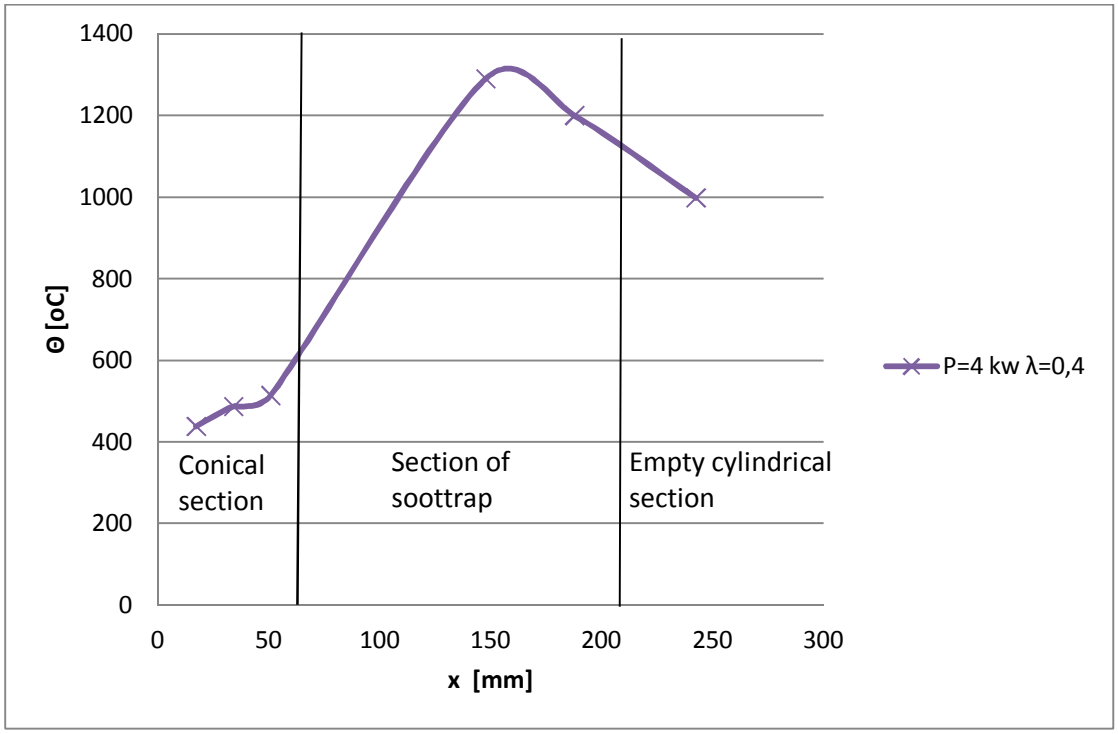

Fig.4.50. Temperature profiles were measured within the reaction region of the soottrap based reformer, for reactants preheated at 400°C, thermal load of 4 kW and air equivalence ratio of 0.4.

Second experiment version of soottrap based reformer

From the experimental investigation at the second version of soottrap recorded the temperatures for thermal load of 1.5kW. The temperature profiles are presented below.

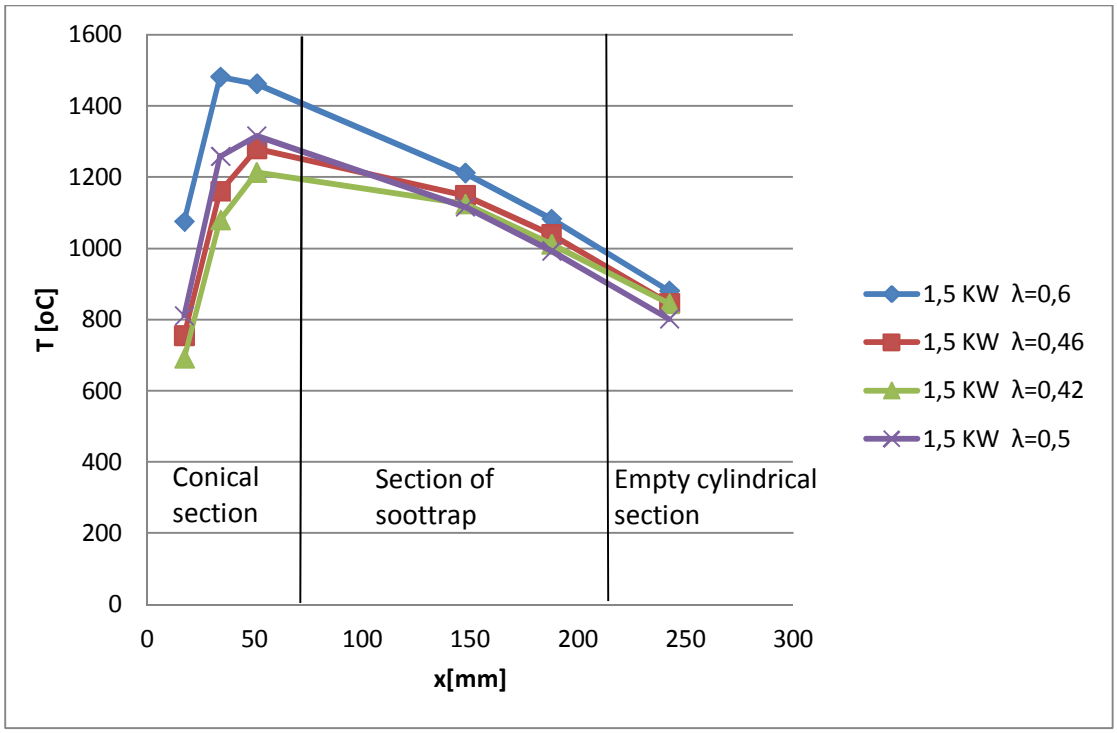

Fig.4.51. Temperature profiles were measured for different equivalence ratios within the reaction region of the soottrap based reformer, for reactants preheated at 400°C and thermal load of 1.5 kW.

The temperature levels in both versions show the expected behaviour, increasing by increasing the air equivalence ratio and the maximum temperature in each profile is an indication for the position where the reaction front stabilizes. The profiles show, how the variation in the cross-sectional area affects the process of flame stabilization within the reformer. The flame is self-adjustable to a new position according to the imposed operating conditions. This is shown at figure 4.51 where the maximum temperature for 1.5 kW, λ=0.6 appears downstream in comparison with the cases of lower λ. The downstream self-adjustment in this case was expected since for higher air equivalence ratios the velocity is increased and a downstream movement would be expected for the same thermal load. Furthermore the self adjustment was not possible in this size of conical section for higher thermal loads and as is shown in figure 4.50 the front of flame moved upstream inside of the soottrap.

Major species of both versions

The time evolution of reactions within a premixed rich-flame can be divided into two distinct zones; the flame front region where fast oxidation reactions take place and the post-flame region, which is dominated by slow endothermic reforming reactions [1].Such reactions increase the concentrations of H_2 and CO and decrease the respective ones of CH_4 and H_2O, towards equilibrium conditions. For the range of equivalence ratios like the ones applied for this study, extremely long times are required to reach equilibrium compositions and practically this cannot be achieved for reformers with a reasonable length in terms of practical applicability. However, it is important to enable residence times within which equilibrium concentrations can be approached to the most possible extent.

Measurements of major species for first version experiment of soottrap based reformer

The volume fractions of species in the dry syngas for the test cases are presented at the follow tables:

Table 4.5

Case 1,5 kW	Volume fractions				
λ	H_2 %	CO %	CO_2 %	CH_4 %	C_2H_2 %
0,4	18,18	13,24	2,58	5,18	0,026
0,42	18,65	13,22	2,7	4,17	0,051
0,45	19,895	13,855	3,255	1,105	0,009
0,5	19,96	13,84	3,22	1,31	0,014
0,52	19,83	13,87	3,29	0,9	0,004

Table 4.6

Case 2 kW	Volume fractions				
λ	H_2 %	CO %	CO_2 %	CH_4 %	C_2H_2 %
0,4	16,08	13,7	2,65	6,66	0,003
0,45	18,61	13,47	2,82	3,58	0,006
0,5	18,28	13,4	3,31	2,24	0

Table 4.7

Case 1,7 kW	Volume fractions				
λ	H_2 %	CO %	CO_2 %	CH_4 %	C_2H_2 %
0,47	20,16	13,42	3,02	2,31	0,04

Table 4.8

Case 4 kW	Volume fractions				
λ	H_2 %	CO %	CO_2 %	CH_4 %	C_2H_2 %
0,4	20,51	13,71	2,65	5,49	0,074

In the following figures are presented the volume fractions of species for the cases of 1,5 kW and 2kW. As a first look is shown that the soottrap based reformer can yield about 20% H_2 and 14% CO in the produced syngas for the case of 1,5 kW and it yields a little bit less syngas for the case of 2 kW. Furthermore CH_4 and C_2H_2 are increased as the air equivalence ratio decreasing. However, it can be observed that for very low air equivalence ratios the volume fraction of C_2H_2 is reduced and this could be attributed in that the C_2H_2 is characterized as the main precursor of soot and when the soot point was approached, C_2H_2 fed the creation of soot which was leaded to its consumption and to its low measured volumetric fraction.

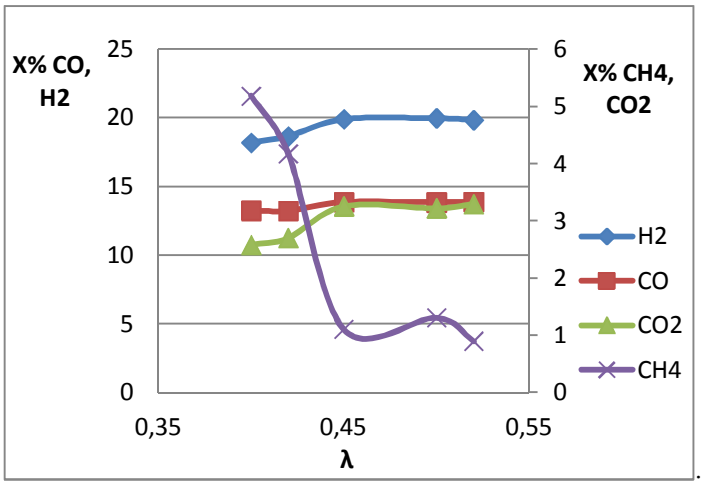

Fig.4.52 Exhaust gas composition in major species and methane for the soottrap based reformer, for reactants preheated at 400°C, thermal load of 1,5 kW and different air equivalence ratios. (Sampling byG.A.1)

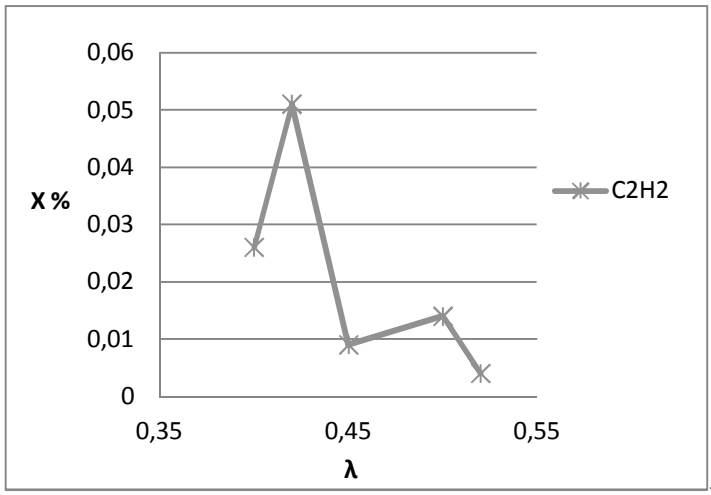

Fig.4.53 Exhaust gas composition of acetylene for the soottrap based reformer, for reactants preheated at 400°C, thermal load of 1,5 kW and different air equivalence ratios. (Sampling by G.A.1)

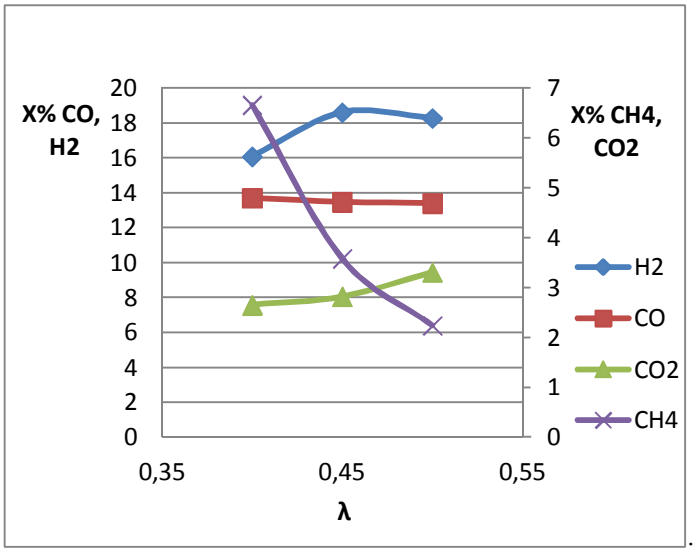

Fig.4.54 Exhaust gas composition in major species and methane for the soottrap based reformer, for reactants preheated at 400°C, thermal load of 2 kW and different air equivalence ratios.(Sampling by G.A.1)

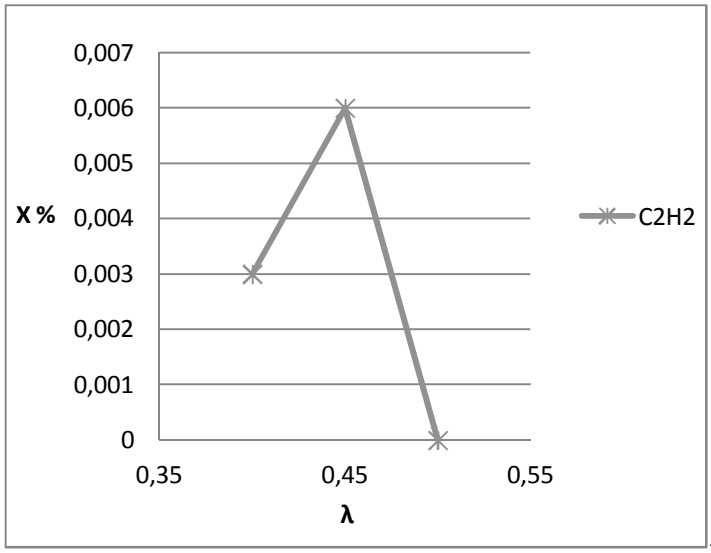

Fig.4.55 Exhaust gas composition in acetylene for the soottrap based reformer, for reactants preheated at 400°C, thermal load of 2 kW and different air equivalence ratios. (Sampling by G.A.1)

Measurements of major species for second version experiment of soottrap based reformer

In the table 4.9 is presented the species volume and mass fractions of some cases which were selected from table 4.4 for plotting. The mass fractions was calculated by the equation:

$$Y_i = X_i \cdot \frac{MW_i}{\overline{MW}} \quad for \quad i: every\ chemical\ species \qquad \text{Eq.}\{4.14\}$$

$$\overline{MW} = \sum_{i=1}^{N} x_i \cdot Mw_i \qquad \text{Eq.}\{4.15\}$$

. As it can been seen by the table 4.9 and figures 4.56 or 4.58 the H_2 yield initially was increased by decreasing of λ (0,50 to 0,46) as was expected but thereafter the hydrogen yield was decreased for λ=0,42 and 0,4 while was increased again for λ=0,6. This behaviour could be attributed in the loading and regeneration of carbon in the sootrap. In the section 4.3.7 and from the figure 4.6 will be proved that for the air ratios of 0,42 and 0,4 the soot trap channels was loaded by soot. This leads the syngas yield to be reduced and to increased again, after the increasing of air ratio to 0,6 where the Boudouard reactions (section 2.3) were activated and the regeneration of carbon increased the H_2 and CO volume fractions.

$$C + CO_2 \rightarrow 2CO \quad (\Delta H = 131\ kj/mol)$$

$$C + H_2O \rightarrow CO + H_2 \quad (\Delta H = 172\ kj/mol)$$

Boudouard reactions (by section 2.3)

In the table 4.10 it can be observed that the volume fraction of water is reduced from 9,88% to7,57% which indicates for sure the activation of the second Boudouard reaction.

Regarding the volume fraction of C_2H_2 it can be observed the same behaviour as the first verson experiment, and will be discussed more in 3.7.2 section.

Table 4.9

		Composition of dry syngas					
		Volume fractions					
cases	λ	XH2 %	Xco %	Xco2 %	Xch4 %	Xc2h2 %	XN2 %
4	0,50	19,61	13,37	3,19	1,65	0,0430	62,14
3	0,52	18,22	13,04	3,41	1,47	0,0450	63,82
5	0,46	19,15	13,18	2,97	2,78	0,0470	61,87
10	0,42	14,82	11,80	2,92	6,25	0,0560	64,15
11	0,4	15,86	11,97	3,56	3,58	0,039	64,991
14	0,60	18,15	14,10	3,66	0,44	0,0010	63,65
		Mass fractions					
cases	λ	YH2 %	Yco %	Yco2 %	Ych4 %	Yc2h2 %	YN2 %
4	0,50	1,67	15,91	5,97	1,12	0,05	73,95
3	0,52	1,54	15,45	6,35	1,00	0,06	75,61
5	0,46	1,65	15,93	5,64	1,92	0,06	74,80
10	0,42	1,25	13,92	5,41	4,21	0,07	75,68
11	0,40	1,32	13,96	6,52	2,39	0,05	75,77
14	0,60	1,52	16,58	6,76	0,30	0,00	74,84

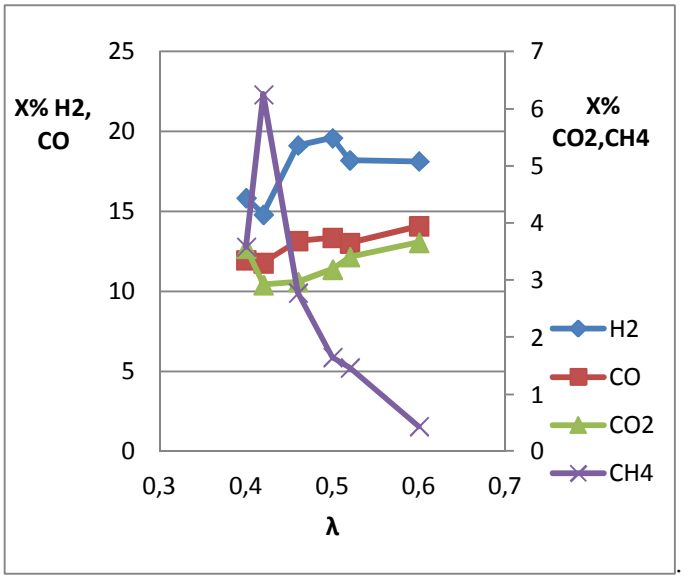

Fig.4.56 Exhaust gas composition in major species and methane for the soottrap based reformer, for reactants preheated at 400°C, thermal load of 1,5 kW and different air equivalence ratios. (Sampling by G.A.2)

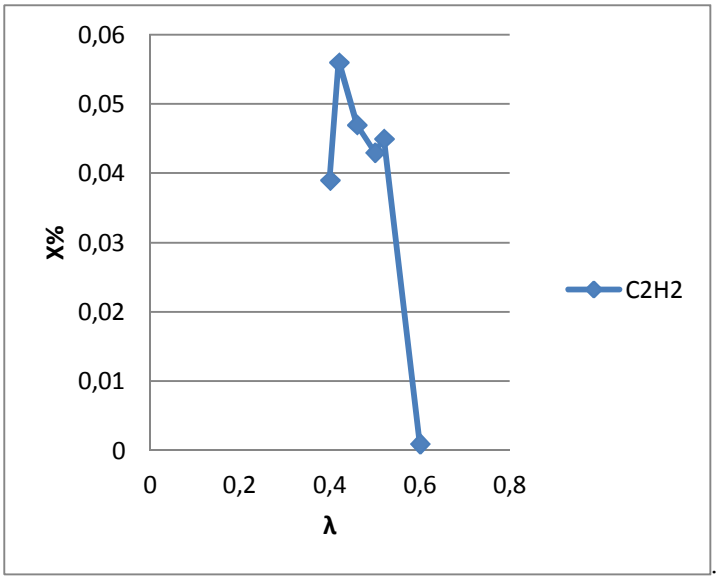

Fig.4.57 Exhaust gas composition in acetylene for the soottrap based reformer, for reactants preheated at 400°C, thermal load of 1,5 kW and different air equivalence ratios. (Sampling by G.A.2)

Calculation of wet syngas

The amount of water in the produced gas was estimated using the oxygen balance as it is shown below and then the measured concentrations were rescaled on the basis of the calculated mole flow of wet syngas for each case of equivalence ratio table 4.4.

Calculation of water from balance of oxygen

The general chemical reaction is:

$$n_{CH_4}\boldsymbol{CH_4} + n_{O_2}\boldsymbol{O_2} + n_{N_2}\boldsymbol{N_2} \rightarrow$$

$$n_{CO_2}\,\boldsymbol{CO_2} + n_{CO}\,\boldsymbol{CO} + n_{H_2}\,\boldsymbol{H_2} + n_{N_2}\,\boldsymbol{N_2} + n_{H_2O}\,\boldsymbol{H_2O} + n_{CH_4}\,\boldsymbol{CH_4} + n_{C_2H_2}\,\boldsymbol{C_2H_2} \qquad \textit{React.\{4.1\}}$$

After calculations the follow equation was resulted for the water volume fraction:

$$\boldsymbol{X'_{H_2O}} = \frac{a}{a+1} \qquad where \qquad a = 2\cdot\frac{n_{O_2}}{n_{N_2}}\cdot X_{N_2} - 2\cdot X_{CO_2} - 2\cdot X_{CO} \qquad \text{Eq.\{4.16\}}$$

$\frac{n_{O_2}}{n_{N_2}} = \frac{\dot{Q}_{O2} \cdot \rho_{O2} \cdot Mw_{N2}}{\dot{Q}_{N2} \cdot \rho_{N2} \cdot Mw_{O2}}$ where $\dot{Q}$ the volumetric flow, ρ the density and MW the molar weight

Xi: volume fraction for species of dry syngas

X'i: volume fractions for species of wet syngas

i: represents every chemical species

Therefore, applied the value of water volume fraction to the following equation, the wet syngas was calculated:

$$X'_i = X_i \cdot \left(1 - X'_{H_2O}\right) \qquad \text{Eq.\{4.17\}}$$

Table 4.10

	Calculated composition of wet syngas							
		Volume fractions						
cases	λ	X'H_2 %	X'co %	X'co_2 %	X'ch_4 %	X'c_2h_2 %	X'N_2 %	X'H_20 %
4	0,5	17,91	12,21	2,91	1,51	0,0393	56,76	8,65
3	0,52	16,59	11,87	3,10	1,34	0,0410	58,11	8,95
5	0,46	17,46	12,02	2,71	2,54	0,0429	56,42	8,81
10	0,42	13,29	10,59	2,62	5,61	0,0502	57,55	10,29
11	0,4	14,29	10,79	3,21	3,23	0,04	58,57	9,88
14	0,6	16,78	13,03	3,38	0,41	0,0009	58,83	7,57
		Mass fractions						
cases	λ	Y'H_2 %	Y'co %	Y'co_2 %	Y'ch_4 %	Y'c_2h_2 %	Y'N_2 %	Y'H_20 %
4	0,5	1,57	15,02	5,63	1,06	0,0518	69,82	6,84
3	0,52	1,43	14,37	5,91	0,93	0,0531	70,34	6,96
5	0,46	1,54	14,82	5,25	1,79	0,0566	69,57	6,98
10	0,42	1,14	12,74	4,95	3,86	0,0648	69,28	7,96
11	0,4	1,22	12,90	6,03	2,20	0,05	70,02	7,59
14	0,6	1,44	15,61	6,37	0,28	0,0012	70,48	5,83

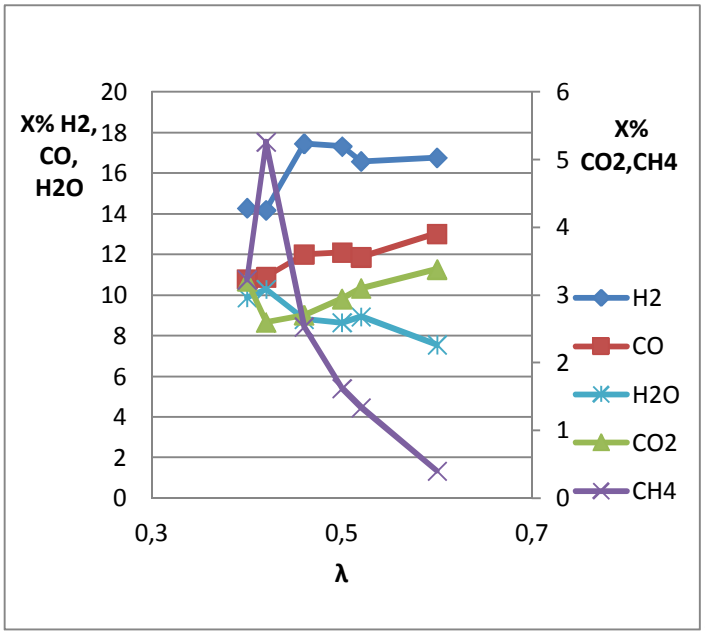

Fig.4.58 Calculated composition of wet syngas for the soottrap based reformer, for reactants preheated at 400°C, thermal load of 1,5 kW and different air equivalence ratios. (Sampling by G.A.2)

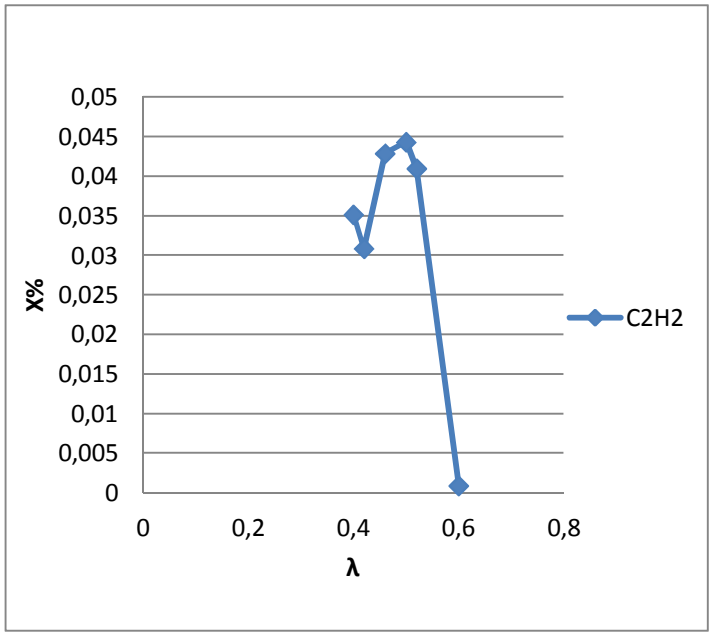

Fig.4.59 Calculated composition of acetylene in the wet syngas for the soottrap based reformer, for reactants preheated at 400°C, thermal load of 1,5 kW and different air equivalence ratios. (Sampling by G.A.2)

Verification of mass conservation between reactants and products

In order to check the mass conservation, the balance of H and C had to be calculated. Based on the general reaction 4.1 the mass of H and C at the products, which originates by CH4 partial oxidation, was calculated. In additional, the mass of O which exist at the measured species was calculated at products based on the same reaction. The third constituent of reactants N_2, since it is inert, its mass calculated in the reactants. The sum of mass products which is originated by methane $m_{CH4,pr}$, by oxygen $m_{o2,pr}$ and the mass of nitrogen m_{N2}, was compared with the sum mass of reactants $m_{CH4} + m_{o2} + m_{N2}$.

Balance of H-C

$$m_{CH4,pr} = AW_C(n_{co2} + n_{co} + n_{CH4} + 2n_{C2H2}) + AW_H(2n_{H2} + 2n_{H2O} + 4n_{CH4} + 2n_{C2H2}) \quad \text{Eq.\{4.18\}}$$

dividing with the products mix mole volume n'_{mix} which is calculated by nitrogen conservation $n'_{mix} = \frac{n_{N_2}}{X_{N_2} - (1 - X'_{H_2O})}$, we get the following equation:

$$\boldsymbol{m_{CH_4,pr}} = \frac{n_{N_2}}{X_{N_2} - (1 - X'_{H_2O})} \cdot \left[AW_C \cdot (X'_{CO_2} + X'_{CO} + X'_{CH_4} + 2 \cdot X'_{C_2H_2}) + AW_H \cdot (2 \cdot X'_{H_2} + 2 \cdot X'_{H_2O} + 4 \cdot X'_{CH_4} + 2 \cdot X'_{C_2H_2})\right] \quad \text{Eq.\{4.19\}}$$

balance of O

The equation of $\boldsymbol{m_{O_2,pr}}$ is resulted by the same way:

$$\boldsymbol{m_{O_2,pr}}=\frac{n_{N_2}}{X_{N_2}-\left(1-X'_{H_2O}\right)}\cdot AW_o\cdot\left(2\cdot X'_{CO_2}+X'_{CO}+X'_{H_2O}\right) \qquad \text{Eq.\{4.20\}}$$

Mass of N_2

It is calculated in the reactants for each case.

Thereafter, the percentage mass deviation between reactants and measured products was calculated by equation 4.21:

$$Dm_{\%}=\frac{\left(m_{CH_4}+m_{O_2}+m_{N2}\right)-\left(m_{CH_4,pr}+m_{O_2,pr}+m_{N2}\right)}{\left(m_{CH_4}+m_{O_2}+m_{N2}\right)}*100 \qquad \text{Eq.\{4.21\}}$$

$$m_{mix,pr}=m_{CH_4}+m_{O_2}+m_{N2} \qquad \text{Eq.\{4.22\}}$$

Error propagation

The mass deviations which were calculated from the equation above 4.21, are shown in Appendix A.The mass which is measured is slightly more than the mass which is introduced in the reformer. This deviation will be proved bellow that is in the range of mass error and therefore is acceptable. In additional the results of the error calculation are also presented at Appendix B for comparison.

The mass at the exit is calculated from the measured species. In order to calculate its error, the error species propagation via involved equations must be calculated.

Since the measurements was for dry syngas where the errors are known, the error of water volume fraction must firstly be calculated, after the new errors of species of wet syngas and then the mass final error.

Absolute error of water

The water equation 4.16 consist of two parts. Firstly the error of α was calculated:

$$\delta_a=\pm\sqrt{(2k)^2{\delta_{Xi}}^2+(-2)^2{\delta_{Xi}}^2+(-1)^2{\delta_{Xi}}^2}\Longrightarrow\delta_a=\pm\delta_{Xi}\sqrt{4k^2+5} \qquad \text{Eq.\{4.23\}}$$

where $k=\frac{n_{O_2}}{n_{N_2}}$ and δ_{Xi} the error of dry species which is the same for all.

Therefore from the first part of equation 4.16 the final absolute error of water was calculated by the equation:

$$\delta_{X'_{H2O}} = \pm X'_{H2O}\sqrt{\left(\frac{\delta_\alpha}{\alpha}\right)^2} \qquad \text{Eq.}\{4.24\}$$

Absolute error of species in wet mixture

For this error must be combined the errors of species of dry syngas and the error of water because of equation 4.17.The final calculated expression is:

$$\delta_{X'_i} = \pm\sqrt{{X'_{H2O}}^2{\delta_{Xi}}^2 + {X_i}^2{\delta_{X'_{H2O}}}^2 + {\delta_{Xi}}^2} \qquad \text{Eq.}\{4.25\}$$

where δ_{Xi} is the error of species of dry syngas and i represents every species.

Absolute error of mass oxygen $m_{o2,pr,}$ calculated from syngas.

The error of $m_{o2,pr}$ because of its equation 4.20, was calculated in two stages:

$$\boldsymbol{m_{O_2,pr}} = \underbrace{\frac{n_{N_2}}{X_{N_2}-\left(1-X'_{H_2O}\right)}\cdot AW_o}_{A}\cdot\underbrace{\left(2\cdot X'_{CO_2} + X'_{CO} + X'_{H_2O}\right)}_{B} \qquad \text{(Eq.}\{4.20\})$$

$$\delta_B = \pm\sqrt{2^2{\delta_{X'_{CO_2}}}^2 + {\delta_{X'_{CO}}}^2 + {\delta_{X'_{H_2O}}}^2} \qquad \text{Eq.}\{4.26\}$$

$$\delta_A = \pm A\sqrt{\left(\frac{\delta_{X'_{N2}}}{X'_{N2}}\right)^2} \qquad \text{Eq.}\{4.27\}$$

Therefore,

$$\delta_{m_{O_2,pr}} = \pm m_{O_2,pr}\sqrt{\left(\frac{\delta_A}{A}\right)^2 + \left(\frac{\delta_B}{B}\right)^2} \qquad \text{Eq.}\{4.28\}$$

Absolute error of mass oxygen $m_{CH4,pr,}$ calculated from syngas.

The error of $m_{CH4,pr}$ because of its equation 4.20, was calculated in four stages:

$$\boldsymbol{m_{CH_4,pr}} = \underbrace{\frac{n_{n2}\cdot AW_C}{X'_{N2}}}_{\Gamma}\cdot\underbrace{\left(X'_{CO_2} + X'_{CO} + X'_{CH_4} + 2\cdot X'_{C_2H_2}\right)}_{\Delta} + \underbrace{\frac{n_{n2}\cdot AW_H}{X'_{N2}}}_{E}\cdot\underbrace{\left(2\cdot X'_{H_2} + 2\cdot X'_{H_2O} + 4\cdot X'_{CH_4} + 2\cdot X'_{C_2H_2}\right)}_{Z} \qquad \text{(Eq.}\{4.19\})$$

where: $n_{n2} = \frac{\dot{Q}_{N2}\rho_{N2}}{28}$

$$\delta_{\Delta} = \pm\sqrt{{\delta_{X'_{CO_2}}}^2 + {\delta_{X'_{CO}}}^2 + {\delta_{X'_{CH_4}}}^2 + 4\cdot {\delta_{X'_{C_2H_2}}}^2} \quad \text{Eq.\{4.29\}}$$

$$\delta_{\Delta\Gamma} = \pm(\Delta\cdot\Gamma)\sqrt{\left(\frac{\delta_{\Delta}}{\Delta}\right)^2 + \left(\frac{\delta_{\Gamma}}{\Gamma}\right)^2} \quad \text{Eq.\{4.30\}}$$

$$\delta_{\Delta\Gamma} = \pm(\Delta\cdot\Gamma)\sqrt{\left(\frac{\delta_{\Delta}}{\Delta}\right)^2 + \left(\frac{\delta_{\Gamma}}{\Gamma}\right)^2} \quad \text{Eq.\{4.31\}}$$

$$\delta_{Z} = \pm\sqrt{4{\delta_{X'_{H_2}}}^2 + 4{\delta_{X'_{H_2O}}}^2 + 16{\delta_{X'_{CH_4}}}^2 + 4{\delta_{X'_{C_2H_2}}}^2} \quad \text{Eq.\{4.32\}}$$

$$\delta_{E} = \pm E\sqrt{\left(\frac{\delta_{X'_{N2}}}{X'_{N2}}\right)^2} \quad \text{Eq.\{4.33\}}$$

$$\delta_{ZE} = \pm(Z\cdot E)\sqrt{\left(\frac{\delta_{Z}}{Z}\right)^2 + \left(\frac{\delta_{E}}{E}\right)^2} \quad \text{Eq.\{4.34\}}$$

Therefore,

$$\delta_{m_{CH_4,pr}} = \pm m_{CH_4,pr}\sqrt{{\delta_{\Delta\Gamma}}^2 + {\delta_{ZE}}^2} \quad \text{Eq.\{4.35\}}$$

Finally the relative error in the mass of mixture at the exit ($m_{mix,pr}$), is:

$$\frac{\delta_{m_{mix,pr}}}{m_{mix,pr}} = \pm\sqrt{{\delta_{m_{CH4,pr}}}^2 + {\delta_{m_{O_2,pr}}}^2} \quad \text{Eq.\{4.36\}}$$

The error of nitrogen mass which is introduced by the flow controller was not calculated and it was not included at the equation 4.36 since from the result of this form we are already able to deduce if the mass deviation which is calculated at equation 4.21 is in the range of error of equation 4.36.

The results from absolute and relative errors are shown in the Appendix A. The masses of methane and oxygen which were calculated from wet syngas and the mass deviation which was calculated from equation 4.21 are shown in the following Appendix B. In table 4.12 and 4.13 presented only the mass deviations in comparison with relative errors of mass of wet syngas for the two version of experiments.

1st experiment	Table 4.11		
N [kW]	λ	Dm	$\frac{\delta_{m_{mix,pr}}}{m_{mix,pr}}$
1,5	0,4	-0,64%	±3,18%
1,5	0,42	-0,62%	±3,14%
1,5	0,45	-0,94%	±3,11%
1,5	0,5	-1,15%	±3,05%
1,5	0,52	-1,24%	±3,02%
2	0,4	-1,59%	±3,23%
2	0,45	-1,09%	±3,11%
2	0,5	-1,29%	±3,02%

2nd experiment	Table 4.12		
N [kW]	λ	Dm	$\frac{\delta_{m_{mix,pr}}}{m_{mix,pr}}$
1	0,6	-0,90%	±2,79%
1,5	0,5	-0,94%	±2,99%
1,5	0,52	-0,99%	±2,96%
1,5	0,5	0,14%	±2,94%
1,5	0,46	-0,79%	±3,07%
1,5	0,42	-0,64%	±3,12%
1,5	0,42	-0,88%	±3,10%
1,5	0,42	-0,81%	±3,09%
1,5	0,42	-0,76%	±3,08%
1,5	0,42	-0,65%	±3,06%
1,5	0,4	1,39%	±2,96%
1,5	0,5	-1,14%	±2,97%
1,5	0,5		
1,5	0,6	-2,18%	±2,95%
1,5	0,6	-1,97%	±2,94%

The calculations of mass conservation equations were shown that in the most cases negative mass deviation between inlet and outlet of the reformer was found, which means that more mass was measured. This mass deviation as is shown in tables 4.11 and 4.12 is too small and in the range of calculated error which is shown at the fourth column. Therefore, we can deduce that the mass conservation was verified and there was not leakages at the experimental set up.

4.3.7 Reforming efficiency /soot regeneration/ soot distributions

In this section will be evaluated the reforming efficiency of the soottrap based reformer and will be used the experimental data by the second version experiment . This type of reformer utilizes ceramic porous medium (soot trap is made by SiC material) as all the reformers but the difference is that the soot is retained within of the soot trap and the reforming efficiency could be affected by the dynamic soot regeneration. For this reason the regeneration of soot will be studied in the same section.

The measurement of pressure drop is an indirect index of the soot loading. Furthermore, the operating time of each case and the sequence of the experimental operating conditions are important parameters for the soot loading, soot regeneration and affects the reformer's efficiency. The evolution of soot trap pressure drop as function of time and conditions of each case of table 4.2, is presented at the follow figure 4.60:

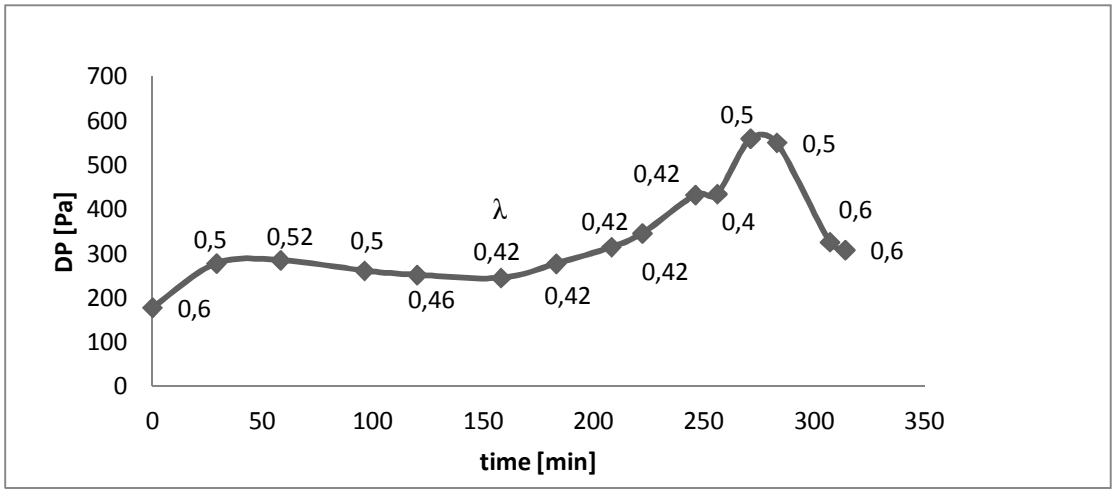

Fig. 4.60 : The evolution of pressure drop in the soot trap as function of time during experimental procedure for all tested cases.

The pressure drop of soottrap is increased for λ=0,42 as can be observed in figure 4.60. The pressure drop is increased as the time passes and this is the evidence that the soot production loads the soot trap. The inlet temperature of soottrap for all cases of λ=0,42 was about 1200^{o}C. Decreasing more the λ to 0,4 a sharp increase of pressure drop is observed because the production of soot become more. Thereafter, the λ was increased to 0,5 and a steep decrease in the pressure drop is observed which indicates the soot regeneration. The inlet temperature of soottrap for λ=0,5 was about 1300^{o}C. The volume fractions of species in the wet syngas for all cases are shown to the following table 4.13. As expected a trend of increasing H2 , CO and CH4 by the decreasing of λ is observed and this happens until the soot point, for λ=0,42 where the amounts of H2 and CO start decreasing. Furthermore, the increase H2, CO and the decrease of H2O can be observed for the cases of λ=0,5 and λ=0,6 where the regeneration of soot was taken place. This indicates the activity of Boudouard reactions which have already mentioned in 2.3 section and are repeated below.

$$C + CO_2 \rightarrow 2CO \quad (\Delta H = 131\ kj/mol)$$

$$C + H_2O \rightarrow CO + H_2 \quad (\Delta H = 172\ kj/mol)$$

Boudouard reactions (by section 2.3)

Table 4.13

cases	N [kW]	λ	X'H2 %	X'co %	X'co2 %	X'ch4 %	X'c2h2 %	X'N2 %	X'H2O%
1	1	0,6	13,54	10,61	3,66	0,68	0,04	61,01	10,45
2	1,5	0,5	16,70	11,98	2,97	1,73	0,05	57,67	8,91
3	1,5	0,52	16,59	11,87	3,10	1,34	0,04	58,11	8,95
4	1,5	0,5	17,97	12,25	2,92	1,51	0,04	56,93	8,39
5	1,5	0,46	17,46	12,02	2,71	2,54	0,04	56,42	8,81
6	1,5	0,42	16,31	11,46	2,55	4,29	0,04	55,91	9,45
7	1,5		14,25	10,99	2,64	5,36	0,02	56,66	10,08
8	1,5		13,76	10,75	2,63	5,53	0,02	56,87	10,44
9	1,5		13,46	10,79	2,57	5,54	0,02	57,01	10,60
10	1,5		13,21	10,52	2,60	5,57	0,05	57,18	10,88
11	1,5	0,4	14,27	10,77	3,20	3,22	0,04	58,48	10,03
12	1,5	0,5	14,83	10,87	3,20	2,98	0,04	58,25	9,83
13	1,5								
14	1,5	0,6	16,78	13,03	3,38	0,41	0,00	58,83	7,57
15	1,5		17,09	12,59	3,35	0,33	0,00	58,64	8,00

It would be interesting to be observed how the volume fraction of C_2H_2 was evolved (figure 4.61) during the experiment, in comparison with the pressure drop, which indicates soot loading and regeneration from figure 4.60. As it can been seen from the comparison of these figures when the soot point appears for λ=0,42 the volume fraction of acetylene decreasing as was expected because of its consumption into soot. Firstly for λ=0,42 a sharp decreasing was observed because the new conditions favor the formation of soot, thereafter the volume fraction of acetylene remains stable in an equilibrium where acetylene consumed into soot. Then, when the conditions doesn't anymore favor the more increasing of soot, a sharp increasing of acetylene appears again. Thereafter when new conditions of a lower λ=0,4 was imposed a sharp decreasing of acetylene observed again due to its consumption into soot which can be more in the new equilibrium. Furthermore, when the λ increased to 0,5 its volume fraction increasing because the conditions in this cases doesn't favor the formation of soot and when the λ increased to 0,6 the acetylene in the mixture eliminated.

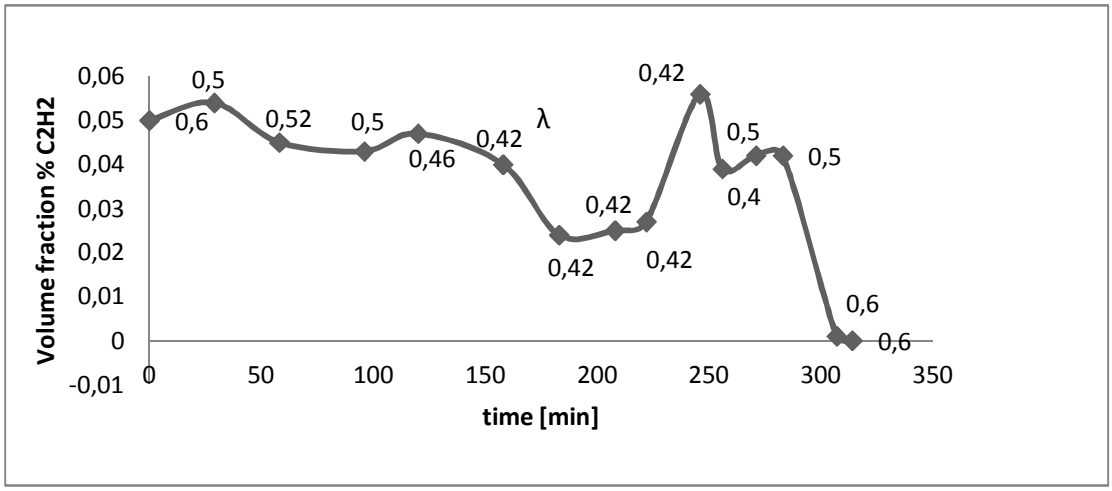

Fig.4.61. The evolution of C_2H_2 volume fraction as function of time during experimental procedure for all tested cases.

The efficiency of the reformer can be calculated by the following equations and the efficiency of each case is presented at the table 4.14 and figure 4.62.

The efficiency is defined as:

$$\eta = \frac{n_{H2} \cdot LHV_{H2} + n_{CO} \cdot LHV_{CO}}{n_{CH4} \cdot LHV_{CH4}} \qquad \text{Eq.\{4.37\}}$$

By the rearrangement of equation 4.37 with known magnitudes, we get the following equation :

$$\eta = \frac{n_{N2}}{n_{CH4}} \cdot \frac{(X'_{H2} \cdot LHV_{H2} + X'_{CO} \cdot LHV_{CO})}{X'_{N2} \cdot LHV_{CH4}} \qquad \text{Eq.\{4.38\}}$$

Where,

$$n_{N2} = \frac{\dot{Q}_{N2} \cdot \rho_{N2}}{28} \qquad \text{Eq.\{4.39\}}$$

$$n_{N2} = \frac{\dot{m}_{CH4}}{16} \qquad \text{Eq.\{4.40\}}$$

$$LHV_{H2} = 119494 \left[\frac{kJ}{kg}\right] \cdot \frac{101326 \cdot 1}{8314 \cdot 273{,}15} \left[\frac{kg}{m^3}\right] = 5331{,}58 \left[\frac{kj}{m^3}\right] \qquad \text{Eq.\{4.41\}}$$

$$LHV_{CO} = 119494\left[\frac{kJ}{kg}\right] \cdot \frac{101326 \cdot 28}{8314 \cdot 273{,}15}\left[\frac{kg}{m^3}\right] = 12630{,}45\left[\frac{kj}{m^3}\right] \quad \text{Eq.}\{4.42\}$$

$$LHV_{CH4} = 119494\left[\frac{kJ}{kg}\right] \cdot \frac{101326 \cdot 16}{8314 \cdot 273{,}15}\left[\frac{kg}{m^3}\right] = 35633{,}68\left[\frac{kj}{m^3}\right] \quad \text{Eq.}\{4.43\}$$

cases	N [kW]	λ	η
1	1	0,6	44%
2	1,5	0,5	45%
3	1,5	0,52	46%
4	1,5	0,5	47%
5	1,5	0,46	43%
6	1,5	0,42	38%
7	1,5	0,42	35%
8	1,5	0,42	34%
9	1,5	0,42	33%
10	1,5	0,42	32%
11	1,5	0,4	32%
12	1,5	0,5	40%
13	1,5	0,5	
14	1,5	0,6	56%
15	1,5	0,6	56%

Table 4.14. The values of syngas production efficiency for the tested cased of second experiment version

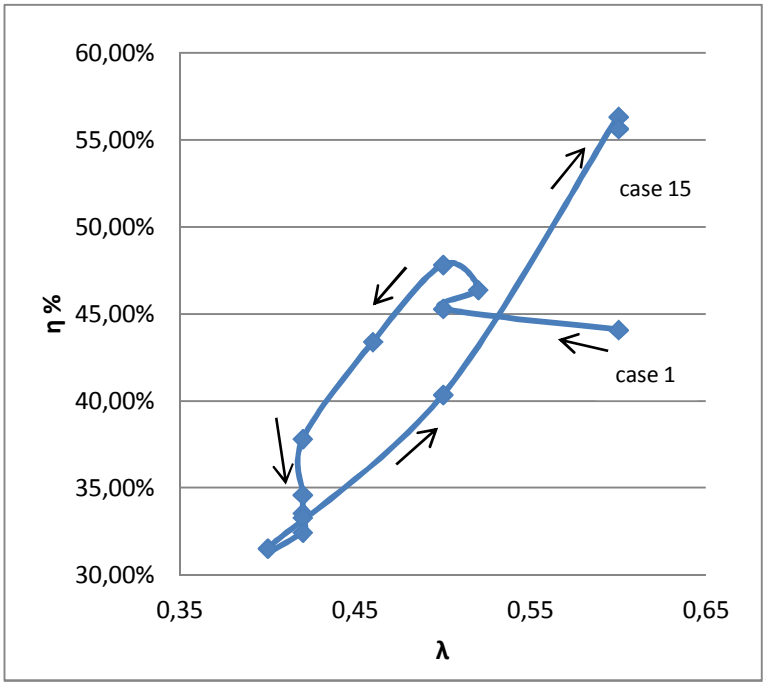

Fig.4.62:The syngas production efficiency for the second version experiment as it was evolved during the operation of the experimental sequence.

In figure 4.62 is shown the evolution of reformer's efficiency from one test case to the other according to the sequence of test cases which were conducted in the experiment. It can been seen that the reformer's efficiency was increasing by the reducing of λ in the first cases and decreasing when soot point comes for λ=0,42. When the λ was increased again, the efficiency increased and the values of efficiency for the case of λ=0,6 were too high. As we referred and proved in previous paragraphs, at the last cases the activity of Boudouard reactions were taken place and the high efficiency values could be attributed at the more production of H2 and CO by the gasification of carbon. As a remark we can say that for the investigated cases this type of reformer without loading of soot and regeneration, accomplished an efficiency about 47%.

Soot distributions

The soot measurements was conducted in the second version experiment for thermal load 1.5 kW and for air equivalence ratios 0.5, 0.46 and 0.42. The sequence of the tested cases is shown at the following table where the conditions of the test setup are also presented.

Table 4.15.*Tested cases and conditions of soot measurement system*

N[kW]	λ	QN2 [lt/min]	Tmix [lt/min]	Qpump [lt/min]	DR (Dilution Ratio)	sample number
1,5	0,50	21	160	26	5,5	11
1,5	0,46	21	160	26	5,5	11
1,5	0,42	21	160	26	5,5	12
1,5	0,42	21	160	26	5,5	9
1,5	0,50	21	160	26	5,5	9
1,5	0,60	21	160	26	5,5	6

Figure 4.63 illustrates the electrical mobility diameter distributions of the detected soot particles within the exhaust gas of the soot trap based reformer, for reactants preheated to 400^{o}C. The presented results correspond to the test cases of table 4.4.
As we have already mentioned, the sample was diluted by nitrogen, its temperature decreased thus was imposed a fluctuation in its volume and in the concentration of its particles. Furthermore diffusion losses were realized in the tubes and thus the particles in the sample decreased . All these variation in the sample was calculated and the first soot distributions of the SMPS were corrected and essentially scaled back to the exhaust conditions.

The changes in important characteristics of the presented distributions (mean diameter, standard deviation, particle number density and mass density) for each case of tested air equivalence ratio have been summarized in Table 4.15.

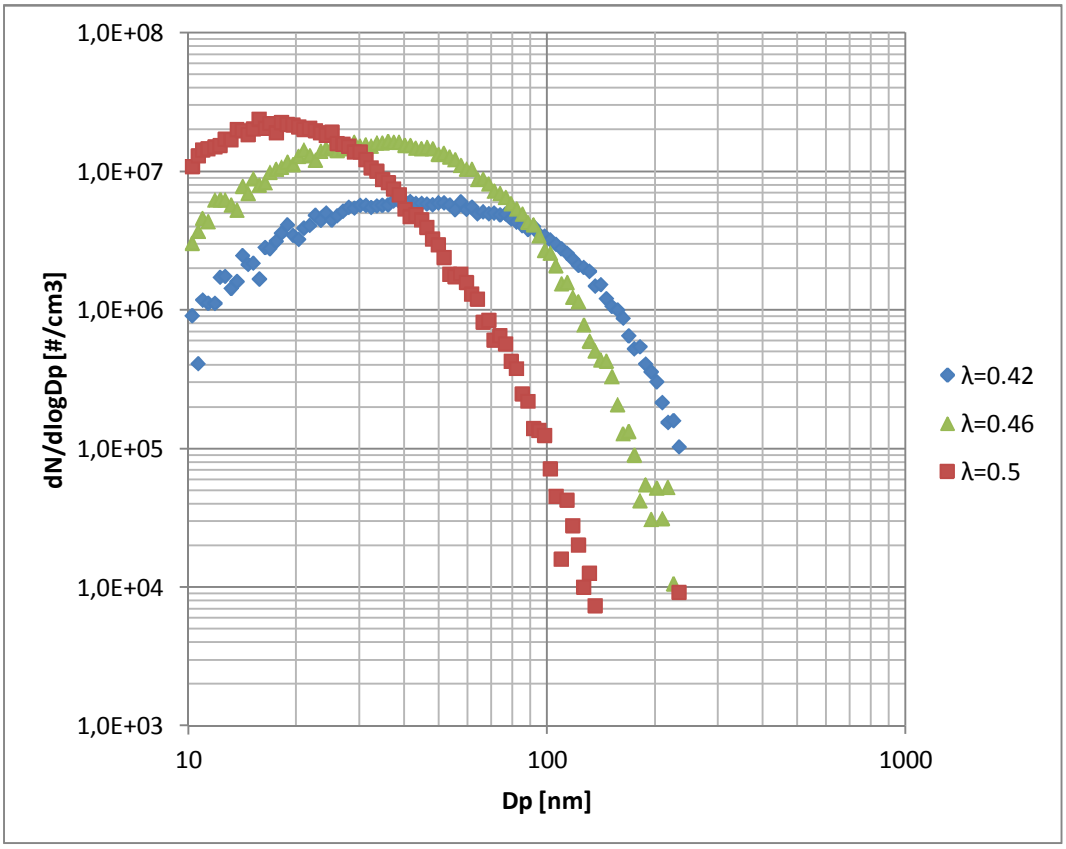

Fig.4.63. Variation of the soot size distributions at the exit of the soottrap based reformer for different equivalence ratios, reactants preheated at 400°C and thermal load 1.5 kW.

λ	Mean diameter Dp [nm]	Standard deviation Sg	Number concentrations [#/cm^3]	Mass concentrations [mg/cm^3]
0,5	21,25	1,60	1,17E+07	1,53E-04
0,46	38,35	1,79	1,11E+07	1,63E-04
0,42	51,87	1,97	4,85E+06	3,71E-04
0,5	17,47	1,65	3,33E+09	5,40E-07
0,6	No particles detected	No particles detected	No particles detected	No particles detected

Table 4.15. Soot characteristics of each tested case for the soottrap based reformer, for preheating 400°C and thermal load 1,5 kW.

The results show that the majority of the detected particles are sized in the range of 10 nm up to 110 nm. As was expected the mean diameter increase by decreasing air equivalence ratio. The number of concentrations would be expected to increase but as is shown in table 4.15 decreasing from λ=0.46 to 0,42. This could be attributed in that the soottrap efficiency retaining particles increase by increasing particle diameters. When the regeneration starts for λ=0,5 the agglomerates was starting to be decomposed and a bigger number of particles was measured.

Chapter 5th Simulation of Chemical kinetics in the Reformer

5.1Basic theory for a reacting flow

5.1.1 Mathematical description

In order to describe a reacting flow, we need a closed system of equations which describes the mass flux and the reacting fluid. By the study of mass flux and considered that is composed of two parts an advective (bulk fluid motion) and a diffusive part (given by Fick's Law) , we derived the governing equation for the species mass fractions as shown below:

$$\frac{\partial(\rho Y_i)}{\partial t}+\frac{\partial(\rho U Y_i)}{\partial x}=\frac{\partial}{\partial x}\left(\rho D\frac{\partial Y_i}{\partial x}\right)+\dot{w}_i \qquad \text{Eq.\{5.1\}}$$

Yi: the mass fraction , ρ:density, U:velocity, D:diffusion coefficient, $\dot{w}_i$: the net rate of generation for species i.

Fick's Law states that the mass flux is proportional to the gradient of the mass fraction of the species. This is a diffusion process because it tends to make concentration gradients more uniform, it mixes the various species together. The coefficient D (m^2 s^{-1}) is the diffusion coefficient and in general, depends on the nature of the diffusing species and the nature of the species it diffuses into. Thus, the Di of a chemical institute is really a function of the whole mixture. However, it is a good approximation to take Di=D to be the same for all species. For simplicity, we will further assume that it is constant. It is also common approximation that the diffusion of heat and mass follow the same rate i.e D is related to the conductivity λ:

$$\rho D=\frac{\lambda}{c_p} \qquad \text{Eq.\{5.2\}}$$

The non-dimensional number λ/ρDCp is called Lewis number Le. It is common assumption in combustion that Le=1 that implies that from tabulated values of conductivity we can estimate D.

For low Mach number flows with negligible contribution of the kinetic and gravitational energy to the total energy of the fluid, and assuming equal diffusivities and Le=1, the principle of conservation of energy, with our standard assumption of constant Cp, is written as:

$$\rho c_p\frac{\partial T}{\partial t}+\rho c_p U\frac{\partial T}{\partial x}=\frac{\partial P}{\partial t}+\frac{\partial}{\partial x}\left(\lambda\frac{\partial T}{\partial x}\right)-Q\dot{w}_{fuel} \qquad \text{Eq.\{5.3\}}$$

The first term in the l.h.s, the unsteady term, is the net rate of the temperature rise. The second term in the l.h.s describes convection. The first term in the r.h.s is heating due to compression and is important for internal combustion engines. This term is zero if the pressure is constant. The second term in the r.h.s is due to heat conduction and the last term is the heat released by combustion.

In this point, in order to completely clolse our system of equations that describe a reacting flow an expression for the rate of the reaction $\dot{w}$ needed. The rate of reaction comes from Chemical Kinetics.

5.1.2 Chemical Kinetics

Global and elementary reactions

The *global reaction* expresses the overall process of combustion and correlates the reactants directly to the finished products. A global reaction does not represent the real physic of combustion, because it would be impossible to break too many bonds of molecules and to redistributed to the final products in one step. However, a global reaction helps to visualize the overall process and stoichiometry. The real combustion process follows hundreds or thousands intermediate reactions which call *elementary reactions* and many intermediate species which call radicals. The radicals are very reactive unstable molecules. The series of elementary reactions that finally describes the overall process called a *reaction mechanism or detailed chemical mechanism*.

The Law of Mass Action

The Law of Mass Action is a very important concept in Chemical Kinetics. It relates how quickly the reaction proceeds as a function of how much reactant is available. It is valid only for elementary reactions. Consider the generic elementary reaction

$$a_1R_1 + a_2R_2 + a_3R_3 + \ldots + a_MM \rightarrow b_1P_1 + b_2P_2 + b_3P_3 + \ldots + b_MM \qquad \text{React.}\{5.1\}$$

between reactants R1,R2,R3,..., from which products P1,P2,P3,..., are formed. M is an example of species that appears on both sides. The rates of reactants consumption and products formation are given by:

$$\frac{d[R_1]}{dt} = -a_1\omega, \quad \frac{d[R_2]}{dt} = -a_2\omega, \quad \frac{d[R_3]}{dt} = -a_3\omega, \ldots$$
$$\frac{d[P_1]}{dt} = b_1\omega, \quad \frac{d[P_2]}{dt} = b_2\omega, \quad \frac{d[P_3]}{dt} = b_3\omega, \ldots \qquad \text{Eqs.}\{5.4\}$$
$$\frac{d[M]}{dt} = b_M\omega - a_M\omega$$

with ω [kmole m^{-3} s^{-1}] being the reaction rate and should not be confused with the net rate of generation $\dot{w}_i$ for species i .

$$\omega = k[R_1]^{a_1}[R_2]^{a_2}[R_3]^{a_3}\ldots \qquad \text{Eq.}\{5.5\}$$

The parameter k is the reaction rate constant and $[R_1]$ is the concentration in [kmole/m^3] of reactant R_1 etc. The amount of R_1 that has reacted is related to how much R2 , R3 has reacted. I f a species M appears in both the reactants and the products, the then what multiplies ω is the

difference (b_M-α_M). If b_M=α_M , then M is called a third body: it may not be altered, but its presence is crucial for the success of the reaction, as it provides energy to, or takes energy away from, the collision between the reactants.

Equation 3.40 is the Law of Mass Action and states that the reaction rate is proportional to the reactants concentrations, raised to their respective stoichiometric coefficients (i.e. α1,α2, etc). The amount of products does not affect ω. The reaction rate constant k is not a function of the reactants concentration and it is specific to the elementary reaction.

The reaction rate Constant

The reaction rate constant is given by the Arrhenius law

$$k = A\exp\left(-\frac{E_{act}}{R^0 T}\right) \qquad \text{Eq.}\{5.6\}$$

where A is the pre-exponential factor and Eact is the activation energy.These quantities come from experiment or statistical mechanics calculations. The presence of the exponential can be understood by the following argument. Not all molecular collisions will result in reaction, but only those with kinetic energy higher than the energy needed to break bond inside the reactants' molecules. This energy barrier described by the activation energy. The proportion of collisions occurring between molecules that have kinetic energy higher than Eact is given by exp(-Eact/R^0T); this results from Kinetic Theory of Gases. The important point to notice is that the reaction rate constant increases very fast with temperature and this is the fundamental reason why combustion reactions occur at high temperatures and not at room temperature.

Reaction mechanisms

If many elementary reactions take place, the net amount of reactant or product consumed or produced will come from adding the contribution from each elementary reaction. In general, species will participate in some reactions as reactants and in others as products. The overall consumption or generation rate will be the net outcome of all elementary reactions.

Forward and backward reactions

Many elementary reactions can proceed in both directions. Hence the products can become reactants and vice versa. The specific reaction rates will, in general, be very different. The reaction rate constants for the forward and backward reaction are related through the equilibrium constant of the reaction. So, in general, knowing the rate constant of the forward reaction suffices.

Types of elementary reactions

Elementary reactions can be classified according to the number of molecules participating in the reactants side. For the generic elementary reaction

$$a_1R_1 + a_2R_2 + a_3R_3 + \ldots + a_MM \rightarrow b_1P_1 + b_2P_2 + b_3P_3 + \ldots + b_MM \qquad \text{React.}\{5.2\}$$

this reaction is of overall order (α1+α2+α3+...).The overall order is also called molecularity. Depending on the molecularity, we have the following types of elementary reactions :

1.First order:
This reaction is an idealization, since the molecules normally do not disintegrate spontaneously. The rate is given by $\omega = -\kappa[R_1]$ and k has units (1/s).

2.Second order:
This is the most common reaction in combustion since the collision probability is highest for two molecules. The rate is given by $\omega = -\kappa[R_1]\,[R_2]$ and k has units (kmole/m^3)$^{-1}$ s^{-1}.

3.Third order:
The probability that tree molecules collide is small, but nevertheless third-order reactions are very important. Radical recombination reactions, for example OH and H to produce water, take place only if a third body M participates in the collision and hence these are third-order reactions. The reason a third body is needed is that recombination reactions are exothermic and the third body must carry away some of energy.
The rate is $\omega = -\kappa[R_1]\,[R_2]\,[R_3]$ and k has units (kmole/m^3)$^{-2}$s^{-1}.

Simplified chemical mechanisms

Empirical one-step combustion mechanisms

The global reactions do not represent an actual reaction that occurs during a collision, the combustion processes follows many elementary reactions. However, global reactions represent very well the overall fate of the fuel and the overall stoichiometry. Such engineering approximations to the overall rate of combustion exist and are called reduced reaction mechanisms. Reduced mechanisms are a sequence of artificial steps that range in number from, say ten to one. Based on experiments, such one-step mechanisms have been developed for most hydrocarbon fuels and provide useful approximations for many flame problems. In the context of a one-step reaction, the combustion of a hydrocarbon is written as:

$$C_xH_y + (x+y/4)(O_2 + \frac{0.79}{0.21}N_2) \rightarrow xCO_2 + \frac{y}{2}H_2O + \frac{(x+y/4)0.79}{0.21}N_2 \qquad \text{React.}\{5.3\}$$

The rate of the global reaction is written empirically as

$$\frac{d[C_xH_y]}{dt} = -A_G \exp\left(-E_{act}/R^0T\right)[C_xH_y]^p[O_2]^q \qquad \text{Eq.}\{5.7\}$$

with p,q,A_G and E_{act} obtained from experiments and numerical optimization so that Eq.3.42 gives an overall rate of fuel and oxygen consumption close to that of the data or to that of a detailed reaction mechanism. Must be noted that p and q have nothing to do with the stoichiometric coefficients.

Systematically-reduced combustion mechanisms

A more scientific way to reduce a detailed chemical mechanism is to use the *steady-state approximation* and the *partial equilibrium assumption.*
The steady-state approximation refers to a species: species A is said to be in steady state if d[A]/dt≈0, i.e. if its net production rate from the mechanism is approximately zero. This assumption leads many species to eliminate from the reaction rate expressions by relating their concentrations to those of other species.
The partial equilibrium assumption refers to a reaction and states that the forward and backward rates of an elementary reaction are equal. An elementary reaction will be in partial equilibrium if both its forward and backward rates are very much faster than those of the other reactions in the mechanism.
For realistic combustion mechanisms the same concepts are used in complicated computer programs. The identification of steady-state species and partial-equilibrium reactions is currently the subject of intensive research in the combustion community.

Hydrocarbon combustion chemistry

The elementary reactions forming a detailed reaction mechanism for hydrocarbon combustion could number many hundreds of reactions in which 40-200 stable species and radicals may participate. The overall features, which also explain some experimental observations, are approximately the same for all hydrocarbons. The reaction sequence is very complex, but we can describe the basic ideas as a series of three steps.

Typical combustion sequence

Step 1: Breakdown of the fuel into smaller hydrocarbons from radical attack. These smaller hydrocarbons could also be stable species, not necessarily radicals. For example, significant amounts of C_2H_2 are found in the initial stages of the combustion of almost all fuels.

Step2:All the carbon from the fuel eventually results in CO and the hydrogen results in H_2.

Step3: Final oxidation of CO and H_2 into CO_2 and H_2O. A large part of the heat release associated by combustion occurs here.

Other features

1.Rich combustion
If combustion is rich then, fuel fragments may collide to form larger hydrocarbons. This process leads to **soot**, which are agglomerated solid particles. Soot radiates intensely in the hot flame products and gives rich flames their characteristic yellow colour.
2.Radical formation
None of the steps above (fuel breakdown, partial oxidation into CO and H2, and final oxidation) can occur if radicals such as O,H, and OH are absent. One of the most important elementary reactions in combustion is:

$$O2 + H \longrightarrow OH+O \qquad \text{React.}\{5.4\}$$

which is a chain-branching reaction and proceeds at appreciable rates only at high temperatures (>1500 K) as it has a high activation energy. This reaction is one of the few that produces the O atom. Hence, if its rate drops below that of the chain-terminating reactions, the flame will not stay alight.

5.2 Simulation of partial methane oxidation in the Reformer utilizing a GRI mechanism of 19 chemical species.

A simulation of partial methane oxidation was conducted in the soottrap based reformer. The geometry and the meshing for this simulation was described at 3.1 (2nd prototype) and 3.3 paragraph respectively.

The reduced GRI-MECH

A reduced GRI-MECH which is consisted of 19 species for methane combustion was introduced. This reduced mechanism was made by Andrei Kazakov and Michael Frenklach of University of California at Berkeley [17]. The reduction in size followed a technique of detailed reduction described in publications [18],[19],[20]. The technique is based on flux analysis performed using simple, zero-dimension calculations with a "full" detailed chemical reaction mechanism. The following criteria are applied to identify the non-contributing reactions:

$| R(i) | < e(r) | R(ref) |$ and $| R(i)\ delta\text{-}H(i) | < e(q)\ Q$

where R(i) is the rate of reaction i, R(ref) is the rate of a reference reaction (e.g., the maximum rate), delta-H(i) is the enthalpy change of reaction i, Q is the maximum value among all the terms |R(i) delta-H(i)|, and e(R) and e(Q) are the chosen parameters considerably smaller than unity. The first criterion tests the contribution a given reaction makes to the main chain branching while the second criterion tests the contribution to the heat release. Reactions whose rates, both forward and reverse, satisfy the above inequalities at all grid points of the calculation are removed from the mechanism. This procedure eliminates a specific species when all reactions of such a species happen to be removed.
The present reduction was performed using e(r) = e(q) = 0.02, under the following test conditions: shock-tube ignition of methane-air mixtures at wide ranges of initial conditions (equivalence ratio PHI = 0.2 - 2.0, initial pressure Po = 0.1 - 50 atm, and initial temperature To = 1300-2500 K); and methane-air adiabatic flames at 1 and 20 atm. This procedure generated a 22-species, 104 reactions set, which is referred to as DRM22.
Additional analysis of reaction fluxes and sensitivities to removal of selected species was performed on DRM19. Those chemical species which were showed near-zero sensitivity were removed. This resulted in a smaller set, 19-species and 84 reactions, which is referred to as DRM19.

The elementary reactions of reduced GRI-MECH DRM19 are given in Appendix C and the chemical species which is consisted of, are given below:

ELEMENTS
O H C N AR
SPECIES
H2 H O O2 OH H2O HO2
CH2 CH2(S) CH3 CH4 CO CO2 HCO
CH2O CH3O C2H4 C2H5 C2H6
N2 AR

Cases of numerical study

The numerical study was conducted for four different conditions of combustion. In particular, for thermal load 1.5 kW and for four different air equivalence ratios, 0.42, 0.46, 0.5 and 0.6 . Furthermore, for each case the appropriate coefficients for the porous domain was calculated according to the equations of paragraph 3.6.2, in order to represent the soottrap as porous packed bed in ANSYS aiming to simulate the real pressure drop in the porous-"soottrap" domain insofar this is possible. The thermal losses were not calculated in detail but they were approached by the comparing of the temperature profile of simulation with experiment. It must be said that the results of this simulation will be compared with the experimental results of the experimental study of 4 Chapter. For this reason some experimental measurements of temperature and volume fractions of species were used for better calculation of the simulation initial conditions.

5.2.1 Calculations of the initial conditions

Inlet velocity / Inlet volume fractions of CH_4, O_2 and N_2/ Coefficients of porous domain

- ***Inlet velocity***

Mass flow rates $\dot{m}\left[\frac{kg}{s}\right]$, volumetric flow rates of methane and air in flow controllers $\dot{Q}_{mix,f.c}$ $[\frac{lt}{min}]$ and the average density of mixture $\rho_{mix,f.c.}\left[\frac{kg}{m^3}\right]$, calculated based on thermal power N[kW] , equivalence air ratio λ and also considering that the volumetric flow rate in flow controllers results for temperature $T_{f.c} = 273{,}15\,K$. The calculation of the above quantities for each case was carried out in accordance of the following equations:

$$\dot{m}_{CH4} = \frac{N}{Hu} \qquad \text{Eq.\{5.8\}}$$

where, $Hu = 50050\ \left[\frac{kJ}{kg}\right]$ the lower heating value of methane and N is the thermal power [kW].

The air equivalence ratio defined as:

$$\lambda = \frac{\left(\frac{\dot{m}_{air}}{\dot{m}_{CH4}}\right)}{\left(\frac{\dot{m}_{air}}{\dot{m}_{CH4}}\right)_{st}} \rightarrow \quad \boldsymbol{\dot{m}_{air}} = \lambda \cdot \left(\frac{\dot{m}_{air}}{\dot{m}_{CH4}}\right)_{st} \cdot \dot{m}_{CH4} \qquad \text{Eq.\{5.9\}}$$

Where the stoichiometric air-methane ratio is:

$$\left(\frac{\dot{m}_{air}}{\dot{m}_{CH4}}\right)_{st} = 17.167 \qquad \text{Eq.\{5.10\}}$$

The reference conditions at the flow controllers are:

$$P = 101325\ Pa$$

$$T_{f.c} = 273{,}15\ K$$

The densities can be calculated from ideal gas equation and the units are [Pa] for pressure P, [g/mole] for molar weight Mw, [J/kg K] for gas constant and [K] for the temperature.

$$\rho_{air,f.c.} = \frac{P\ MW_{air}}{R\ T_{f.c}} \cdot 10^{-3} \ \left[\frac{kg}{m^3}\right] \qquad \text{Eq.\{5.11\}}$$

$$\dot{Q}_{air,f.c} = \frac{\dot{m}_{air}}{\rho_{air,f.c.}} \ \left[\frac{m^3}{s}\right] \qquad \text{Eq.\{5.12\}}$$

$$\rho_{CH4,f.c.} = \frac{P\ MW_{CH4}}{R\ T_{f.c}} \cdot 10^{-3} \ \left[\frac{kg}{m^3}\right] \qquad \text{Eq.\{5.13\}}$$

$$\dot{Q}_{CH4,f.c} = \frac{\dot{m}_{CH4}}{\rho_{air,f.c.}} \ \left[\frac{m^3}{s}\right] \qquad \text{Eq.\{5.14\}}$$

$$\dot{Q}_{mix,f.c} = \dot{Q}_{air,f.c} + \dot{Q}_{CH4,f.c} \qquad \text{Eq.\{5.15\}}$$

The average molar weight of mixture at flow controllers can be calculated by the following equation:

$$\overline{MW}_{CH4,air} = \left.\frac{\dot{Q}_{CH4}}{\dot{Q}_{mix}}\right|_{f.c} MW_{CH4} + \left.\frac{\dot{Q}_{air}}{\dot{Q}_{mix}}\right|_{f.c} MW_{air} \quad [24] \qquad \text{Eq.\{5.16\}}$$

Therefore, the density of mixture the mass flow of the mixture can be calculated now from the following equations:

$$\rho_{mix,f.c.} = \frac{P\ \overline{MW}_{CH4,air}}{R\ T_{f.c}} \cdot 10^{-3} \quad \text{Eq.\{5.17\}}$$

$$\dot{m}_{mix} = \rho_{mix,f.c.} \cdot \dot{Q}_{mix,f.c} \quad \text{Eq.\{5.18\}}$$

Now, we are able to calculate the **inlet velocity** of the mixture, take under consideration that the inlet diameter in the geometry of model is D_{in}=13mm.

$$\boldsymbol{U_{inlet}} = \frac{4 \cdot \dot{m}}{\rho_{mix,in} \cdot \pi \cdot {D_{in}}^2} \quad \text{Eq.\{5.19\}}$$

where the density of mixture at the inlet results from the following equation, for preheating inlet temperature T_{in} same with the experimental temperature in order to represent the same conditions.

$$\rho_{mix,in} = \frac{P\ \overline{MW}_{CH4,air}}{R\ T_{in}} \cdot 10^{-3} \quad \text{Eq.\{5.20\}}$$

- ***Inlet volume fractions of CH_4, O_2 and N_2***

In order to calculate the volume fraction of CH_4, O_2 and N_2, first the density of air and methane is calculated at inlet for temperature T_{in}.

$$\rho_{air,in} = \frac{P\ MW_{air}}{R\ T_{in}} \cdot 10^{-3} \ \left[\frac{kg}{m^3}\right] \quad \text{Eq.\{5.21\}}$$

$$\rho_{CH4,in} = \frac{P\ MW_{CH4}}{R\ T_{in}} \cdot 10^{-3} \ \left[\frac{kg}{m^3}\right] \quad \text{Eq.\{5.22\}}$$

Thus, the volumetric flows of air and methane can be calculated since their mass flows are known from previous calculations.

$$\dot{Q}_{CH4,in} = \frac{\dot{m}_{CH4}}{\rho_{CH4,in}} \quad \text{Eq.\{5.23\}}$$

$$\dot{Q}_{air,in} = \frac{\dot{m}_{air}}{\rho_{air,in}} \quad \text{Eq.\{5.24\}}$$

Therefore,

$$\dot{Q}_{O2,in} = 0.21 \cdot \dot{Q}_{air,in} \quad \text{Eq.\{5.25\}}$$

$$\dot{Q}_{N2,in} = 0.79 \cdot \dot{Q}_{air,in} \quad \text{Eq.\{5.26\}}$$

Thus, the inlet volume fractions were calculated by the equations:

$$\boldsymbol{X_{CH4,in}} = \frac{\dot{Q}_{CH4,in}}{\dot{Q}_{CH4,in} + \dot{Q}_{air,in}} \quad \text{Eq.\{5.27\}}$$

$$\boldsymbol{X_{O2,in}} = \frac{\dot{Q}_{O2,in}}{\dot{Q}_{CH4,in} + \dot{Q}_{air,in}} \quad \text{Eq.\{5.28\}}$$

$$\boldsymbol{X_{N2,in}} = \frac{\dot{Q}_{N2,in}}{\dot{Q}_{CH4,in} + \dot{Q}_{air,in}} \quad \text{Eq.\{5.29\}}$$

- ***Coefficients of porous domain***

The coefficients of porous domain, C_2 inertial resistance [1/m] and Kan permeability [m^2] were calculated according the equations 3.33, 3.34 which were resulted from Konstandopoulos-Johnson model in combining with ANSYS equations as is described in paragraph 3.6.2, in order to be simulated the same pressure drop of soottrap by porous packed bed in ANSYS.

According to the equations 3.33, 3.34 the volumetric flow at the exit of the porous-"soottrap" domain is needed.

The average density at the exhaust of soottrap, the dynamic viscosity and the final calculation of volumetric flow rate at the exhaust which needed at the equation 3.33 based on the following equations and the temperature of the exit of the soottrap Tex_1 was used from the experimental measurements as was described in Chapter 4.

$$\rho_{mix,ex1} = \frac{P\ \overline{MW}_{products}}{R\ T_{ex1}} \cdot 10^{-3} \quad \text{Eq.\{5.30\}}$$

$$\overline{MW}_{products} = \sum_{i=1}^{N} x_i \cdot Mw_i \quad \text{Eq.\{5.31\}}$$

$$\dot{Q}_{ex1} = \frac{\rho_{mix\ f.c.}}{\rho_{mix\ ex.1}}\ \dot{Q}_{mix,f.c} \qquad \text{Eq.\{5.32\}}$$

The exhaust dynamic viscosity $\mu\left[\frac{g}{cm\ s}\right]$ *can be calculated approximated as air by Sutherland equation:*

$$\mu = \frac{b\ T^{3/2}}{T+S} \cdot 10\ \left[\frac{g}{cm\ s}\right] \qquad \text{Eq.\{5.33\}}$$

The constants b and S for air are:

$$b = 1{,}458 \cdot 10^{-6}\ \left[\frac{\text{kg}}{\text{m s K}^{1/2}}\right]$$

$$\text{S} = 110{,}4\ \text{[K]}$$

The characteristics of soottrap and its type which also needed for the equations 3.33 and 3.34, are given by the tables 4.1 and 4.2 of chapter 4.

Table 5.1 The initial conditions for ANSYS simulation based on the above equations

N[kW]	λ	Tmix [K]	Uin [m/s]	X_{CH4}	X_{O2}	X_{N2}	$C_2\left[1/m\right]$	$\frac{1}{K_{an}}\left[1/m^2\right]$
1.5	0.42	680.45	3.93	0.9419	0.0122	0.0459	10860.785	31176902.42
	0.46	689.85	4.286	0.935	0.0137	0.0515	9421.77	29308145.41
	0.5	691.15	4.598	0.9292	0.0148	0.0559	8746.675	29308145.41
	0.6	663.15	5.14	0.9235	0.0161	0.0605	8297.097	32781854.28

5.2.2 Concerning the convergence of the simulation

To achieve convergence was important to be followed a sequence of actions. Firstly, only the velocity field without chemistry was solved. The solution was saved in order to be used later as the initial field for the chemistry simulation. Except of this, in the initialization for the chemistry simulation was also included the estimation and setting in the field of some of the most important magnitudes. It was important the temperature of reaction zone to be above of 1600 [K] and it was also important to be estimated the values of some important chemical species in the field.

The relaxations factors which are essentially the solution controls must be varied between 0.95 and 1 for the chemical species. The convergence of the current simulations were achieved starting with the relaxation factors of chemical species to 1 only for the first solution and after interruption these changed to 0.95. [16]

Concerning the order of magnitude of convergence criterion, was $5*10^{-4}$ for mass, 10^{-3} for the chemical species and 10^{-5} for the energy.

5.2.3 Results of simulation and comparison with the experimental results

The resutls of simulation are presented in this section and compared with the experimental results from the experimental part of this diploma thesis in chapter 4. As was described in Chapter 4 two experiments was conducted and two versions of the same reformer were constructed. The experimental results which presented to the follow table 5.2 are from the second version experiment of reformer and will be used for comparison with the simulation results here.

Table 5.2. Experimental results of wet syngas and pressure drop in soot trap in the second version experiment

λ	X'H2 %	X'co %	X'co2 %	X'ch4 %	X'H20 %	Dpsoottrap [Pa]
0,42	14,192 ±0,149	10,898 ±0,113	2,600 ±0,026	5,262 ±0,053	10,291 ±0,211	245 ±1,96
0,46	17,463 ±0,189	12,019 ±0,125	2,708 ±0,027	2,535 ±0,027	8,811 ±0,183	252 ±2,02
0,5	17,329 ±0,187	12,113 ±0,126	2,946 ±0,030	1,621 ±0,016	8,649 ±0,181	262 ±2,1
0,6	16,776 ±0,180	13,033 ±0,137	3,383 ±0,034	0,407 ±0,004	7,569 ±0,160	308 ±2,46

Case: 1.5 kW and λ=0.42

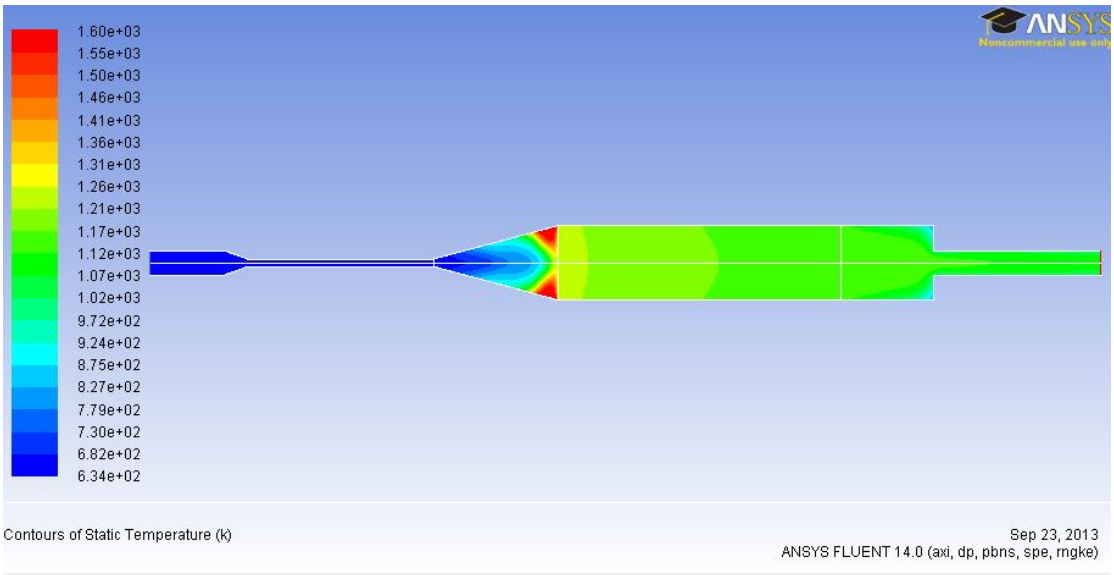

Fig.5.1 Contour of **temperature** for thermal power 1.5kW and air equivalence ratio 0.42

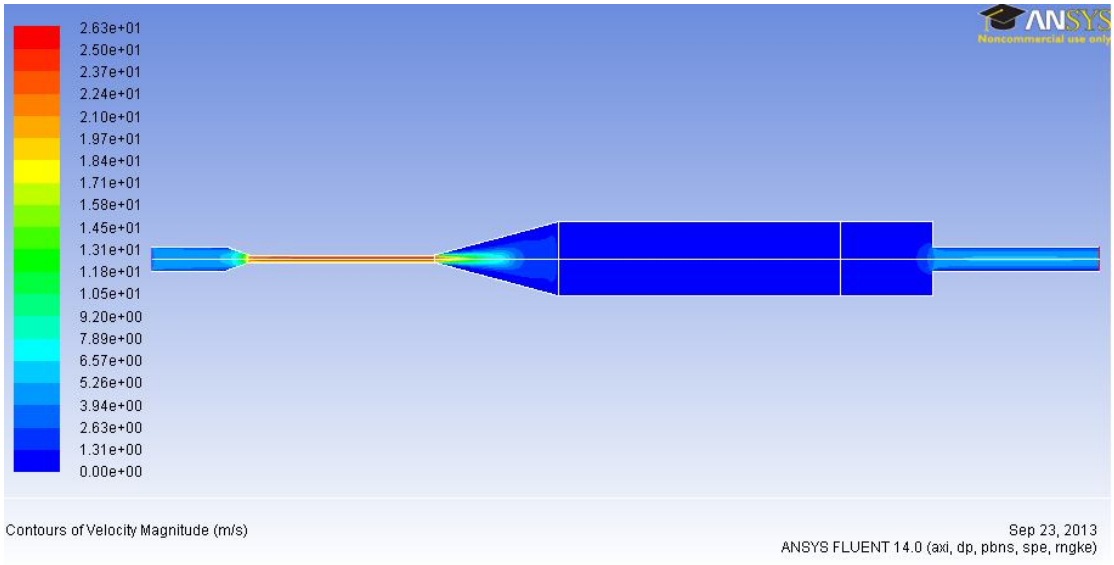

Fig.5.2 Contour of **velocity** for thermal power 1.5kW and air equivalence ratio 0.42

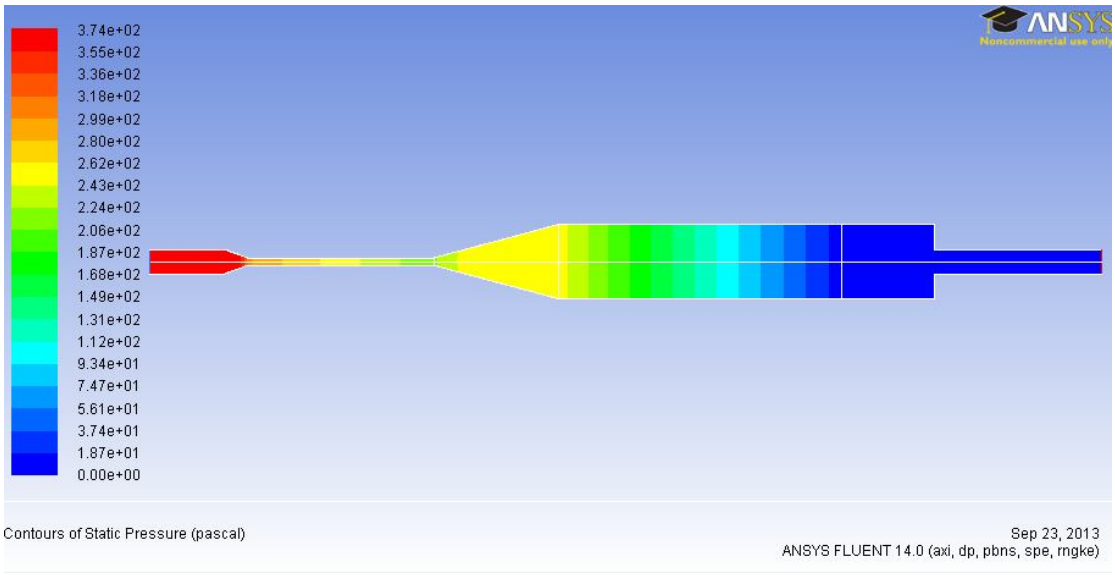

Fig.5.3 Contour of **pressure drop** for thermal power 1.5kW and air equivalence ratio 0.42

Table 5.3	Value of soottrap pressure drop [Pa]
Simulation	242.89
Experiment	245±1.96

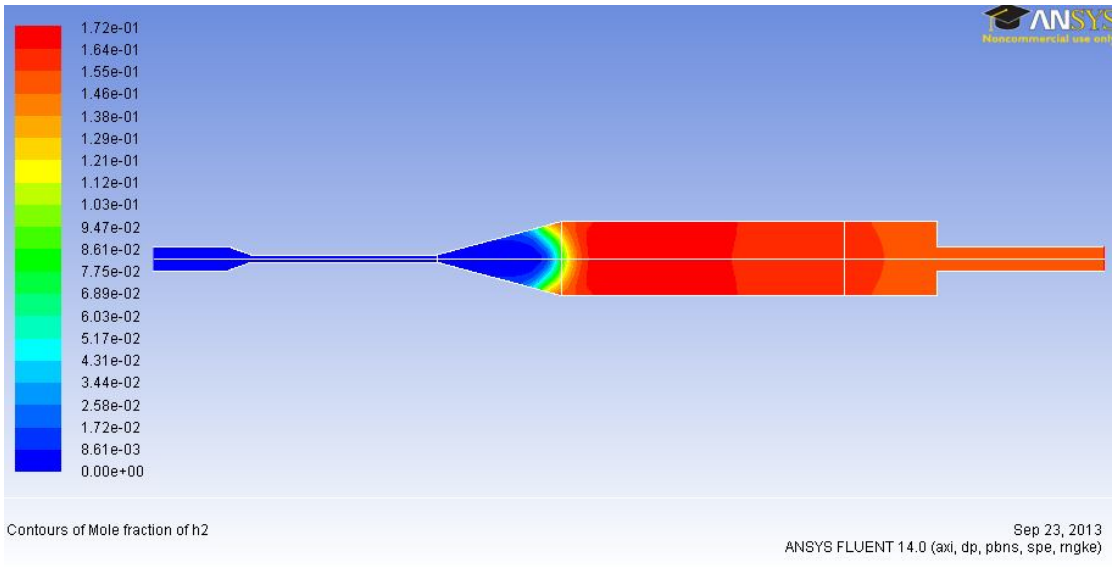

Fig.5.4 Contour of **H_2 volume fraction** for thermal power 1.5kW and air equivalence ratio 0.42

Table 5.4	Value of H2 volume fraction % at the exit
Simulation	15.50
Experiment	14.192±0.149

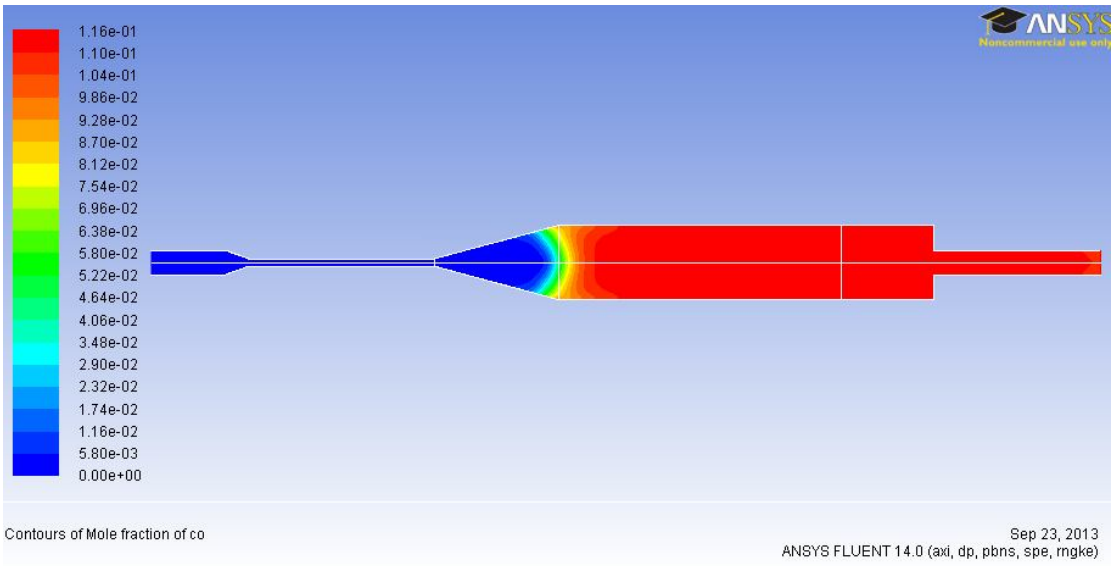

Fig.5.5 Contour of **CO volume fraction** for thermal power 1.5kW and air equivalence ratio 0.42

Table 5.5	Value of CO volume fraction % at the exit
Simulation	11.6
Experiment	10.898±0.113

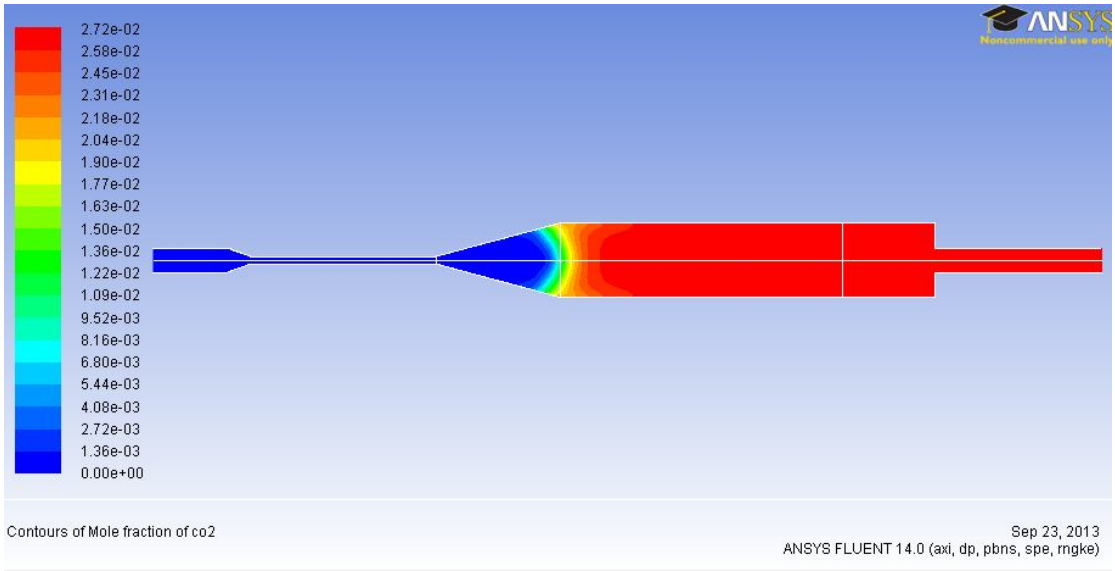

Fig.5.6 Contour of **CO_2 volume fraction** for thermal power 1.5kW and air equivalence ratio 0.42

Table 5.6	Value of CO2 volume fraction % at the exit
Simulation	2.72
Experiment	2.600±0.026

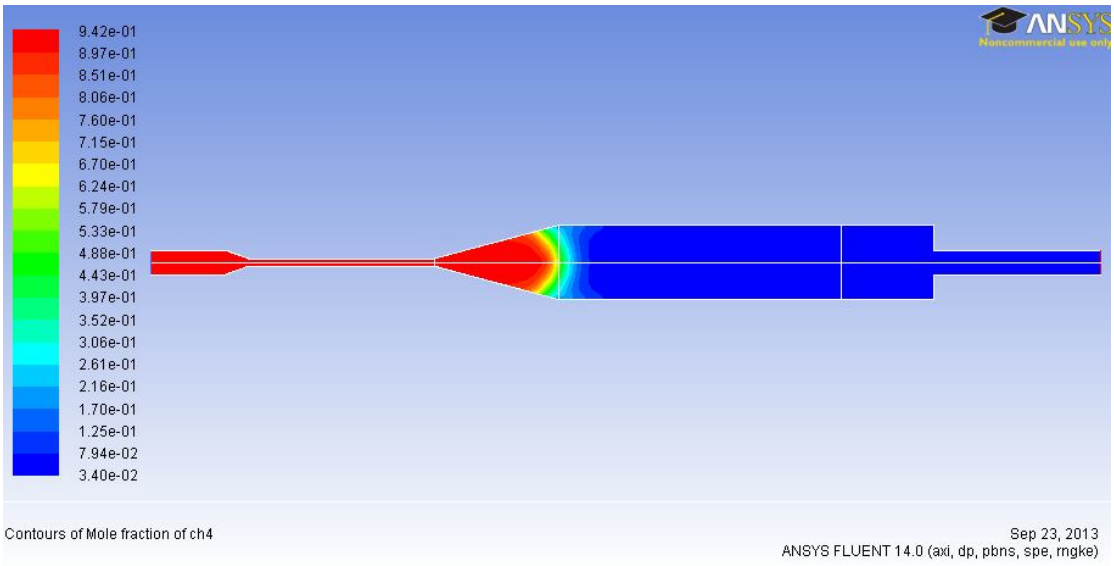

Fig.5.7 Contour of **CH_4 volume fraction** for thermal power 1.5kW and air equivalence ratio 0.42

Table 5.7	Value of CH4 volume fraction % at the exit
Simulation	7.9
Experiment	5.262±0.053

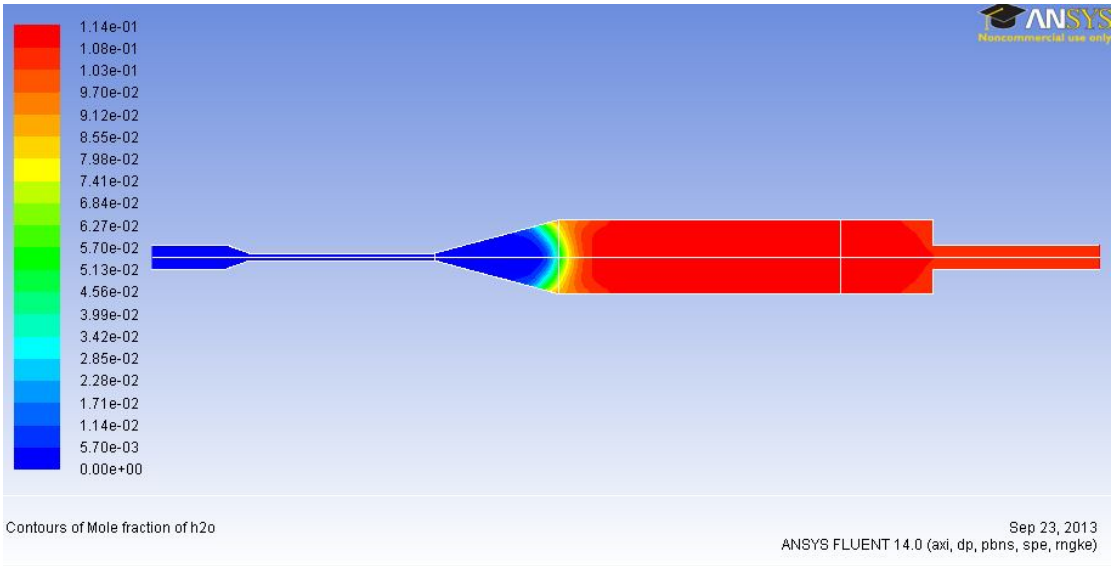

Fig.5.8 Contour of **H_2O volume fraction** for thermal power 1.5kW and air equivalence ratio 0.42

Table 5.8	Value of H_2O volume fraction % at the exit
Simulation	10.83
Experiment	10.291±0.211

Case: 1.5 kW and λ=0.46

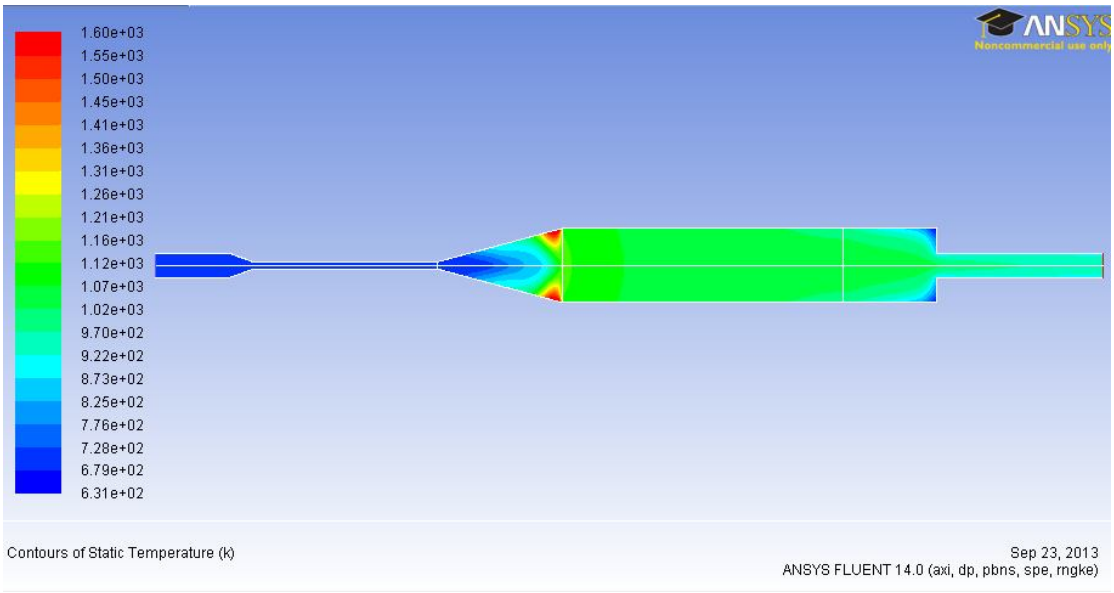

Fig.5.9 Contour of **temperature** for thermal power 1.5kW and air equivalence ratio 0.46

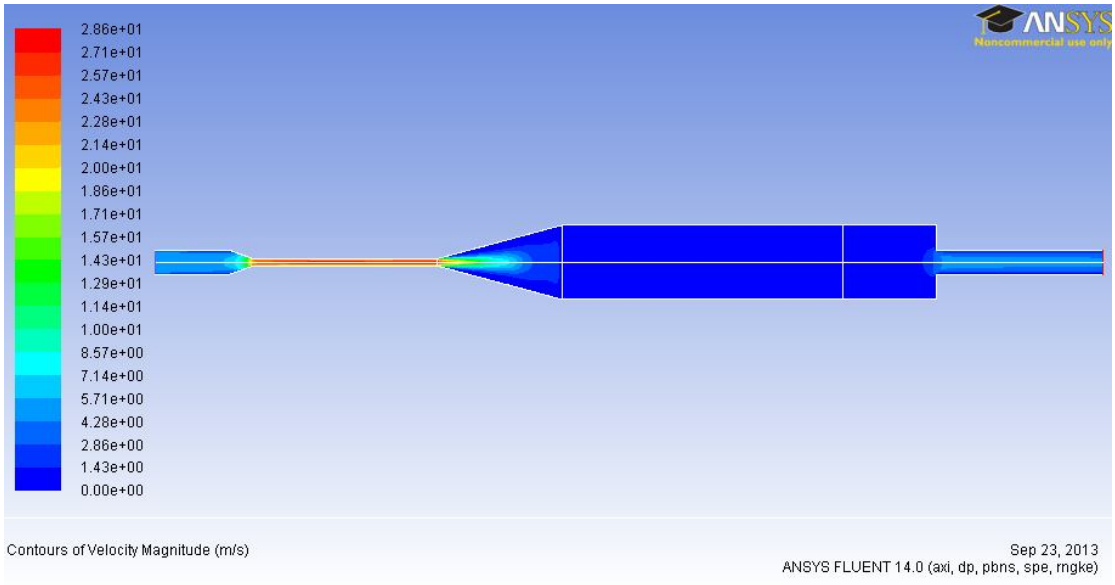

Fig.5.10 Contour of **velocity** for thermal power 1.5kW and air equivalence ratio 0.46

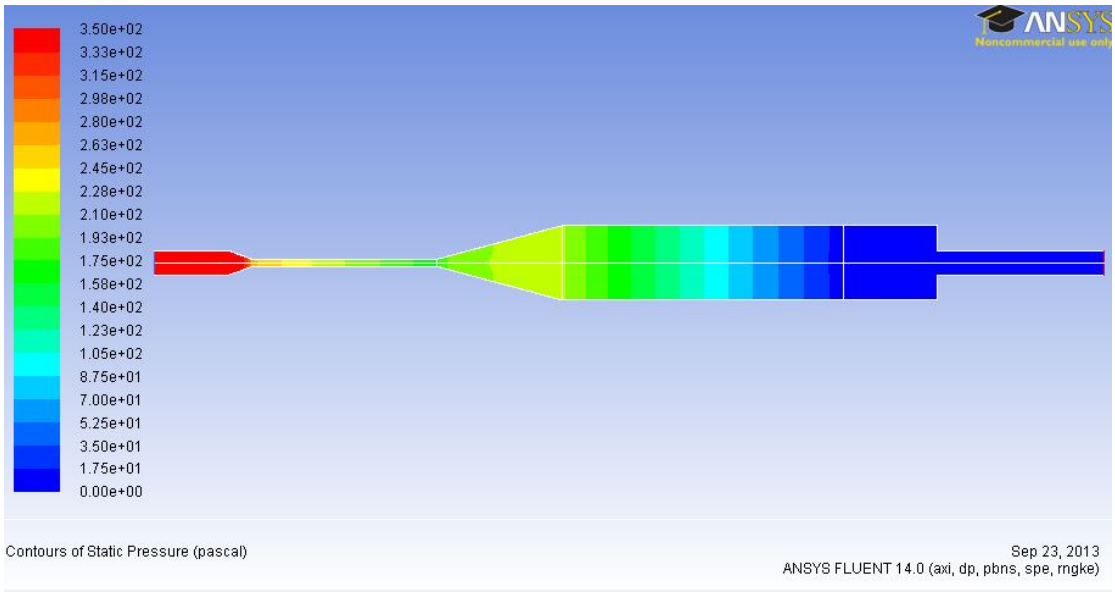

Fig.5.11 Contour of **pressure drop** for thermal power 1.5kW and air equivalence ratio 0.46

Table 5.9	Value of soottrap pressure drop [Pa]
Simulation	210.6
Experiment	252±2.02

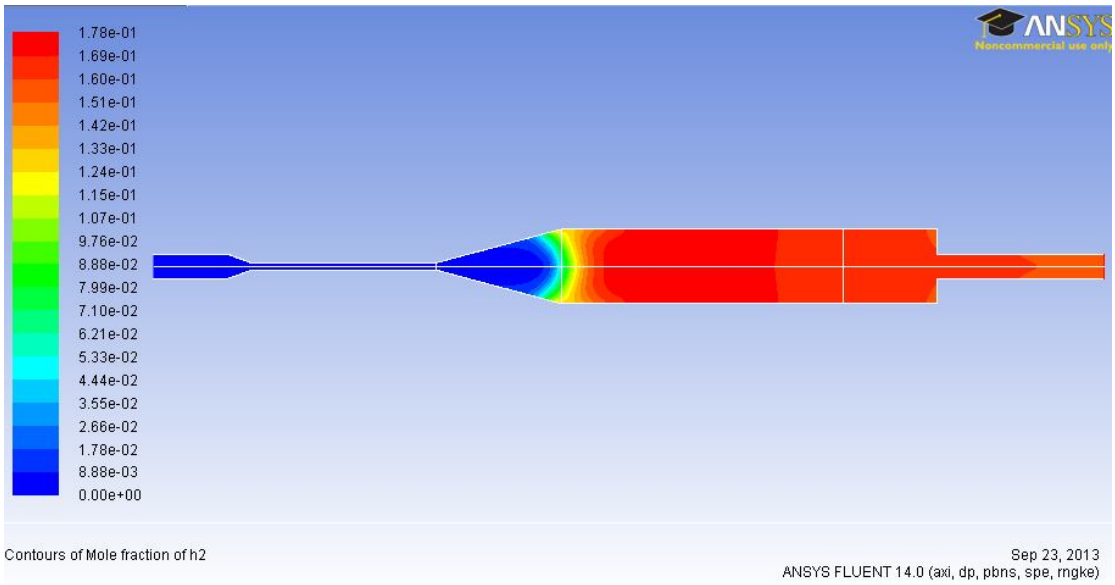

Fig.5.12 Contour of **H_2 volume fraction** for thermal power 1.5kW and air equivalence ratio 0.46

Table 5.10	Value of H2 volume fraction % at the exit
Simulation	16.00
Experiment	17.493±0.189

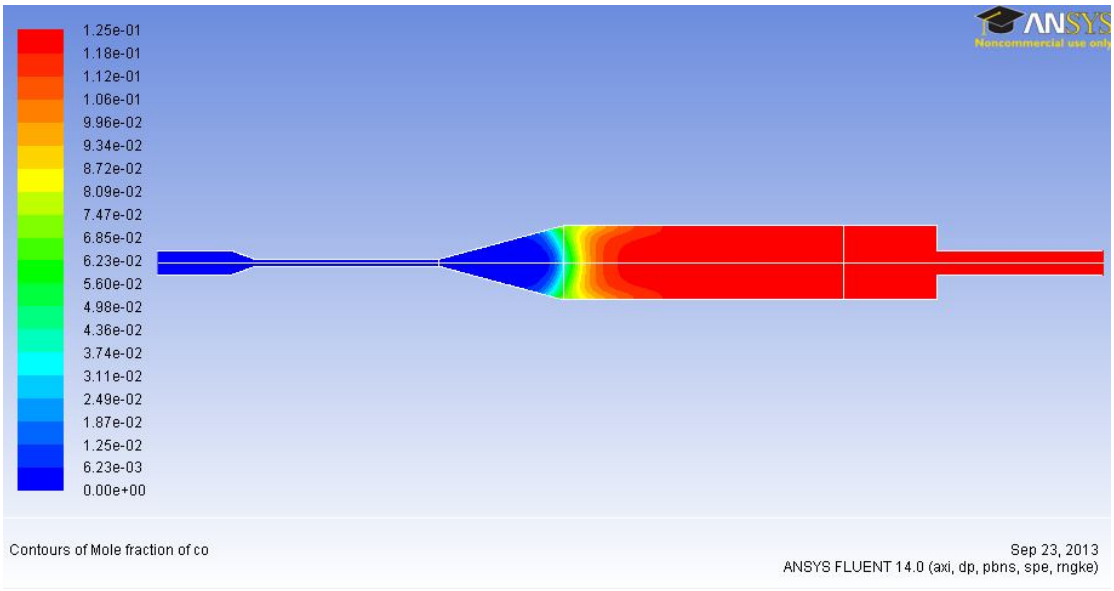

Fig.5.13 Contour of **CO volume fraction** for thermal power 1.5kW and air equivalence ratio 0.46

Table 5.11	Value of CO volume fraction % at the exit
Simulation	12.45
Experiment	12.019±0.125

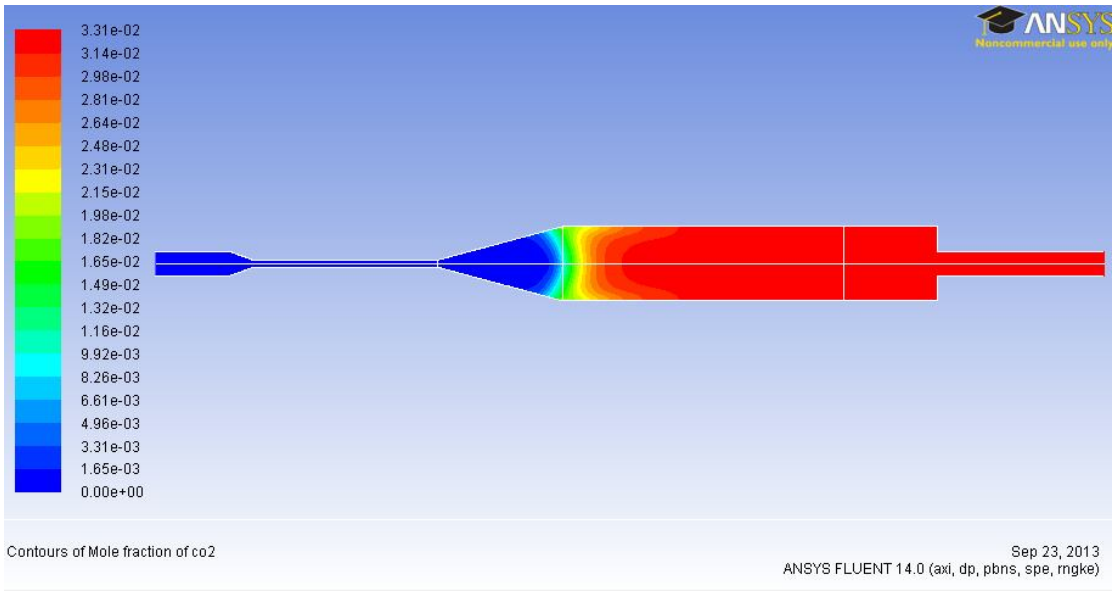

Fig.5.14 Contour of **CO_2 volume fraction** for thermal power 1.5kW and air equivalence ratio 0.46

Table 5.12	Value of CO2 volume fraction % at the exit
Simulation	3.3
Experiment	2.708±0.027

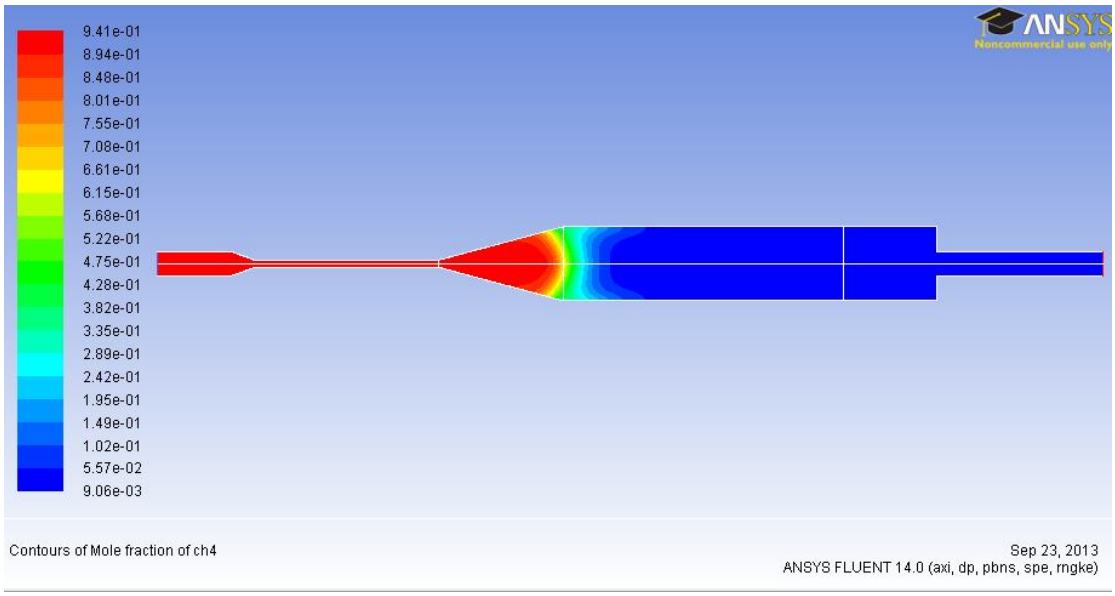

Fig.5.15 Contour of **CH_4 volume fraction** for thermal power 1.5kW and air equivalence ratio 0.46

Table 5.13	Value of CH4 volume fraction % at the exit
Simulation	5.57
Experiment	2.535±0.027

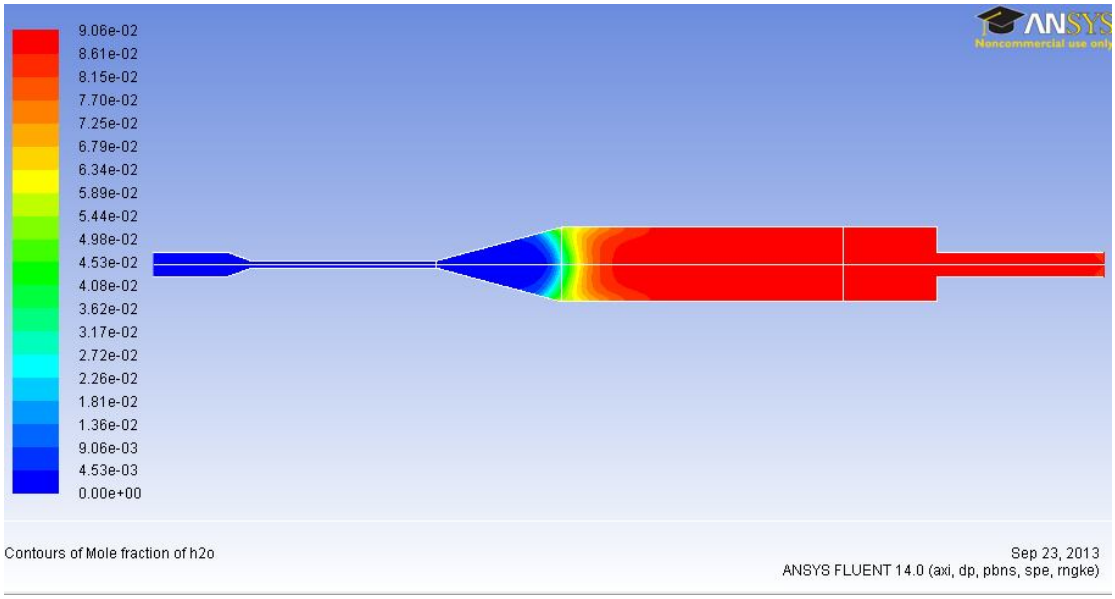

Fig.5.16 Contour of **H_2O volume fraction** for thermal power 1.5kW and air equivalence ratio 0.46

Table 5.14	Value of H_2O volume fraction % at the exit
Simulation	9.05
Experiment	8.811±0.183

Case: 1.5 kW and λ=0.5

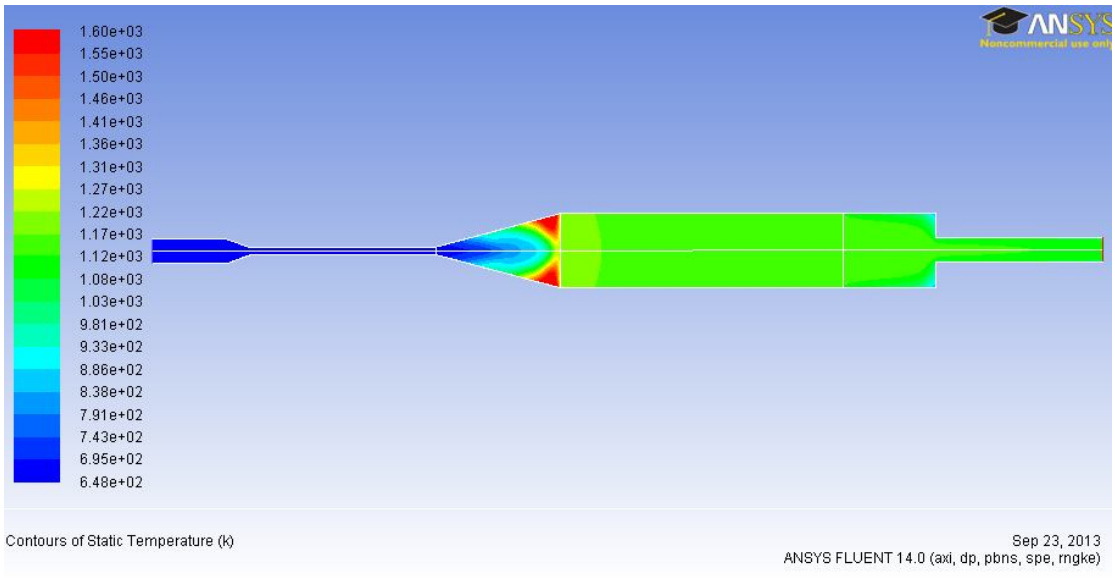

Fig.5.17 Contour of **temperature** for thermal power 1.5kW and air equivalence ratio 0.5

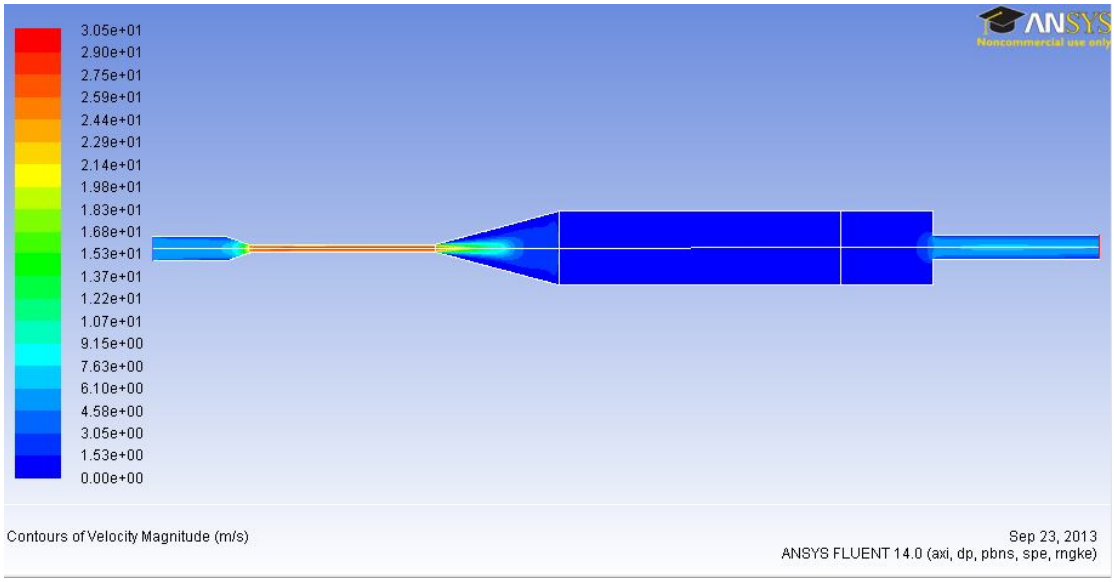

Fig.5.18 Contour of **velocity** for thermal power 1.5kW and air equivalence ratio 0.5

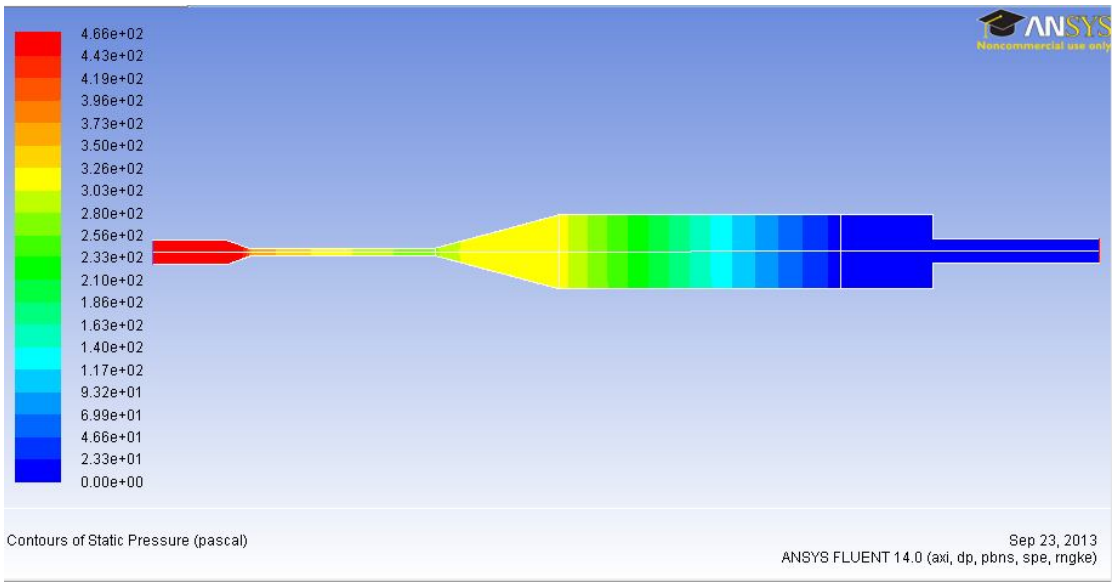

Fig.5.19 Contour of **pressure drop** for thermal power 1.5kW and air equivalence ratio 0.5

Table 5.15	Value of soottrap pressure drop [Pa]
Simulation	302.92
Experiment	262±2.10

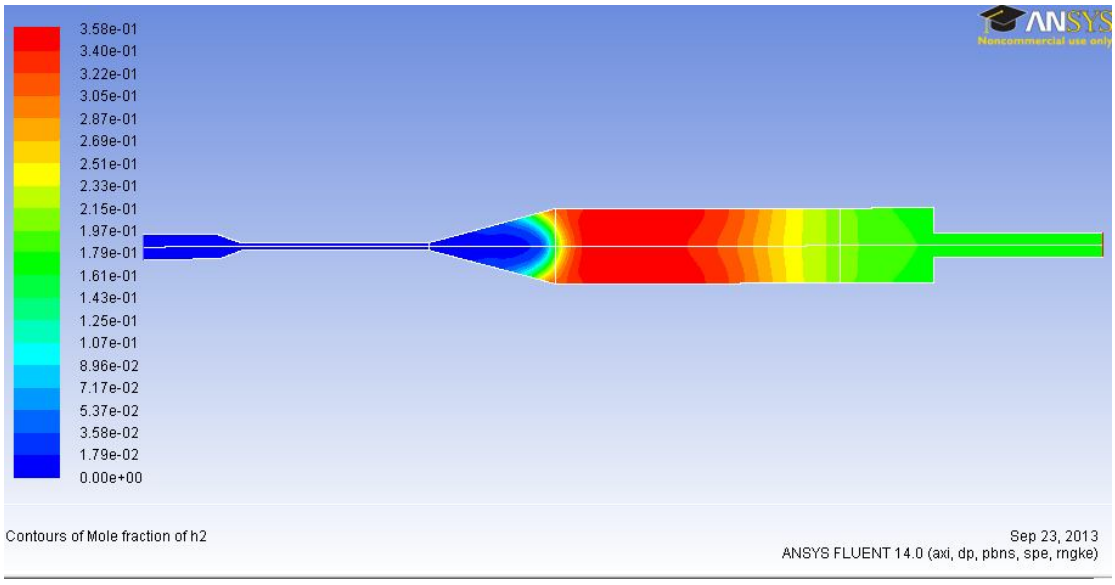

Fig.5.20 Contour of **H_2 volume fraction** for thermal power 1.5kW and air equivalence ratio 0.5

Table 5.16	Value of H2 volume fraction % at the exit
Simulation	17.92
Experiment	17.329±0.187

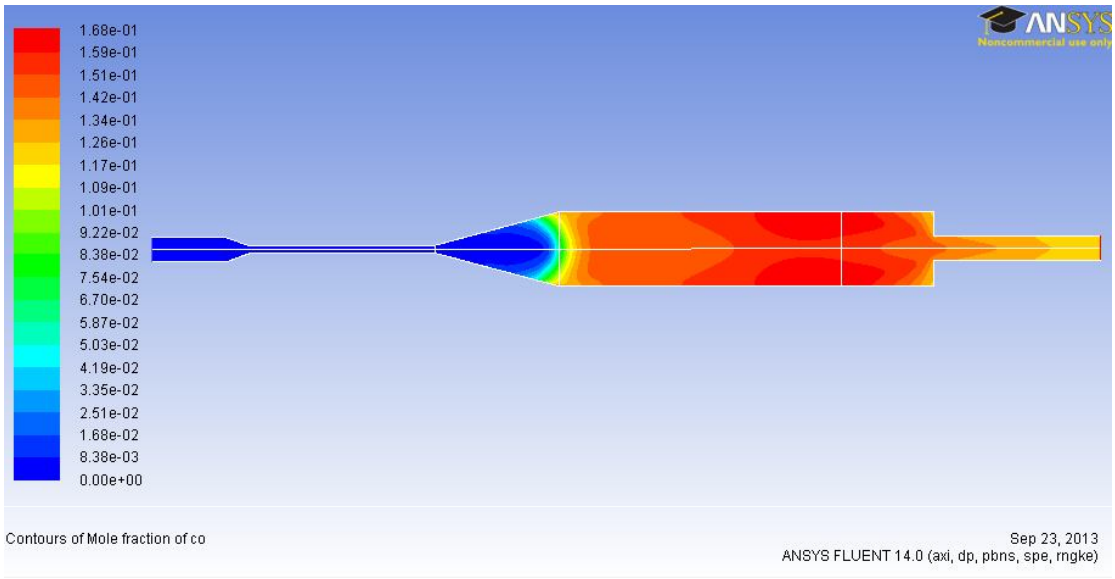

Fig.5.21 Contour of **CO volume fraction** for thermal power 1.5kW and air equivalence ratio 0.5

Table 5.17	Value of CO volume fraction % at the exit
Simulation	12.57
Experiment	12.113±0.126

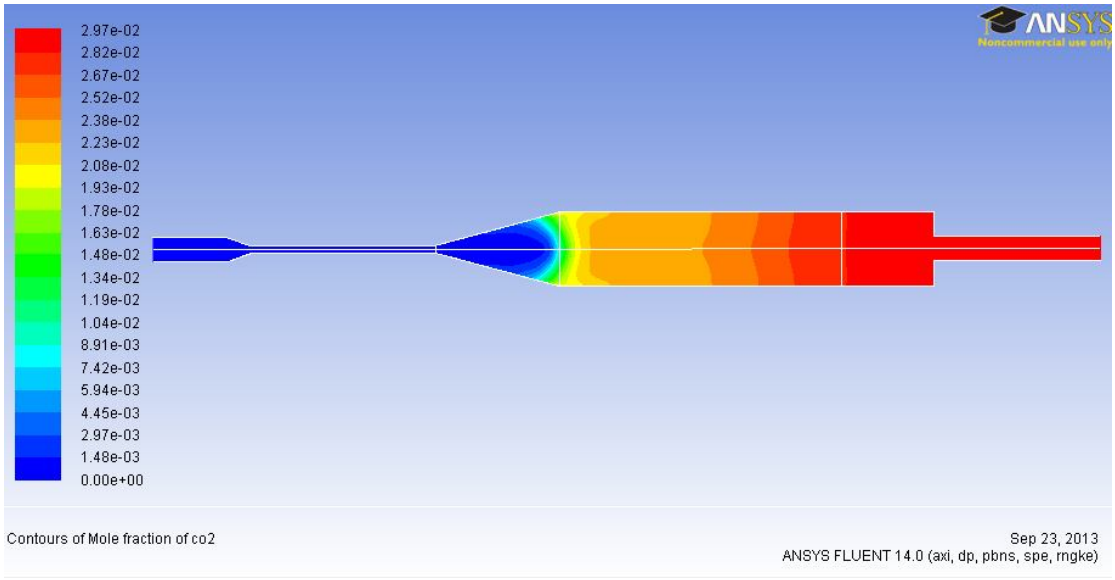

Fig.5.22 Contour of **CO_2 volume fraction** for thermal power 1.5kW and air equivalence ratio 0.5

Table 5.18	Value of CO2 volume fraction % at the exit
Simulation	2.97
Experiment	2.946±0.030

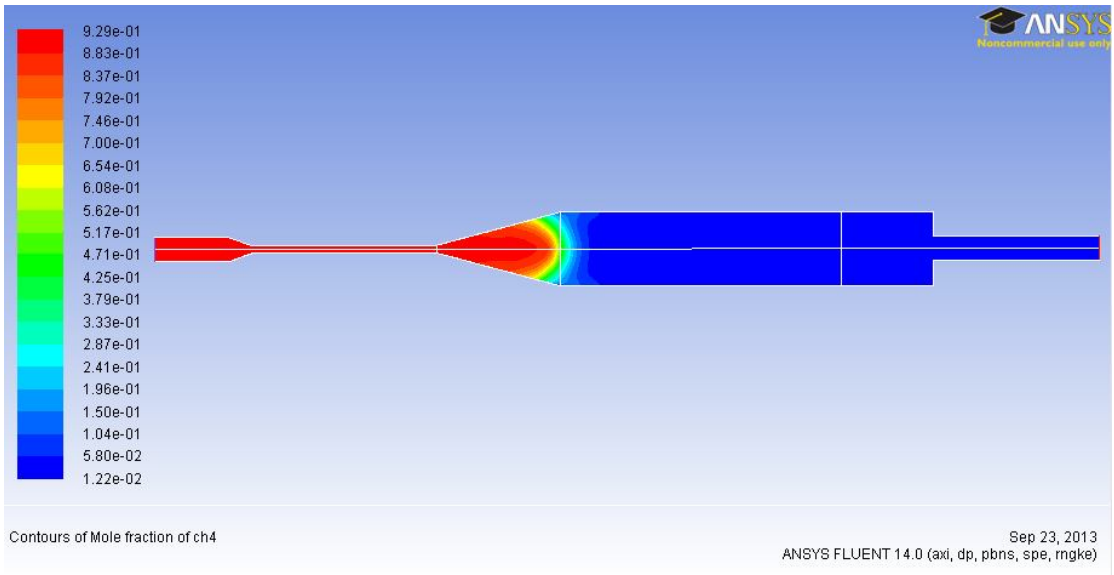

Fig.5.23 Contour of **CH_4 volume fraction** for thermal power 1.5kW and air equivalence ratio 0.5

Table 5.19	Value of CH4 volume fraction % at the exit
Simulation	5.8
Experiment	1.621±0.016

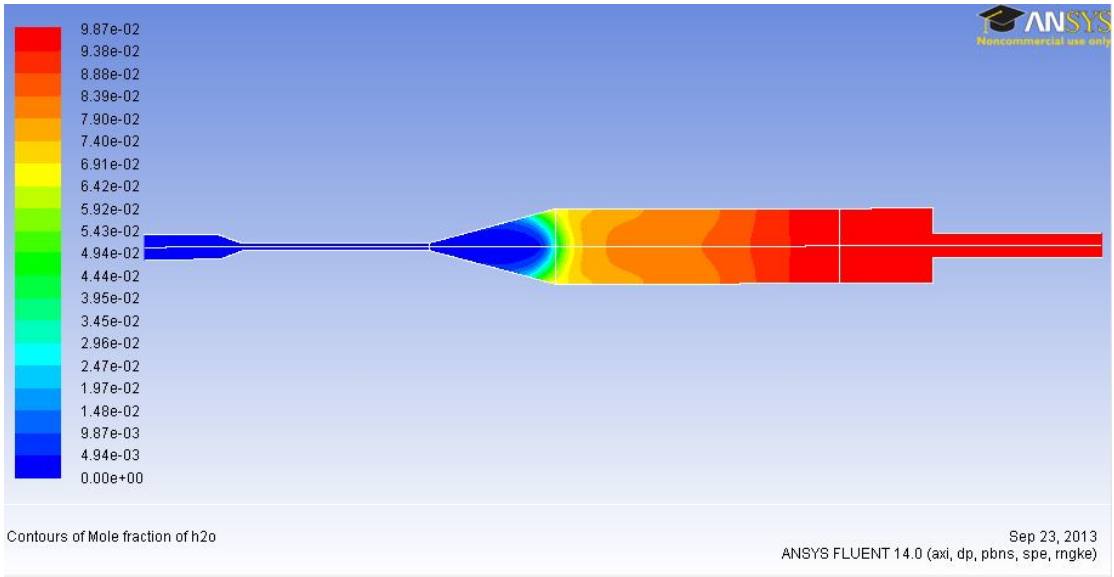

Fig.5.24 Contour of **H_2O volume fraction** for thermal power 1.5kW and air equivalence ratio 0.5

Table 5.20	Value of H_20 volume fraction % at the exit
Simulation	9.87
Experiment	8.649±0.181

Case: 1.5 kW and λ=0.6

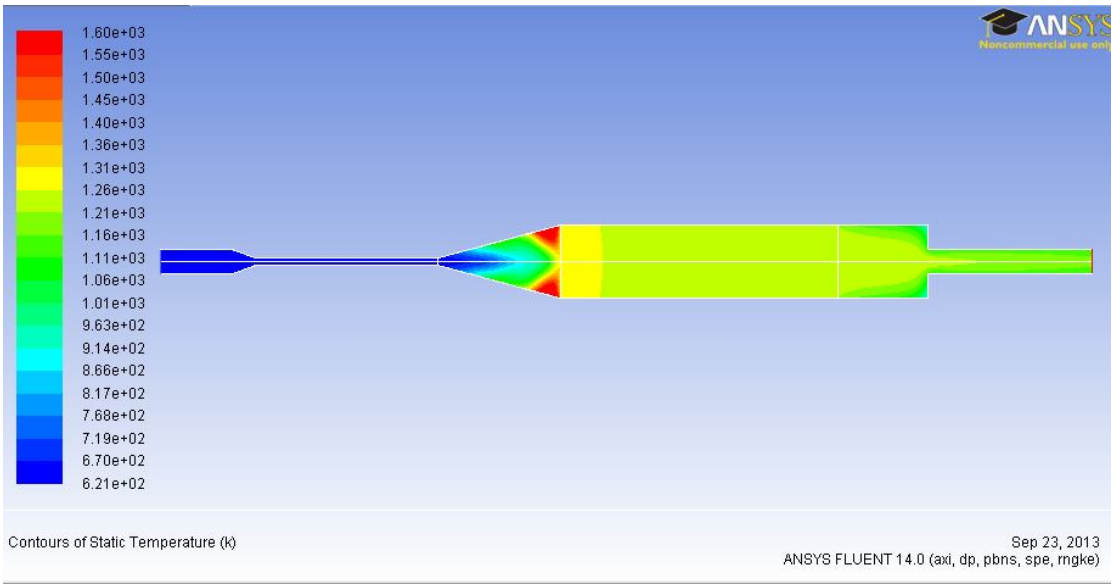

Fig.5.25 Contour of **temperature** for thermal power 1.5kW and air equivalence ratio 0.6

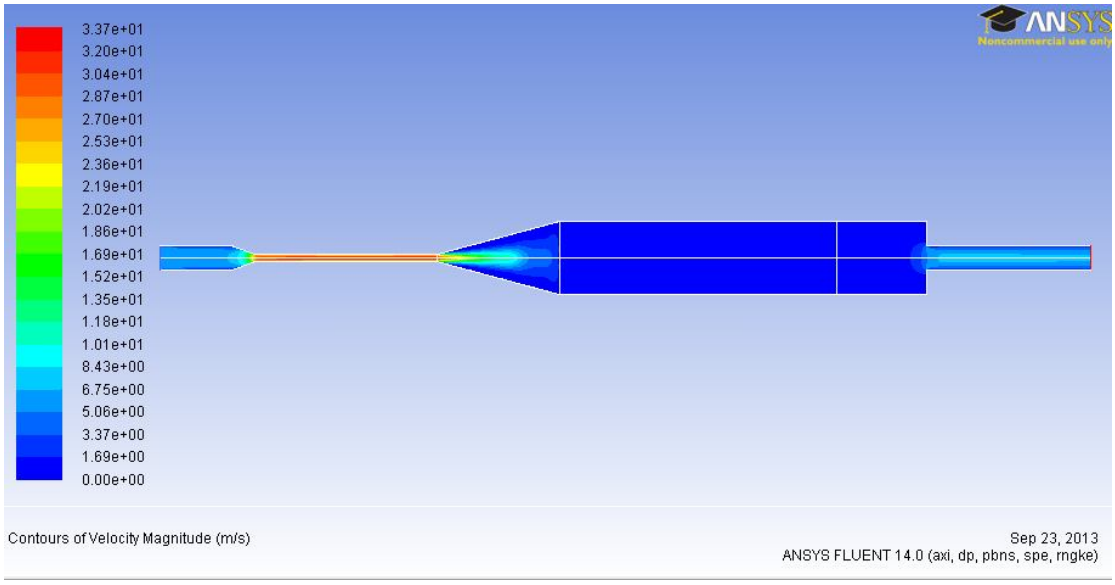

Fig.5.26 Contour of **velocity** for thermal power 1.5kW and air equivalence ratio 0.6

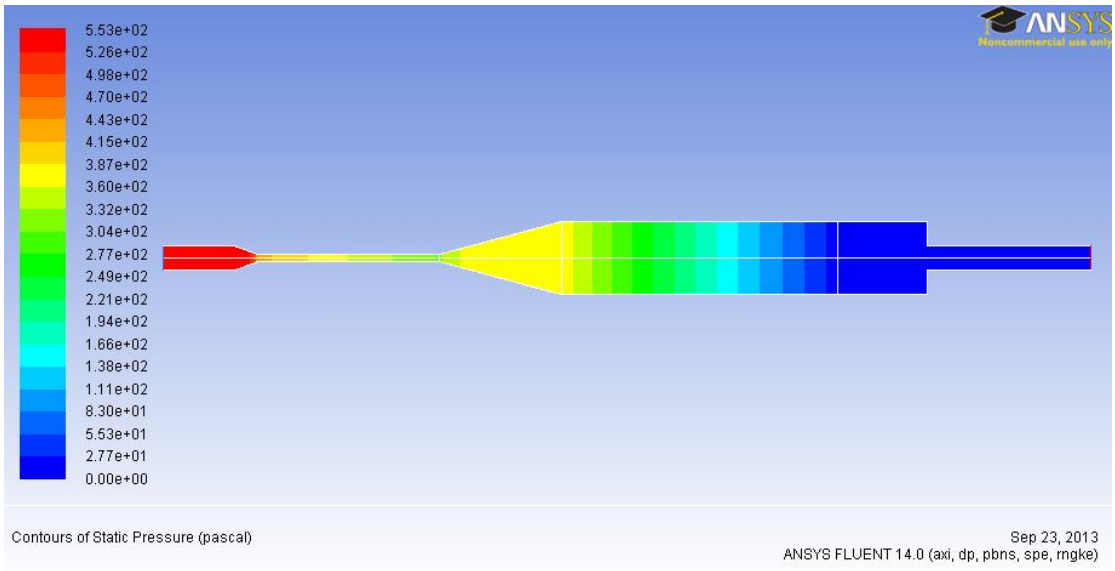

Fig.5.27 Contour of **pressure drop** for thermal power 1.5kW and air equivalence ratio 0.6

Table 5.21	Value of soottrap pressure drop [Pa]
Simulation	359.66
Experiment	308±2.46

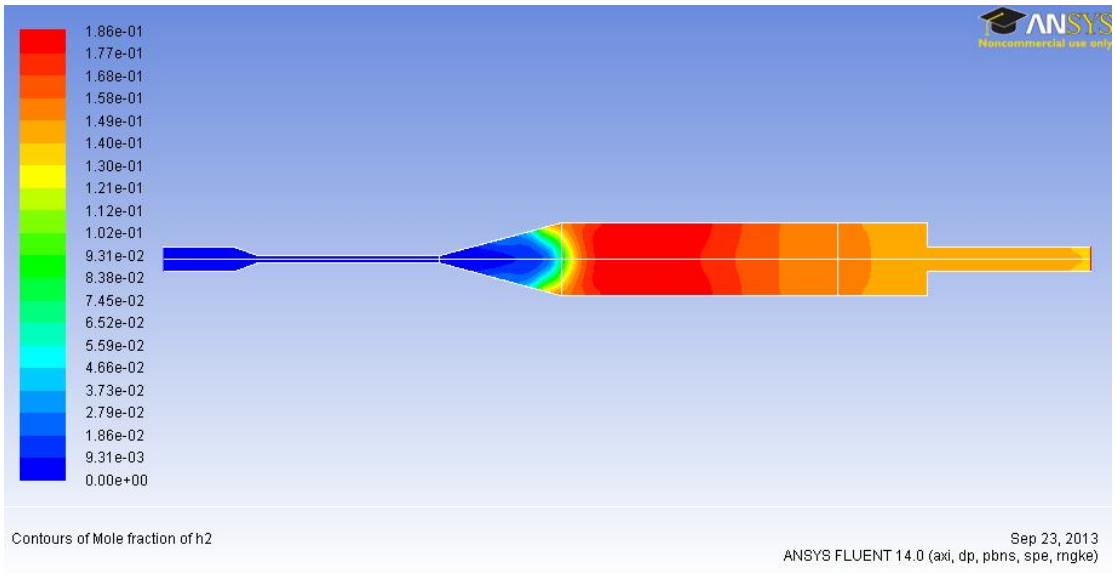

Fig.5.28 Contour of **H_2 volume fraction** for thermal power 1.5kW and air equivalence ratio 0.6

Table 5.22	Value of H2 volume fraction % at the exit
Simulation	14.9
Experiment	16.776±0.180

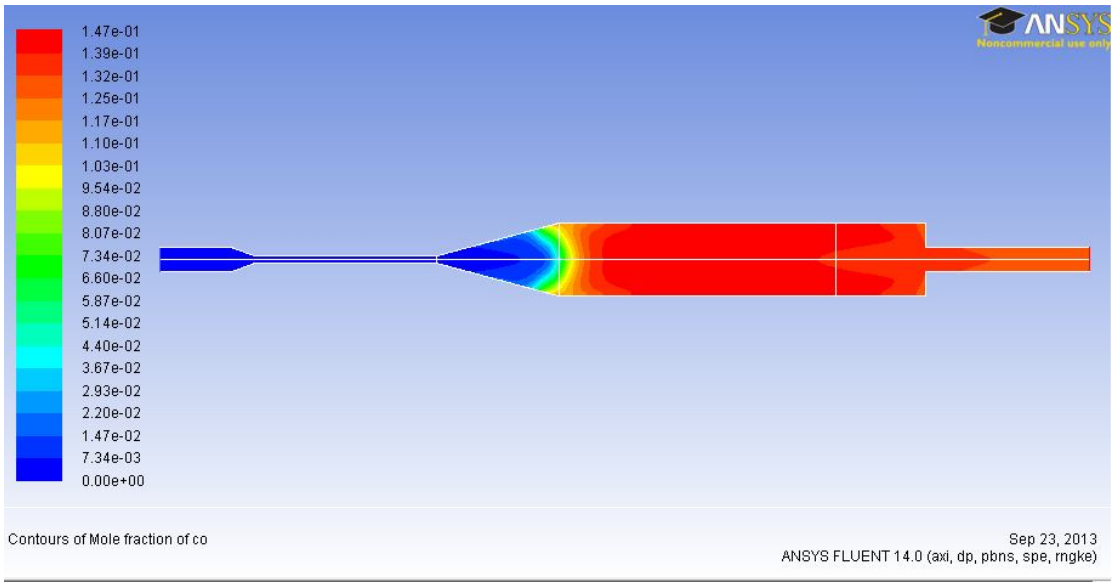

Fig.5.29 Contour of **CO volume fraction** for thermal power 1.5kW and air equivalence ratio 0.6

Table 5.23	Value of CO volume fraction % at the exit
Simulation	13.2
Experiment	13.033±0.137

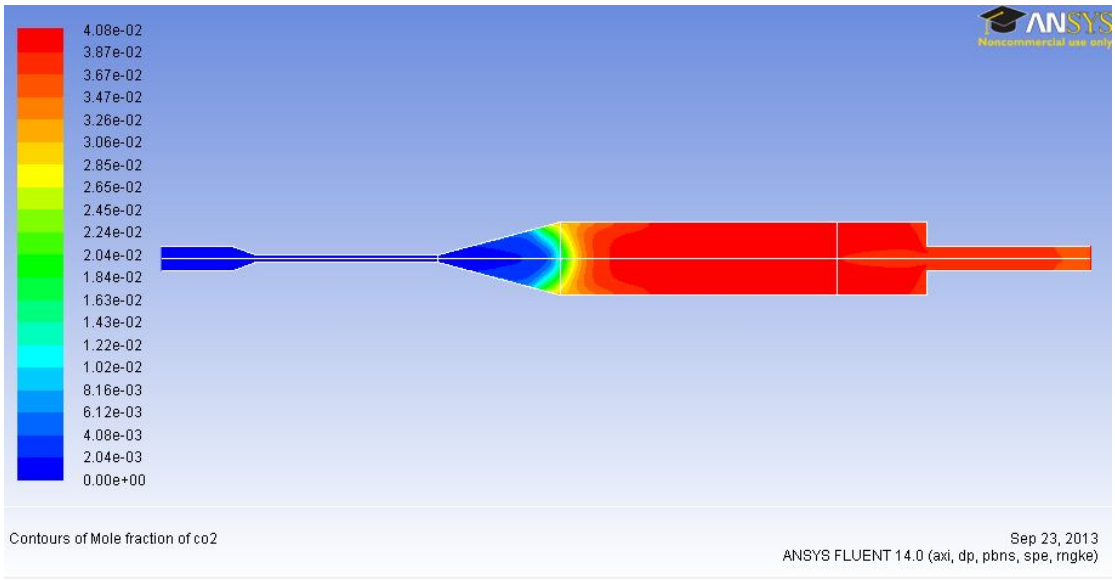

Fig.5.30 Contour of **CO_2 volume fraction** for thermal power 1.5kW and air equivalence ratio 0.6

Table 5.24	Value of CO2 volume fraction % at the exit
Simulation	3.67
Experiment	3.383±0.034

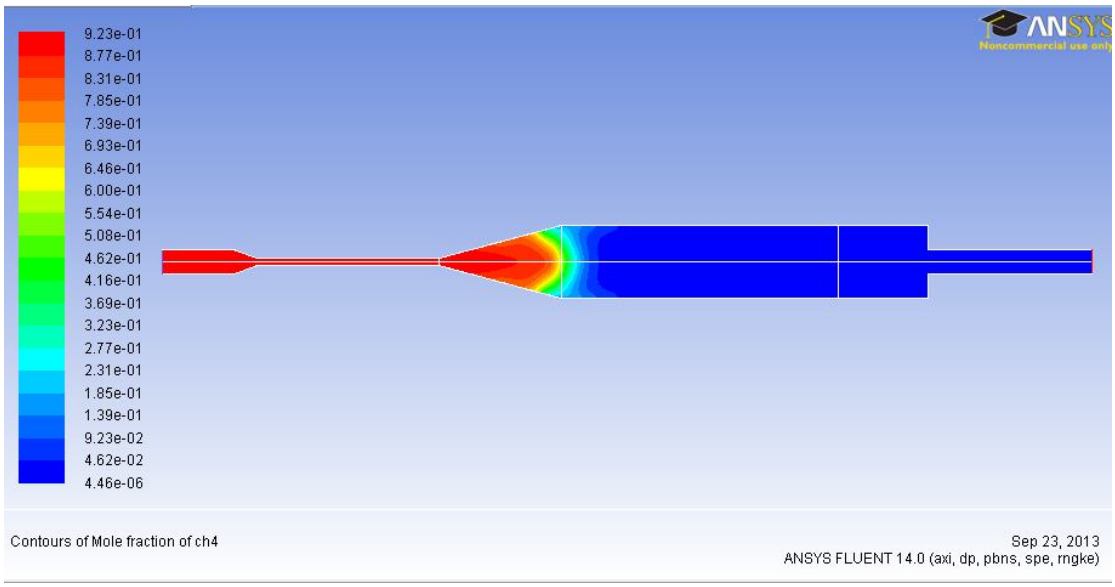

Fig.5.31 Contour of **CH_4 volume fraction** for thermal power 1.5kW and air equivalence ratio 0.6

Table 5.25	Value of CH4 volume fraction % at the exit
Simulation	4.61
Experiment	0.407±0.004

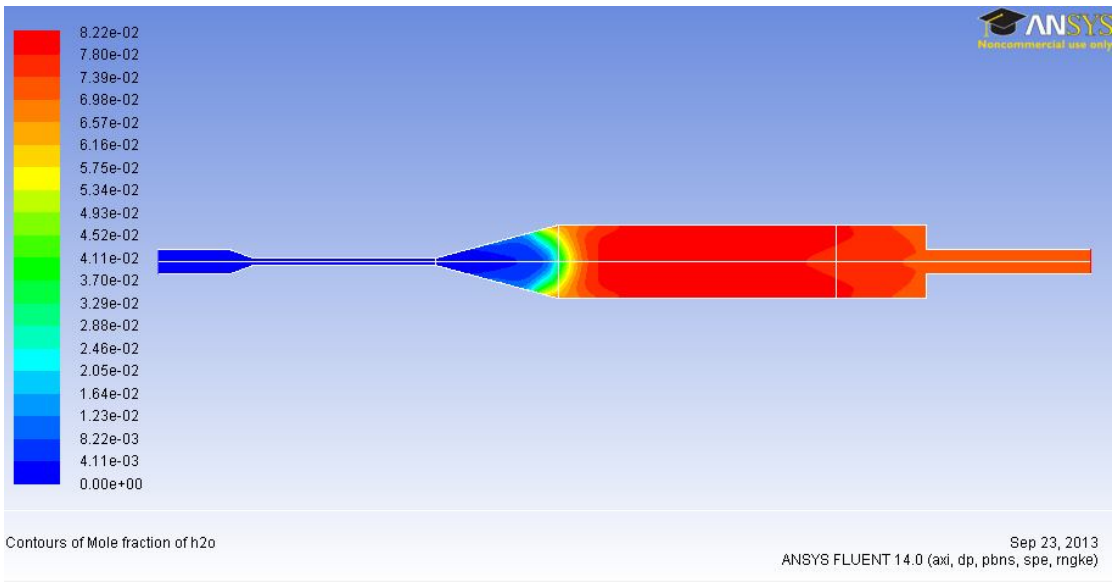

Fig.5.32 Contour of **H_2O volume fraction** for thermal power 1.5kW and air equivalence ratio 0.6

Table 5.26	Value of CH4 volume fraction % at the exit
Simulation	7.39
Experiment	7.569±0.160

Diagrams for comparison between the cases

In the figures below are presented the experimental and simulated results for each chemical species as well as the pressure drop in the soot trap. The sampling of the experimental measurements was at the exit of the reformer and the values of simulated results were taken at the same position in the domain. The results are shown that the reduced GRI-MECH DRM19 is able to predict the most of the chemical species volume fractions sufficiently except from the case of methane where the values are over predicted. This could be attributed in that the reactions path of C_2 which consume the CH_4 and leads to the precursors of soot does not exist in this reduced mechanism. This is important since the cases which were simulated were understoichiometric. Furthermore the GRI-MECH DRM19 such as the most GRI-MECH are optimized for stoichiometric and lean combustion. It is also interesting to be observed that the tendency of the values from one case to another in most cases follows the experimental tendency in a good manner. Furthermore, it can be observed in figure 3.61 that the pressure drop was sufficiently predicted by the simulating of the soot trap as porous packed bed according to the paragraph 3.6.2. However the non real geometry of soot trap domain, allowed the convergence of the front of flame more downstream in comparison with the experiment as it is observed from all the figures above.

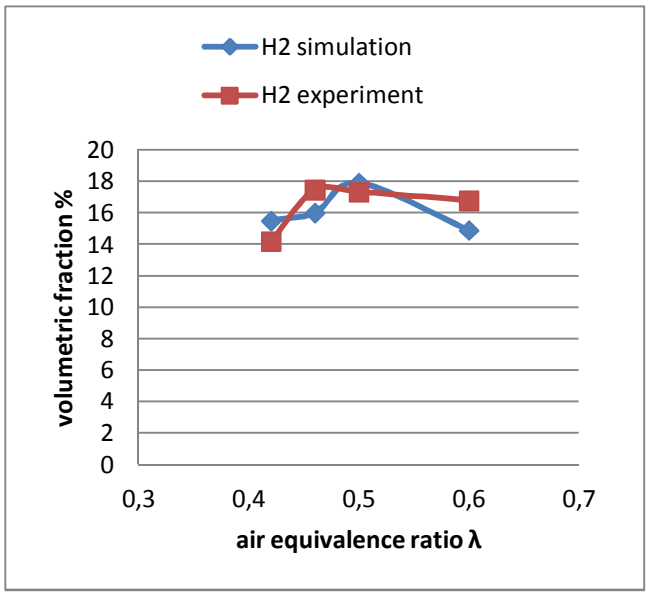

Fig.5.33: Comparison between experimental and simulation results of **H_2** , for thermal power 1.5kW and air equivalence ratios 0.42, 0.46, 0.5, 0.6

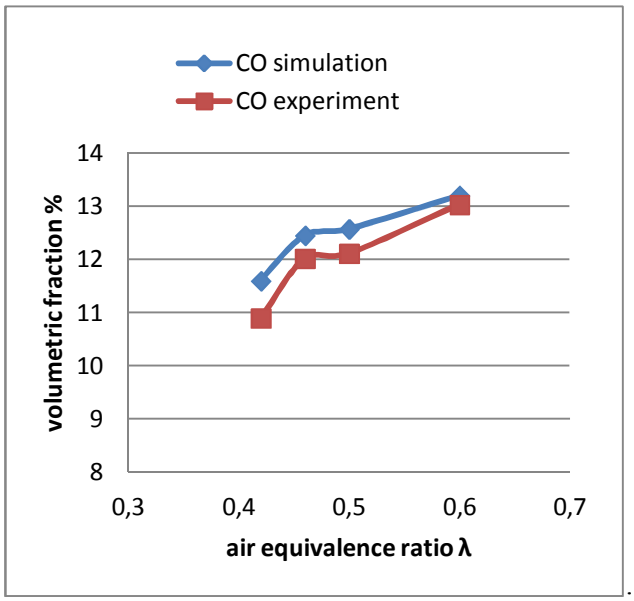

Fig.5.34: Comparison between experimental and simulation results of **CO** , for thermal power 1.5kW and air equivalence ratios 0.42, 0.46, 0.5, 0.6

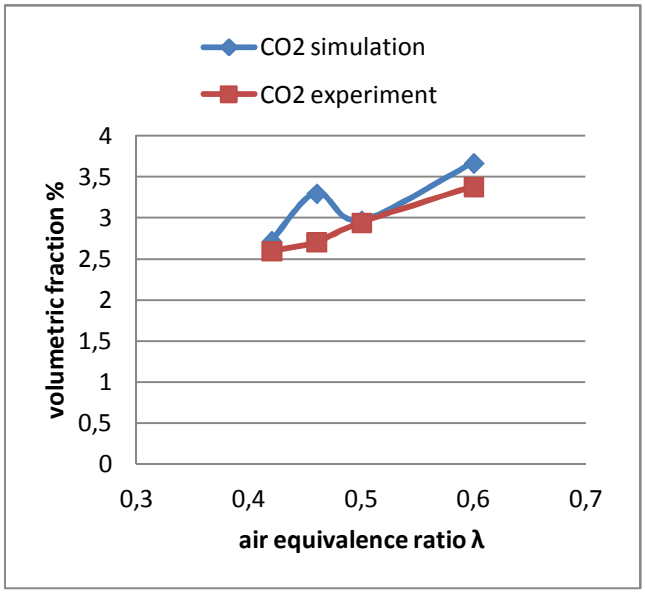

Fig.5.35: Comparison between experimental and simulation results of **CO_2** , for thermal power 1.5kW and air equivalence ratios 0.42, 0.46, 0.5, 0.6

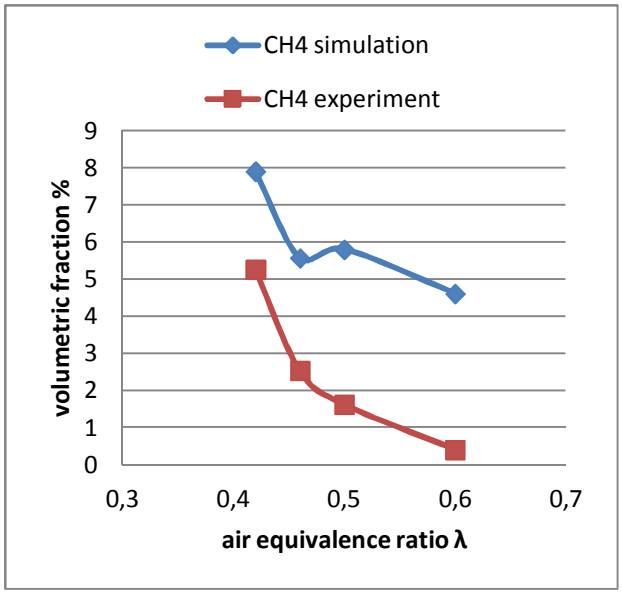

Fig.5.36: Comparison between experimental and simulation results of **CH_4** , for thermal power 1.5kW and air equivalence ratios 0.42, 0.46, 0.5, 0.6

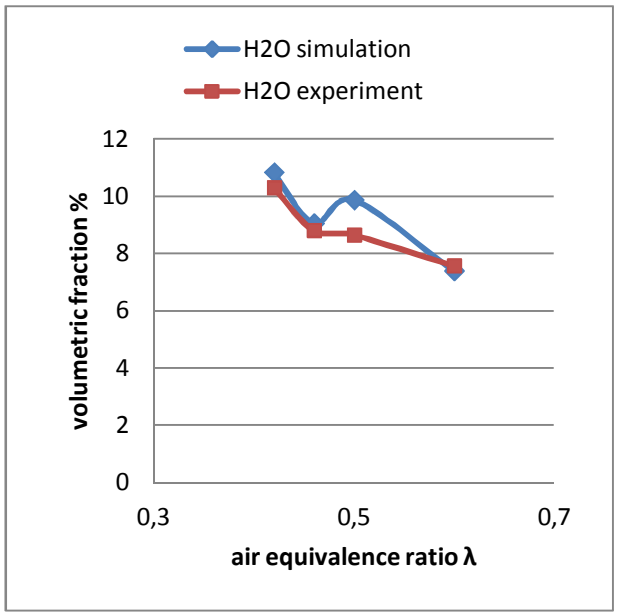

Fig.5.37: Comparison between experimental and simulation results of **H_2O** , for thermal power 1.5kW and air equivalence ratios 0.42, 0.46, 0.5, 0.6

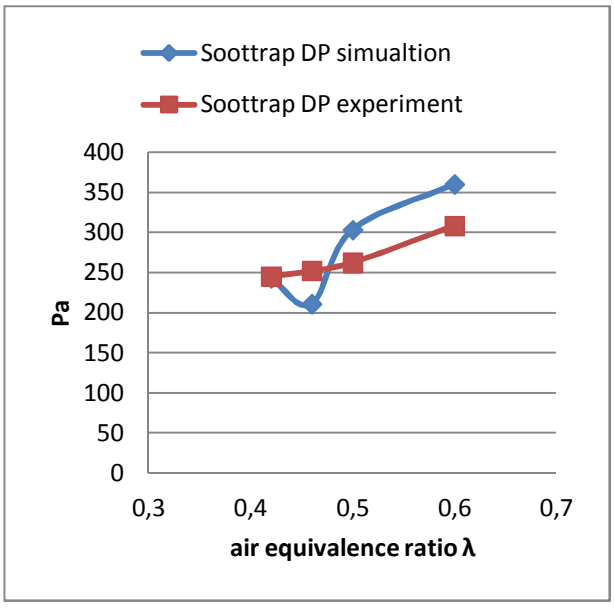

Fig.5.38: Comparison between experimental and simulation results of soottrap **pressure drop**, for thermal power 1.5kW and air equivalence ratios 0.42, 0.46, 0.5, 0.6

Chapter 6th:Summary, concluding remarks and outlook

An experimental and a numerical study was conducted for a thermal partial oxidation process of methane in a fuel reformer based on a wall flow filter or as so called soot trap. Since this diploma thesis relates with the reforming process which their characteristics enhanced by ceramic porous structures such as the soot trap, firstly a review in the hydrogen technology was realized and in particular in the reforming process, the role of porous media in such processes and a review of previous research works in the principles of combustion in porous media.

Thereafter, preliminary numerical simulations was conducted for the preparation of the numerical model of the reformer. In this stage was investigated the possibility to be simulated and the characteristics of a porous material in ANSYS. Two important parameters, the particle porous diameter and the porosity, was needed for the determination of coefficients which need for porous packed bed simulation. A parameterization study was conducted aiming to reveal their influence in the flow field.

An algebraic model of Konstandopoulos and Johnson for the prediction of pressure drop of wall flow filters were studied. By the combination of this model equations, with the equation of pressure drop for porous packed bed in ANSYS, was achieved to be simulated the soot trap as porous packed bed in ANSYS where the needed coefficients based on the real characteristics of the soot trap. The second numerical simulation in this thesis was conducted in order to verify that the pressure drop predictions of Konstandopoulos and Johnson model is in a good agreement with the results of pressure drop in a porous packed bed domain in ANSYS where its coefficients based on soot trap characteristics. The results for an isothermal air flow stream in 500^{o}C and for 17, 27, 35 [lt/min] volumetric flow rates, were shown good agreement, however for higher volumetric flow rates seems to be deviated.

Results from experimental investigations on a TPOX wall flow filter based reformer running on methane have been presented too. The reformer has been designed with the aim of having a stationary TPOX process, which is accomplished within a single component geometry. This geometry consists of two sections, a conical one, which enables a self-adjustment in the position of the stationary combustion zone depending on operating conditions and a cylindrical one where slow endothermic reforming reactions take place inside of the soot trap. It is chosen a small diameter tube for reactants' inlet aiming to increase the momentum and to prevent the possibilities of flash back since the thermal load would be low and therefore the velocities. The same design of the reformer was constructed twice and two version experiments were conducted.

In the first version experiment the operating range of reformer were investigated and the temperature profiles, chemical species volume fractions and pressure drops in the reformer and in the soot trap were recorded. The temperature profiles revealed the stabilization of flame within the conical section for thermal loads 1,5 to 2 kW ,the hydrogen reaches the yield of about 20% and 14% for carbon oxide in the dry syngas, for thermal load 1,5kW and for air equivalence ratio in the range of 0,45 to 0,52.

In the second version experiment and in particular for the thermal load of 1,5 kW and for air equivalence ratio in the range of 0,4 to 0,6, the soot point as well as the soot regeneration were

investigated. Furthermore, a soot measurement sampling system were incorporated in the experimental set up and particles concentrations for each case were measured. The results showed that the soot point detected for air equivalence ratio 0,42 and temperature about 1200 ^{o}C where the soot trap was loaded by soot. The pressure drop was an indirect index for this ascertainment but further the decreasing in the volume fraction of acetylene is an evidence of soot formation, because it correlates with a path of reactions for soot formation and for this reason concerning as the main precursor of soot. The regeneration was observed for air equivalence ratio 0,5 and temperature about 1300^{o}C, and this was reflected in all measurements. The soot trap pressure drop was decreased, the concentration of measured particles were increased because of the disintegration of the soot agglomerates, and further the Boudouard reactions appears to be activated as was expected since the water volume fraction was decreased. In particular, in the regeneration stage the particulate emissions were higher and the measured value was $3{,}33*10^{9}$ [particles/cm^{3}]. Furthermore the measured volume fractions shows that hydrogen reaches the yield of about 20% and 13,5% for carbon oxide in the dry syngas as in the first version experiment. The amount of water and therefore the wet syngas, was calculated by the balance of oxygen. In concerning the efficiency of the reformer, a 47% was reached for 1,5 kW thermal load and 0,5 air equivalence ratio in operation conditions where no soot was existing. However, decreasing of efficiency was observed for air equivalence ratio 0,42 where the soot point appears and a sharp increasing of efficiency to 56% during the regeneration for air equivalence ratio to 0,6 was observed as was expected due to the more production of hydrogen and carbon oxide from Boudouard reactions.

The results showed that efficiency of the reformer based on a wall flow filter was notable and the regeneration was feasible. However, the design of the reformer was for low thermal loads and cases for higher thermal loads were not investigated. Therefore of a future work, it is possible in a bigger reformer of this type, for higher thermal loads the soot point to be reduced in lower air equivalence ratios of 0,42 and in combined with an optimization design, the efficiency could be increased remarkable. Since the reformer based on porous material can reach an efficiency of 62% [1], a more thoroughly investigation of the soottrap based reformer and an optimized design, could make it competitive.

In the third numerical study of this diploma thesis a chemical kinetic simulation in a model of the reformer were conducted. The domain which represented the soot trap was an empty space which was simulated as a porous packed bed and had not the real geometry, however was tried to represent the real pressure drop according the aforementioned of second simulation.. The thermal losses were not calculated in detail but they were approached by the comparing of the temperature profile of simulation with experiment. A reduced mechanism of 19 species were used. The cases which was simulated were for air equivalence ratios 0,42, 0,46, 0,5, 0,6 and for thermal load 1,5kW. The results of the chemical species were compared with the experimental at the exit of the reformer and it was observed a good agreement except from the methane volume fractions where the simulation over predicted it .This was attributed in that the reactions path of C_2 which consume the CH_4 and leads to the precursors of soot, does not exist in this reduced mechanism.This is important since the cases which were simulated were understoichiometric. Furthermore the GRI-MECH DRM19 such as the most GRI-MECH are optimized for stoichiometric and lean combustion. Therefore in a future work a bigger mechanism could be used and also a more detail calculation in the thermal losses could be achieved. Concerning the pressure drop in soot trap the agreement between experiment and

simulation was satisfactory. Although this approach has the disadvantage of non real residence time of the flow in the domain of soot trap. However in a future work could be used for a numerical study which was the first idea of this diploma thesis but was not realized. The first step would be a chemical kinetic study in the conical section. This requests a real pressure drop downstream which results from the characteristics of soot trap and this has already achieved in this thesis. In a second step a symmetric model channel of the soot trap would be created and would have for initial condition the results of the exit of conical sections of first step simulation. This aims to study the flow and chemical kinetics inside of the soot trap.

List of References

[1] Experimental study of hydrogen production and soot particulate matter emissions from rich-combustion in inert porous media (Alexandra Loukou et al. 2012)

[2] Experimental analysis of soot abatement in reducing syngas for high temperature fuel cell feeding (A. Raimondi et al. 2011)

[3] Hydrogen production by thermal partial oxidation of hydrocarbon fuels in porous media based reformer (Z. Al-Hamamre et al. 2008)

[4] New concept for soot removal from a syngas mixture (A. Raimondi et al. 2009)

[5] Flame stabilization of highly diffusive gas mixtures in porous inert media (Trimis and Wawrzinek 2003)

[6] Detailed kinetic modeling of the T-POX reforming process using a reactor network approach (G. Vourliotakis et al. 2008)

[7] Quasi-1D and 3D TPOX porous media diffuser reformer model (J.M.C Pereira et al. 2010)

[8] Heat transfer characteristics of a porous radiant burner under the influence of a 2-D radiation field (Prabal Talukdar et al. 2004)

[9] Hydrogen production from rich combustion in porous media (H. Pedersen-Mjaanes et al. 2004)

[10] Theoretical analysis of porous radiant burners under 2-D radiation field using discrete ordinates method (Keshtkar and Nassab 2009)

[11] Turns, S.R. “An Introduction to Combustion”, McGraw-Hill, 2000

[12] Spalding, D.B. “Combustion and Mass Transfer”, Pergamon Press, 1978

[13] Glassman, I. “Combustion”, 3rd Ed., Academic Press, 1996

[14]Kuo, K.K. “Principles of Combustion”, Wiley, 1984

[15] Di Huang, 2011, *Modeling of Diesel Particulate Filter Filtration and regeneration for transient driving schedules,* Michigan Technological University, 75 p.

[16] Modeling reacting flows with ANSYS CFD http://www.ansys.com/Resource+Library/Webinars/Modeling+Reacting+Flows+with+ANSYS+CFD+(Part+-+3)

[17] http://www.me.berkeley.edu/drm/#performance Reduced Reaction Sets based on GRI-Mech 1.2, University of California at Berkeley (Andrei Kazakov and Michael Frenklach)

[18] "Systematic Development of Reduced Reaction Mechanisms for Dynamic Modeling," M. Frenklach, K. Kailasanath and E. S. Oran, *Progress in Astronautics and Aeronautics* **105**(2), 365-376 (1986).

[19] "Detailed Reduction of Reaction Mechanisms for Flame Modeling," H. Wang and M. Frenklach, *Combust. Flame* **87**, 365-370 (1991).

[20] "Reduction of Chemical Reaction Models," M. Frenklach, in *Numerical Approaches to Combustion Modeling* (E. S. Oran and J. P. Boris, Eds.), Progress in Astronautics and Aeronautics, Vol. 135, American Institute of Aeronautics and Astronautics, Washington, D.C., 1991, pp. 129-154.

[21] K. Siegmann, K. Sattler, and H.C. Siegmann: Clustering at high temperatures: carbon formation in combustion, Journal of Electron Spectroscopy and Related Phenomena, Vol. 126, p. 191-202, 2002.

[22] M.S. Skjoth-Rasmussen: Modelling of Soot Formation in Autothermal Reforming, Ph.D. Thesis, Kongens Lyngby, 2003.

[23] H. Bockhorn: Soot Formation in Combustion, Mechanisms and Models, Springer Verlag, 1994.

[24] Michael Frenklach: Reaction mechanisms of soot formation in flames, Phys. Chem. Cem. Phys., Vol. 4, p. 2028-2037, 2002.

[25] H.F. Calcote and R.J. Gill in Soot Formation and Combustion, Mechanisms and Models, H. Bockhorn (ed.), Springer-Verlag, Berlin, p. 442, 1994.

[26] H. Richter and J.B. Howard: Formation of polycyclic aromatic hydrocarbons and their growth to soot—a review of chemical reaction pathways, Progress in Energy and Combustion Science, Vol. 26, p. 565–608, 2000.

[27] P.A. Baron and K. Willeke: Aerosol measurement; Principles, Techniques, and Applications, second edition, Wiley-Interscience, 2001.

[28] H. Burtscher: Physical characterization of particulate emissions from diesel engines: a review, Aerosol Science, Vol. 36, p. 896-932, 2005.

[29] A. De Filippo, L.A. Sgro, G. Lanzuolo, and A. D'Alessio: Probe measurement and numerical model predictions of evolving size distributions in premixed flames, Combustion and Flame, Vol. 156, p. 1744-1754, 2009.

[30] Ch. Asbach, H. Kaminski, H. Fissan, Ch. Monz, D. Dahmann, S. Mülhopt, H.R. Paur, H.J. Kiesling, F. Herrmann, M. Voetz, T. A. J. Kuhlbusch: Comparison of four mobility particle sizers with different time resolution for stationary exposure measurements, Journal Nanopart. Res., Vol. 11, p.1593–1609, Springer, 2009.

[31] Ü.Ö. Köylü, C.S. McEnally, D.E. Rosner, and L.D. Pfefferle: Simultaneous Measurements of Soot Volume Fraction and Particle Size / Microstructure in Flames Using a Thermophoretic Sampling Technique, Combustion and Flame, Vol. 110, p. 494-507, 1997.

[32] H. Hepp and K. Siegmann: Mapping of Soot Particles in a Weakly Sooting Diffusion Flame by Aerosol Techniques, Combustion and Flame, Vol. 115, p. 275–283, 1998.

[33] M.M. Maricq: Size and charge of soot particles in rich premixed ethylene flames, Combustion and Flame, Vol. 137, p. 340–350, 2004.

[34] S. J. Harris and M. M. Maricq: Signature size distributions for diesel and gasoline engine exhaust particulate matter, Aerosol Science, Vol. 32, p. 749-764, 2001.

[35] Aerosol Instrument Manager, Software for Scanning Mobility Particle Sizer TM (SMPSTM) Spectrometer, User's Manual, P/N 1930038, Revision G, October 2006.

[36] Diploma thesis with the topic: Study on the influence of water addition on the characteristics of thermal partial oxidation. Technical University Bergakademie Freiberg(Isabel Frenzel, 2010)

[37] J.S. Bhatt and R.P. Lindstedt: Analysis of the impact of agglomeration and surface chemistry models on soot formation and oxidation, Proceedings of the Combustion Institute, Vol. 32, p. 713–720, 2009.

[38] B. Zhao, Z. Yang, M.V. Johnston, H. Wang, A.S. Wexler, Michael Balthasar, and M. Kraft: Measurement and numerical simulation of soot particle size distribution functions in a laminar premixed ethylene oxygen- argon flame, Combustion and Flame, Vol. 133, p. 173–188, 2003.

[39] M.M. Maricq, S. J. Harris, and J.J. Szente: Soot size distributions in rich premixed ethylene flames, Combustion and Flame, Vol. 132, p. 328–342, 2003.

[40] S.L. Manzello, D.B. Lenhert, A. Yozgatligil, M.T. Donovan, G.W. Mulholland, M.R. Zachariah, and Wing Tsang: Soot particle size distributions in a well-stirred reactor/plug flow reactor, Proceedings of the Combustion Institute, Vol. 31, p. 675–683, 2007.

Appendix

Appendix A

The relative and absolute errors of oxygen, methane and mixture mass as was calculated from the products based on the accuracy of gas analyzer

1st exp.				Eq.{4.28}	Eq.{4.35}			Eq.{4.36}
N [kW]	λ	δ_{Xi}	$\frac{\delta_{m_{O_2,pr}}}{m_{O_2,pr}}$	$\delta_{m_{O_2,pr}}$	$\delta_{m_{CH_4,pr}}$	$\frac{\delta_{m_{CH_4,pr}}}{m_{CH_4,pr}}$	$\delta_{m_{mix,pr}}$	$\frac{\delta_{m_{mix,pr}}}{m_{mix,pr}}$
1,5	0,4	±1,00%	±11,94%	±5,16196E-06	±5,50963E-06	±17,51%	±7,54996E-06	±3,18%
1,5	0,42	±1,00%	±11,86%	±5,3828E-06	±5,59796E-06	±17,78%	±7,76606E-06	±3,14%
1,5	0,45	±1,00%	±11,80%	±5,73948E-06	±5,85397E-06	±18,05%	±8,19821E-06	±3,11%
1,5	0,5	±1,00%	±11,69%	±6,31784E-06	±6,20047E-06	±18,63%	±8,85217E-06	±3,05%
1,5	0,52	±1,00%	±11,61%	±6,52468E-06	±6,33301E-06	±18,81%	±9,09277E-06	±3,02%
2	0,4	±1,00%	±11,89%	±6,85235E-06	±7,70671E-06	±17,14%	±1,03125E-05	±3,23%
2	0,45	±1,00%	±11,78%	±7,63928E-06	±7,85631E-06	±17,95%	±1,09581E-05	±3,11%
2	0,5	±1,00%	±11,53%	±8,30605E-06	±8,27223E-06	±18,42%	±1,17226E-05	±3,02%
2nd exp.								
1	0,6	±1,00%	±10,76%	±4,65032E-06	±4,31989E-06	±19,62%	±6,3472E-06	±2,79%
1,5	0,5	±1,00%	±11,47%	±6,19507E-06	±6,07694E-06	±18,60%	±8,67802E-06	±2,99%
1,5	0,52	±1,00%	±11,38%	±6,39322E-06	±6,18951E-06	±18,81%	±8,8985E-06	±2,96%
1,5	0,5	±1,00%	±11,40%	±6,15715E-06	±5,74173E-06	±19,43%	±8,41891E-06	±2,94%
1,5	0,46	±1,00%	±11,72%	±5,82702E-06	±5,84445E-06	±18,23%	±8,25299E-06	±3,07%
1,5	0,42	±1,00%	±11,79%	±5,35125E-06	±5,58257E-06	±17,70%	±7,73311E-06	±3,12%
1,5	0,42	±1,00%	±11,60%	±5,26442E-06	±5,61531E-06	±17,48%	±7,69713E-06	±3,10%
1,5	0,42	±1,00%	±11,54%	±5,23566E-06	±5,58242E-06	±17,47%	±7,65347E-06	±3,09%
1,5	0,42	±1,00%	±11,50%	±5,21837E-06	±5,56386E-06	±17,48%	±7,6281E-06	±3,08%
1,5	0,42	±1,00%	±11,45%	±5,19636E-06	±5,52183E-06	±17,49%	±7,5824E-06	±3,06%
1,5	0,4	±1,00%	±11,25%	±4,86001E-06	±4,86977E-06	±18,25%	±6,88E-06	±2,96%
1,5	0,5	±1,00%	±11,30%	±6,10435E-06	±6,08713E-06	±18,31%	±8,62069E-06	±2,97%
1,5	0,5							
1,5	0,6	±1,00%	±11,32%	±7,33924E-06	±7,10578E-06	±19,03%	±1,02155E-05	±2,95%
1,5	0,6	±1,00%	±11,33%	±7,34581E-06	±7,01756E-06	±19,15%	±1,01591E-05	±2,94%

Appendix B

The masses of methane and oxygen which were calculated from wet syngas and the mass deviation which was calculated from equation 4.21.

1st exp.			Eq.{4.19}		Eq.{4.20}		Eq.{4.22}		Eq.{4.21}
N [kW]	λ	m_{N2} [kg]	$m_{ch4,pr}$ [kg]	$m_{ch4\ f.c}$ [kg]	$m_{o2,pr}$ [kg]	$m_{O2,f.c}$ [kg]	$m_{mix,pr}$[kg]	$m_{mix\ f.c}$ [kg]	Dm
1,5	0,4	0,00016258	3,1472E-05	2,997E-05	4,322E-05	4,322E-05	0,00023727	0,00023577	-0,64%
1,5	0,42	0,00017071	3,1485E-05	2,997E-05	4,538E-05	4,538E-05	0,00024757	0,00024606	-0,62%
1,5	0,45	0,0001829	3,2425E-05	2,997E-05	4,862E-05	4,862E-05	0,00026395	0,00026149	-0,94%
1,5	0,5	0,00020323	3,3287E-05	2,997E-05	5,402E-05	5,402E-05	0,00029053	0,00028722	-1,15%
1,5	0,52	0,00021135	3,3663E-05	2,997E-05	5,618E-05	5,618E-05	0,0003012	0,00029751	-1,24%
2	0,4	0,00021677	4,4955E-05	3,996E-05	5,762E-05	5,762E-05	0,00031935	0,00031436	-1,59%
2	0,45	0,00024387	4,3772E-05	3,996E-05	6,483E-05	6,483E-05	0,00035247	0,00034866	-1,09%
2	0,5	0,00027097	4,4907E-05	3,996E-05	7,203E-05	7,203E-05	0,0003879	0,00038296	-1,29%
2nd exp.									
1	0,6	0,00016258	2,2014E-05	1,998E-05	4,322E-05	4,322E-05	0,00022781	0,00022578	-0,90%
1,5	0,5	0,00020323	3,2669E-05	2,997E-05	5,402E-05	5,402E-05	0,00028992	0,00028722	-0,94%
1,5	0,52	0,00021135	3,2905E-05	2,997E-05	5,618E-05	5,618E-05	0,00030044	0,00029751	-0,99%
1,5	0,5	0,00020323	2,9555E-05	2,997E-05	5,402E-05	5,402E-05	0,0002868	0,00028722	0,14%
1,5	0,46	0,00018697	3,2066E-05	2,997E-05	4,97E-05	4,97E-05	0,00026873	0,00026664	-0,79%
1,5	0,42	0,00017071	3,1541E-05	2,997E-05	4,538E-05	4,538E-05	0,00024763	0,00024606	-0,64%
1,5	0,42	0,00017071	3,2128E-05	2,997E-05	4,538E-05	4,538E-05	0,00024822	0,00024606	-0,88%
1,5	0,42	0,00017071	3,196E-05	2,997E-05	4,538E-05	4,538E-05	0,00024805	0,00024606	-0,81%
1,5	0,42	0,00017071	3,1837E-05	2,997E-05	4,538E-05	4,538E-05	0,00024792	0,00024606	-0,76%
1,5	0,42	0,00017071	3,1565E-05	2,997E-05	4,538E-05	4,538E-05	0,00024765	0,00024606	-0,65%
1,5	0,4	0,00016258	2,6683E-05	2,997E-05	4,322E-05	4,322E-05	0,00023248	0,00023577	1,39%
1,5	0,5	0,00020323	3,3252E-05	2,997E-05	5,402E-05	5,402E-05	0,0002905	0,00028722	-1,14%
1,5	0,5								
1,5	0,6	0,00024387	3,7338E-05	2,997E-05	6,483E-05	6,483E-05	0,00034604	0,00033867	-2,18%
1,5	0,6	0,00024387	3,664E-05	2,997E-05	6,483E-05	6,483E-05	0,00034534	0,00033867	-1,97%

Appendix C

The reduced GRI-MECH (DRM 19) of Andrei Kazakov and Michael Frenklach of University of California at Berkeley

```
!<><><><><><><><><><><><><><><><><><><><><><><><><><><><><><><><><><><><
><><!
!  Reduced version of GRI-MECH 1.2. 19 species ( + N2, AR); 84
reactions. !
!                                 PennState Dec, 1994
!
!<><><><><><><><><><><><><><><><><><><><><><><><><><><><><><><><><><><><
><><!
ELEMENTS
O  H  C  N  AR
END
SPECIES
H2      H       O       O2      OH      H2O     HO2
CH2     CH2(S)  CH3     CH4     CO      CO2     HCO
CH2O    CH3O    C2H4    C2H5    C2H6
N2      AR
END
REACTIONS
O+H+M<=>OH+M                             5.000E+17   -1.000      0.00
H2/2.00/ H2O/6.00/ CH4/2.00/ CO/1.50/ CO2/2.00/ C2H6/3.00/ AR/0.70/
O+H2<=>H+OH                              5.000E+04    2.670   6290.00
O+HO2<=>OH+O2                            2.000E+13    0.000      0.00
O+CH2<=>H+HCO                            8.000E+13    0.000      0.00
O+CH2(S)<=>H+HCO                         1.500E+13    0.000      0.00
O+CH3<=>H+CH2O                           8.430E+13    0.000      0.00
O+CH4<=>OH+CH3                           1.020E+09    1.500   8600.00
O+CO+M<=>CO2+M                           6.020E+14    0.000   3000.00
H2/2.00/ O2/6.00/ H2O/6.00/ CH4/2.00/ CO/1.50/ CO2/3.50/ C2H6/3.00/
AR/0.50/
O+HCO<=>OH+CO                            3.000E+13    0.000      0.00
O+HCO<=>H+CO2                            3.000E+13    0.000      0.00
O+CH2O<=>OH+HCO                          3.900E+13    0.000   3540.00
O+C2H4<=>CH3+HCO                         1.920E+07    1.830    220.00
O+C2H5<=>CH3+CH2O                        1.320E+14    0.000      0.00
O+C2H6<=>OH+C2H5                         8.980E+07    1.920   5690.00
O2+CO<=>O+CO2                            2.500E+12    0.000  47800.00
O2+CH2O<=>HO2+HCO                        1.000E+14    0.000  40000.00
H+O2+M<=>HO2+M                           2.800E+18   -0.860      0.00
O2/0.00/ H2O/0.00/ CO/0.75/ CO2/1.50/ C2H6/1.50/ N2/0.00/ AR/0.00/
H+2O2<=>HO2+O2                           3.000E+20   -1.720      0.00
H+O2+H2O<=>HO2+H2O                       9.380E+18   -0.760      0.00
H+O2+N2<=>HO2+N2                         3.750E+20   -1.720      0.00
H+O2+AR<=>HO2+AR                         7.000E+17   -0.800      0.00
H+O2<=>O+OH                              8.300E+13    0.000  14413.00
2H+M<=>H2+M                              1.000E+18   -1.000      0.00
H2/0.00/ H2O/0.00/ CH4/2.00/ CO2/0.00/ C2H6/3.00/ AR/0.63/
2H+H2<=>2H2                              9.000E+16   -0.600      0.00
2H+H2O<=>H2+H2O                          6.000E+19   -1.250      0.00
2H+CO2<=>H2+CO2                          5.500E+20   -2.000      0.00
H+OH+M<=>H2O+M                           2.200E+22   -2.000      0.00
H2/0.73/ H2O/3.65/ CH4/2.00/ C2H6/3.00/ AR/0.38/
H+HO2<=>O2+H2                            2.800E+13    0.000   1068.00
H+HO2<=>2OH                              1.340E+14    0.000    635.00
H+CH2(+M)<=>CH3(+M)                      2.500E+16   -0.800      0.00
     LOW  /  3.200E+27   -3.140   1230.00/
```

```
     TROE/  0.6800   78.00  1995.00  5590.00 /
H2/2.00/ H2O/6.00/ CH4/2.00/ CO/1.50/ CO2/2.00/ C2H6/3.00/ AR/0.70/
H+CH3(+M)<=>CH4(+M)                       1.270E+16   -0.630    383.00
     LOW  /  2.477E+33   -4.760   2440.00/
     TROE/  0.7830   74.00  2941.00  6964.00 /
H2/2.00/ H2O/6.00/ CH4/2.00/ CO/1.50/ CO2/2.00/ C2H6/3.00/ AR/0.70/
H+CH4<=>CH3+H2                            6.600E+08    1.620  10840.00
H+HCO(+M)<=>CH2O(+M)                      1.090E+12    0.480   -260.00
     LOW  /  1.350E+24   -2.570   1425.00/
     TROE/  0.7824  271.00  2755.00  6570.00 /
H2/2.00/ H2O/6.00/ CH4/2.00/ CO/1.50/ CO2/2.00/ C2H6/3.00/ AR/0.70/
H+HCO<=>H2+CO                             7.340E+13    0.000      0.00
H+CH2O(+M)<=>CH3O(+M)                     5.400E+11    0.454   2600.00
     LOW  /  2.200E+30   -4.800   5560.00/
     TROE/  0.7580   94.00  1555.00  4200.00 /
H2/2.00/ H2O/6.00/ CH4/2.00/ CO/1.50/ CO2/2.00/ C2H6/3.00/
H+CH2O<=>HCO+H2                           2.300E+10    1.050   3275.00
H+CH3O<=>OH+CH3                           3.200E+13    0.000      0.00
H+C2H4(+M)<=>C2H5(+M)                     1.080E+12    0.454   1820.00
     LOW  /  1.200E+42   -7.620   6970.00/
     TROE/  0.9753  210.00   984.00  4374.00 /
H2/2.00/ H2O/6.00/ CH4/2.00/ CO/1.50/ CO2/2.00/ C2H6/3.00/ AR/0.70/
H+C2H5(+M)<=>C2H6(+M)                     5.210E+17   -0.990   1580.00
     LOW  /  1.990E+41   -7.080   6685.00/
     TROE/  0.8422  125.00  2219.00  6882.00 /
H2/2.00/ H2O/6.00/ CH4/2.00/ CO/1.50/ CO2/2.00/ C2H6/3.00/ AR/0.70/
H+C2H6<=>C2H5+H2                          1.150E+08    1.900   7530.00
H2+CO(+M)<=>CH2O(+M)                      4.300E+07    1.500  79600.00
     LOW  /  5.070E+27   -3.420  84350.00/
     TROE/  0.9320  197.00  1540.00 10300.00 /
H2/2.00/ H2O/6.00/ CH4/2.00/ CO/1.50/ CO2/2.00/ C2H6/3.00/ AR/0.70/
OH+H2<=>H+H2O                             2.160E+08    1.510   3430.00
2OH<=>O+H2O                               3.570E+04    2.400  -2110.00
OH+HO2<=>O2+H2O                           2.900E+13    0.000   -500.00
OH+CH2<=>H+CH2O                           2.000E+13    0.000      0.00
OH+CH2(S)<=>H+CH2O                        3.000E+13    0.000      0.00
OH+CH3<=>CH2+H2O                          5.600E+07    1.600   5420.00
OH+CH3<=>CH2(S)+H2O                       2.501E+13    0.000      0.00
OH+CH4<=>CH3+H2O                          1.000E+08    1.600   3120.00
OH+CO<=>H+CO2                             4.760E+07    1.228     70.00
OH+HCO<=>H2O+CO                           5.000E+13    0.000      0.00
OH+CH2O<=>HCO+H2O                         3.430E+09    1.180   -447.00
OH+C2H6<=>C2H5+H2O                        3.540E+06    2.120    870.00
HO2+CH2<=>OH+CH2O                         2.000E+13    0.000      0.00
HO2+CH3<=>O2+CH4                          1.000E+12    0.000      0.00
HO2+CH3<=>OH+CH3O                         2.000E+13    0.000      0.00
HO2+CO<=>OH+CO2                           1.500E+14    0.000  23600.00
CH2+O2<=>OH+HCO                           1.320E+13    0.000   1500.00
CH2+H2<=>H+CH3                            5.000E+05    2.000   7230.00
CH2+CH3<=>H+C2H4                          4.000E+13    0.000      0.00
CH2+CH4<=>2CH3                            2.460E+06    2.000   8270.00
CH2(S)+N2<=>CH2+N2                        1.500E+13    0.000    600.00
CH2(S)+AR<=>CH2+AR                        9.000E+12    0.000    600.00
CH2(S)+O2<=>H+OH+CO                       2.800E+13    0.000      0.00
CH2(S)+O2<=>CO+H2O                        1.200E+13    0.000      0.00
CH2(S)+H2<=>CH3+H                         7.000E+13    0.000      0.00
CH2(S)+H2O<=>CH2+H2O                      3.000E+13    0.000      0.00
CH2(S)+CH3<=>H+C2H4                       1.200E+13    0.000   -570.00
CH2(S)+CH4<=>2CH3                         1.600E+13    0.000   -570.00
CH2(S)+CO<=>CH2+CO                        9.000E+12    0.000      0.00
```

```
CH2(S)+CO2<=>CH2+CO2                      7.000E+12    0.000       0.00
CH2(S)+CO2<=>CO+CH2O                      1.400E+13    0.000       0.00
CH3+O2<=>O+CH3O                           2.675E+13    0.000   28800.00
CH3+O2<=>OH+CH2O                          3.600E+10    0.000    8940.00
2CH3(+M)<=>C2H6(+M)                       2.120E+16   -0.970     620.00
     LOW  /  1.770E+50   -9.670   6220.00/
     TROE/  0.5325  151.00  1038.00  4970.00 /
H2/2.00/ H2O/6.00/ CH4/2.00/ CO/1.50/ CO2/2.00/ C2H6/3.00/ AR/0.70/
2CH3<=>H+C2H5                             4.990E+12    0.100   10600.00
CH3+HCO<=>CH4+CO                          2.648E+13    0.000       0.00
CH3+CH2O<=>HCO+CH4                        3.320E+03    2.810    5860.00
CH3+C2H6<=>C2H5+CH4                       6.140E+06    1.740   10450.00
HCO+H2O<=>H+CO+H2O                        2.244E+18   -1.000   17000.00
HCO+M<=>H+CO+M                            1.870E+17   -1.000   17000.00
H2/2.00/ H2O/0.00/ CH4/2.00/ CO/1.50/ CO2/2.00/ C2H6/3.00/
HCO+O2<=>HO2+CO                           7.600E+12    0.000     400.00
CH3O+O2<=>HO2+CH2O                        4.280E-13    7.600   -3530.00
C2H5+O2<=>HO2+C2H4                        8.400E+11    0.000    3875.00
END
```